UNIVERSITY OF CALIFORNIA SAN DIEGO

# High-Throughput Screening of Metal-Organic Framework and Polymer Composites for Degradation of Nerve Agent Simulants

A dissertation submitted in partial satisfaction of the requirements
for the degree Doctor of Philosophy

in

Chemistry

by

Joseph M. Palomba

Committee in charge:

Professor Seth M. Cohen, Chair
Professor Joshua S. Figueroa
Professor Kamil Godula
Professor Darren J. Lipomi
Professor Jeffery D. Rinehart

2021

The Dissertation of Joseph M. Palomba is approved, and it is acceptable in quality and form for publication on microfilm and electronically:

_____

_____

_____

_____

_____

Chair

University of California San Diego

2021

DEDICATION

To all those who I loved and lost during my Ph. D.-

*Mark Dobrott*

*Aunt (Suzanne) Susie Sandock*

*Aunt Judy and Uncle Don*

*Uncle (Sebastian) Sam and Aunt Carmie Calabro*

*Professor Chia-Kuang (Frank) Tsung, you supported me on this path from day one,*

*but most of all you inspired me.*

*Mary (Granny) Palomba-Bourke, I will miss you the most.*

To my enormous support system of family and friends- I could not have done it

without you and I had some good laughs along the way

To Alyssa- the best sister someone could ask for

To Mom and Dad- for all the support and patience

To Tash- for everything

# EPIGRAPH

*Our successes and failures come and go—*

*They neither define us nor do they determine our worthiness.*

*-Kristen Neff*

TABLE OF CONTENTS

LIST OF FIGURES

LIST OF TABLES

ACKNOWLEDGEMENTS

I would like to acknowledge my advisor Seth M. Cohen for his support of my research over my doctoral study. I have learned a great deal from you and the people who you surround yourself with. You gave me the opportunity to grow and learn how to be a professional scientist.

I would like to acknowledge all my collaborators from other labs who I had the pleasure of exchanging ideas with and learning from. My work and training as a scientist were especially supported by Gregory W. Peterson and Dr. Jared B. DeCoste who helped me in many projects.

I would like to acknowledge my mentors both in and out of lab since I began as a scientist: Prof. Frank C. K. Tsung, Dr. Joseph V. Morabito, Prof. Alexandre Lieb, Dr. Jakob G. Eggebrecht, Dr. Michael S. Denny Jr., Dr. Cy V. Credille, Dr. Jessica C. Moreton, Dr. Sergio Ayala Jr., Dr. Katherine A. Nadler, Dr. Christine N. Morrison, Dr. Yuji Katayama, Dr. Kyle C. Bentz, and Dr. Kathleen E. Prosser. You answered my questions even when they never stopped, you demonstrated the way when things seemed hard, you were motivated when I was not, and most of all you were friends when I needed them.

I also would like to acknowledge the members of the Cohen Lab, I relied on you a lot over the years and learned even more from this wonderful and diverse group.

Chapter 2, in part, is a reprint of the following material “Joseph M. Palomba, Cy V. Credille, Mark Kalaj, Jared B. DeCoste, Gregory W. Peterson, Trenton M. Tovar, and Seth M. Cohen, High-throughput screening of solid-state catalysts for nerve agent

degradation, *Chem. Commun.* **2018,** *54*, 5768-5771." The dissertation author was the primary author this manuscript and gratefully acknowledges the contributions of coauthors.

Chapter 3, in part, is a reprint of the following materials as listed: "Mark Kalaj, Joseph M. Palomba, Kyle C. Bentz, Seth M. Cohen, Multiple functional groups in UiO-66 improve chemical warfare agent simulant degradation *Chem. Commun.,* **2019***, 55,* 5367-5370;" "Mark Kalaj, Mohammad R. Momeni, Kyle C. Bentz, Kyle S. Barcus, Joseph M. Palomba, Francesco Paesani, Seth M. Cohen, Halogen bonding in UiO-66 frameworks promotes superior chemical warfare agent simulant degradation *Chem. Commun.,* **2019***, 55,* 3481-3484;" "Mark Kalaj, Michael S. Denny Jr., Kyle C. Bentz, Joseph M. Palomba, Seth M. Cohen, Nylon–MOF Composites through Postsynthetic Polymerization" *Angew. Chem. Int. Ed.,* **2019**, *58*, 2336;" "Jessica C. Moreton, Joseph M. Palomba, Seth M. Cohen, Liquid-Phase Applications of Metal–Organic Framework Mixed-Matrix Membranes Prepared from Poly(ethylene-co-vinyl acetate) *ACS Appl. Polym. Materials* **2020,** *2*, 2063-2069." The dissertation author was a coauthor of these manuscripts and gratefully acknowledges the contributions of coauthors.

Chapter 4, in part, is a reprint of the following material "Joseph M. Palomba, Steven P. Harvey, Mark Kalaj, Brian R. Pimentel, Jared B. DeCoste, Gregory W. Peterson, and Seth M. Cohen, High-Throughput Screening of MOFs for Breakdown of V-Series Nerve Agents *ACS Appl. Mater. Interfaces* **2020,** *12*, 14672-14677." The dissertation author was the primary author of this manuscript and gratefully acknowledges the contributions of coauthors.

Chapter 5, in part, is a reprint of the following material “Joseph M. Palomba, David M. Wirth, Jin Yeong Kim, Evan M. Clarke, Gregory W. Peterson, Jonathan K. Pokorski, and Seth M. Cohen, Strong, Ductile MOF-Polyurethane Urea Composites” submitted for publication. The dissertation author was the primary author of this manuscripts and gratefully acknowledges the contributions of coauthors.

# VITA

## Education

2011 Bachelor of Science, Boston College

2017 Master of Science, University of California San Diego

2021 Doctor of Philosophy, University of California San Diego

## Publications

Palomba J. M., Wirth D. M., Kim J. Y., Clarke E. M., Peterson G. W., Pokorski J. K. Cohen S. M., "Strong, Ductile MOF-Polyurethane Urea Composites" *Submitted for Publication*

Moreton J. C., Palomba J. M., Cohen S. M., "Liquid-Phase Applications of Metal-Organic Framework Mixed-Matrix Membranes Prepared from Poly(ethylene-co-vinyl acetate)" *ACS Appl. Polym. Mater.*, **2020**, *2*, 2063-2069

Palomba J. M., Harvey S. P., Kalaj M., Pimentel B. R., DeCoste J. B., Peterson G. W., Cohen S. M., "High-Throughput Screening of MOFs for Breakdown of V-Series Nerve Agents" *ACS Appl. Mater. Interfaces*, **2020**, *12*, 14672-14677

Kalaj M., Bentz K. C., Ayala Jr. S., Palomba J. M., Barcus K. S., Katayama Y., Cohen S. M. "MOF-Polymer Hybrid Materials: From Simple Composites to Tailored Architectures" *Chem. Rev.*, **2020**, *120*, 8267-8302

Kalaj M., Palomba J. M., Bentz K. C., Cohen S. M. "Multiple functional groups in UiO-66 improve chemical warfare agent simulant degradation" *Chem. Commun.*, **2019**, *55*, 5467-5370

Kalaj M., Momeni M. R., Bentz K. C., Barcus K. S., Palomba J. M., Paesani F., Cohen S. M. "Halogen bonding in UiO-66 frameworks promotes superior chemical warfare agent simulant degradation" *Chem. Commun.*, **2019**, *55*, 3481-3484

Kalaj M., Denny M. S., Bentz K. C., Palomba J. M., Cohen S. M. "Nylon-MOF Composites via Postsynthetic Polymerization" *Angew. Chem., Int. Ed.*, **2018**, *58*, 2336-2340

Palomba J. M., Ayala S., Cohen S. M. "polyMOF Formation from Kinked Polymer Ligands via ortho-Substitution" *Isl. J. Chem.*, **2018**, *58*, 1123-1126

Palomba J. M., Credille C. V., Kalaj M., DeCoste J. B., Peterson G. W., Tovar T. M., Cohen S. M. "High-Throughput Screening of Solid-State Catalysts for Nerve Agent Degradation" *Chem. Commun.*, **2018**, *54*, 5768-5771

Morabito J. V., Chou L., Li Z., Manna C. M., Petroff C. A., Kyada R. J., Palomba J. M., Byers J. A., and Tsung C. K. "Molecular Encapsulation beyond the Aperture Size Limit through Dissociative Linker Exchange in Metal-Organic Framework Crystals" *J. Am. Chem. Soc.*, **2014**, *136*, 12540-12543

Honors and Awards

| | |
|---|---|
| 2018 | Best Inorganic Poster – UC Chemical Symposium |
| 2019/ 2020 | Bouchet Honor Society – Honorable Mention |
| 2019 | Teddy Traylor Award for Research Excellence |
| 2019-2021 | Science Mathematics and Research for Transformation (SMART) Scholarship Program Awardee |

ABSTRACT OF THE DISSERTATION

High-Throughput Screening of Metal-Organic Framework and Polymer Composites for Degradation of Nerve Agent Simulants

by

Joseph M. Palomba

Doctor of Philosophy in Chemistry

University of California San Diego, 2021

Professor Seth M. Cohen, Chair

Metal-organic frameworks (MOFs) are crystalline porous materials with excellent gas storage capacities and unique chemical tunability. Their application as

new materials to uptake and degrade chemical warfare agents has been the topic of intense study over the last half-decade. Work by others proved that Zr-MOFs and polymer composites made from them are contenders for the next generation of personal protective equipment (PPE) for combatting nerve agents.

In an attempt to speed up discovery and understanding of MOF catalysts for nerve agent degradation, a high-throughput screening (HTS) assay was developed for a common nerve agent simulant. Chapter 2 outlines the development of this assay as well as the curation and screening results from the library of 93 MOFs and related materials.

Successful development and validation of the HTS assay led to targeted attempts to apply this method for both a wider array of MOFs as well as MOF-polymer composites. Chapter 3 uses the speed of HTS to investigate two groups of closely related MOFs that result in a wide range of catalytic activities. This chapter also adapts the HTS assay to analyze composites and again finds that small differences in materials changes the outcome of catalyst performance.

Chapter 4 describes the development of a new HTS assay with another nerve agent simulant that can be directly compared to results of the assay developed in Chapter 2. This new assay expands understanding of the degradation attempts by MOF catalysts to date. In addition, this new HTS method was compared to a medium-throughput method for monitoring breakdown of nerve agent VX and was confirmed by literature assay using $^{31}P$ NMR.

MOF catalysts design was paired with MOF-polymer composite design, when a new strong, ductile hybrid was developed in Chapter 5. Catalytically active MOFs were combined with a spandex polymer to target composites for durable PPE. The HTS assay was used to show catalytic ability of these composites and three processing methods demonstrated the versatility of these MOF-polymer composites.

# Chapter 1: An Introduction to Metal-Organic Frameworks and High-Throughput Screening

## 1.1 Metal-Organic Frameworks

Metal-organic frameworks (MOFs) are two- and three-dimensional porous solid-state materials that combine organic ligands and inorganic metal ions or clusters known as secondary building units (SBUs).[1, 2] By choosing multitopic organic ligands that bind two or more SBUs, an extended, crystalline material with permanent porosity can be formed. Since their discovery and description in 1990[3] (and the term MOF coined in 1995),[4] MOFs have become an active area of research as they provide both chemical tunability and possess high internal surface areas (typically >1000 $m^2/g$)[5-8] that makes them attractive for applications including gas/liquid uptake and separations. Furthermore, their crystallinity allows for atomic scale characterization not available for amorphous solids.[9-12]

## 1.2 Synthesis and Characterization of Metal-Organic Frameworks

MOFs are typically synthesized using solvothermal crystal growth conditions.[13] In recent years, as the field looks to scale up production, a number of new synthetic routes have been developed, including electrochemical, mechanochemical, and sonochemical techniques.[13-15] Ligand and metal combinations have provided access to a seemingly endless combination of two- and three-dimensional MOF structures and there has been modest success in designing these architectures de novo.[16-19] Relative reagent concentrations, solvents, and reaction conditions, including additives such as acids or bases have been used to alter the growth kinetics and have had some success in controlling crystal morphology. The use of monotopic carboxylic acids as “modulators”

has been studied for their effect on crystal size and shape, as well as the defects they introduce into the crystals.[20, 21]

While in principle, MOF ligands can be derived from any number of metal coordinating groups, in practice the field has extensively studied rigid, multi-carboxylate ligands. The diversity of MOFs can be seen in the preparation of materials with the same organic ligand, benzene dicarboxylic acid ($H_2$bdc, terephthalic acid), with three different metal sources: Zn(II), Al(III), or Zr(IV) (Figure 1.1). The most widely studied Zn-bdc MOF isomer, MOF-5(Zn) (a.k.a., isoreticular MOF-1, IRMOF-1) forms a $Zn_4O$ SBU at the corners of cubic pores formed by the ligand that extends in all three dimensions (Figure 1.1).[5] In contrast, a common Al-bdc MOF (MIL-53(Al), MIL = Materials Institute Lavoisier) forms a 1-D chain of $Al_2O_3$ as a SBU with diamond shaped pores that can expand or compress depending on the guest molecule (Figure 1.1).[22] Lastly, the common Zr-bdc MOF, UiO-66(Zr) (UiO = Universitetet i Oslo), forms a $Zr_6O_4(OH)_4$ SBU with 12 carboxylates that make a pore system with adjoined octahedral and tetrahedral pores (Figure 1.1).[23] A similar diversity in structure is observed with benzene tricarboxylic acid ($H_3$btc, trimesic acid) and Cu(II), Al(III), or Zr(IV) which give the structures CuBTC (a.k.a., HKUST-1(Cu), HKUST = Hong Kong University Science and Technology),[24] MIL-100(Al),[25] and MOF-808(Zr),[26] respectively (Figure 1.1). This diversity has been iterated many times with different metals and ligands to form tens of thousands of MOFs in the last 20 years.[27]

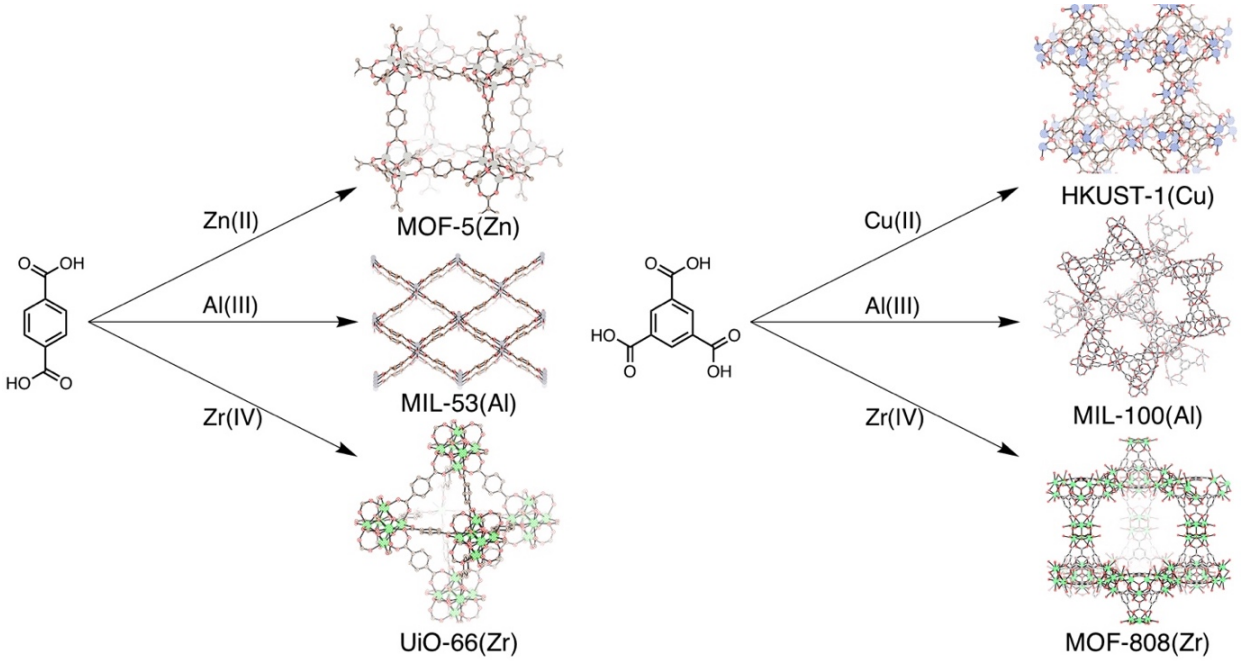


**Figure 1.1.** Common metal-organic frameworks (MOFs) built from simple carboxylates terephthalic acid (*left*, MOF-5(Zn), MIL-53(Al), and UiO-66(Zr)) and trimesic acid (*right*, HKUST-1(Cu), MIL-100(Al), and MOF-808(Zr)).

Materials are typically categorized as MOFs, as opposed to simple coordination polymers, based on their permanent porosity. The crystalline structures of MOFs are characterized through X-ray diffraction techniques, most common of which is powder X-ray diffraction (PXRD), where the bulk material is analyzed for long-range order. Early in MOF research the structure of many materials could only be solved using single-crystal X-ray diffraction (SCXRD), but synchrotron PXRD has been employed with Rietveld Refinement to solve powder-only crystal structures.[28] To assess porosity of these frameworks, MOFs are frequently dried and dosed with $N_2$ gas and analyzed using Brunauer–Emmett–Teller (BET) or Langmuir theory to determine the extent and volume of micropores in the material.[29, 30]

## 1.3 Modularity in Metal-Organic Frameworks

MOFs are synthesized as solid-state materials, but they can be readily modified by chemical modification and exchange. For example, using a ligand with a non-coordinating ancillary group like 2-bromoterephthalic acid under conditions for MOF-5(Zn) synthesis, a MOF can be formed with the functional ligand, termed MOF-5(Zn)-Br (a.k.a., IRMOF-2) (Figure 1.2).[19] Ligands functionalized with amino groups like 2-aminoterephthalic acid, can be similarly incorporated and the corresponding MOF-5(Zn)-$NH_2$ (a.k.a., IRMOF-3) can be prepared (Figure 1.2).[19] However, when functional groups on the ligand have a strong affinity for metal ions, the coordination of the ligands can result in a non-regular geometry. This is the case for 2-hydroxyterephthalic acid, where MOF-5(Zn)-OH cannot be directly synthesized as a pure phase (Figure 1.2).[31] The effect of ligand functionality is further exemplified by use of 2,5-dihydroxyterephthalic acid with Zn(II) salts that results in direct coordination of the hydroxyl groups and a structurally distinct MOF, CPO-27(Zn) (a.k.a., MOF-74(Zn)), with a chain of metals as the SBU and hexagonal channels (Figure 1.2).[32, 33]

The range of chemical functionality tolerated by MOF structures is broad,[34] including a single MOF with multiple ligands, termed a multivariate (MTV) MOF.[35] The benefit of MTV MOFs was first shown by Yaghi et. al. with an increase in gas selectivity using MOF-5(Zn) with three different functional ligands.[36] The strategy of using a mixture of building blocks to make an isostructural MOF has also been successful with mixed metal MOFs.[37] MOFs synthesized with either multiple ligands or multiple metals often have distinct, unexpected properties from their component building blocks.[35-37]

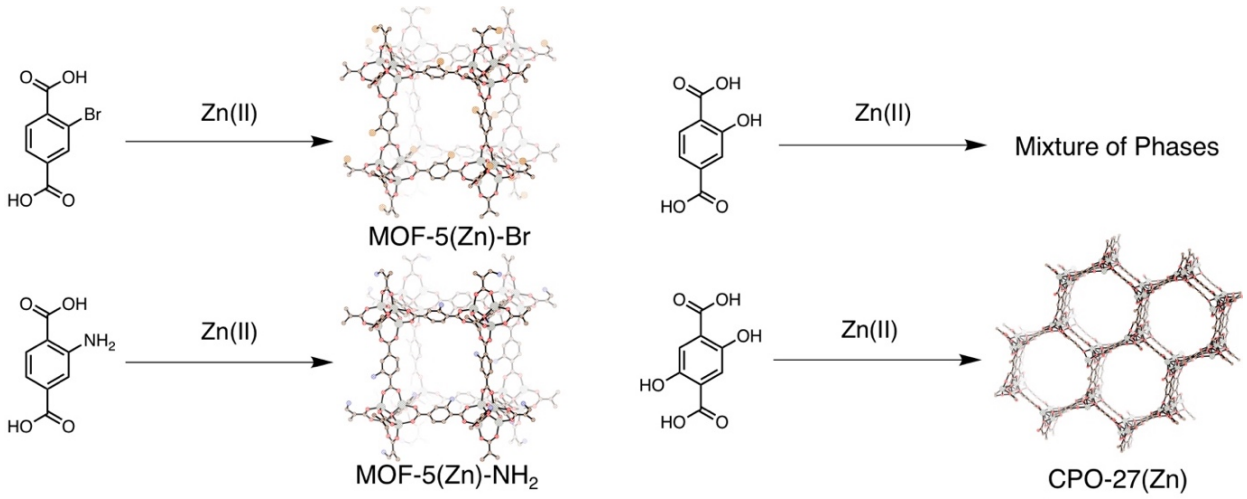


**Figure 1.2.** Examples of simple ligand substitutions that result in isostructural MOF-5(Zn) MOFs (*left*) and other ligand substitutions that result in a mixture or a different MOF phase (*right*).

To overcome some of the shortcomings of presynthetic functionality and greatly expand the scope organic functionality in MOFs, a number of postsynthetic techniques have been developed.[38] Postsynthetic techniques are chemical reactions carried out after formation and isolation of the MOF that impart some change on the material. An example of this was demonstrated with the canonical zeolitic imidazolate framework (ZIF) MOF, ZIF-8(Zn), that is synthesized with 2-methylimidazole, but cannot be made with imidazole (Figure 1.3).[39, 40] Through postsynthetic ligand exchange (PSE), the imidazole ligand can be incorporated without degrading the framework and the PSE results in a change in the pore size of the MOF (Figure 1.3). This concept of PSE can also be broadened to include the exchange of metals in the SBU. MOFs with liable metal-ligand bonds can be formed with one metal and incubated with another metal to achieve partial or full exchange. This was elegantly shown with SUMOF-1-Zn (SU = Stockholm

University) MOF, where, after incubation with Cu(II) ions, a single crystal-to-single crystal transformation occurs and the MOF is isolated as SUMOF-1-Cu.[41] Through these established methods, as well as an ever-evolving toolkit of synthetic approaches,[42, 43] the possibilities for designing and optimizing MOFs far exceeds those that can be accessed by direct solvothermal synthesis.

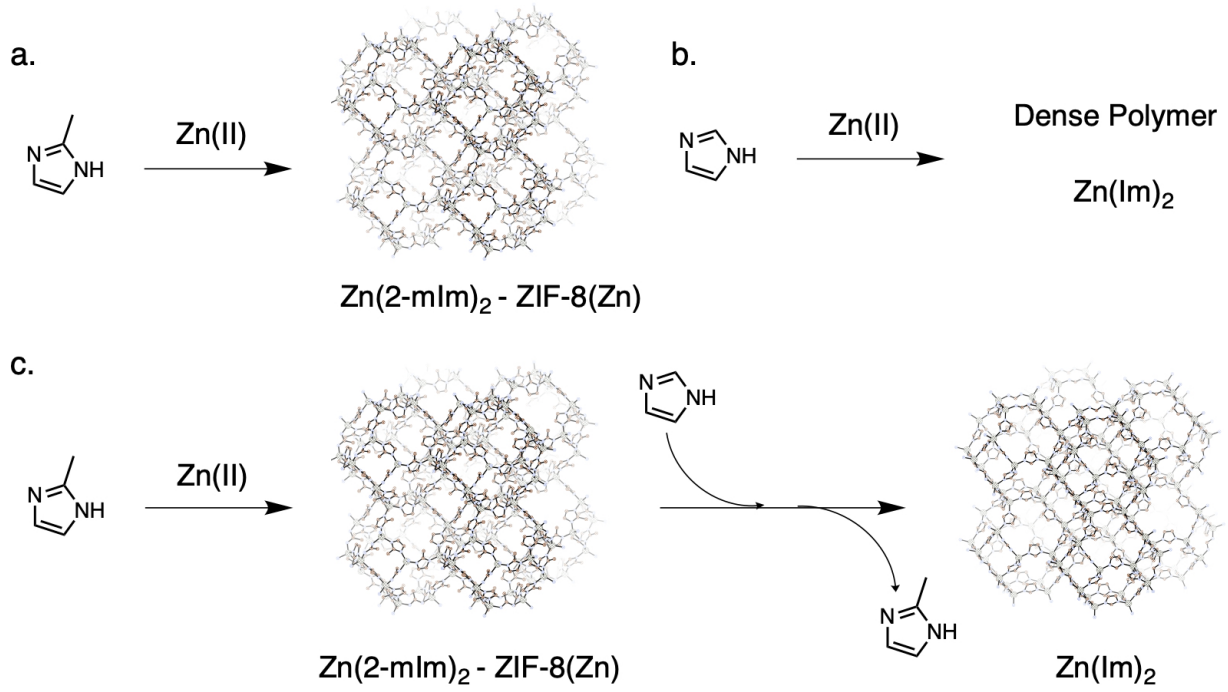


**Figure 1.3.** ZIF-8(Zn) 3D porous framework is formed from Zn(II) and 2-methylimidizole (2-mIm) (a) but the analogous framework cannot be formed from Zn(II) and imidazole (Im) and the synthesis results only in a dense coordination polymer (b). By synthesizing ZIF-8(Zn) first, a subsequent postsynthetic exchange reaction allows access to $Zn(Im)_2$ framework with same topology as parent ZIF-8(Zn) MOF (c).

In addition to exchange of ligands and metals, it is also possible to modify existing MOFs. The process of postsynthetic modification (PSM) is well demonstrated by the functionalization of MOF-5(Zn)-$NH_2$ with various alkyl anhydrides to form the amide

bonds.[44] The use of a ligand with long (>6 carbons), hydrophobic alkyl chains to form the MOF-5(Zn) framework directly (e.g., presynthetically) would be problematic because of solubility and sterics. This method was expanded to other frameworks including use in UiO-66(Zr) MOFs[17, 45] and has been iterated in many new and interesting ways.[38]

While controlled ligand and metal functionalization have been exploited to achieve a range of designer porous materials, equally important factors to consider for solid-state materials are the physical characteristics of the crystal. Factors like crystallite size and defect levels have a profound effect on the bulk properties of MOFs.[46-48] Crystallite size has been shown to affect gas sorption,[49] electrochemical processes,[50] and dynamics.[51] As MOFs move towards commercialization, methods to tune their properties have been more carefully studied.[52] The discovery and exploration of defective MOFs has also been investigated more closely in the past 8-10 years.[20, 21, 53, 54] Like any crystalline material, MOFs have imperfections in the order of their arrangements of atoms, most commonly missing or additional atoms. Specifically for MOFs, missing ligands and SBUs have been systematically studied.

A series of methods for identifying and quantifying defects has been proposed for specific systems, but due to the difficulty of completely understanding these defects, the number of systems explored is relatively low. In one example, the group of Lillereud used the combination of four experimental techniques to understand the relative defect levels and types in UiO-66(Zr) MOF (Figure 1.4).[21] The study showed that slight changes in synthetic conditions, such as p$K_a$ of acid modulator used, have a profound impact on resulting MOF defect levels and type (missing ligand or missing cluster). There are over

100 synthetic methods for UiO-66(Zr) reported in the literature using different reaction times, temperatures, and acid modulators, resulting in the chemical properties of these materials differing in defect types and quantities.

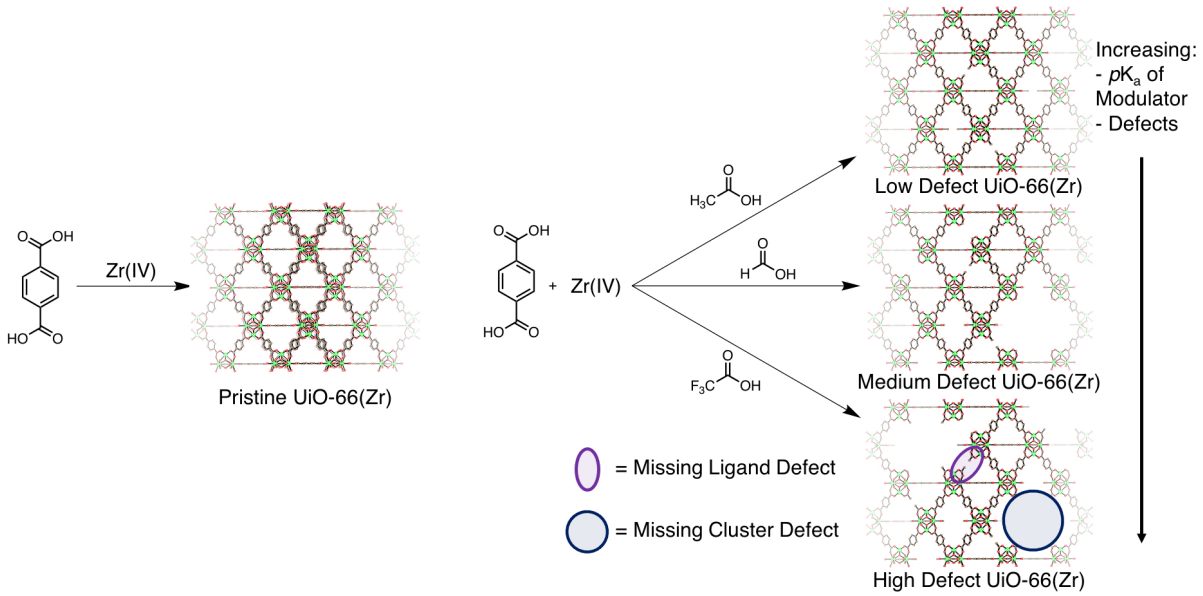


**Figure 1.4**. Pristine UiO-66(Zr) synthesized without acid modulator under high temperature and pressure (*left*) and defective UiO-66(Zr) synthesized under typical conditions with carboxylate modulators that give different amounts and types of defects based on p$K_a$ (*right*).

## 1.4 Catalysis in Metal-Organic Frameworks

Solid-state catalysts provide easy purification from liquid and gas substrates which makes them ideal for large-scale production applications.[55] MOFs have the opportunity to be the next generation of heterogenous catalysts over other materials like zeolites or metal oxides. As outlined in Sections 1.2 and 1.3, unlike other solid-state materials, MOFs can be easily tailored chemically and characterized crystallography, so they can be potentially designed and engineered for a wider range of reactions. This modularity,

combined with micro- and meso-porous environments that can accommodate and isolate organic substrates, has led to the comparison of MOFs to synthetic enzymes.[56, 57] There are many cases of MOF-based catalysts, but the majority fall in two categories: metal catalysts encapsulated into MOFs and catalytic MOFs.

MOFs have been explored as a way to protect or enhance existing catalysts by means of encapsulation. Many efforts have used MOFs as shells for metal nanoparticles to help with properties like reactant selectivity,[58] shielding against sintering,[59] and tandem catalysis.[60] A recent elegant example of this demonstrates the synthesis of Pd nanoparticles embedded in UiO-66(Zr)-$(OH)_2$ with both protection from particle aggregation and selectivity for substrates with smaller molecular diameter (Figure 1.5).[61] MOFs have also been used as a scaffold for coordination complexes, either by encapsulation of the intact complex or appendage to organic ligands of the MOF. The latter is illustrated by the use of expanded ligand UiO-type MOF, UiO-67(Zr), with 25% 2,2'-bipyridine-dicarboxylic acid as the MOF scaffold to which Ir(III) precursor is added to form the appended catalyst (Figure 1.5).[62] The newly formed heterogeneous catalyst greatly shifts the product selectivity from undesired dimerization to desired trifluoroethylation (Figure 1.5). These types of designer catalysts are enabled by the modularity of MOFs and allow for chemical transformations to be considered in an entirely new way.

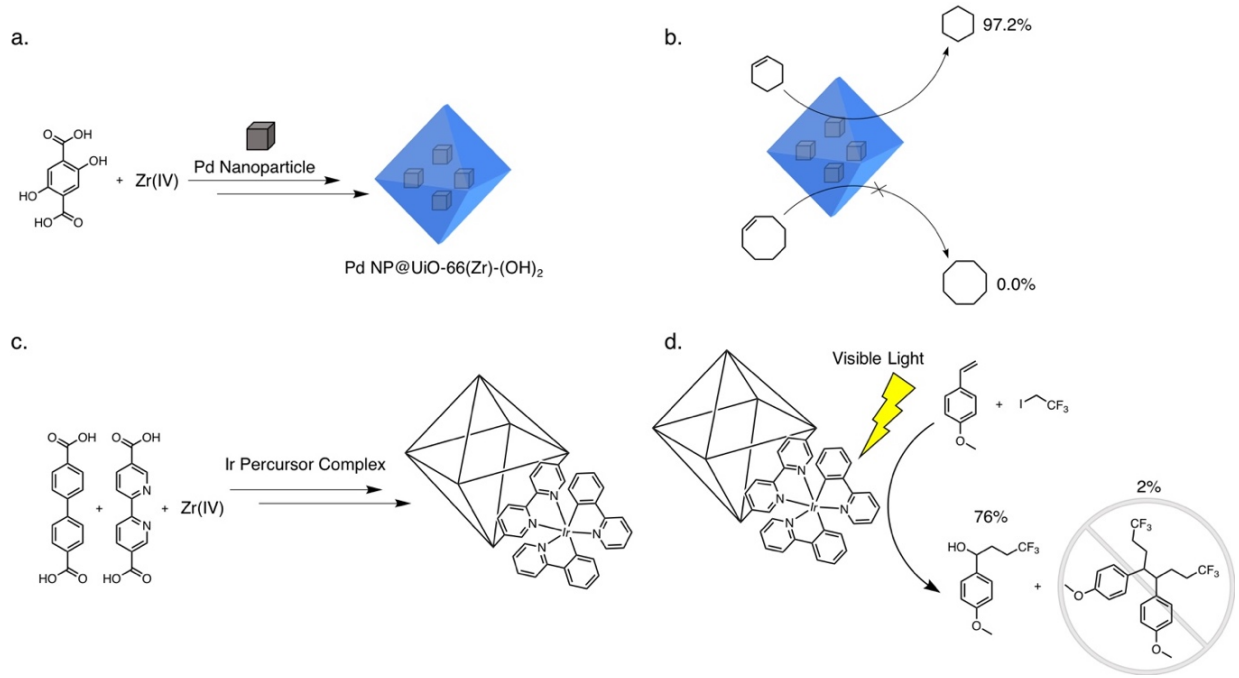


**Figure 1.5.** Encapsulation of Pd nanoparticles in MOF framework (a) and selectivity of resulting hybrid materials (b) for hydrogenation of cyclohexene over cyclooctene; (c) postsynthetic incorporation of Ir catalyst into UiO-67(Zr) type framework and (d) selectivity of this catalyst for trifluoroethylation over dimerization.

MOFs have also been considered for their intrinsic catalytic ability, specifically through open-metal and defect sites in the frameworks. Due to the ligand coordination modes adopted in MOFs, some SBUs have free ligand binding sites that are occupied by solvent or completely unoccupied. The highly connected framework structure can act as a support to hold metal clusters intact when solvent is replaced or removed by reduced pressure. In the case of Cu-paddlewheel MOFs, such as HKUST-1(Cu), the axial coordination sites are accessible and have been shown to activate substrates like epoxides for $CO_2$ fixation.[63] Zr-based MOFs have shown exceptional catalytic activity for the hydrolysis of chemical nerve agents, originally through UiO-66(Zr) defect sites[64] and later through similar sites built into the crystal structure of other Zr-MOFs.[65] These

systems, which will be explored in detail in Chapters 2, 3, and 4 have been used to assess the parameters of open-metal site catalysis in systematic ways like intentionally varying defects in UiO-66(Zr)-$NH_2$ and observing an increase in rate with increasing defect content.[66]

An important consideration for the use of MOFs as catalysts is their stability under the reaction conditions. While some MOFs are robust to heating and ambient moisture, and can stabilize otherwise unstable inorganic complexes,[67] many MOFs undergo destructive ligand exchange with solvent upon heating or introduction of acid or base.[68] For example, in nerve agent degradation applications, MOFs must be, at a minimum, stable to ambient conditions, including water. These MOFs are intended to be used in protective equipment that would be exposed to conditions such as humid air and perspiration. For this reason, some catalysts may be excluded from analysis, but may be suited to other applications where the MOF is exposed only to organic solvents or for a single use.

## 1.5 Metal-Organic Frameworks for Chemical Weapons Mediation

Despite the international ban of use of chemical weapons and a growing understanding of the effect of chemicals on the environment, there continues to be global instances of the use of toxic chemicals that cause human harm.[69-71] These toxic chemicals fall into two main categories: chemical warfare agents (CWAs) and toxic industrial chemicals (TICs). CWAs are a class of deadly chemicals including organophosphorus nerve agents like VX and GB (a.k.a., sarin) and cholorosulfanylalkane

vesicants like sulfur mustard (Figure 1.6).[72, 73] These chemicals, which were developed during WWII, have returned to use in warzones around the world, including in Syria as recently as 2017.[69] In addition to the threat of CWAs, there has also been an increase in use of less toxic TICs. TICs are gases like $NH_3$, $Cl_2$, and $H_2S$ (Figure 1.6) that are widely used in industrial processes and are not subject to regulation like CWAs, but can be harmful to human life if deployed in large doses.[74] The threat of TICs extends also to civilians working at or around factories where these chemicals are used in the event of an accident. It is therefore necessary to develop high-level protective equipment including gas masks, protective garments, and air filtrations systems to address issues surrounding both CWAs and TICs.

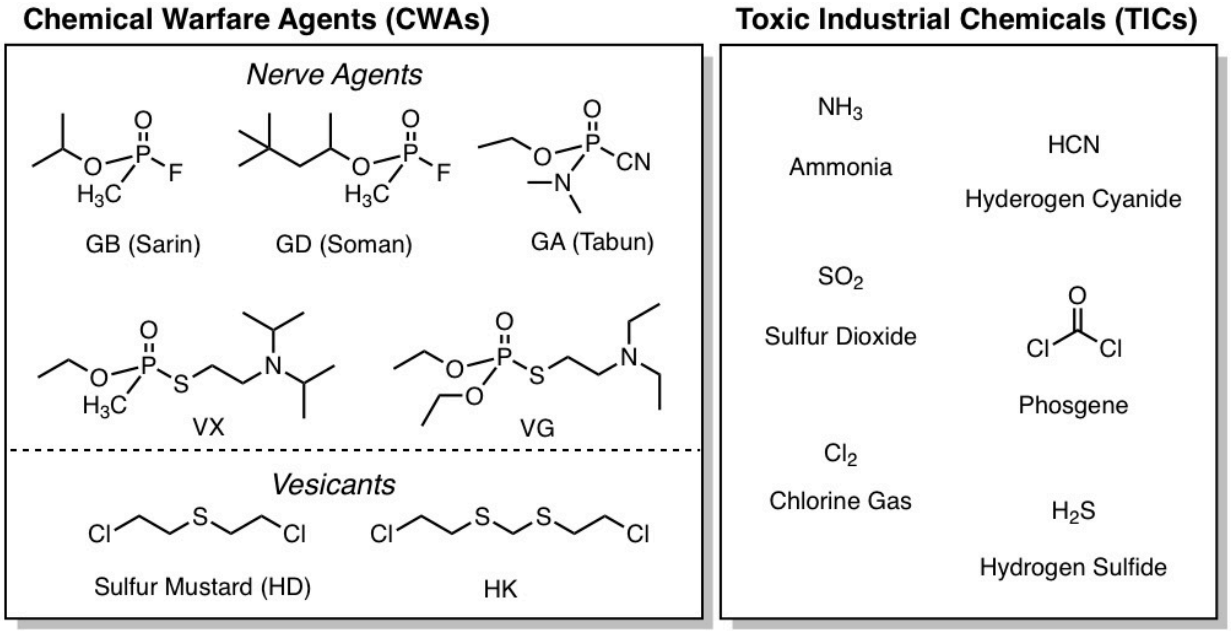


**Figure 1.6.** A selection of chemical warfare agents (CWAs) including both nerve agents and vesicants (*left*) and toxic industrial chemicals (TICs, *right*).

With their high gravimetric surface areas and chemical tunability, MOFs are poised to provide next-generation protection solutions for toxic chemicals.[75] While MOFs are not yet mass produced as ubiquitously as zeolites or porous carbons, they offer the ability to target specific threats and provide a greater level of protection. This becomes important for military applications where weight is a factor, or no suitable protection exists. Recent studies have shown instances of both metals and ligands of MOFs utilized for targeted CWA or TIC uptake.[75-77] In one example, MOFs are shown to have greatly improved sorption capacity for the uptake $Cl_2$ gas over currently technology of metal-impregnated porous carbons. In the case of UiO-66(Zr)-$NH_2$, aromatic substitution onto the ligand occurs that aids in a 9-fold increase in $Cl_2$ capacity.[78] As more studies illustrate the parameters for optimizing CWA and TIC sorption, the potential for a designer MOF or series of MOFs to replace current technology becomes more likely.

While high sorptive capacities and covalent trapping of threats with MOFs is attractive, they suffer from decontamination safety issues if the threat is not neutralized, especially with higher threat CWAs. The optimal solution for CWA remediation would involve built-in degradation of the threat in the protection system. This makes storage and disposal of protective gear that has been exposed a much lower health hazard. MOFs have also been actively investigated for the catalytic breakdown of both nerve agents and vesicants. For safety reasons, most research on these CWAs has been carried out with simulant molecules, which seek to mimic the chemical feature targeted for degradation while being safer to handle. It is then ultimately important to coordinate

these simulant efforts with government research labs with access and expertise to test materials on the actual CWAs of interest.

Research into vesicant degradation has been largely been through selective oxidation of sulfur mustard (HD) to the less toxic bis(2-chloroethyl) sulfoxide (Figure 1.6). The typical simulant for HD is 2-chloroethyl ethyl sulfide (2-CEES) which has about half the toxicity of the agent and has been proven to be a suitable stand in. Oxidation of mustards has been achieved in MOFs by use of photosensitizing ligands to promote generation of singlet oxygen ($^1O_2$) under light irradiation. Initially this was done with PCN-222(Zr), a MOF with porphyrin-based ligands, where the sample was purged with $O_2$ and irritated with a blue LED.[79, 80] Since these reports there have been studies with other ligands including pyrene-based NU-1000(Zr) ligand and perylene,[81] but little success oxidizing 2-CEES in air without use of LEDs. The future of research into vesicant degradation will involve moving materials towards wearable technology that is useful in field conditions.

The progress on finding suitable materials for capture and degradation of nerve agents has been more successful. Prior to 2014, there was substantial research into solid-state materials for the catalytic degradation of nerve agents including successful use of $Zr(OH)_4$ for V-agents[82] and a few preliminary reports exploring MOFs.[83, 84] However, since the discovery of the high catalytic activity of UiO-66(Zr) for hydrolysis of the nerve agent simulant dimethyl-4-nitrophenylphosphate (DMNP), research has progressed rapidly.[64] In this first report, it was found that Lewis acidic Zr(IV) sites could bind both the organophosphate and activate a neighboring hydroxyl group for hydrolysis

reaction in basic solutions (Figure 1.7). Detailed in situ spectroscopy and simulations have revealed that binding of the phosphonyl pulls electron density towards the metal and polarizes the P-X bond allowing it to be readily hydrolyzed by neighboring hydroxide (or hydrogen bonded water) (Figure 1.7).[85] The kinetics of the hydrolysis are determined by access to these metal sites and hydroxides, strength of association and dissociation of organophosphate, and three functional groups bound to phosphorous. Keeping the active sites the same, the hydrolysis rate of various organophosphate can be hard to determine experimentally because simulants that more accurately mimic the chemistry also increase in toxicity.

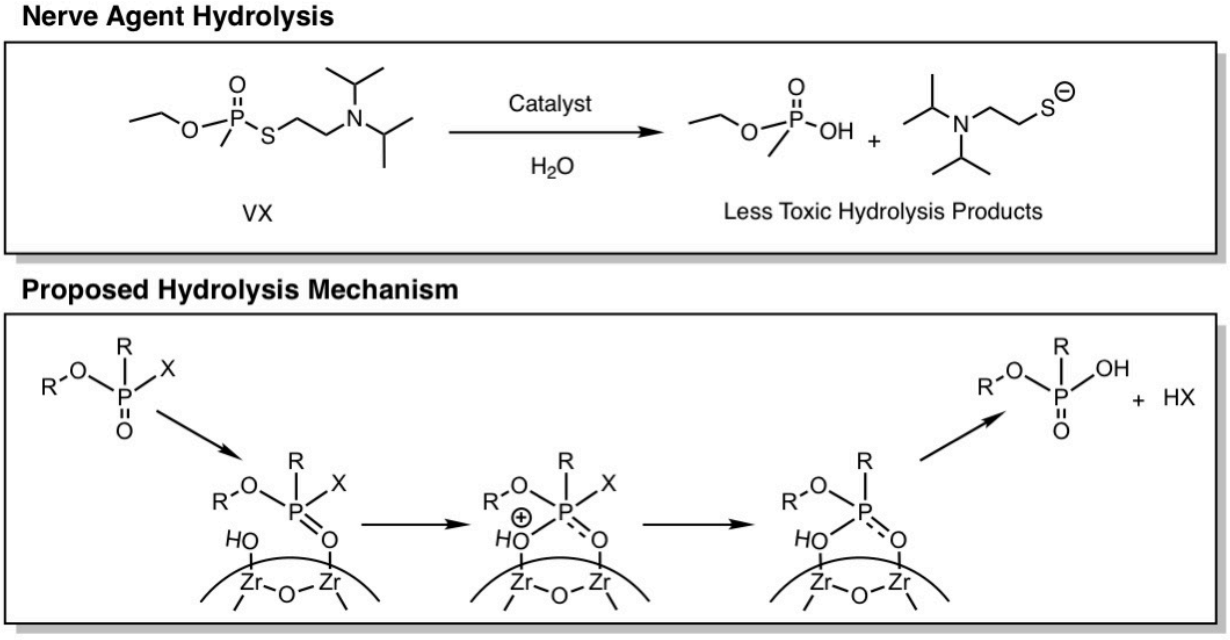


**Figure 1.7.** Example of productive nerve agent hydrolysis (*top*) and proposed mechanism for Zr-MOF hydrolysis of nerve agents and simulants (*bottom*).

Subsequent work has used DMNP as a simulant for the ease of the spectroscopic detection of the yellow *p*-nitrophenoxide product (Figure 1.8).[86] Using this method and a basic solution (pH ~10.5), many reports of Zr-MOFs sought to understand the parameter space of this hydrolysis reaction. The most convincing of these reports show that MOF pore size,[87] defect density,[66] and identity of functional groups on organic ligands,[87] all have an impact on the rate of degradation using various Zr-MOFs. The best iterations of these were large pore MOFs with low coordinate nodes like NU-1000(Zr) and MOF-808(Zr) with small crystallite sizes (<500 nm).[86] It is clear there are many variables that control this hydrolysis, and this is illustrated even between reports using the same materials report different rates: UiO-66(Zr) has been reported as having a half-life for degrading DMNP of 45[64] and 35 min[87] by the same research group and 17 min by others.[88] The optimization of materials has progressed towards finding materials that perform well outside of basic solution, as field applications would not have soluble base.

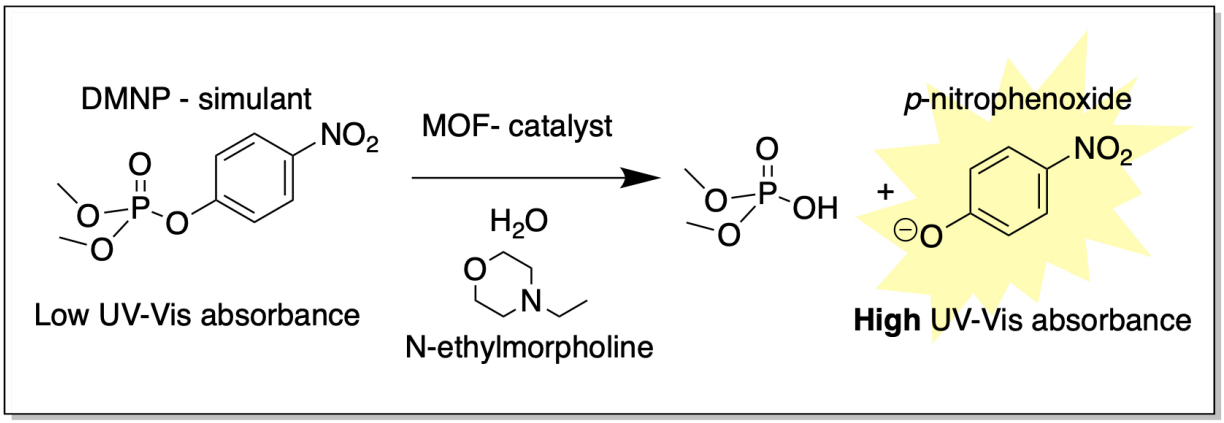


**Figure 1.8.** Overview of DMNP hydrolysis to *p*-nitrophenoxide using MOF catalyst.

In addition to simulant studies, select reports have used MOFs for actual nerve agent testing. This is a challenge because access to agents is restricted to a few facilities globally and tests require extensive safety protocols. Within the limited studies, only the top performing materials are tested and are rapidly consumed (under 2 min) making understanding of trends and kinetics difficult or impossible.[86] One example of an effort to shed light on the differences between agent and simulant used four MOFs and two different conditions (base and pure water) with simulant and three agents.[89] This report showed that there is no correlation between the simulant, diethyl-4-nitrophenylphosphate (DENP or POX), and the agents GA, GD, and VX.[89] Studies conducted in this way have shifted the focus from simple materials discovery to tailoring of materials to perform well against the threats in more realistic conditions.

Another set of realistic conditions for application of MOFs for CWA protection is to test MOFs as part of the larger system they are intended to be used in. MOFs as granular powders are not the ideal form factor for use in suits, masks, or air filters, so development of methods for processing MOFs in a way that allows them to retain their protective qualities is critical (Figure 1.9). Work in this area has largely been dominated by MOF-polymer composites. Atomic layer deposition (ALD) has been used to coat polymer fibers with metal oxides with subsequent MOF growth from the oxide surfaces. By coating the PA-6 (nylon) fibers with $TiO_2$, three MOFs were successfully grown from the surface, UiO-66(Zr), UiO-66(Zr)-$NH_2$ and UiO-67(Zr), and the formed composite was able to degrade both nerve agent simulant DMNP and also nerve agent GD.[90]

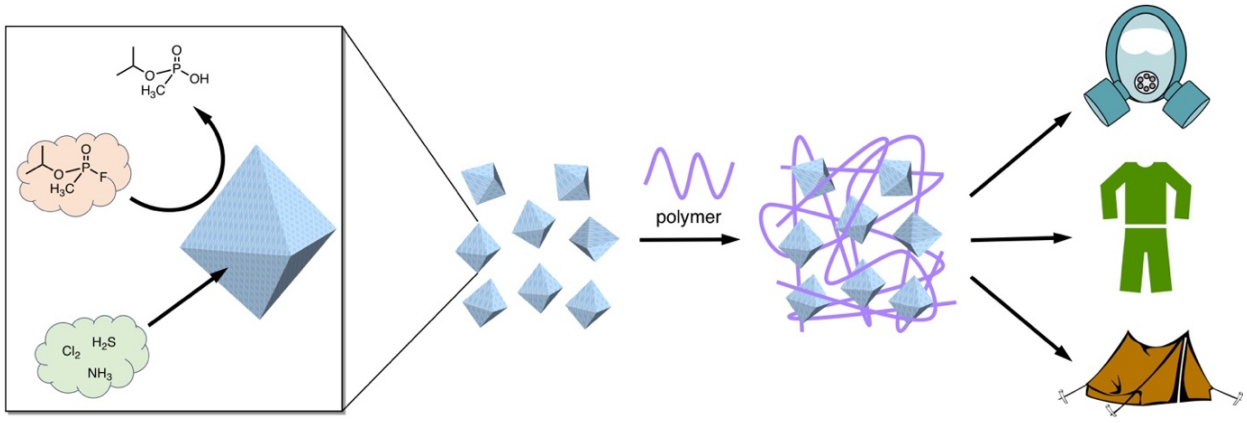


**Figure 1.9.** Multifunctional MOF powders that can adsorb and breakdown toxic chemicals (*left*) and strategy to incorporate powdery MOFs into flexible composites for field applications such as gas masks, suits, and shelters (*right*).

Research since has explored expanding and simplifying composites to make MOF-polymer hybrids compatible with a wide range of materials and form factors. The most prominent examples include MOFs directly electrospun into fibers[91-94] and physical mixtures of MOF and polymers to form mixed-matrix membranes (MMMs).[95, 96] In one particularly interesting example, $ZrO_2$ films were electrospun into a flexible mat and Zr-MOFs were directly synthesized from the $ZrO_2$ mat to form a free-standing, MOF-dominant film that is active towards hydrolysis of DMNP.[97] These bendable films are >90 wt% and MOF showed potential for MOFs in personal protective equipment (PPE), because even in this form factor, the material retains high surface area and degrades chemical warfare agent simulant equal to or faster than MOF alone. Other reports have made use of polymeric bases to blend with MOF to create the proper environment for degradation in field applications. These studies used linear[98] and branched[99] polyimines to replace the morpholine base traditionally used in solution-state testing. While these polymers do not readily make composites, they could provide a platform for future

multicomponent systems. The application of MOFs for CWA and TIC mitigation will rely heavily on the design of these composite systems.

## 1.6 High-Throughput Screening of Solid-State Materials

In organic synthesis, when making high-value molecules such as pharmaceuticals, high-throughput screening (HTS) can be used to quickly find conditions with high yields.[100] These techniques use parallel reactions to compare catalysts, additives, solvents, temperature, etc. in simple test reactions (Figure 1.10). The hits from initial screens can be narrowed and cross-screened until the best route is isolated (Figure 1.10).[101, 102] Research into MOF catalysts can be seen as an analogous process, where a range of materials can be screened for catalytic ability. The structural diversity of MOFs highlighted in Section 1.3 allows for controlled chemical modification of MOFs to grow libraries of materials easily. With the breadth of MOF diversity possible, studies would benefit from methods to simultaneously analyze many samples.

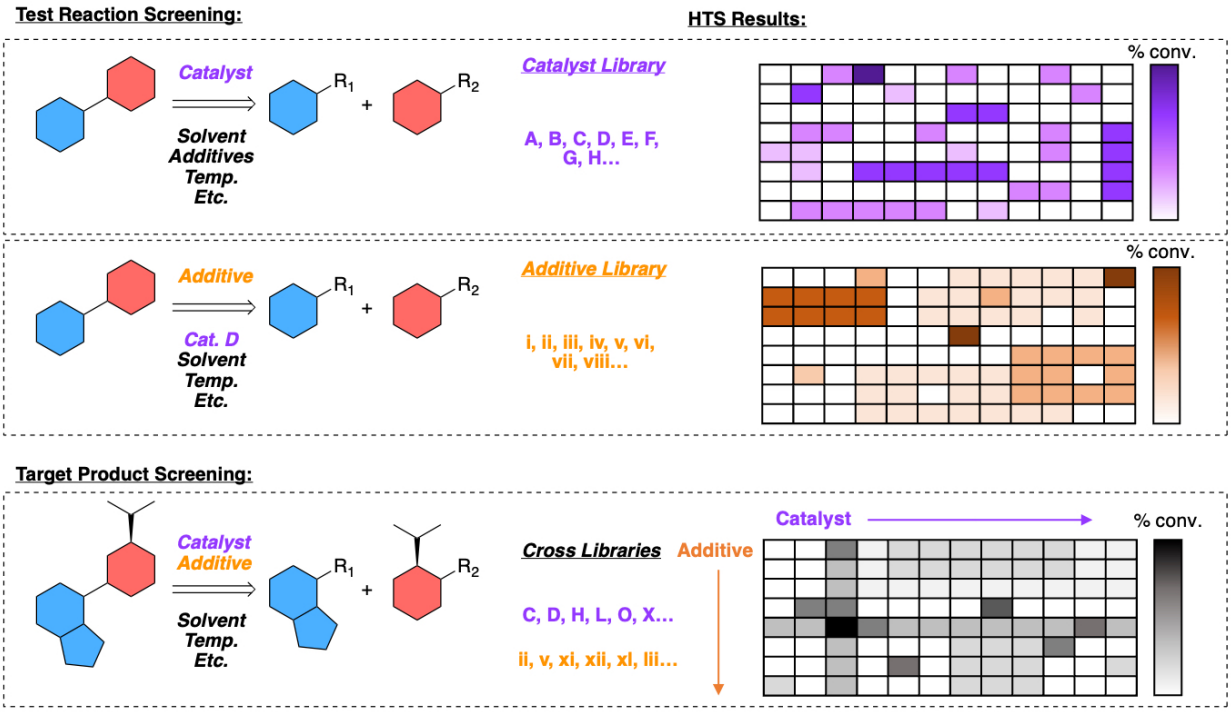


**Figure 1.10.** An overview of high-throughput screening (HTS) in reaction discovery, from condition screening using test reactions (*top*) to multiple variable optimization for high-value products (*bottom*).

When planning a HTS campaign, there are three important factors to consider: library synthesis, fitness screening, and data analysis.[103] Most of the studies involving high-throughput techniques have required fabrication of custom reactors and analysis instruments.[102, 104] Many reactions also rely on mass spectrometry as the analysis method which increases ability to identify gas-phase products, but this limits the rate and types of samples that can be analyzed.[105, 106] There are a number of examples of electrocatalytic processes monitored by the turn on of a fluorescent dye on simple arrayed electrodes, but still require custom-built analytical tools.[107, 108] With the reports on data management and resurgence of genetic algorithms and machine learning in recent years, the utilization of HTS should is not limited by data analysis.[109-111]

To take advantage of high-throughput techniques for academic research of MOF catalysis discovery, plate readers can be utilized. Commercial plate readers for UV-visible and fluorescence spectroscopy that can measure standard 24, 96, and 384 well plates can be purchased for under $20,000 and technology has recently been developed as open source for $3,500.[112] With these readily available technologies as well as standard micropipettes, a wide range of chemical reactions can be accessed quickly. The main criteria for a reaction to be considered are exhibition of an optical (absorbance or fluorescence) change and ability to screen near ambient conditions (20-45 °C in air). Reactions can be monitored in situ as kinetic evaluations or by endpoint analysis after a heating and shaking step (Figure 1.11). This technology can easily increase the number of materials screened from dozens to hundreds in a fraction of the time.

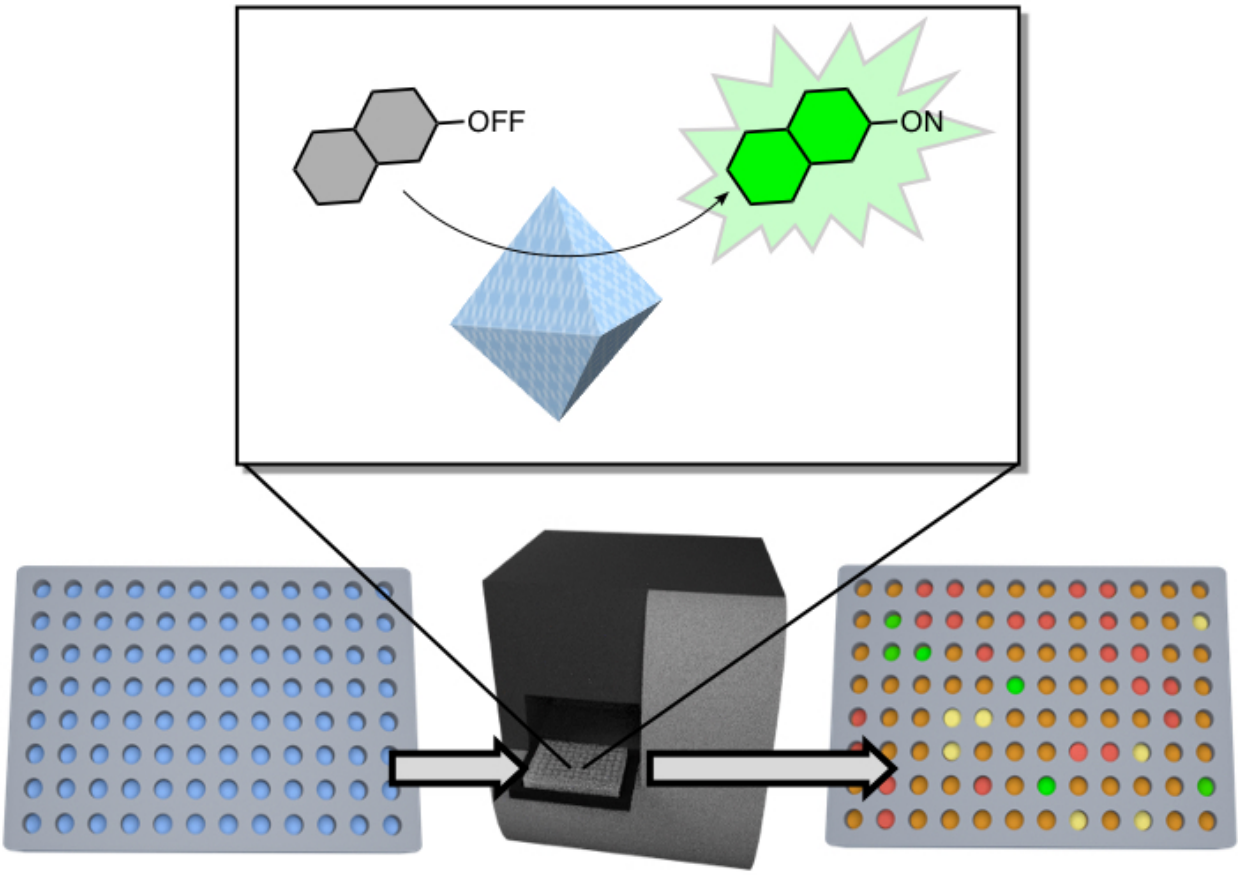


**Figure 1.11.** Example of the ease of screening using a 96-well plate reader to monitor a simple fluorescence or color change. The number of samples allows quickly sorting of candidates into hits (green) and misses (red), with the option to explore intermediate compounds (yellow and orange) if necessary.

MOFs are especially positioned to take advantage of ease of screening with readily constructed combinatorial libraries. First, as discussed in Section 1.2, there are a large number of materials reported to choose from. Second, as highlighted in Section 1.3, there is modularity in existing classes of MOFs that can be easily tuned with selection of ligand or metal starting material and with well-established postsynthetic methods. Simple linear combinations of a single MOF that can be made with two distinct metal ions and five functionalized ligands would yield 93 materials ($3 \times 31 = 93$) and furthering this to three

metals and six ligands would yield 434 materials (7 × 62 = 434) (Figure 1.12). Finally, research into MOF catalysis is still in its infancy so little is known about which materials would best promote particular reactions so purely exploratory screens have the possibility to turn up new, interesting hits.

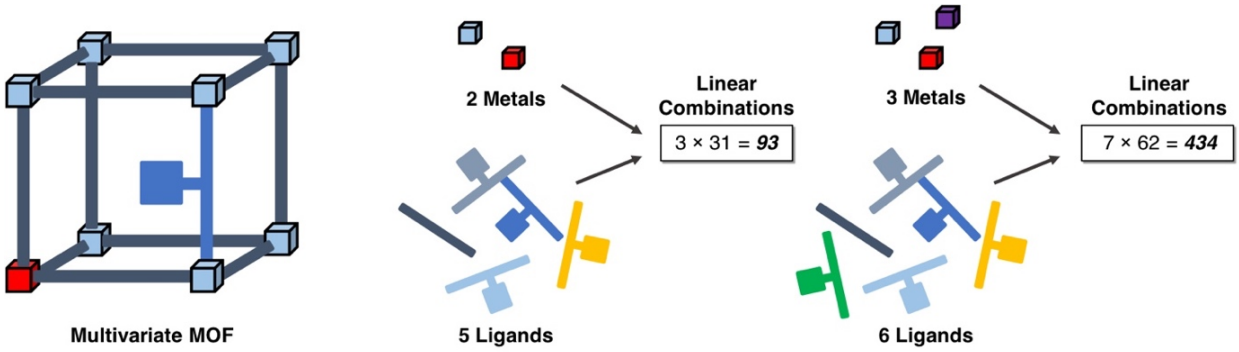


**Figure 1.12.** Example of power of HTS due to the ease of making large libraries of multivariate MOFs with simple linear combinations of metals and ligands.

## 1.7 Scope of this Dissertation

This dissertation will discuss the application of HTS to the identification and understanding of MOF catalysts. Chapter 2 describes the development and validation of HTS to screen solid-state materials for catalytic breakdown of CWA simulants. This work outlines the effectiveness of this technique to rapidly screen a library of 93 materials at two different pH conditions and shows how preparation of material and reaction environment play an important role in performance.

Chapter 3 provides practical examples of how HTS can be used as an effective tool to speed up the discovery and understanding of degradation of CWA by MOFs. Two projects involving screening simple ligand modifications of UiO-66(Zr) enabled by rapid

testing resulted in interesting changes in activity against simulant hydrolysis. An additional two studies demonstrate the ability to adapt HTS methods to screen polymer-MOF composites so that new materials and controls may be run in a fraction of the time.

Chapter 4 describes the expansion of the HTS technique for identifying CWA degradation catalysts with a new simulant that required a signaling molecule to detect. This signaling complex was then applied to the actual nerve agent VX in a medium-throughput spectroscopic assay that was validated by $^{31}$P NMR. In this work it was shown that over a series of MOFs, subtle changes in simulants and agents had profound effects on hydrolysis rates and new correlations must be established.

Chapter 5 expands the scope of MOF-polymer composites for CWA mitigation by using an elastomer to target mechanical properties necessary for PPE. A poly(urethane urea) polymer was synthesized and MOF composites were formed with up to 50 wt% MOF showing ductile and strong mechanical properties and ability to break down CWA simulants using the HTS method developed in Chapters 2 and 3.

## 1.8 Acknowledgements

The dissertation author gratefully acknowledges the editing help of Dr. Kathleen E. Prosser, Dr. Johannes Karges, Dr. Sergio Ayala Jr., Ryjul W. Stokes, and Mark Kalaj.

## 1.9 References

1. Furukawa, H.; Cordova, K. E.; O'Keeffe, M.; Yaghi, O. M., The Chemistry and Applications of Metal-Organic Frameworks. *Science* **2013,** *341*, 1230444.

2. Kitagawa, S.; Kitaura, R.; Noro, S.-i., Functional Porous Coordination Polymers. *Angew. Chem., Int. Ed.* **2004,** *43*, 2334-2375.

3. Hoskins, B. F.; Robson, R., Design and construction of a new class of scaffolding-like materials comprising infinite polymeric frameworks of 3D-linked molecular rods. A reappraisal of the zinc cyanide and cadmium cyanide structures and the synthesis and structure of the diamond-related frameworks [N(CH3)4][CuIZnII(CN)4] and CuI[4,4',4'',4'''-tetracyanotetraphenylmethane]BF4.xC6H5NO2. *J. Am. Chem. Soc.* **1990,** *112*, 1546-1554.

4. Yaghi, O. M.; Li, G.; Li, H., Selective binding and removal of guests in a microporous metal–organic framework. *Nature* **1995,** *378*, 703-706.

5. Li, H.; Eddaoudi, M.; O'Keeffe, M.; Yaghi, O. M., Design and synthesis of an exceptionally stable and highly porous metal-organic framework. *Nature* **1999,** *402*, 276-279.

6. Farha, O. K.; Eryazici, I.; Jeong, N. C.; Hauser, B. G.; Wilmer, C. E.; Sarjeant, A. A.; Snurr, R. Q.; Nguyen, S. T.; Yazaydın, A. Ö.; Hupp, J. T., Metal–Organic Framework Materials with Ultrahigh Surface Areas: Is the Sky the Limit? *J. Am. Chem. Soc.* **2012,** *134*, 15016-15021.

7. Furukawa, H.; Ko, N.; Go, Y. B.; Aratani, N.; Choi, S. B.; Choi, E.; Yazaydin, A. Ö.; Snurr, R. Q.; O'Keeffe, M.; Kim, J.; Yaghi, O. M., Ultrahigh Porosity in Metal-Organic Frameworks. *Science* **2010,** *329*, 424.

8. Zhou, H.-C.; Long, J. R.; Yaghi, O. M., Introduction to Metal–Organic Frameworks. *Chem. Rev.* **2012,** *112*, 673-674.

9. Wang, L.; Moore, C. E.; Cohen, S. M., Correction to Coordinative Alignment To Achieve Ordered Guest Molecules in a Versatile Molecular Crystalline Sponge. *Cryst. Growth Des.* **2018,** *18*, 2665-2665.

10. Tanabe, K. K.; Allen, C. A.; Cohen, S. M., Photochemical Activation of a Metal–Organic Framework to Reveal Functionality. *Angew. Chem., Int. Ed.* **2010,** *49*, 9730-9733.

11. Park, S. S.; Hontz, E. R.; Sun, L.; Hendon, C. H.; Walsh, A.; Van Voorhis, T.; Dincă, M., Cation-Dependent Intrinsic Electrical Conductivity in Isostructural Tetrathiafulvalene-Based Microporous Metal–Organic Frameworks. *J. Am. Chem. Soc.* **2015,** *137*, 1774-1777.

12. Rowsell, J. L. C.; Spencer, E. C.; Eckert, J.; Howard, J. A. K.; Yaghi, O. M., Gas Adsorption Sites in a Large-Pore Metal-Organic Framework. *Science* **2005,** *309*, 1350.

13. Stock, N.; Biswas, S., Synthesis of Metal-Organic Frameworks (MOFs): Routes to Various MOF Topologies, Morphologies, and Composites. *Chem. Rev.* **2012,** *112*, 933-969.

14. Rubio-Martinez, M.; Avci-Camur, C.; Thornton, A. W.; Imaz, I.; Maspoch, D.; Hill, M. R., New synthetic routes towards MOF production at scale. *Chem. Soc. Rev.* **2017,** *46*, 3453-3480.

15. Ren, J.; Dyosiba, X.; Musyoka, N. M.; Langmi, H. W.; Mathe, M.; Liao, S., Review on the current practices and efforts towards pilot-scale production of metal-organic frameworks (MOFs). *Coordin. Chem. Rev.* **2017,** *352*, 187-219.

16. Guillerm, V.; Kim, D.; Eubank, J. F.; Luebke, R.; Liu, X.; Adil, K.; Lah, M. S.; Eddaoudi, M., A supermolecular building approach for the design and construction of metal–organic frameworks. *Chem. Soc. Rev.* **2014,** *43*, 6141-6172.

17. Garibay, S. J.; Cohen, S. M., Isoreticular synthesis and modification of frameworks with the UiO-66 topology. *Chem. Commun.* **2010,** *46*, 7700-7702.

18. Zhao, D.; Timmons, D. J.; Yuan, D.; Zhou, H.-C., Tuning the Topology and Functionality of Metal–Organic Frameworks by Ligand Design. *Accounts Chem. Res.* **2011,** *44*, 123-133.

19. Eddaoudi, M.; Kim, J.; Rosi, N.; Vodak, D.; Wachter, J.; Keeffe, M.; Yaghi, O. M., Systematic Design of Pore Size and Functionality in Isoreticular MOFs and Their Application in Methane Storage. *Science* **2002,** *295*, 469.

20. Cheetham, A. K.; Bennett, T. D.; Coudert, F.-X.; Goodwin, A. L., Defects and disorder in metal organic frameworks. *Dalton Trans.* **2016,** *45*, 4113-4126.

21. Shearer, G. C.; Chavan, S.; Bordiga, S.; Svelle, S.; Olsbye, U.; Lillerud, K. P., Defect Engineering: Tuning the Porosity and Composition of the Metal–Organic Framework UiO-66 via Modulated Synthesis. *Chem. Mater.* **2016,** *28*, 3749-3761.

22. Férey, G.; Latroche, M.; Serre, C.; Millange, F.; Loiseau, T.; Percheron-Guégan, A., Hydrogen adsorption in the nanoporous metal-benzenedicarboxylate M(OH)(O2C–C6H4–CO2) (M = Al3+, Cr3+), MIL-53. *Chem. Commun.* **2003**, 2976-2977.

23. Cavka, J. H.; Jakobsen, S.; Olsbye, U.; Guillou, N.; Lamberti, C.; Bordiga, S.; Lillerud, K. P., A New Zirconium Inorganic Building Brick Forming Metal Organic Frameworks with Exceptional Stability. *J. Am. Chem. Soc.* **2008,** *130*, 13850-13851.

24. Chui, S. S. Y.; Lo, S. M. F.; Charmant, J. P. H.; Orpen, A. G.; Williams, I. D., A Chemically Functionalizable Nanoporous Material [Cu3(TMA)2(H2O)3]n. *Science* **1999,** *283*, 1148.

25. Horcajada, P.; Serre, C.; Vallet-Regí, M.; Sebban, M.; Taulelle, F.; Férey, G., Metal–Organic Frameworks as Efficient Materials for Drug Delivery. *Angew. Chem., Int. Ed.* **2006,** *45*, 5974-5978.

26. Furukawa, H.; Gándara, F.; Zhang, Y.-B.; Jiang, J.; Queen, W. L.; Hudson, M. R.; Yaghi, O. M., Water Adsorption in Porous Metal–Organic Frameworks and Related Materials. *J. Am. Chem. Soc.* **2014,** *136*, 4369-4381.

27. Moghadam, P. Z.; Li, A.; Wiggin, S. B.; Tao, A.; Maloney, A. G. P.; Wood, P. A.; Ward, S. C.; Fairen-Jimenez, D., Development of a Cambridge Structural Database Subset: A Collection of Metal–Organic Frameworks for Past, Present, and Future. *Chem. Mater.* **2017,** *29*, 2618-2625.

28. Gandara, F.; Bennett, T. D., Crystallography of metal-organic frameworks. *IUCrJ* **2014,** *1*, 563-570.

29. Walton, K. S.; Snurr, R. Q., Applicability of the BET Method for Determining Surface Areas of Microporous Metal–Organic Frameworks. *J. Am. Chem. Soc.* **2007,** *129*, 8552-8556.

30. Rouquerol, J.; Llewellyn, P.; Rouquerol, F., Is the BET Equation Applicable to Microporous Adsorbents? *Stud. Surf. Sci. Catal.* **2007,** *160*, 49-56.

31. Kubo, M.; Hagi, H.; Shimojima, A.; Okubo, T., Facile Synthesis of Hydroxy-Modified MOF-5 for Improving the Adsorption Capacity of Hydrogen by Lithium Doping. *Chem. Asian J.* **2013,** *8*, 2801-2806.

32. Rosi, N. L.; Kim, J.; Eddaoudi, M.; Chen, B.; O'Keeffe, M.; Yaghi, O. M., Rod Packings and Metal–Organic Frameworks Constructed from Rod-Shaped Secondary Building Units. *J. Am. Chem. Soc.* **2005,** *127*, 1504-1518.

33. Dietzel, P. D. C.; Morita, Y.; Blom, R.; Fjellvåg, H., An In Situ High-Temperature Single-Crystal Investigation of a Dehydrated Metal–Organic Framework Compound and Field-Induced Magnetization of One-Dimensional Metal–Oxygen Chains. *Angew. Chem., Int. Ed.* **2005,** *44*, 6354-6358.

34. Xu, W.; Tu, B.; Liu, Q.; Shu, Y.; Liang, C.-C.; Diercks, C. S.; Yaghi, O. M.; Zhang, Y.-B.; Deng, H.; Li, Q., Anisotropic reticular chemistry. *Nat. Rev. Mater.* **2020,** *5*, 764-779.

35. Helal, A.; Yamani, Z. H.; Cordova, K. E.; Yaghi, O. M., Multivariate metal-organic frameworks. *Natl. Sci. Rev.* **2017,** *4*, 296-298.

36. Deng, H.; Doonan, C. J.; Furukawa, H.; Ferreira, R. B.; Towne, J.; Knobler, C. B.; Wang, B.; Yaghi, O. M., Multiple Functional Groups of Varying Ratios in Metal-Organic Frameworks. *Science* **2010,** *327*, 846.

37. Wang, L. J.; Deng, H.; Furukawa, H.; Gándara, F.; Cordova, K. E.; Peri, D.; Yaghi, O. M., Synthesis and Characterization of Metal–Organic Framework-74 Containing 2, 4, 6, 8, and 10 Different Metals. *Inorg. Chem.* **2014,** *53*, 5881-5883.

38. Cohen, S. M., The Postsynthetic Renaissance in Porous Solids. *J. Am. Chem. Soc.* **2017,** *139*, 2855-2863.

39. Morabito, J. V.; Chou, L.-Y.; Li, Z.; Manna, C. M.; Petroff, C. A.; Kyada, R. J.; Palomba, J. M.; Byers, J. A.; Tsung, C.-K., Molecular Encapsulation beyond the Aperture Size Limit through Dissociative Linker Exchange in Metal–Organic Framework Crystals. *J. Am. Chem. Soc.* **2014,** *136*, 12540-12543.

40. Karagiaridi, O.; Lalonde, M. B.; Bury, W.; Sarjeant, A. A.; Farha, O. K.; Hupp, J. T., Opening ZIF-8: A Catalytically Active Zeolitic Imidazolate Framework of Sodalite Topology with Unsubstituted Linkers. *J. Am. Chem. Soc.* **2012,** *134*, 18790-18796.

41. Yao, Q.; Sun, J.; Li, K.; Su, J.; Peskov, M. V.; Zou, X., A series of isostructural mesoporous metal–organic frameworks obtained by ion-exchange induced single-crystal to single-crystal transformation. *Dalton Trans.* **2012,** *41*, 3953-3955.

42. Kim, M.; Cahill, J. F.; Fei, H.; Prather, K. A.; Cohen, S. M., Postsynthetic Ligand and Cation Exchange in Robust Metal–Organic Frameworks. *J. Am. Chem. Soc.* **2012,** *134*, 18082-18088.

43. Dodson, R. A.; Kalenak, A. P.; Matzger, A. J., Solvent Choice in Metal–Organic Framework Linker Exchange Permits Microstructural Control. *J. Am. Chem. Soc.* **2020,** *142*, 20806-20813.

44. Tanabe, K. K.; Wang, Z.; Cohen, S. M., Systematic Functionalization of a Metal–Organic Framework via a Postsynthetic Modification Approach. *J. Am. Chem. Soc.* **2008,** *130*, 8508-8517.

45. Wang, Z.; Cohen, S. M., Postsynthetic modification of metal–organic frameworks. *Chem. Soc. Rev.* **2009,** *38*, 1315-1329.

46. Kim, Y. K.; Hyun, S.-m.; Lee, J. H.; Kim, T. K.; Moon, D.; Moon, H. R., Crystal-Size Effects on Carbon Dioxide Capture of a Covalently Alkylamine-Tethered Metal-Organic Framework Constructed by a One-Step Self-Assembly. *Sci. Rep.* **2016,** *6*, 19337.

47. Taylor, J. M.; Dekura, S.; Ikeda, R.; Kitagawa, H., Defect Control To Enhance Proton Conductivity in a Metal–Organic Framework. *Chem. Mater.* **2015,** *27*, 2286-2289.

48. Krause, S.; Reuter, F. S.; Ehrling, S.; Bon, V.; Senkovska, I.; Kaskel, S.; Brunner, E., Impact of Defects and Crystal Size on Negative Gas Adsorption in DUT-49 Analyzed by In Situ 129Xe NMR Spectroscopy. *Chem. Mater.* **2020,** *32*, 4641-4650.

49. Jiang, D.; Burrows, A. D.; Edler, K. J., Size-controlled synthesis of MIL-101(Cr) nanoparticles with enhanced selectivity for CO2 over N2. *CrystEngComm* **2011,** *13*, 6916-6919.

50. Zhou, J.; Yu, X.; Fan, X.; Wang, X.; Li, H.; Zhang, Y.; Li, W.; Zheng, J.; Wang, B.; Li, X., The impact of the particle size of a metal–organic framework for sulfur storage in Li–S batteries. *J. Mater. Chem. A* **2015,** *3*, 8272-8275.

51. Linder-Patton, O. M.; Bloch, W. M.; Coghlan, C. J.; Sumida, K.; Kitagawa, S.; Furukawa, S.; Doonan, C. J.; Sumby, C. J., Particle size effects in the kinetic trapping of a structurally-locked form of a flexible MOF. *CrystEngComm* **2016,** *18*, 4172-4179.

52. Marshall, C. R.; Staudhammer, S. A.; Brozek, C. K., Size control over metal–organic framework porous nanocrystals. *Chem. Sci.* **2019,** *10*, 9396-9408.

53. Bennett, T. D.; Cheetham, A. K.; Fuchs, A. H.; Coudert, F.-X., Interplay between defects, disorder and flexibility in metal-organic frameworks. *Nature Chem.* **2017,** *9*, 11-16.

54. Halbherr, O.; Fischer, R. A., Defects and Disorder in MOFs. *The Chemistry of Metal–Organic Frameworks* **2016**, 795-822.

55. Bavykina, A.; Kolobov, N.; Khan, I. S.; Bau, J. A.; Ramirez, A.; Gascon, J., Metal–Organic Frameworks in Heterogeneous Catalysis: Recent Progress, New Trends, and Future Perspectives. *Chem. Rev.* **2020,** *120*, 8468-8535.

56. Nath, I.; Chakraborty, J.; Verpoort, F., Metal organic frameworks mimicking natural enzymes: a structural and functional analogy. *Chem. Soc. Rev.* **2016,** *45*, 4127-4170.

57. Cohen, S. M.; Zhang, Z.; Boissonnault, J. A., Toward “metalloMOFzymes”: Metal–Organic Frameworks with Single-Site Metal Catalysts for Small-Molecule Transformations. *Inorg. Chem.* **2016,** *55*, 7281-7290.

58. Kuo, C.-H.; Tang, Y.; Chou, L.-Y.; Sneed, B. T.; Brodsky, C. N.; Zhao, Z.; Tsung, C.-K., Yolk–Shell Nanocrystal@ZIF-8 Nanostructures for Gas-Phase Heterogeneous Catalysis with Selectivity Control. *J. Am. Chem. Soc.* **2012,** *134*, 14345-14348.

59. Li, B.; Zeng, H. C., Synthetic Chemistry and Multifunctionality of an Amorphous Ni-MOF-74 Shell on a Ni/SiO2 Hollow Catalyst for Efficient Tandem Reactions. *Chem. Mater.* **2019,** *31*, 5320-5330.

60. Wang, Q.; Zhang, X.; Huang, L.; Zhang, Z.; Dong, S., GOx@ZIF-8(NiPd) Nanoflower: An Artificial Enzyme System for Tandem Catalysis. *Angew. Chem., Int. Ed.* **2017,** *56*, 16082-16085.

61. Luo, L.; Lo, W.-S.; Si, X.; Li, H.; Wu, Y.; An, Y.; Zhu, Q.; Chou, L.-Y.; Li, T.; Tsung, C.-K., Directional Engraving within Single Crystalline Metal–Organic Framework Particles via Oxidative Linker Cleaving. *J. Am. Chem. Soc.* **2019,** *141*, 20365-20370.

62. Yu, X.; Cohen, S. M., Photocatalytic Metal–Organic Frameworks for Selective 2,2,2-Trifluoroethylation of Styrenes. *J. Am. Chem. Soc.* **2016,** *138*, 12320-12323.

63. Gao, W.-Y.; Chen, Y.; Niu, Y.; Williams, K.; Cash, L.; Perez, P. J.; Wojtas, L.; Cai, J.; Chen, Y.-S.; Ma, S., Crystal Engineering of an nbo Topology Metal–Organic Framework for Chemical Fixation of CO2 under Ambient Conditions. *Angew. Chem., Int. Ed.* **2014,** *53*, 2615-2619.

64. Katz, M. J.; Mondloch, J. E.; Totten, R. K.; Park, J. K.; Nguyen, S. T.; Farha, O. K.; Hupp, J. T., Simple and Compelling Biomimetic Metal–Organic Framework Catalyst for the Degradation of Nerve Agent Simulants. *Angew. Chem., Int. Ed.* **2014,** *53*, 497-501.

65. Moon, S.-Y.; Liu, Y.; Hupp, J. T.; Farha, O. K., Instantaneous Hydrolysis of Nerve-Agent Simulants with a Six-Connected Zirconium-Based Metal–Organic Framework. *Angew. Chem., Int. Ed.* **2015,** *54*, 6795-6799.

66. Peterson, G. W.; Destefano, M. R.; Garibay, S. J.; Ploskonka, A.; McEntee, M.; Hall, M.; Karwacki, C. J.; Hupp, J. T.; Farha, O. K., Optimizing Toxic Chemical Removal through Defect-Induced UiO-66-NH2 Metal–Organic Framework. *Chem. Eur. J.* **2017,** *23*, 15913-15916.

67. Pullen, S.; Fei, H.; Orthaber, A.; Cohen, S. M.; Ott, S., Enhanced Photochemical Hydrogen Production by a Molecular Diiron Catalyst Incorporated into a Metal–Organic Framework. *J. Am. Chem. Soc.* **2013,** *135*, 16997-17003.

68. Burtch, N. C.; Jasuja, H.; Walton, K. S., Water Stability and Adsorption in Metal–Organic Frameworks. *Chem. Rev.* **2014,** *114*, 10575-10612.

69. Council, U. N. S., Seventh report of the Organisation for the Prohibition of Chemical Weapons-United Nations Joint Investigative Mechanism. General Distribution, 2017.

70. Hess, G., Syria and Islamic State used banned agents. *C&EN Global Enterprise* **2016,** *94*, 21-21.

71. Schmitt, E., ISIS Used Chemical Arms at Least 52 Times in Syria and Iraq, Report Says. *New York Times* Nov. 21, 2016

, 2016.

72. Brown, M. A.; Brix, K. A., Review of health consequences from high-, intermediate- and low-level exposure to organophosphorus nerve agents. *J. Appl. Toxicol.* **1998,** *18*, 393-408.

73. *Memorandum Subject: Implementation Guidance Policy for New Airborne Exposure Limits for GB. GA, GD, GF, VX, H, HD, and HTsigned by Mr. Raymond J. Fatz, Deputy Assistant Secretary of the Army*; Department of the Army: OASA(I&E), June 18, 2004, 2004.

74. Tomassoni, A. J.; French, R. N. E.; Walter, F. G., Toxic Industrial Chemicals and Chemical Weapons: Exposure, Identification, and Management by Syndrome. *Emerg. Med. Clin. N. Am.* **2015,** *33*, 13-36.

75. DeCoste, J. B.; Peterson, G. W., Metal–Organic Frameworks for Air Purification of Toxic Chemicals. *Chem. Rev.* **2014,** *114*, 5695-5727.

76. Liu, Y.; Howarth, A. J.; Vermeulen, N. A.; Moon, S.-Y.; Hupp, J. T.; Farha, O. K., Catalytic degradation of chemical warfare agents and their simulants by metal-organic frameworks. *Coordin. Chem. Rev.* **2017,** *346*, 101-111.

77. Islamoglu, T.; Chen, Z.; Wasson, M. C.; Buru, C. T.; Kirlikovali, K. O.; Afrin, U.; Mian, M. R.; Farha, O. K., Metal–Organic Frameworks against Toxic Chemicals. *Chem. Rev.* **2020,** *120*, 8130-8160.

78. DeCoste, J. B.; Browe, M. A.; Wagner, G. W.; Rossin, J. A.; Peterson, G. W., Removal of chlorine gas by an amine functionalized metal–organic framework via electrophilic aromatic substitution. *Chem. Commun.* **2015,** *51*, 12474-12477.

79. Liu, Y.; Howarth, A. J.; Hupp, J. T.; Farha, O. K., Selective Photooxidation of a Mustard-Gas Simulant Catalyzed by a Porphyrinic Metal–Organic Framework. *Angew. Chem., Int. Ed.* **2015,** *54*, 9001-9005.

80. Liu, Y.; Moon, S.-Y.; Hupp, J. T.; Farha, O. K., Dual-Function Metal–Organic Framework as a Versatile Catalyst for Detoxifying Chemical Warfare Agent Simulants. *ACS Nano* **2015,** *9*, 12358-12364.

81. Buru, C. T.; Majewski, M. B.; Howarth, A. J.; Lavroff, R. H.; Kung, C.-W.; Peters, A. W.; Goswami, S.; Farha, O. K., Improving the Efficiency of Mustard Gas Simulant Detoxification by Tuning the Singlet Oxygen Quantum Yield in Metal–Organic Frameworks and Their Corresponding Thin Films. *ACS Appl. Mater. Interfaces* **2018,** *10*, 23802-23806.

82. Bandosz, T. J.; Laskoski, M.; Mahle, J.; Mogilevsky, G.; Peterson, G. W.; Rossin, J. A.; Wagner, G. W., Reactions of VX, GD, and HD with Zr(OH)4: Near Instantaneous Decontamination of VX. *J. Phys. Chem. C* **2012,** *116*, 11606-11614.

83. Wang, S.; Bromberg, L.; Schreuder-Gibson, H.; Hatton, T. A., Organophophorous Ester Degradation by Chromium(III) Terephthalate Metal–Organic Framework (MIL-101) Chelated to N,N-Dimethylaminopyridine and Related Aminopyridines. *ACS Appl. Mater. Interfaces* **2013,** *5*, 1269-1278.

84. Peterson, G. W.; Wagner, G. W., Detoxification of chemical warfare agents by CuBTC. *J. Porous Mater.* **2014,** *21*, 121-126.

85. Grissom, T. G.; Plonka, A. M.; Sharp, C. H.; Ebrahim, A. M.; Tian, Y.; Collins-Wildman, D. L.; Kaledin, A. L.; Siegal, H. J.; Troya, D.; Hill, C. L.; Frenkel, A. I.; Musaev, D. G.; Gordon, W. O.; Karwacki, C. J.; Mitchell, M. B.; Morris, J. R., Metal–Organic Framework- and Polyoxometalate-Based Sorbents for the Uptake and Destruction of Chemical Warfare Agents. *ACS Appl. Mater. Interfaces* **2020,** *12*, 14641-14661.

86. Kirlikovali, K. O.; Chen, Z.; Islamoglu, T.; Hupp, J. T.; Farha, O. K., Zirconium-Based Metal–Organic Frameworks for the Catalytic Hydrolysis of Organophosphorus Nerve Agents. *ACS Appl. Mater. Interfaces* **2020,** *12*, 14702-14720.

87. Katz, M. J.; Moon, S.-Y.; Mondloch, J. E.; Beyzavi, M. H.; Stephenson, C. J.; Hupp, J. T.; Farha, O. K., Exploiting parameter space in MOFs: a 20-fold enhancement of phosphate-ester hydrolysis with UiO-66-NH2. *Chem. Sci.* **2015,** *6*, 2286-2291.

88. Ploskonka, A. M.; DeCoste, J. B., Insight into organophosphate chemical warfare agent simulant hydrolysis in metal-organic frameworks. *J. Hazard. Mater.* **2019,** *375*, 191-197.

89. de Koning, M. C.; van Grol, M.; Breijaert, T., Degradation of Paraoxon and the Chemical Warfare Agents VX, Tabun, and Soman by the Metal–Organic Frameworks UiO-66-NH2, MOF-808, NU-1000, and PCN-777. *Inorg. Chem.* **2017,** *56*, 11804-11809.

90. Zhao, J.; Lee, D. T.; Yaga, R. W.; Hall, M. G.; Barton, H. F.; Woodward, I. R.; Oldham, C. J.; Walls, H. J.; Peterson, G. W.; Parsons, G. N., Ultra-Fast Degradation of Chemical Warfare Agents Using MOF–Nanofiber Kebabs. *Angew. Chem., Int. Ed.* **2016,** *55*, 13224-13228.

91. Lu, A. X.; McEntee, M.; Browe, M. A.; Hall, M. G.; DeCoste, J. B.; Peterson, G. W., MOFabric: Electrospun Nanofiber Mats from PVDF/UiO-66-NH2 for Chemical Protection and Decontamination. *ACS Appl. Mater. Interfaces* **2017,** *9*, 13632-13636.

92. McCarthy, D. L.; Liu, J.; Dwyer, D. B.; Troiano, J. L.; Boyer, S. M.; DeCoste, J. B.; Bernier, W. E.; Jones, J. W. E., Electrospun metal–organic framework polymer composites for the catalytic degradation of methyl paraoxon. *New J. Chem.* **2017,** *41*, 8748-8753.

93. Peterson, G. W.; Lu, A. X.; Epps, T. H., Tuning the Morphology and Activity of Electrospun Polystyrene/UiO-66-NH2 Metal–Organic Framework Composites to Enhance Chemical Warfare Agent Removal. *ACS Appl. Mater. Interfaces* **2017,** *9*, 32248-32254.

94. Lu, A. X.; Ploskonka, A. M.; Tovar, T. M.; Peterson, G. W.; DeCoste, J. B., Direct Surface Growth Of UIO-66-NH2 on Polyacrylonitrile Nanofibers for Efficient Toxic Chemical Removal. *Ind. Eng. Chem. Res.* **2017,** *56*, 14502-14506.

95. Peterson, G. W.; Browe, M. A.; Durke, E. M.; Epps, T. H., Flexible SIS/HKUST-1 Mixed Matrix Composites as Protective Barriers against Chemical Warfare Agent Simulants. *ACS Appl. Mater. Interfaces* **2018,** *10*, 43080-43087.

96. Peterson, G. W.; Lu, A. X.; Hall, M. G.; Browe, M. A.; Tovar, T.; Epps, T. H., MOFwich: Sandwiched Metal–Organic Framework-Containing Mixed Matrix Composites for Chemical Warfare Agent Removal. *ACS Appl. Mater. Interfaces* **2018,** *10*, 6820-6824.

97. Liang, H.; Yao, A.; Jiao, X.; Li, C.; Chen, D., Fast and Sustained Degradation of Chemical Warfare Agent Simulants Using Flexible Self-Supported Metal–Organic Framework Filters. *ACS Appl. Mater. Interfaces* **2018,** *10*, 20396-20403.

98. Moon, S.-Y.; Proussaloglou, E.; Peterson, G. W.; DeCoste, J. B.; Hall, M. G.; Howarth, A. J.; Hupp, J. T.; Farha, O. K., Detoxification of Chemical Warfare Agents Using a Zr6-Based Metal–Organic Framework/Polymer Mixture. *Chem. Eur. J.* **2016,** *22*, 14864-14868.

99. Chen, Z.; Islamoglu, T.; Farha, O. K., Toward Base Heterogenization: A Zirconium Metal–Organic Framework/Dendrimer or Polymer Mixture for Rapid Hydrolysis of a Nerve-Agent Simulant. *ACS Appl. Nano Mater.* **2019,** *2*, 1005-1008.

100. Krska, S. W.; DiRocco, D. A.; Dreher, S. D.; Shevlin, M., The Evolution of Chemical High-Throughput Experimentation To Address Challenging Problems in Pharmaceutical Synthesis. *Acc. Chem. Res.* **2017,** *50*, 2976-2985.

101. Buitrago Santanilla, A.; Regalado, E. L.; Pereira, T.; Shevlin, M.; Bateman, K.; Campeau, L.-C.; Schneeweis, J.; Berritt, S.; Shi, Z.-C.; Nantermet, P.; Liu, Y.; Helmy, R.; Welch, C. J.; Vachal, P.; Davies, I. W.; Cernak, T.; Dreher, S. D., Nanomole-scale high-throughput chemistry for the synthesis of complex molecules. *Science* **2015,** *347*, 49.

102. Perera, D.; Tucker, J. W.; Brahmbhatt, S.; Helal, C. J.; Chong, A.; Farrell, W.; Richardson, P.; Sach, N. W., A platform for automated nanomole-scale reaction screening and micromole-scale synthesis in flow. *Science* **2018,** *359*, 429.

103. Senkan, S., Combinatorial Heterogeneous Catalysis—A New Path in an Old Field. *Angew. Chem., Int. Ed.* **2001,** *40*, 312-329.

104. Cong, P.; Doolen, R. D.; Fan, Q.; Giaquinta, D. M.; Guan, S.; McFarland, E. W.; Poojary, D. M.; Self, K.; Turner, H. W.; Weinberg, W. H., High-Throughput Synthesis and Screening of Combinatorial Heterogeneous Catalyst Libraries. *Angew. Chem., Int. Ed.* **1999,** *38*, 483-488.

105. Yao, Y.; Huang, Z.; Li, T.; Wang, H.; Liu, Y.; Stein, H. S.; Mao, Y.; Gao, J.; Jiao, M.; Dong, Q.; Dai, J.; Xie, P.; Xie, H.; Lacey, S. D.; Takeuchi, I.; Gregoire, J. M.; Jiang, R.; Wang, C.; Taylor, A. D.; Shahbazian-Yassar, R.; Hu, L., High-throughput, combinatorial synthesis of multimetallic nanoclusters. *Proc. Natl. Acad. Sci. U.S.A.* **2020,** *117*, 6316.

106. Busico, V.; Cipullo, R.; Mingione, A.; Rongo, L., Accelerating the Research Approach to Ziegler–Natta Catalysts. *Ind. Eng. Chem. Res.* **2016,** *55*, 2686-2695.

107. Reddington, E.; Sapienza, A.; Gurau, B.; Viswanathan, R.; Sarangapani, S.; Smotkin, E. S.; Mallouk, T. E., Combinatorial Electrochemistry: A Highly Parallel, Optical Screening Method for Discovery of Better Electrocatalysts. *Science* **1998,** *280*, 1735.

108. Han, G. D.; Choi, H. J.; Bae, K.; Choi, H. R.; Jang, D. Y.; Shim, J. H., Fabrication of Lanthanum Strontium Cobalt Ferrite–Gadolinium-Doped Ceria Composite Cathodes Using a Low-Price Inkjet Printer. *ACS Appl. Mater. Interfaces* **2017,** *9*, 39347-39356.

109. Borboudakis, G.; Stergiannakos, T.; Frysali, M.; Klontzas, E.; Tsamardinos, I.; Froudakis, G. E., Chemically intuited, large-scale screening of MOFs by machine learning techniques. *npj Comput. Mater.* **2017,** *3*, 40.

110. Raccuglia, P.; Elbert, K. C.; Adler, P. D. F.; Falk, C.; Wenny, M. B.; Mollo, A.; Zeller, M.; Friedler, S. A.; Schrier, J.; Norquist, A. J., Machine-learning-assisted materials discovery using failed experiments. *Nature* **2016,** *533*, 73-76.

111. Takahashi, K.; Takahashi, L.; Miyazato, I.; Fujima, J.; Tanaka, Y.; Uno, T.; Satoh, H.; Ohno, K.; Nishida, M.; Hirai, K.; Ohyama, J.; Nguyen, T. N.; Nishimura, S.; Taniike, T., The Rise of Catalyst Informatics: Towards Catalyst Genomics. *ChemCatChem* **2019,** *11*, 1146-1152.

112. Szymula, K. P.; Magaraci, M. S.; Patterson, M.; Clark, A.; Mannickarottu, S. G.; Chow, B. Y., An Open-Source Plate Reader. *Biochemistry* **2019,** *58*, 468-473.

# Chapter 2: Development and Validation of High-Throughput Screening of Solid-State MOF Catalysts

## 2.1 Introduction

As introduced in Chapter 1, MOFs are a potential replacement to activated carbon that has been used in personal protective equipment (PPE) since WWI. Specifically, Zr-MOFs have gained attention for their promise as hydrolysis catalysts for detoxification of nerve agents. MOFs sharing the same $Zr_6O_6$ node such as UiO-66(Zr) , NU-1000(Zr), and MOF-808(Zr) have been reported for this hydrolysis using nerve agent simulants and nerve agents such as GB, GD, and VX (Figure 2.1).[1] The large body of literature on Zr-MOFs has enabled the study of factors that may affect CWA degradation. Features such as pore size,[2] SBU connectivity, and addition of functional groups on the ligand struts[3, 4] have been examined, leading to steady improvements in catalytic activity. However, efforts to establish broader structure-activity relationships (SARs) over a greater number of solid-state materials has been hindered by time-consuming, low-throughput assays, which limit the number of materials examined.

As discussed in Section 1.6, using high-throughput screening (HTS) provides an opportunity to evaluate a wider set of materials under a wider range of conditions. To screen large sets of materials in parallel, a standard 96-well plate reader was used to monitor the kinetics of organophosphate hydrolysis by capitalizing on the strong absorption of hydrolysis product of the nerve agent simulant dimethyl 4-nitrophenyl phosphate (DMNP, Figure 2.2). HTS requires scaling down of the reaction into a small volume (< 200 µL) and assembly of a library of materials to screen. A library was built to both expand on Zr-MOFs previously studied, but also other materials, including MOFs with different SBUs and other solid-state materials.

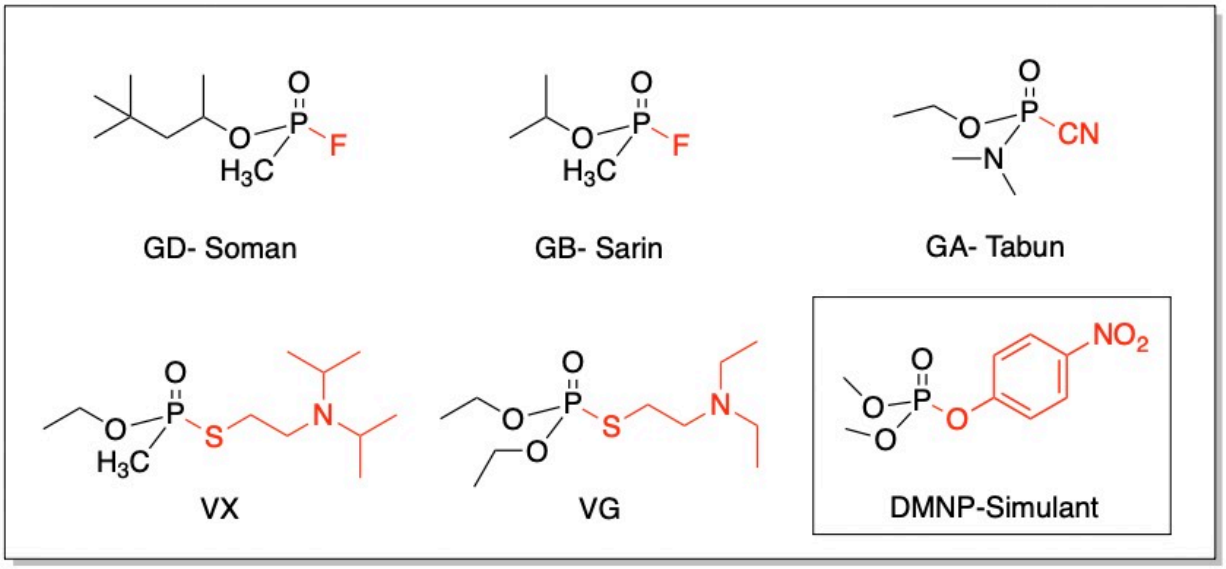


**Figure 2.1.** Chemical structures of a selection of nerve agents and DMNP simulant with leaving groups highlighted in red.

## 2.2 Validation of HTS for Nerve Agent Simulant Degradation

The catalytic degradation assay typically utilized to examine CWA detoxification requires serial measurement of reaction progress.[1] This assay was carried out by adding DMNP directly to a suspension of MOF in buffer, then diluted at regular intervals, transferred to a cuvette, and measured in a spectrophotometer (Figure 2.2).[5] This serial method is accurate, but requires manual monitoring and removal of aliquots over the course of the reaction (up to 3 h). In this work, the serial method was scaled down to run in a 96-well plate in an unmodified, commercial plate reader (Figure 2.2). Development of a HTS assay was based on similar colorimetric assays routinely employed in drug discovery.[6] As configured, this assay can analyze 24 materials simultaneously in triplicate in under one hour. Modifications were made to the previously reported assay

conditions for DMNP (Figure 2.2) simulant hydrolysis, to ensure compatibility and reproducibility in individual assay plate wells. The total volume for each analysis was reduced to 100 µL, and dilution of both simulant and MOF was required to avoid signal saturation. The substrate, DMNP, has limited solubility in water so it was necessary to employ methanol as a solubilizing agent (see Appendix).

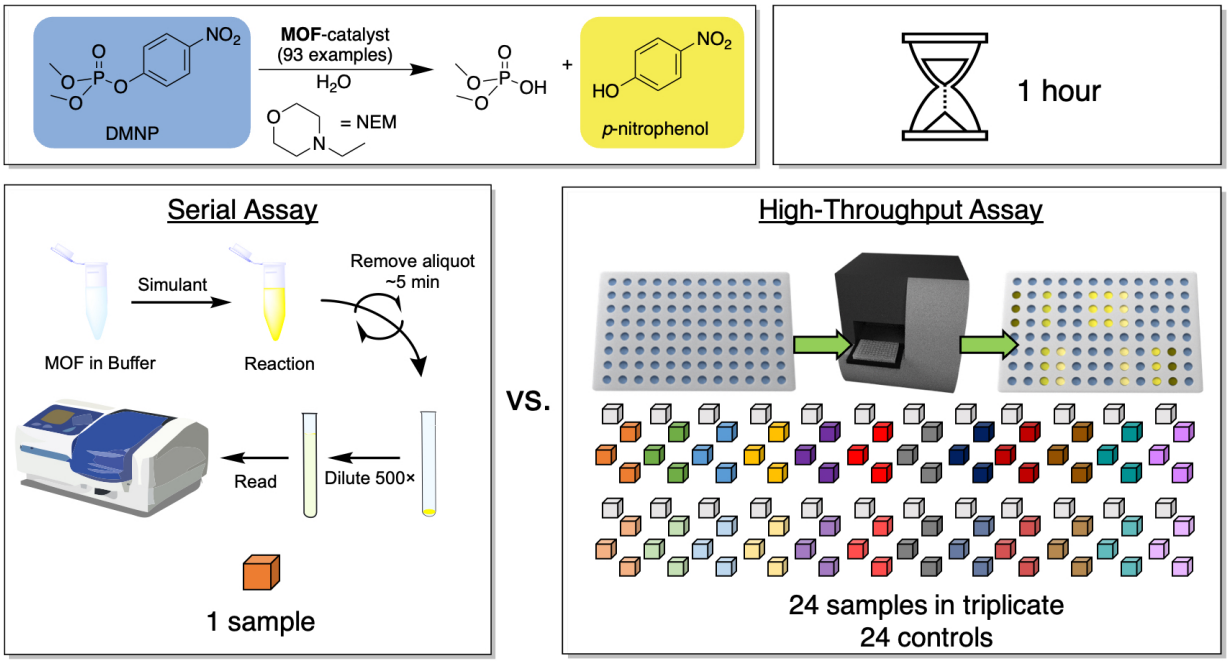


**Figure 2.2**. *Top*: Hydrolysis scheme for DMNP and time for assays. *Bottom*: Comparison of serial assay from literature and HTS assay from this work.

Effective dilution of MOF particles to an optimal concentration posed a technical challenge. A high concentration of MOF particles can result in scattering of the UV-Vis beam during analysis, while low MOF concentrations are difficult to accurately dispense. This challenge is not common in biochemical assays, where all of the assay components are soluble. The accuracy of these HTS assays relies on well-dispersed suspensions

that are diluted and dispensed into each well. Using the materials ZIF-8(Zn), UiO-66(Zr), and NU-1000(Zr) (which were known to have low, medium, and high activity for DMNP degradation, respectively), we demonstrated that controlled amounts of these MOFs could be dispensed into 96-well plates with excellent reproducibility (Figure 2.3). Consistency in the dispersion of our samples was achieved with rigorous centrifugation and vortex mixing procedures (see Appendix).

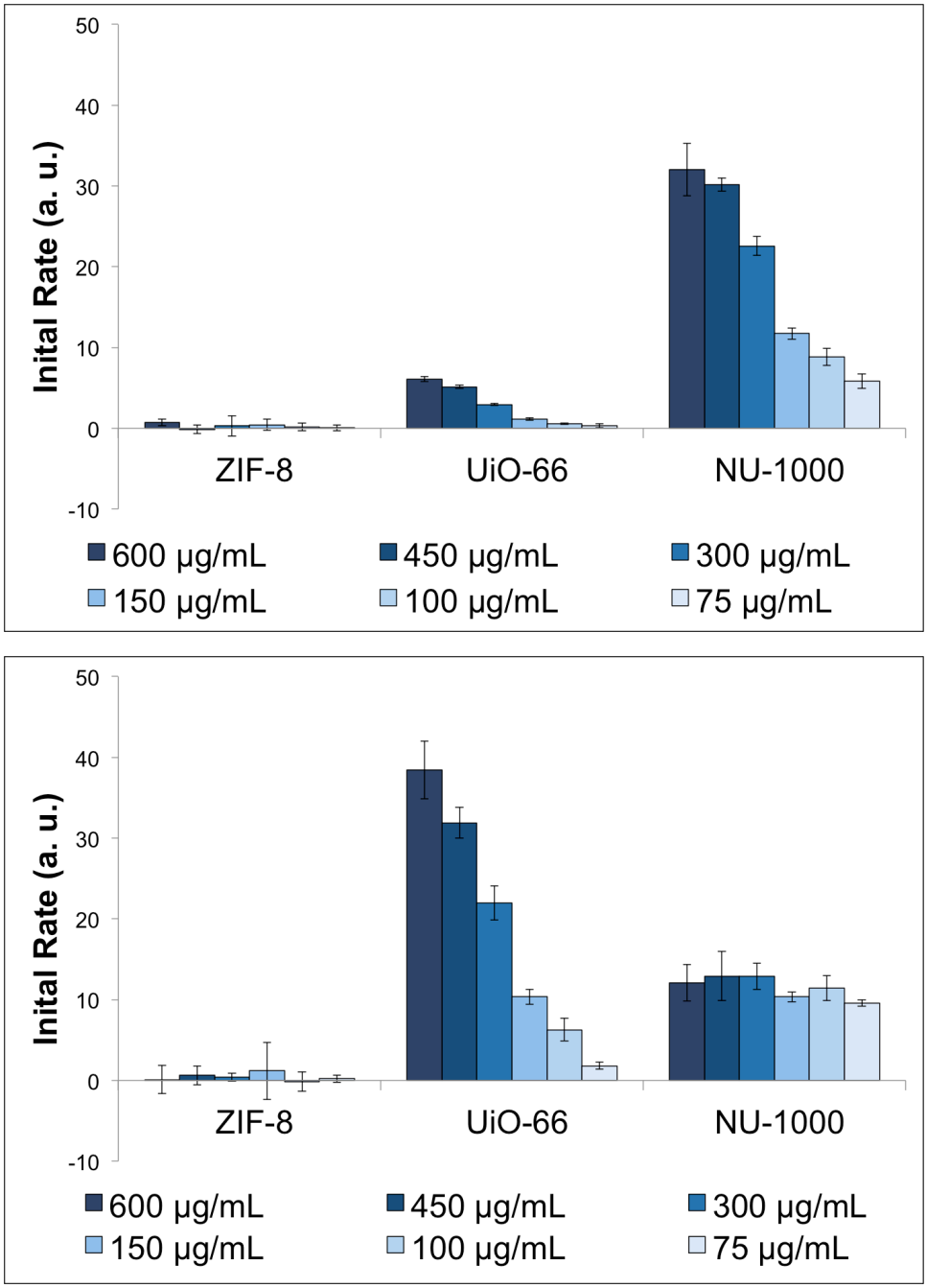


**Figure 2.3.** DMNP hydrolysis rates for ZIF-8(Zn), UiO-66(Zr), and NU-1000(Zr) with *N*-ethylmorpholine at pH = 10.0 (*top*) and pH = 8.0 (*bottom*).

Experiments to validate the HTS assay were performed on a small number of MOF catalysts with *N*-ethylmorpholine buffer at both pH = 10 and 8. The trends in activity of the HTS were in agreement with literature reports of the same materials using a conventional assay (Figure 2.2, Table S2.1). In addition, the Z-factor (or screening window coefficient) of the HTS assay was determined. The Z-factor is a statistical metric for separation of sample and background signal that is a widely accepted parameter of assay quality (Equation 2.1).[7] Assays with a Z-factor >0 are considered valid, while assays with a Z-factor >0.5 are considered excellent (with 1 being ideal). UiO-66(Zr) and NU-1000(Zr) gave calculated Z-factors of >0.45 and >0.50, respectively (Table S2.2). Indeed, evaluation of several MOFs showed generally outstanding Z-factors >0.5 at both pH = 8 and 10 (Table S2.2). This indicates that our assay is statistically meaningful, giving highly reliable data.

$$\boldsymbol{Z = 1 - \frac{(3\sigma_s + 3\sigma_c)}{|\mu_s - \mu_c|}}$$

**Equation 2.1.** Z-factor (screening window coefficient) calculation, where $\mu$ = average slope, $\sigma$ = average standard deviation, s = sample, c = control, the full derivation can be found in the original literature reference.[7]

By running a large number of samples and controls, a Z-factor for both UiO-66(Zr) and NU-1000(Zr) at pH = 8 and pH = 10 were determined. Using the methods described in the Appendix, 14 wells (at 300 μg/mL) were prepared for 6 samples: UiO-66(Zr) (pH = 8 and 10), NU-1000(Zr) (pH = 8 and 10), no MOF control (pH = 8 and 10). The average rates from *t* = 10 min to 50 min were calculated and plotted in Figure 2.4 showing

separation of MOF samples and control wells. In this case background was not subtracted from average slope of MOF samples. Instead, averages and standard deviations ($\mu_s$ and $\sigma_s$) were calculated from all 14 wells for each MOF sample. In addition, averages and standard deviations ($\mu_c$ and $\sigma_c$) were calculated from all 14 wells for each control. These values were applied to Equation 2.1 to determine the Z-factors for both MOFs under each condition (Table S2.2). The Z-factor was also used for evaluating the top 15 MOFs (Figure 2.5 and Table S2.2). The resulting Z-factors indicate that the assay is valid for the top performing MOFs.

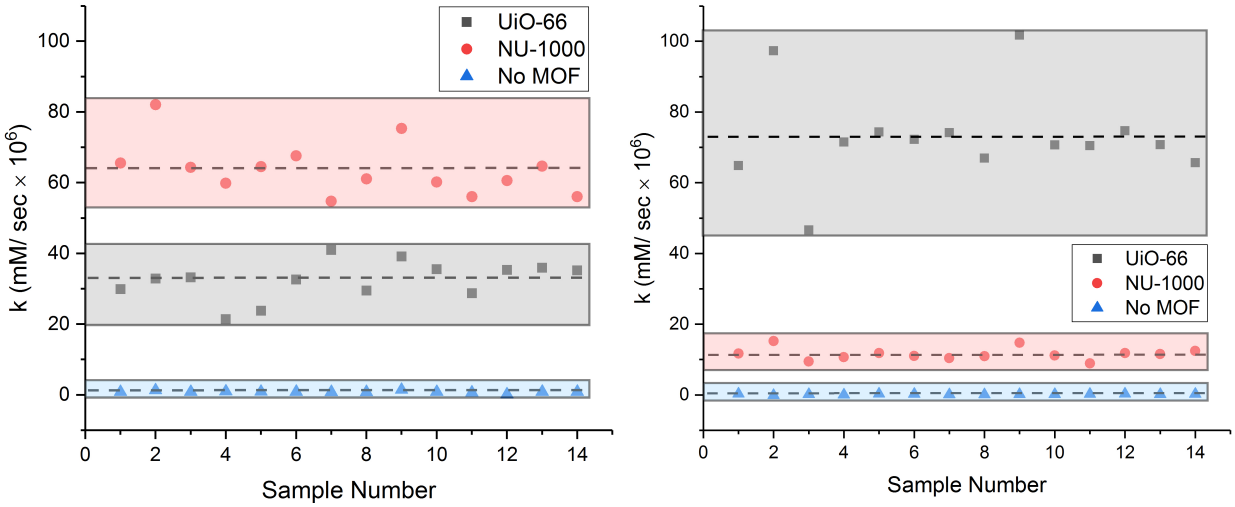


**Figure 2.4.** Individual sample rates for 14 wells of UiO-66, NU-1000, and a control (no MOF) at pH = 10 (*left*) and pH = 8 (*right*).

## 2.3 Library Collection and Screening

Having validated the HTS design, a library of MOFs and related materials were evaluated. Initial linear rates, *k* (mM/sec), were calculated assuming zero-order kinetics using *p*-nitrophenol as a standard for instrument calibration (Equation S2.1, Figure S2.2).

A collection of 93 MOFs, metal oxides, carbons, and zeolites were chosen based on their reported water stability and potential catalytic activity. Among this library of compounds were two sets of distinct UiO-type Zr-MOFs: one set that were prepared using different synthetic procedures, and another set that incorporated modified ligands. This library also contained Al, Cu, Zn, Ti, Co, Hf, and Fe based MOFs not previously studied for CWA degradation, as well as one polyMOF.[8]

Figure 2.5 shows the top 15 MOFs ranked in descending order of activity at pH = 8. The ranking of these materials highlights the lack of correlation between activity at pH = 8 and 10, where catalytic activity at one pH is not predictive of activity at the other. The results of the HTS are consistent with literature reports regarding the effectiveness of MOF materials for organophosphate hydrolysis. Z-factor and regression analysis of these top performers show that reliable, statistically significant data can be gathered using HTS (Table S2.2). None of the zeolite or metal oxide materials show significant hydrolysis activity when compared to the MOFs.

The HTS assay reveals more subtle SAR among related Zr-MOFs that have largely been treated as a common group. The ability to run a large number of samples in parallel allows for small differences in similar materials to be closely examined. Use of chemical modulators during MOF synthesis, the identity of the modulator, and defect density were all found to have a significant effect on catalytic activity and were easily identified with the HTS assay (Figure 2.5).

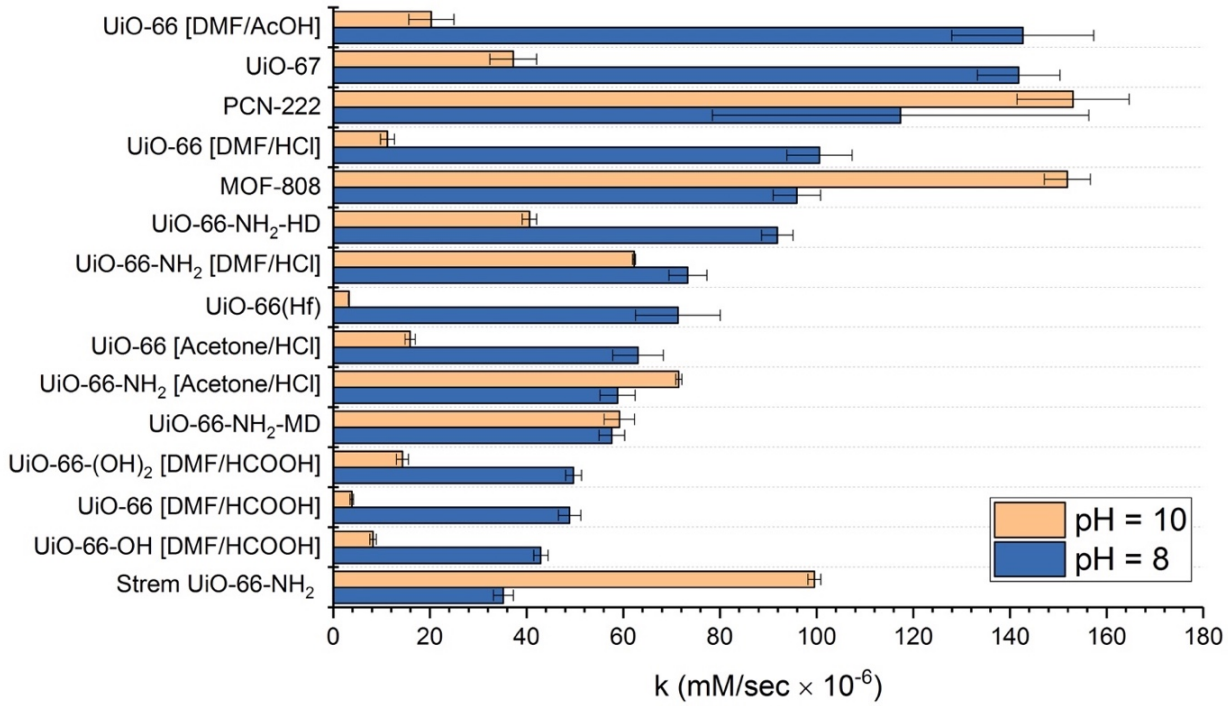


**Figure 2.5.** Top 15 materials ranked based on DMNP degradation at pH = 8. Activity is based on average slope of three independent experiments. The synthesis solvent/modulator in brackets, and detailed synthetic conditions can be found in the Appendix.

## 2.4 Evaluation of MOF Subsets

From within the larger library of materials screened, three sets of compounds were chosen to more closely examine the trends that could be revealed using this HTS method. The first set of compounds consists of UiO-66(Zr) prepared using four different synthetic conditions (i.e., variations in solvent and modulator). These materials show significantly enhanced catalytic activity at pH = 8 vs. pH = 10, across all synthetic preparations for UiO-66(Zr). For each UiO-66(Zr) preparation a >4-fold increase in activity was observed at pH = 8 (Figure 2.6, Table S2.4), consistent with literature reports on the activity of UiO-66(Zr).[9]

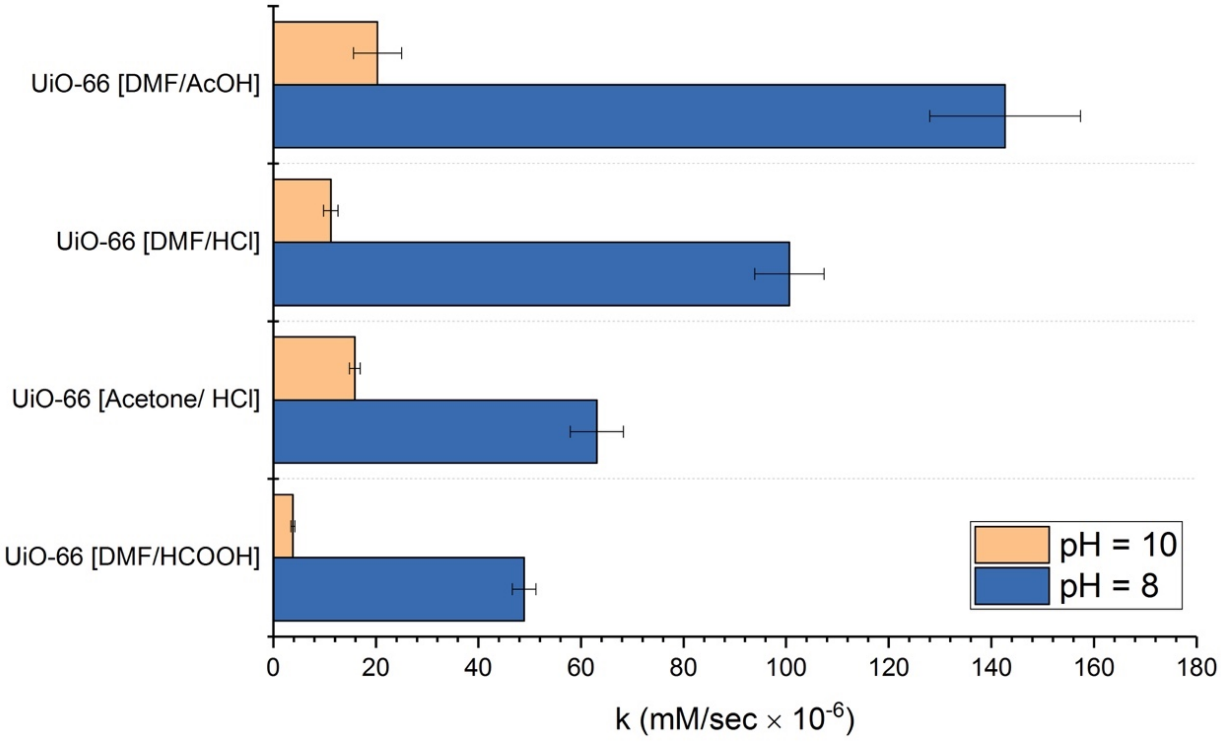


**Figure 2.6.** DMNP degradation rates of UiO-66(Zr) prepared using different synthetic conditions. The synthesis solvent/modulator in brackets.

The UiO-66(Zr) materials used here all have the same bulk structure as determined by PXRD (Figure S2.3-S2.6), but the activity of the materials varies substantially as a function of their synthetic preparation conditions. Simply by changing from formic acid (HCOOH) to acetic acid (AcOH) as the modulator, the activity of UiO-66(Zr) increases from an initial rate of $4.9\times10^{-5}$ to $1.43\times10^{-4}$ mM/sec. The particle size of these four UiO-66(Zr) preparations is similar as determined by SEM, thus variations in activity cannot be attributed to differences in particle size (Figure 2.7).[10] The differences in catalytic activity may be due to the number of lattice defects generated by the different modulators. Overall, these data show that both the reaction pH and the material

preparation are important parameters to consider in evaluation, optimization, and selection of CWA degradation catalysts.

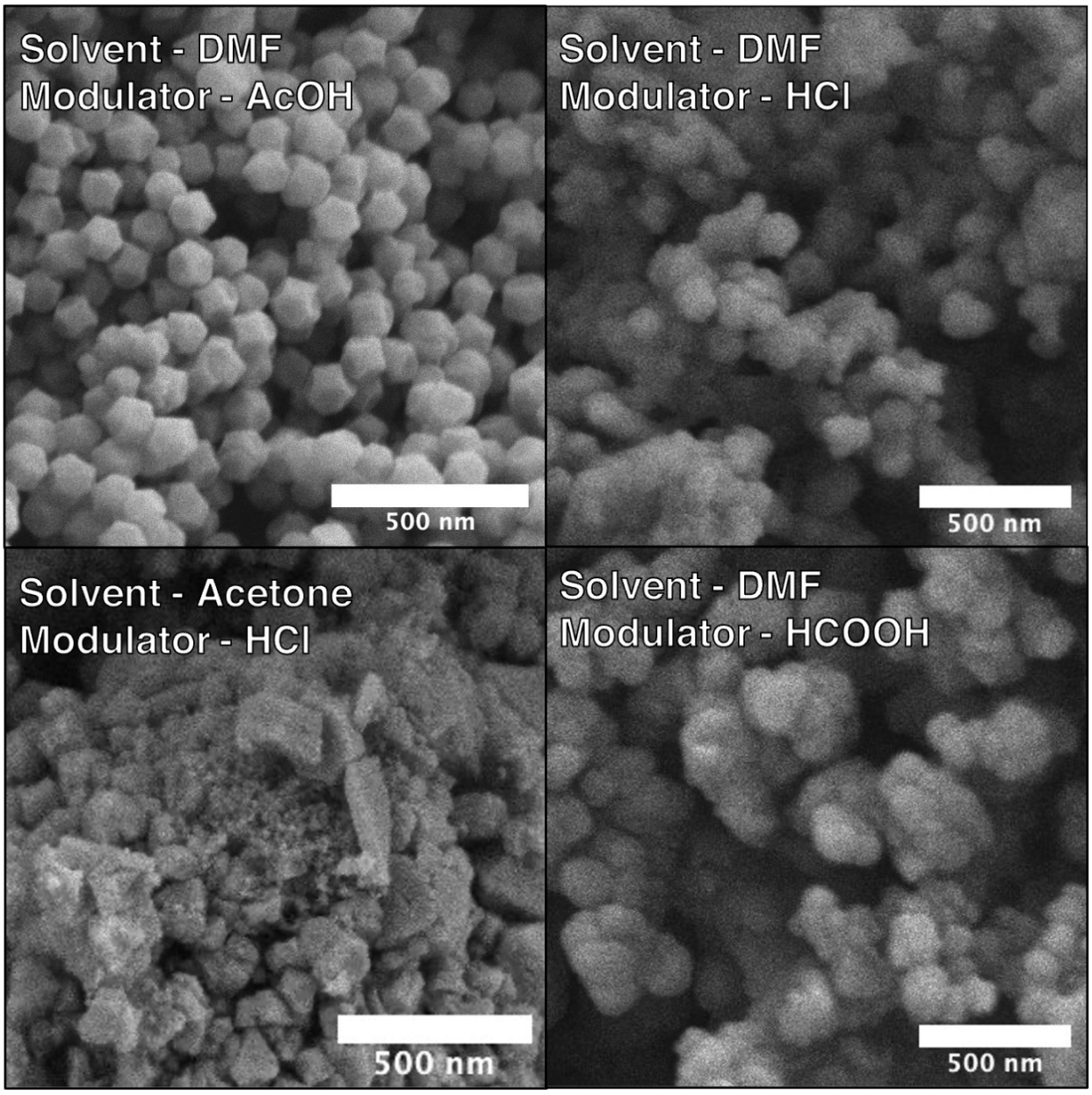


**Figure 2.7.** SEM images of UiO-66(Zr) [DMF/AcOH], UiO-66(Zr) [DMF/HCl], UiO-66(Zr) [Acetone/HCl], and UiO-66(Zr) [DMF/HCOOH].

The high activity of Zr-MOFs has largely been attributed to the Lewis acidity of the Zr metal center.[11] In this screen, the effect of Lewis acidity was tested with a series of four MOFs with Group IV metals (Ti, Zr, Hf). Three tetravalent, terephthalate MOFs with similar topologies to UiO-66(Zr) were examined: MIL-125(Ti)-$NH_2$, PCN-415(Ti/Zr), and UiO-66(Hf). MIL-125(Ti)-$NH_2$ is a Ti(IV)-based MOF that is stable in aqueous environments. PCN-415(Ti/Zr) is a mixed metal MOF (Ti/Zr) that is constructed from a $Ti_6Zr_2O_{12}$ SBU.[12] Finally, UiO-66(Hf) is a direct analog of UiO-66(Zr) that has generally displayed few differences from UiO-66(Zr) in other catalytic reactions.[13] Among these Group IV MOFs, UiO-66(Zr) had the highest catalytic rate (Figure 2.8). Surprisingly, the MOF with the most oxophilic metal in the series, MIL-125(Ti)-$NH_2$, had the lowest activity. Based on these data, it is clear that Lewis acidity alone does not dictate the catalytic degradation rate of the phosphoester bond and other factors potentially serve a more influential role. This suggests that MOFs based on other Lewis acidic metals (e.g., Al or Zn) might show enhanced catalysis in an optimized MOF environment.

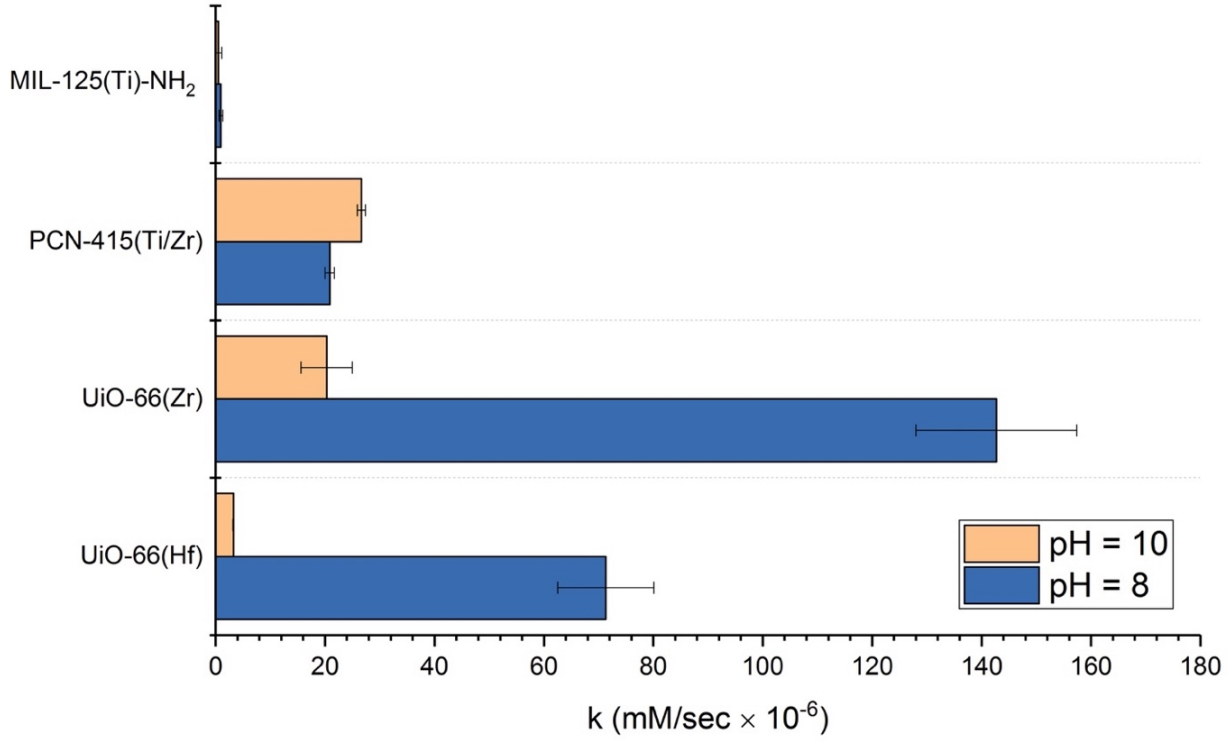


**Figure 2.8.** DMNP degradation rates of Group IV metal MOFs with similar structures.

In addition to Lewis acidity, activity of Zr-MOFs has also been correlated to availability of open metal sites on MOF SBUs. A recent study by Peterson et. al. examined the relationship between defect density and catalytic activity where defects of UiO-66-$NH_2$ are intentionally varied, characterized and effects measured in both simulant and agent hydrolysis.[14] This result indicates that availability of neighboring open metal sites have an effect on catalysis. Data from the HTS supports this hypothesis based on the results with UiO-66(Zr) synthesized under different conditions (Figure 2.6) and from defect regulated UiO-66-$NH_2$ materials (Figure 2.9, Table S2.5) have different hydrolysis rates. In the case of UiO-66-$NH_2$ at pH = 8 and 9, the rate increases with increasing

defects. The HTS assay provides the opportunity to find differences in materials that are nominally the same.

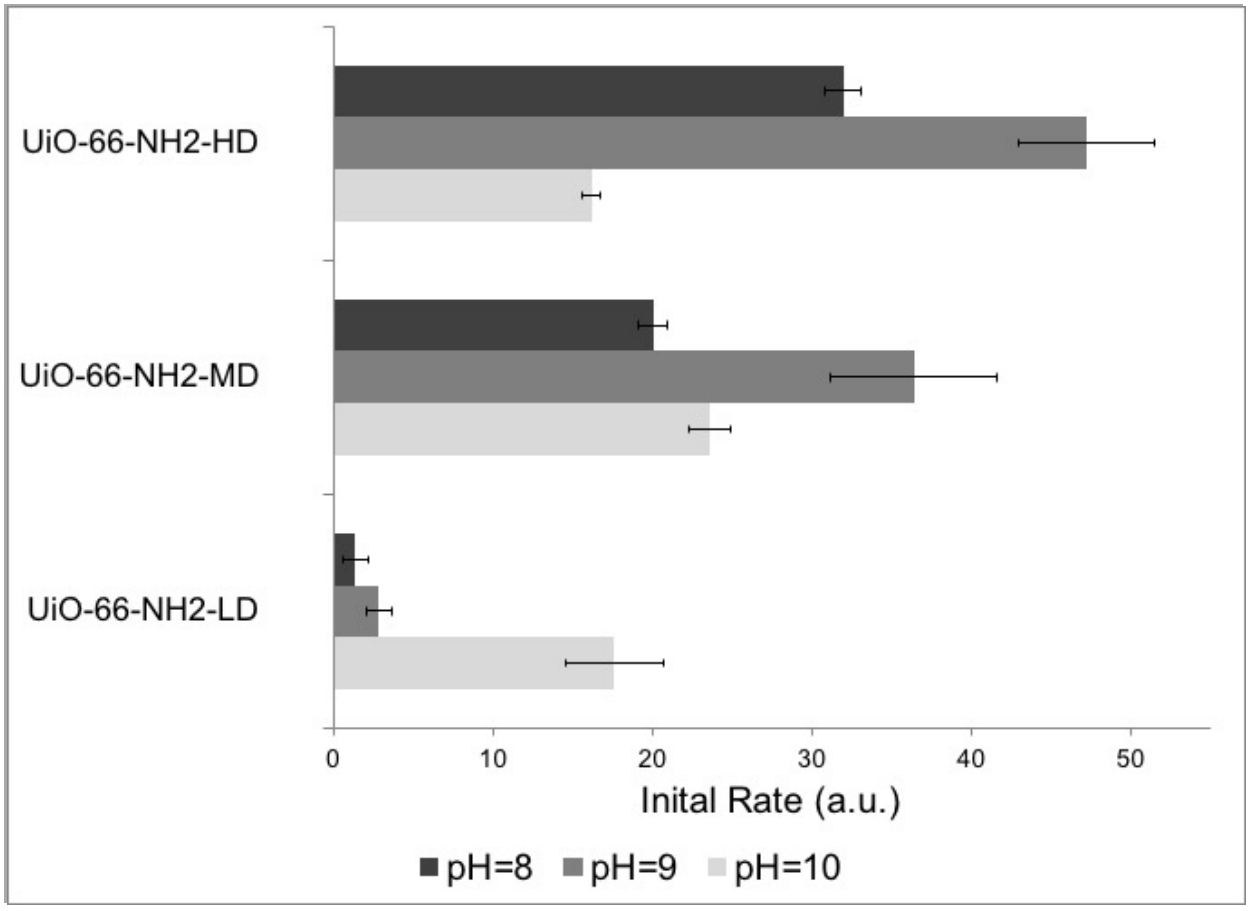


**Figure 2.9.** DMNP hydrolysis rates for UiO-66-$NH_2$ at three concentrations of defects sites (low, medium, and high) in 20 mM *N*-ethylmorpholine at pH = 8, 9, and 10.

## 2.5 Conclusions

An efficient HTS tool was developed for identifying and comparing materials for rapidly advancing catalysts towards a solution to a serious problem. By running MOF samples in parallel, a wider set of materials were tested in a short timeframe. The trends found by this screening effort confirm literature trends for top materials and find new

factors that affect catalyst performance. This work found that solution pH, preparation method, and Lewis acidity create non-linear effects on the hydrolysis rates of MOF catalysts.

The validation of both the technique and library exploration by HTS for MOF discovery opens the possibility to rapidly change the understanding of these solid-state catalytic systems. This tool highlights the gaps in understanding of some key factors related to organophosphate hydrolysis. The ability to change variables and screen quickly with a small amount of active material allows for initial testing to identify interesting phenomenon for further study. Using the simple structural diversity discussed in Section 1.3, the library of MOFs studied can readily be expanded. In addition, considering the large variety of variables MOFs for end use in PPE is important to screen materials and conditions that more closely resemble application of catalysts.

## 2.6 Appendix: Supporting Information

**General Materials and Methods.** Starting materials were purchased and used from commercially available suppliers (Sigma-Aldrich, Acros Organics, Matrix Scientific, and others) without further purification.

**Powder X-ray Diffraction (PXRD).** PXRD data was collected at room temperature on a Bruker D8 Advance diffractometer running at 40 kV, 40 mA for Cu Kα ($\lambda$ = 1.5418 Å), with primary slit of 1 mm, a scan speed of 0.5 sec/step, a step size of 0.01° in 2θ, and a 2θ range of 3-50° at room temperature.

**Scanning Electron Microscopy (SEM).** MOFs were placed on conductive carbon tape on a sample holder and coated by using an Ir sputter-coater for 7 s. A FEI Quanta 250 scanning electron microscope was used for acquiring images using a 10 kV energy source under vacuum at a working distance of 10 mm.

## Experimental

**Synthetic Procedures.** Materials purchased from suppliers were used without further purification. Other materials prepared according to reported literature procedure listed in Table S2.3. All MOFs regardless of synthesis conditions were subjected to overnight activation at 80 °C in a vacuum oven under active vacuum. MOFs were characterized via powder X-ray diffraction (Figure S2.3-S2.88).

**UiO-66(Zr)-$NH_2$ [DMF/AcOH].** The MOF was synthesized according to literature procedure with BDC-$NH_2$ as ligand.[16] This MOF was treated with an additional washing step to avoid formylation found in literature in synthesis of UiO-66-$NH_2$.[17] Using a modified procedure, the formyl groups were restored to free amine. 2 g of UiO-66-$NH_2$ was added to 100 mL MeOH:$H_2O$ 1:1 mixture with 5 mL of conc. HCl and refluxed overnight. Solid was collected by filtration and washed with MeOH. $^1$H NMR was used to characterize the completeness of removal of formyl group as in the reference.[17]

**UiO-66(Zr)-COOH [DMF/AcOH].** Components were mixed together in the following molar ratio in a glass vial with 0.4 vol% di$H_2O$ as an additive and heated at 150 °C for 24 h. $ZrO(NO_3)_2$•$H_2O$/BDC/AcOH/DMF = 1/2/100/90. White solid was collected by centrifugation and washed with DMF and EtOH.

**ZIF-4(Zn).** 1.5 g (5 mmol) of $Zn(NO_3)_2 \cdot 6H_2O$ was added to a 125 mL glass jar with 113 mL of DMF. To this 1.13 g (16.5 mmol) of imidazole was added and mixture was heated to 100 °C for 72 h. A white solid was collected by filtration and washed with DMF and EtOH.

**Preparation of *N*-ethylmorpholine Buffers.** To prepare 20 mM *N*-ethylmorpholine buffer, 0.5 mL (4.0 mmol) of *N*-ethylmorpholine was added to 200 mL of di$H_2O$ with stirring and the pH was monitored. The 20 mM *N*-ethylmorpholine solution produced a pH of 10.4. To adjust to the desired pH (8.0 or 10.0), ~1 M HCl was added dropwise while continuously monitoring the pH.

**Calibration Curves for *p*-Nitrophenol.** In order to determine the relationship between concentration of *p*-nitrophenol and plate reader absorbance, a calibration curve was prepared. Five solutions of *p*-nitrophenol were made at varying concentrations in both pH = 8 and 10 buffers. The absorbance was measured in 8 wells and averaged. Results are shown in Table S2.6 and Figure S2.2. Using the slopes from these curves, the rate of hydrolysis (*k*) can be determined for each sample based on the initial rate calculated from slope (Abs/sec).

**HTS Validation.** Validation tests assays were carried out in Olympus Plastics clear, flat-bottom 96-well plates. Each well was prepared with 100 µL total volume containing: 95 µL buffer (20 mM *N*-ethylmorpholine adjusted to pH 8 or 10); and MOF (X µg/mL, where X = 600, 450, 300, 150, 100, 75); and 5 µL substrate (25 mM stock solution of methyl paraoxon in methanol; 1.25 mM total concentration; 0.125 µmol). Note, methanol was used as solubilizing agent as DMNP has limited solubility in water. The

use of short-chain alcohols or dimethyl sulfoxide as solubilizing agents at concentrations <10% in biological HTS assays is common.[18, 19] MOF suspensions were prepared by weighing 12 mg of MOF powder into a 15 mL centrifuge tube and adding 10 mL of corresponding 20 mM buffer solutions. All suspensions were sonicated in a water-bath for 30 min to disperse the powders. These concentrated suspensions were diluted with buffer solution to achieve final concentrations tested (Table S2.7). Before any transfer, great care was taken to achieve a stable suspension to provide the most accurate dilution following the steps: 1) sonicated suspension for 30 sec; 2) mix with vortex mixer for 15 sec; 3) invert centrifuge tube three times; 4) mix with vortex mixer for an additional 15 sec; 5) transfer immediately to the plate. These suspensions (1 mL total volume) were used to prepare individual wells of the 96-well plate. The same suspension procedure as above was employed before adding 95 µL to each well. In a typical run, six replicates of each condition were prepared by plating 3 wells, repeating the suspension procedure and then plating 3 more wells. In addition, each column included two negative controls: 1) buffer and substrate only (used to calculate background hydrolysis) and 2) buffer and MOF without substrate. Upon the addition of substrate with multi-channel pipette hydrolysis was monitored by change in absorbance at over 60 min at 24 °C with 5 sec shaking of plate every 40 sec ($\lambda_{max}$ = 407 nm). Activity was measured as initial linear rate, measured from 10 to 50 min using Excel software. Reported activity is average slope for six replicates with a background subtraction from the hydrolysis rate in the presence of 20 mM *N*-ethylmorpholine without MOF (Figure 2.3 and Figure 2.4).

**Evaluation of Dispensing of MOFs for HTS.** Precision and accuracy for catalytic

rates for a particular concentration of MOF was evaluated based on suspected error in dispensing. The concentrations of MOF materials were varied and evaluated in the assay. Three MOFs: ZIF-8, UiO-66, and NU-1000(Zr) were assessed based on their anticipated activity (low, medium, and high activity, respectively) to test six different MOF concentrations (Figure 2.3). The results in Figure 2.3 demonstrate that the assay conditions are valid for identifying hits even accounting for variance in quantity of MOF dispersed, and that the observed activity directly tracks with the concentration of MOF added.

**Evaluation of Different Buffers.** To confirm effect of pH on DMNP hydrolysis, two additional buffers were tested: 1) Tris and 2) HEPES. Both buffers were prepared in the same fashion as for *N*-ethylmorpholine and tests for dispensing validation experiments for these buffers were carried out the same as outlined above. Results confirm that MOF activity is pH dependent (Figure S2.1).

**HTS of Library Samples.** All samples were prepared and analyzed using the screening method described above (HTS Validation) at a concentration of 300 μg/mL with one procedure change. Instead of preparing material suspensions in 10 mL of buffer solution, 6 mg of material was diluted with 10 mL of di$H_2O$. 500 μL of this suspension was then diluted with 500 μL of 40 mM *N*-ethylmorpholine of corresponding pH. This resulted in the same final concentration of buffer and allowed for the same di$H_2O$ suspension to be used for all pHs tested. Due to the variety in materials included in library, all materials were prepared in equal mass content (not molar).

## Supplemental Equations

$$\frac{Initial\ Rate\ \left(\frac{Abs}{sec}\right)}{slope\ of\ calibration\ curve\left(\frac{Abs}{mM}\right)} = k\ \left(\frac{mM}{sec}\right)$$

**Equation S2.1.** Hydrolysis rate calculation, see Table S2.3 and Figure S2.2.

## Supplemental Tables

**Table S2.1.** Activity of MOFs based on first-order kinetics screened via HTS method as CWA degradation catalysts. Literature values shown for comparison. Note, $t_{1/2}$ calculation ($t_{1/2}$ = ln(2)/k) is estimated for first-order kinetics in all cases.

| MOF | Literature | | This Work | | | |
|---|---|---|---|---|---|---|
| | pH = 10.4 | | pH = 10.0 | | pH = 8.0 | |
| | MOF conc. | ($t_{1/2}$ in min) | MOF conc. | ($t_{1/2}$ in min) | MOF conc. | ($t_{1/2}$ in min) |
| UiO-66 | 2.5 mg/ mL | 25-45[5] | 0.3 mg/ mL | 900 | 0.3 mg/ mL | 112 |
| UiO-66-$NH_2$ | 2.5 mg/ mL | 1[4] | | 132 | | 164 |
| UiO-67 | 2.5 mg/ mL | 4.5[20] | | 340 | | 40 |
| NU-1000 | 3.0 mg/ mL | 1.5-15[21] | | 108 | | 340 |
| PCN-222 | 2.4 mg/ mL | 8[11] | | 56 | | 88 |

**Table S2.2.** Statistical parameters for UiO-66, NU-1000, and top 15 MOFs at both pH = 8 and 10; $\mu$ = average slope and $\sigma$ = average standard deviation. Control tests are buffer and substrate without MOF. Z-factors were calculated based on Equation S1. "n" indicates number of replicates used for statistics. $R^2$ values were calculated based on average over slope range.

| | pH = 8 | | | | | | |
|---|---|---|---|---|---|---|---|
| **MOF** | **μ- sample** | **σ- sample** | **μ- control** | **σ- control** | **n** | **Z-factor** | **$R^2$ of slope** |
| UiO-66(Zr) [DMF/HCl] | 2.54E-04 | 4.62E-05 | 6.25E-07 | 3.71E-07 | 14 | 0.45 | 0.9995 |
| NU-1000 | 4.02E-05 | 6.00E-06 | 6.25E-07 | 3.71E-07 | 14 | 0.52 | 0.9970 |
| UiO-66(Zr) [DMF/AcOH] | 4.98E-04 | 5.12E-05 | 7.44E-07 | 3.53E-07 | 3 | 0.69 | 0.9995 |
| UiO-67 | 4.95E-04 | 2.97E-05 | 8.78E-07 | 1.57E-07 | 3 | 0.82 | 0.9859 |
| PCN-222 | 4.09E-04 | 1.36E-04 | 8.78E-07 | 1.57E-07 | 3 | 0.00 | 0.9938 |
| MOF-808 | 3.34E-04 | 1.70E-05 | 5.33E-07 | 1.48E-07 | 3 | 0.85 | 0.9987 |
| UiO-66-$NH_2$-HD | 3.21E-04 | 1.12E-05 | 6.67E-07 | 1.81E-07 | 3 | 0.89 | 0.9874 |
| UiO-66-$NH_2$ [DMF/HCl] | 2.57E-04 | 1.37E-05 | 7.44E-07 | 3.53E-07 | 3 | 0.84 | 0.9963 |
| UiO-66(Hf) | 2.49E-04 | 3.06E-05 | 7.18E-07 | 2.22E-07 | 3 | 0.63 | 0.9988 |
| UiO-66(Zr) [Acetone/HCl] | 2.21E-04 | 1.81E-05 | 8.78E-07 | 1.57E-07 | 3 | 0.75 | 0.9983 |
| UiO-66-$NH_2$ [Acetone/HCl] | 2.06E-04 | 1.26E-05 | 8.78E-07 | 1.57E-07 | 3 | 0.81 | 0.9970 |
| UiO-66-NH2-MD | 2.01E-04 | 9.25E-06 | 6.67E-07 | 1.81E-07 | 3 | 0.86 | 0.9445 |
| UiO-66-$(OH)_2$ [DMF/HCOOH] | 3.14E-05 | 2.23E-06 | 8.78E-07 | 1.57E-07 | 3 | 0.77 | 0.9210 |
| UiO-66(Zr) [DMF/HCOOH] | 1.71E-04 | 7.97E-06 | 8.78E-07 | 1.57E-07 | 3 | 0.86 | 0.9975 |
| UiO-66-OH [DMF/HCOOH] | 1.51E-04 | 5.13E-06 | 8.78E-07 | 1.57E-07 | 3 | 0.89 | 0.9978 |
| Strem UiO-66-$NH_2$ | 1.23E-04 | 7.16E-06 | 7.44E-07 | 3.53E-07 | 3 | 0.82 | 0.9989 |
| | **pH = 10** | | | | | | |
| **MOF** | **μ- sample** | **σ- sample** | **μ- control** | **σ- control** | **n** | **Z-factor** | **$R^2$ of slope** |
| UiO-66(Zr) [DMF/HCl] | 1.29E-04 | 2.15E-05 | 2.41E-06 | 1.66E-06 | 14 | 0.46 | 0.9979 |
| NU-1000 | 2.54E-04 | 2.99E-05 | 3.45E-06 | 1.17E-06 | 14 | 0.63 | 0.9962 |
| UiO-66(Zr) [DMF/AcOH] | 8.28E-05 | 1.87E-05 | 2.41E-06 | 1.66E-06 | 3 | 0.24 | 0.9941 |
| UiO-67 | 1.51E-04 | 1.92E-05 | 2.14E-06 | 3.25E-07 | 3 | 0.61 | 0.9979 |
| PCN-222 | 6.13E-04 | 4.63E-05 | 2.14E-06 | 3.25E-07 | 3 | 0.77 | 0.9945 |
| MOF-808 | 6.10E-04 | 1.91E-05 | 4.39E-06 | 1.56E-07 | 3 | 0.90 | 0.9917 |
| UiO-66-$NH_2$-HD | 1.62E-04 | 5.88E-06 | 2.27E-06 | 2.15E-07 | 3 | 0.89 | 0.9972 |
| UiO-66-$NH_2$ [DMF/HCl] | 2.50E-04 | 1.24E-06 | 2.41E-06 | 1.66E-06 | 3 | 0.96 | 0.9933 |

| | | | | | | | |
|---|---|---|---|---|---|---|---|
| UiO-66(Hf) | 1.57E-05 | 3.51E-07 | 2.56E-06 | 5.66E-07 | 3 | 0.79 | 0.9861 |
| UiO-66(Zr) [Acetone/HCl] | 6.55E-05 | 4.20E-06 | 2.14E-06 | 3.25E-07 | 3 | 0.79 | 0.9915 |
| UiO-66-$NH_2$ [Acetone/HCl] | 2.88E-04 | 2.52E-06 | 2.14E-06 | 3.25E-07 | 3 | 0.97 | 0.9972 |
| UiO-66-NH2-MD | 2.38E-04 | 1.26E-05 | 2.27E-06 | 2.15E-07 | 3 | 0.84 | 0.9957 |
| UiO-66-$(OH)_2$ [DMF/HCOOH] | 3.44E-05 | 2.14E-06 | 2.14E-06 | 3.25E-07 | 3 | 0.77 | 0.9558 |
| UiO-66(Zr) [DMF/HCOOH] | 1.72E-05 | 1.49E-06 | 2.14E-06 | 3.25E-07 | 3 | 0.64 | 0.9862 |
| UiO-66-OH [DMF/HCOOH] | 3.36E-05 | 2.64E-06 | 2.14E-06 | 3.25E-07 | 3 | 0.72 | 0.9848 |
| Strem UiO-66-$NH_2$ | 3.99E-04 | 5.34E-06 | 2.41E-06 | 1.66E-06 | 3 | 0.95 | 0.9950 |

**Table S2.3.** Material Identity, Formula Unit, Metal, Metal Atomic Number (Z), and Slope (average of three wells, in mM/sec × $10^{-6}$) for DMNP Hydrolysis at pH = 8 and pH = 10 with standard deviations (σ) for each material tested. Rounded brackets () indicate metal; Square brackets [] indicate modulator used in synthesis. Suppliers (where applicable) are listed before name of material.

| # | Material | Formula Unit[a] | Metal | Z | Slope; pH=8 | σ; pH=8 | Slope; pH=10 | σ; pH=10 | Cit./ Sup.[b] |
|---|---|---|---|---|---|---|---|---|---|
| 1 | PIM-1 | $C_{14}O_2N$ | C | 6 | -4.49 | 6.55 | -0.53 | 1.79 | [22] |
| 2 | Coconut Cabon | C | C | 6 | 1.97 | 4.93 | 0.17 | 1.00 | GA |
| 3 | BPL | C | C | 6 | 8.14 | 6.08 | 1.30 | 1.09 | CCC |
| 4 | $Mg(OH)_2$ | $Mg(OH)_2$ | Mg | 12 | 2.99 | 2.50 | 11.67 | 16.52 | NAM |
| 5 | Al-PMOF | $TCPP(AlOH)_2$ | Al | 13 | -3.18 | 3.01 | -4.78 | 0.30 | [23] |
| 6 | CAU-10-$NH_2$ | $Al(OH)(ISO\text{-}NH_2)$ | Al | 13 | 10.39 | 11.85 | 8.43 | 18.01 | [24] |
| 7 | CAU-10-$CH_3$ | $Al(OH)(ISO\text{-}CH_3)$ | Al | 13 | 14.84 | 25.26 | 8.48 | 13.95 | [24] |
| 8 | CAU-10-OH | Al(OH)(ISO-OH) | Al | 13 | 0.88 | 5.41 | 0.80 | 2.27 | [24] |
| 9 | MIL-96(Al) | $Al_{12}O(OH)_{18}(H_2O)_3(Al_2(OH)_4)(BTC)_6$ | Al | 13 | 0.44 | 1.11 | 1.94 | 3.48 | [25] |
| 10 | MIL-53(Al) | Al(OH)(BDC) | Al | 13 | -2.72 | 1.24 | -0.64 | 0.30 | [26] |
| 11 | MIL-53(Al)-Br | Al(OH)(BDC-Br) | Al | 13 | -1.31 | 4.41 | -1.09 | 0.24 | [26] |
| 12 | MIL-53(Al)-$NH_2$ | $Al(OH)(BDC\text{-}NH_2)$ | Al | 13 | -1.13 | 0.90 | -0.92 | 0.82 | [26] |
| 13 | $Al_2O_3$ | $Al_2O_3$ | Al | 13 | -0.01 | 0.01 | -0.31 | 0.29 | NAM |
| 14 | Silicalite | $SiO_2$ | Si | 14 | 3.83 | 1.16 | 0.22 | 0.35 | GA |
| 15 | SAPO-34 | $SiO_2$ | Si | 14 | -4.29 | 1.58 | -0.42 | 0.37 | GA |
| 16 | H-ZSM-5 | $SiO_2$ | Si | 14 | 2.29 | 3.87 | 0.61 | 0.19 | GA |
| 17 | HY | $(Si)_{0.5}(Al)_{0.5}O_2$ | Si | 14 | -0.08 | 0.43 | 0.74 | 0.76 | GA |
| 18 | Na-ZSM-5 | $(Si)_{0.9}(Al)_{0.1}O_2$ | Si | 14 | -2.58 | 2.84 | 1.32 | 1.45 | GA |
| 19 | Zeolite 4A | $SiO_2$ | Si | 14 | -0.84 | 0.64 | 0.03 | 1.20 | ASGE |
| 20 | Aldrich MCM-41 | $SiO_2$ | Si | 14 | -0.11 | 0.24 | 0.08 | 0.06 | SA |
| 21 | Y-54 DR | $SiO_2$ | Si | 14 | -0.36 | 0.98 | 0.39 | 0.68 | GA |
| 22 | MIL-125(Ti)-$NH_2$ | $Ti_8O_8(OH)_4(BDC\text{-}NH_2)_6$ | Ti | 22 | 0.92 | 0.34 | 0.48 | 0.65 | [27] |
| 23 | $TiO_2$ | $TiO_2$ | Ti | 22 | -1.37 | 0.76 | -0.85 | 0.76 | NAM |
| 24 | Aldrich $TiO_2$ | $TiO_2$ | Ti | 22 | 0.65 | 7.07 | -1.73 | 0.06 | SA |
| 25 | Aldrich $TiO_2$ Anatase | $TiO_2$ | Ti | 22 | 0.64 | 0.97 | -0.23 | 0.29 | SA |
| 26 | Degussa $P_{25}$ $TiO_2$ | $TiO_2$ | Ti | 22 | -2.62 | 3.90 | -1.40 | 0.46 | DC |
| 27 | PCN-415 | $Ti_8Zr_2O_{12}(BDC)_{16}$ | Zr/Ti | 22 | 20.85 | 0.86 | 26.65 | 0.75 | [12] |
| 28 | MIL-101(Cr) | $Cr_3F(H_2O)_2O(BDC)_3$ | Cr | 24 | 1.05 | 4.35 | 2.80 | 12.35 | [28] |
| 29 | MIL-53(Cr) | Cr(OH)(BDC) | Cr | 24 | -1.48 | 0.32 | -1.41 | 0.67 | [29] |
| 30 | PCN-250(Mn) | $Mn_3(\mu_3\text{-}O)(H_2O)_3(ABTEC)_6$ | Mn | 25 | 0.63 | 0.65 | 2.01 | 4.50 | NMT |
| 31 | MIL-53(Fe) | Fe(OH)(BDC) | Fe | 26 | -0.03 | 0.35 | -3.57 | 1.59 | [30] |
| 32 | MIL-88B(Fe) | $Fe_3O(BDC)_3(H_2O)_2(X)$, X=OH, Cl | Fe | 26 | 3.60 | 4.35 | 7.93 | 12.47 | [31] |
| 33 | MIL-100(Fe) | $Fe_3OX(BTC)_2$, X=OH, F, Cl | Fe | 26 | -3.67 | 4.74 | 2.25 | 4.12 | [32] |
| 34 | Aldrich MIL-100(Fe) | Fe(OH)(BTC) | Fe | 26 | -5.59 | 34.54 | -2.43 | 1.06 | SA |
| 35 | Strem PCN-250(Fe) | $Fe_3(\mu_3\text{-}O)(H_2O)_3(ABTEC)_6$ | Fe | 26 | 0.17 | 3.08 | -4.43 | 7.14 | SC |
| 36 | PCN-250(Fe) | $Fe_3(\mu_3\text{-}O)(H_2O)_3(ABTEC)_6$ | Fe | 26 | 1.34 | 0.95 | 0.12 | 0.92 | NMT |
| 37 | $Fe_2O_3$ | $Fe_2O_3$ | Fe | 26 | 6.11 | 5.39 | 3.87 | 1.10 | NAM |
| 38 | ZIF-67 | $Co(MEIM)_2$ | Co | 27 | 3.13 | 4.69 | 2.58 | 6.39 | [33] |
| 39 | Co-NIC | $Co_2(NIC)_4(\mu\text{-}H_2O)$ | Co | 27 | 0.01 | 0.03 | 0.16 | 0.75 | [34] |
| 40 | $Co_3O_4$ | $Co_3O_4$ | Co | 27 | -4.25 | 0.85 | -4.81 | 3.52 | NAM |
| 41 | Zn/Co BTEC | ZnCo(BTEC) | Zn/Co | 27 | 0.72 | 1.40 | -0.22 | 0.27 | [35] |
| 42 | ZIF-8/67 | $ZnCo(MEIM)_4$ | Zn/Co | 27 | 2.29 | 2.38 | 0.52 | 0.61 | [33] |
| 43 | Ni-NIC | $Ni_2(NIC)_4(IH_2O)$ | Ni | 28 | 0.14 | 0.26 | -0.13 | 0.11 | [34] |
| 44 | CuBDC | $CuO(BDC)_2$ | Cu | 29 | 0.99 | 2.82 | -2.22 | 6.59 | [36] |

| | | | | | | | | | |
|---|---|---|---|---|---|---|---|---|---|
| 45 | Cu-PCN | $Cu_2(PCN)_2(H_2O)_2$ | Cu | 29 | -1.21 | 2.16 | 2.06 | 5.84 | [37] |
| 46 | PCN-250(Cu) | $Cu_3(\mu_3\text{-}O)(H_2O)_3(ABTEC)_6$ | Cu | 29 | 1.58 | 2.81 | 6.48 | 8.38 | NMT |
| 47 | MOF-74(Cu) | $Cu_2(DOBDC)$ | Cu | 29 | 6.90 | 7.87 | 1.60 | 4.82 | NMT |
| 48 | Aldrich HKUST-1 | $Cu_3(BTC)_2$ | Cu | 29 | 11.16 | 10.31 | -3.12 | 0.62 | SA |
| 49 | MOF-508 | Zn (BDC) (BPY) | Zn | 30 | -2.43 | 4.30 | 0.48 | 1.08 | [38] |
| 50 | ZIF-8 | $Zn(MEIM)_2$ | Zn | 30 | 0.28 | 5.03 | 0.76 | 3.17 | [33] |
| 51 | ZIF-4 | $Zn(IM)_2$ | Zn | 30 | -0.72 | 2.65 | -0.94 | 1.82 | See Above |
| 52 | ZIF-62 | $Zn(IM)_{1.75}(BIM)_{0.25}$ | Zn | 30 | 0.66 | 1.73 | 1.72 | 1.41 | [39] |
| 53 | ZIF-71 | $Zn(IM\text{-}Cl_2)_2$ | Zn | 30 | 1.77 | 3.41 | -2.02 | 1.12 | [40] |
| 54 | ZnO | ZnO | Zn | 30 | 6.40 | 16.92 | -1.57 | 1.11 | NAM |
| 55 | DMOF-1 | $Zn_2(BDC)_2DABCO$ | Zn | 30 | 5.33 | 7.38 | 0.53 | 1.33 | NMT |
| 56 | PCN-700 | $Zr_6O_8(OH)_8(Me_2\text{-}BPDC)_4$ | Zr | 40 | 8.93 | 4.37 | 13.83 | 13.59 | [41] |
| 57 | MOF-801 | $Zr_6O_4(OH)_4(FUM)_6$ | Zr | 40 | 4.33 | 0.63 | 11.22 | 6.20 | [42] |
| 58 | MOF-802 | $Zr_6O_4(OH)_4(PZDC_4)_5(HCOO)_2(H_2O)_2$ | Zr | 40 | 3.69 | 1.98 | 5.27 | 1.66 | [42] |
| 59 | UiO-66(Zr) [DMF/AcOH] | $Zr_6O_6(BDC)_{12}$ | Zr | 40 | 142.68 | 14.70 | 20.31 | 4.68 | [16] |
| 60 | UiO-66(Zr) [DMF/HCl] | $Zr_6O_6(BDC)_{12}$ | Zr | 40 | 100.62 | 6.77 | 11.21 | 1.44 | [43] |
| 61 | UiO-66-$NH_2$ [DMF/AcOH] | $Zr_6O_6(BDC\text{-}NH_2)_{12}$ | Zr | 40 | 24.28 | 1.02 | 44.86 | 2.70 | [16]* |
| 62 | UiO-66-$NH_2$ [DMF/HCl] | $Zr_6O_6(BDC\text{-}NH_2)_{12}$ | Zr | 40 | 73.34 | 3.94 | 62.24 | 0.31 | [43] |
| 63 | Strem UiO-66-$NH_2$ | $Zr_6O_6(BDC\text{-}NH_2)_{12}$ | Zr | 40 | 35.18 | 2.06 | 99.57 | 1.34 | SC |
| 64 | UiO-66-$SO_3H$ [DMF/BzOH] | $Zr_6O_6(BDC\text{-}SO_3H)_{12}$ | Zr | 40 | 16.63 | 0.80 | 9.68 | 0.36 | [44] |
| 65 | UiO-66-COOH [DMF/AcOH] | $Zr_6O_6(BDC\text{-}COOH)_{12}$ | Zr | 40 | 2.59 | 0.03 | 7.46 | 0.28 | See above |
| 66 | DUT-67(Zr) | $Zr_6O_6(OH)_2(TDC)_4$ | Zr | 40 | 3.46 | 16.78 | 5.66 | 0.52 | [45] |
| 67 | NU-1000 | $Zr_6(OH)_{16}(TBAPY)_2$ | Zr | 40 | 34.71 | 6.49 | 56.57 | 2.96 | NMT |
| 68 | polyUiO-66 | $Zr_6O_6(pbdc8\text{-}a\text{-}u)_6$ | Zr | 40 | 14.30 | 1.93 | 18.25 | 7.36 | [8] |
| 69 | UiO-66-$NH_2$-LD | $Zr_6O_6(BDC\text{-}NH_2)_{12}$ | Zr | 40 | 4.02 | 2.28 | 44.20 | 7.68 | [14] |
| 70 | UiO-66-$NH_2$-MD | $Zr_6O_6(BDC\text{-}NH_2)_{12}$ | Zr | 40 | 57.63 | 2.66 | 59.20 | 3.17 | [14] |
| 71 | UiO-66-$NH_2$-HD | $Zr_6O_6(BDC\text{-}NH_2)_{12}$ | Zr | 40 | 91.86 | 3.23 | 40.58 | 1.47 | [14] |
| 72 | $Zr(OH)_4$ Type B | $Zr(OH)_4$ | Zr | 40 | 4.94 | 2.91 | 2.79 | 3.97 | MEL |
| 73 | $Zr(OH)_4$ Type A | $Zr(OH)_4$ | Zr | 40 | -3.44 | 2.75 | 2.43 | 0.91 | MEL |
| 74 | $Zr(OH)_4$ Type C | $Zr(OH)_4$ | Zr | 40 | 4.18 | 0.48 | 5.63 | 12.90 | MEL |
| 75 | $Zr(OH)_4$ 0880 | $Zr(OH)_4$ | Zr | 40 | 4.24 | 0.64 | 2.30 | 1.63 | MEL |
| 76 | $Zr(OH)_4$ Type C $KMnO_4$ | $Zr(OH)_4$ | Zr | 40 | 4.32 | 2.53 | 0.53 | 3.73 | MEL |
| 77 | UiO-67 | $Zr_6O_6(BPDC)_{12}$ | Zr | 40 | 141.79 | 8.54 | 37.24 | 4.81 | NMT |
| 78 | UiO-66(Zr) [Acetone/HCl] | $Zr_6O_6(BDC)_{12}$ | Zr | 40 | 63.07 | 5.21 | 15.91 | 1.05 | [46] |
| 79 | PCN-222 | $Zr_6(\mu_3\text{-}OH)_8(OH)_8(TCPP)_2$ | Zr | 40 | 117.38 | 38.93 | 153.05 | 11.60 | [47] |
| 80 | UiO-66-$NH_2$ [Acetone/HCl] | $Zr_6O_6(BDC\text{-}NH_2)_6$ | Zr | 40 | 58.83 | 3.63 | 71.50 | 0.63 | [46] |
| 81 | UiO-66-$NH_2$ [DMF/HCOOH] | $Zr_6O_6(BDC\text{-}NH_2)_6$ | Zr | 40 | 18.71 | 2.07 | 2.44 | 0.42 | [44] |
| 82 | UiO-66-$(COOH)_2$ [DMF/HCOOH] | $Zr_6O_6(BDC\text{-}(COOH)_2)_{12}$ | Zr | 40 | 8.81 | 0.64 | 8.03 | 0.54 | [44] |
| 83 | UiO-66-$(OH)_2$ [DMF/HCOOH] | $Zr_6O_6(BDC\text{-}(OH)_2)_{12}$ | Zr | 40 | 49.70 | 1.63 | 14.29 | 1.26 | [44] |
| 84 | UiO-66(Zr) [DMF/HCOOH] | $Zr_6O_6(BDC)_{12}$ | Zr | 40 | 48.89 | 2.29 | 3.83 | 0.37 | [44] |
| 85 | UiO-66-OH [DMF/HCOOH] | $Zr_6O_6(BDC\text{-}OH)_{12}$ | Zr | 40 | 42.96 | 1.47 | 8.20 | 0.66 | [44] |
| 86 | UiO-66-$NO_2$ [DMF/HCOOH] | $Zr_6O_6(BDC\text{-}NO_2)_{12}$ | Zr | 40 | 9.50 | 0.79 | 3.36 | 0.72 | [44] |
| 87 | UiO-66-$OCF_3$ [DMF/HCOOH] | $Zr_6O_6(BDC\text{-}OCF_3)_{12}$ | Zr | 40 | 12.47 | 0.85 | 53.49 | 5.94 | [44] |

| | | | | | | | | | |
|---|---|---|---|---|---|---|---|---|---|
| 88 | MOF-808 | $Zr_6O_4(OH)_4(BTC)_2(COOH)_6$ | Zr | 40 | 95.90 | 4.89 | 151.88 | 4.80 | [42] |
| 89 | UiO-66(Ce) | $Ce_6O_6(BDC)_{12}$ | Ce | 58 | 4.64 | 1.71 | 4.85 | 5.27 | [48] |
| 90 | $CeO_2$ | $CeO_2$ | Ce | 58 | 9.26 | 4.83 | 18.35 | 4.78 | NAM |
| 91 | $Eu_2O_3$ | $Eu_2O_3$ | Eu | 63 | -0.58 | 7.58 | -2.05 | 0.25 | NAM |
| 92 | DUT-67(Hf) | $Hf_6O_6(OH)_2(TDC)_4$ | Hf | 72 | 4.21 | 0.31 | 1.70 | 0.87 | [45] |
| 93 | UiO-66(Hf) | $Hf_6O_6(BDC)_{12}$ | Hf | 72 | 71.31 | 8.78 | 3.24 | 0.09 | [16] |

[a] Ligand Abbreviations: (ISO) = isophthalic acid; (BTC) = benzene-1,3,5-tricarboxylic acid; (BDC) = benzene-1,4-dicarboxylic acid; (ABTEC) = azobenzene tetracarboxylic acid; (MEIM) = 2-methyl-1*H*-imidazole; (NIC) = nicotinic acid; (BTEC) = 1,2,4,5-Benzenetetracarboxylic acid; (PCN) = 4-pyridinecarboxylic acid; (DOBDC) = 2,5-dihydroxyterephthalic acid; (BPY) = 4,4′–bipyridyl; (IM) = 1*H*-imidazole; (BIM) = 1*H*-benzo[*d*]imidazole; (DABCO) = 1,4-diazabicyclo[2.2.2]octane; ($Me_2$-BPDC) = 2,2'-dimethyl-[1,1'-biphenyl]-4,4'-dicarboxylic acid; (FUM) = fumaric acid; (PZDC) = 1*H*-pyrazole-3,5-dicarboxylic acid; (TDC) = 2,5-Thiophenedicarboxylic acid; (TBAPY) = 1,3,6,8-tetrakis(p-benzoate)pyrene; (BPDC) = [1,1'-biphenyl]-4,4'-dicarboxylic acid; (TCPP) = meso-tetra(4-carboxyl-phenyl)porphyrin

[b] Supplier Abbreviations: NAM = Nanostructured & Amorphous Materials; GA = Guild Associates; CCC = Calgon Carbon Corporation; SA = Sigma Aldrich; ASGE = Advanced Specialty Gas Equipment; DC = Degussa Corporation; NMT = NuMat Technologies; SC = Strem Chemicals; MEL = Magnesium Electron, Inc.

**Table S2.4.** Particle size and DMNP hydrolysis rates (average of three wells, in mM/sec × $10^{-6}$) in for four UiO-66(Zr) MOFs in 20 mM N-ethylmorpholine at pH = 8 and 10.

| # | MOF | Particle Size (nm) | | pH=8 | | pH=10 | |
|---|---|---|---|---|---|---|---|
| | | average | std. dev. | Slope | σ | Slope | σ |
| 59 | UiO-66(Zr) [DMF/AcOH] | 131.4 | 15.7 | 49.7 | 5.1 | 8.1 | 1.9 |
| 84 | UiO-66(Zr) [DMF/HCOOH] | 190.5 | 49.9 | 17.0 | 0.8 | 1.5 | 0.1 |
| 78 | UiO-66(Zr) [Acetone/HCl] | 210.8 | 182.5 | 22.0 | 1.8 | 6.3 | 0.4 |
| 60 | UiO-66(Zr) [DMF/HCl] | 145.0 | 35.7 | 38.4 | 3.5 | 2.3 | 0.2 |

**Table S2.5.** DMNP hydrolysis rates (average of three wells, in arbitrary units of rate) of selected MOFs in 20 mM *N*-ethylmorpholine at pH = 8, 9, and 10.

| # | MOF | pH=8 | | pH=9 | | pH=10 | |
|---|---|---|---|---|---|---|---|
| | | Slope | σ | Slope | σ | Slope | σ |
| 69 | UiO-66-$NH_2$-Low Defect | 1.40 | 0.79 | 2.87 | 0.77 | 17.64 | 3.06 |
| 70 | UiO-66-$NH_2$-Mid Defect | 20.07 | 0.92 | 36.40 | 5.19 | 23.62 | 1.26 |
| 71 | UiO-66-$NH_2$-High Defect | 31.99 | 1.12 | 47.27 | 4.23 | 16.19 | 0.59 |

**Table S2.6.** Calibration Curves for p-nitrophenol in buffer solutions.

| pH = 10 | | pH = 8 | |
|---|---|---|---|
| **[p-nitrophenol]** | **Abs** | **[p-nitrophenol]** | **Abs** |
| 0.0000 | 0.0495 | 0.0000 | 0.0494 |
| 0.0766 | 0.3562 | 0.0766 | 0.3265 |
| 0.1531 | 0.6747 | 0.1531 | 0.5921 |
| 0.3063 | 1.2766 | 0.3063 | 1.1318 |
| 0.6125 | 2.4959 | 0.6125 | 2.1853 |
| **slope (Abs/mM)** | 3.9904 | **slope (Abs/mM)** | 3.4825 |
| **$R^2$** | 1.0000 | **$R^2$** | 0.9999 |

**Table S2.7.** Dilution ratios for preparation of MOF suspensions used in development of HTS at different concentrations.

| Concentration (µg/mL) | MOF+Buffer (µL) | Buffer (µL) |
|---|---|---|
| 600 | 500 | 500 |
| 450 | 375 | 625 |
| 300 | 250 | 750 |
| 150 | 125 | 875 |
| 100 | 93.8 | 906.2 |
| 75 | 62.5 | 937.5 |

## Supplemental Figures

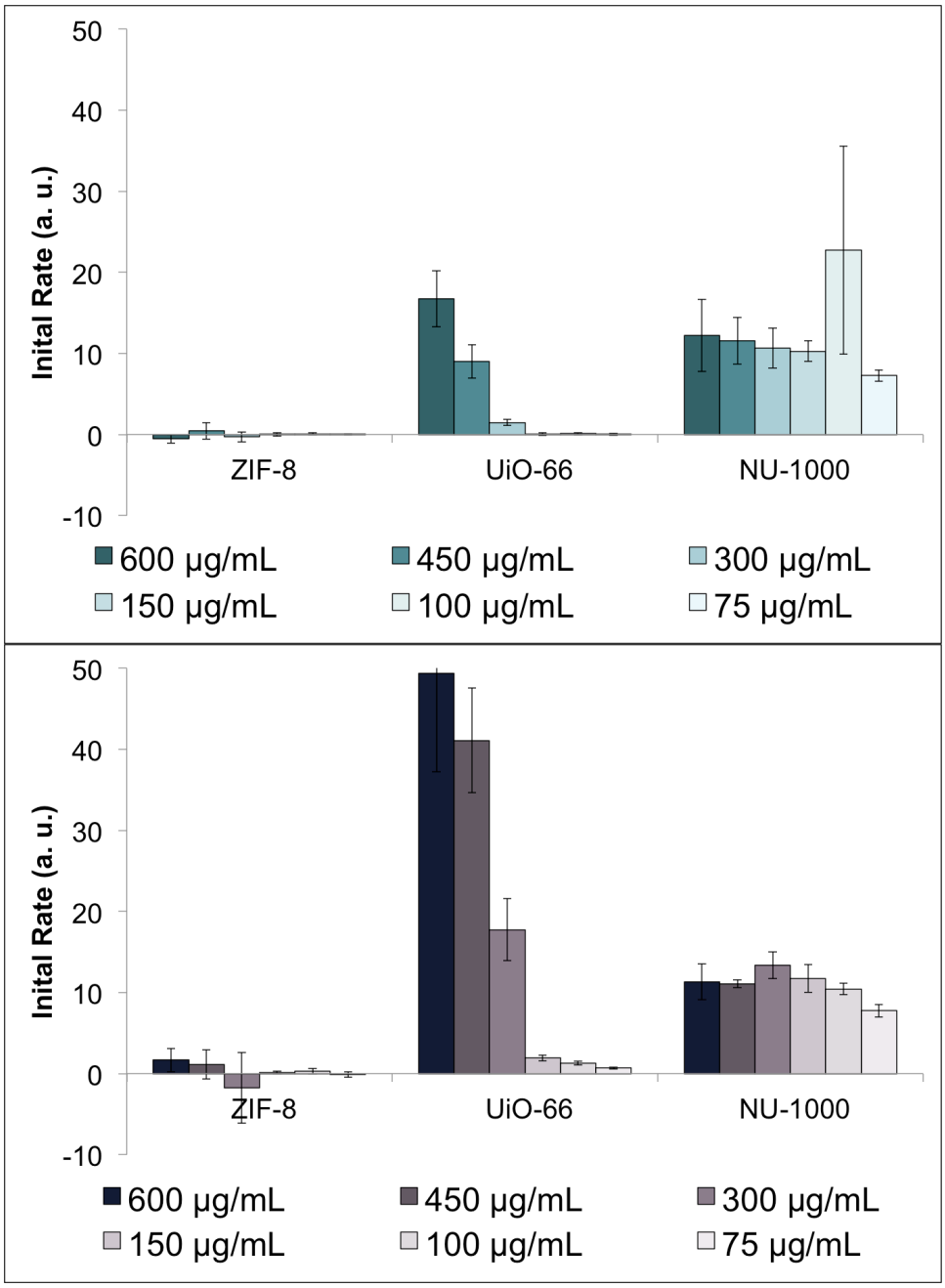


**Figure S2.1.** DMNP hydrolysis rates for ZIF-8, UiO-66, and NU-1000(Zr) for pH = 8.0 in Tris (*top*) and HEPES (*bottom*) buffer.

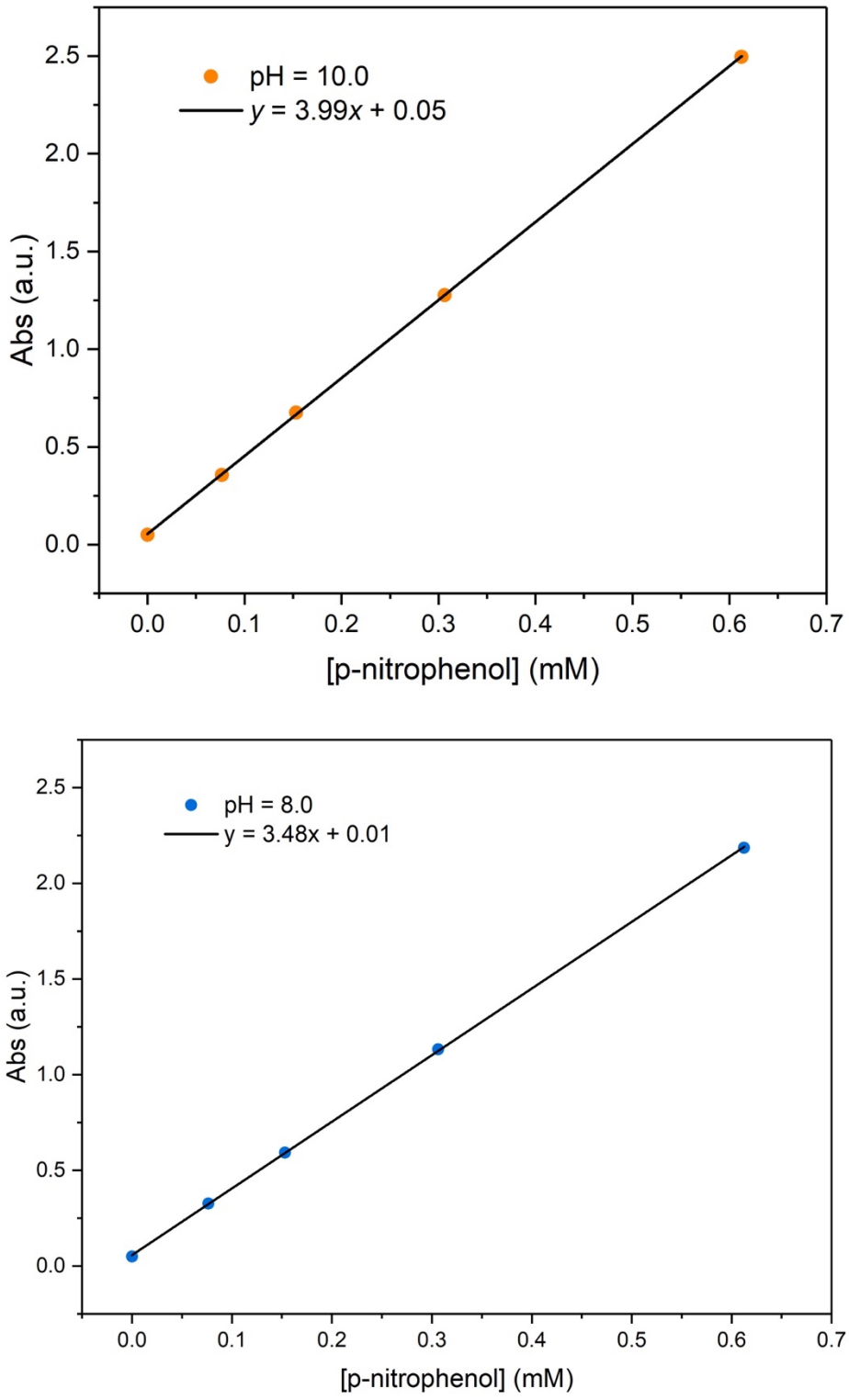


**Figure S2.2.** Calibration Curves for *p*-nitrophenol at pH = 10.0 (*top*) and pH = 8.0 (*bottom*).

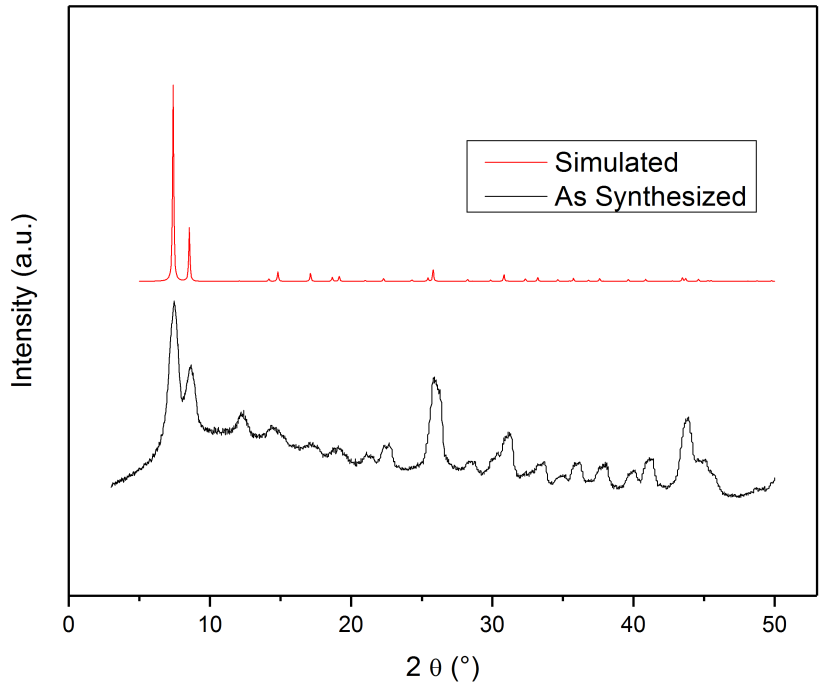


**Figure S2.3.** PXRD of as-synthesized UiO-66(Zr) [Acetone/HCl].

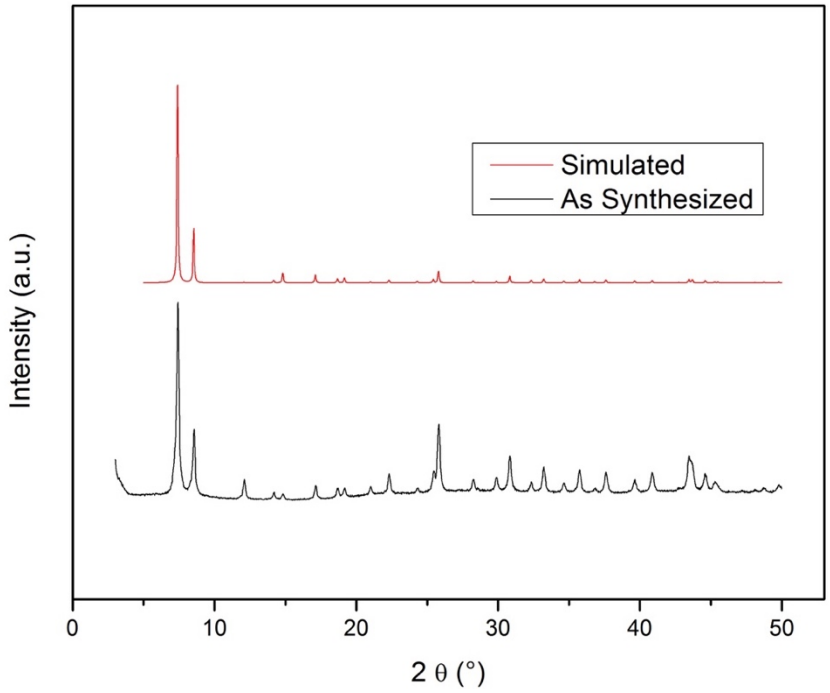


**Figure S2.4.** PXRD of as-synthesized UiO-66(Zr) [DMF/HCl].

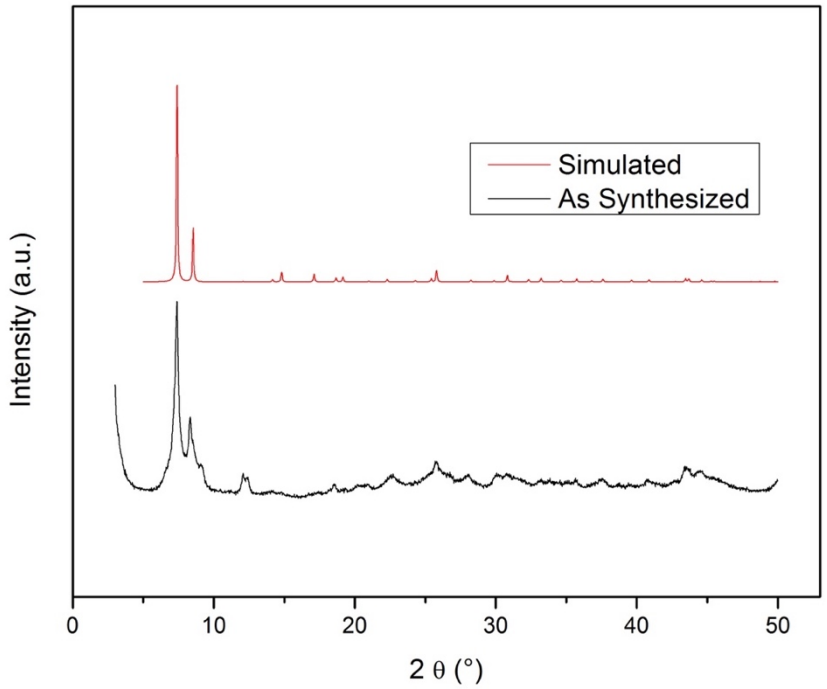


**Figure S2.5.** PXRD of as-synthesized UiO-66(Zr) [DMF/AcOH].

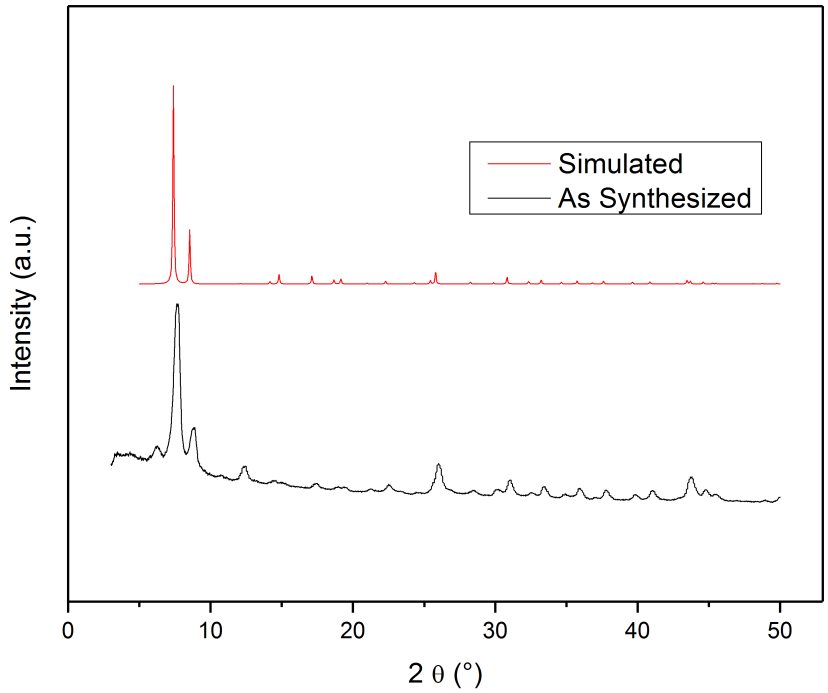


**Figure S2.6.** PXRD of as-synthesized UiO-66(Zr) [DMF/HCOOH].

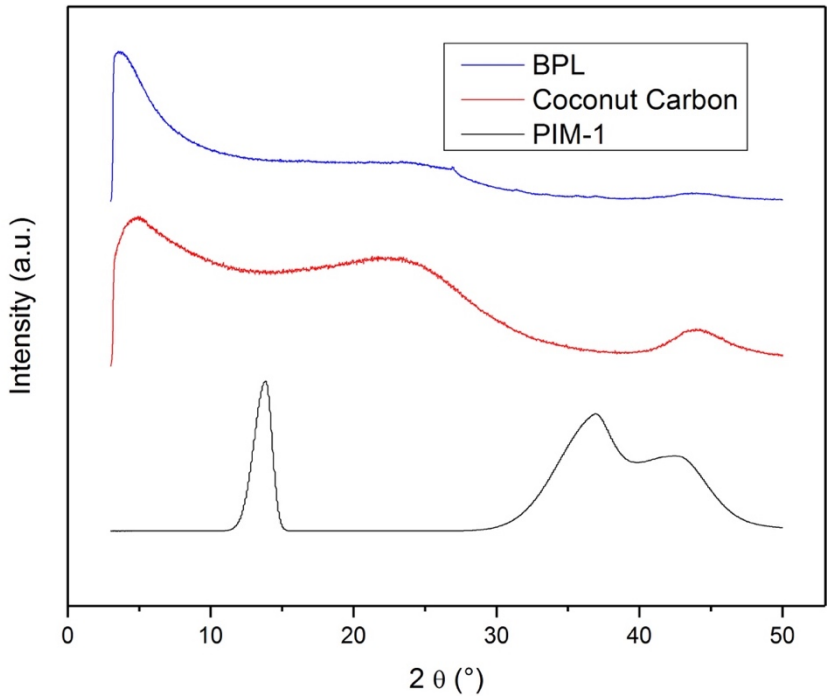


**Figure S2.7.** PXRD of as synthesized carbon materials: PIM-1, Coconut Carbon, and BPL.

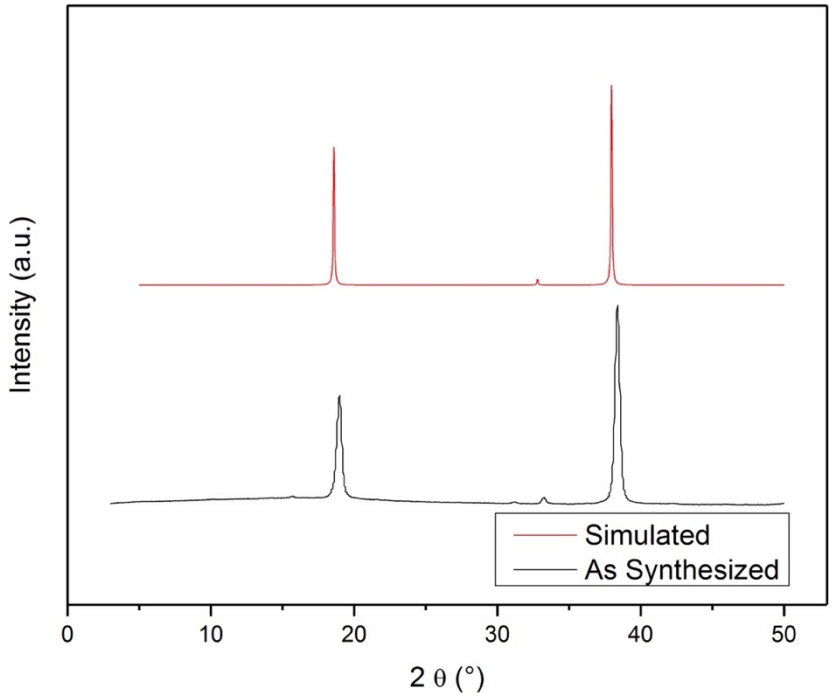


**Figure S2.8.** PXRD of as-purchased $Mg(OH)_2$.

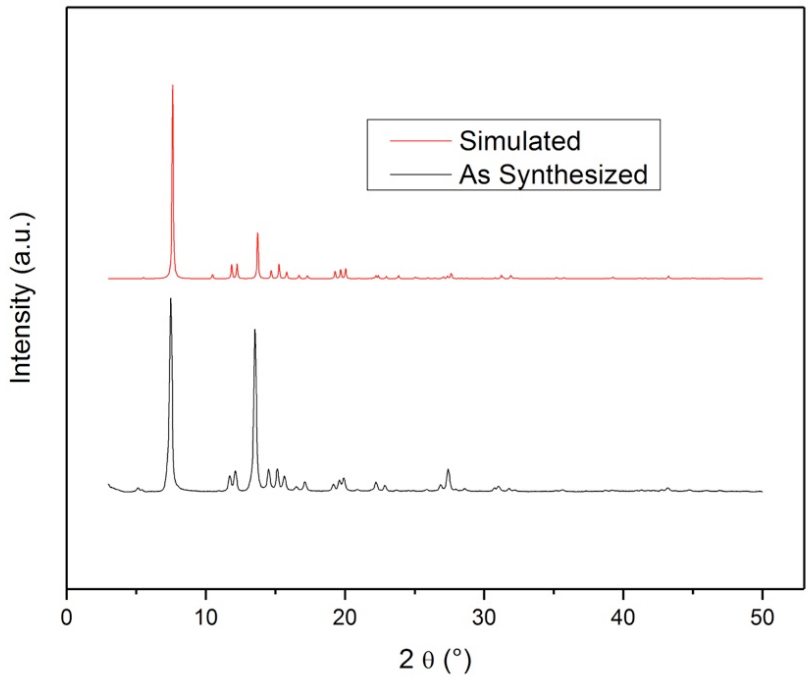


**Figure S2.9.** PXRD of as-synthesized Al-PMOF.

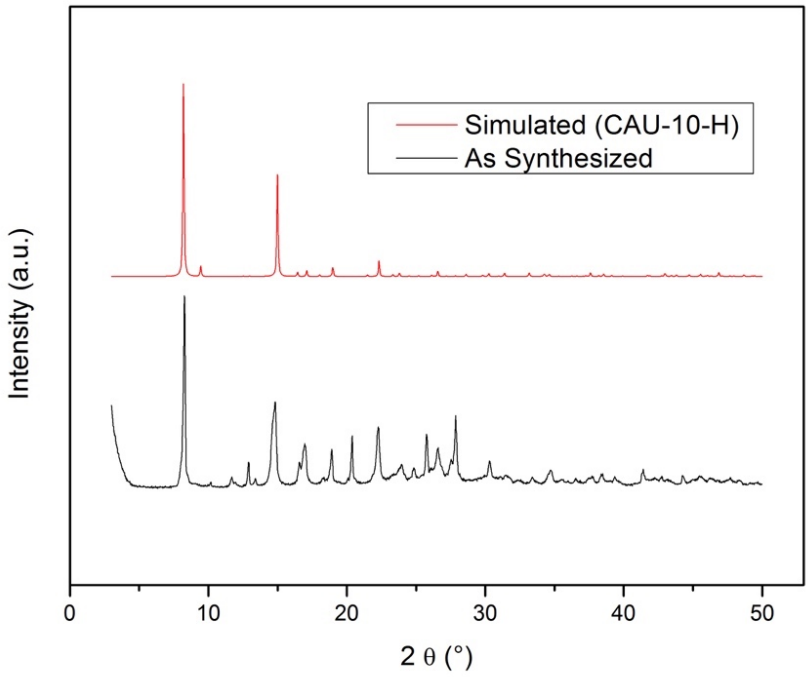


**Figure S2.10.** PXRD of as-synthesized CAU-10(Al)-$NH_2$.

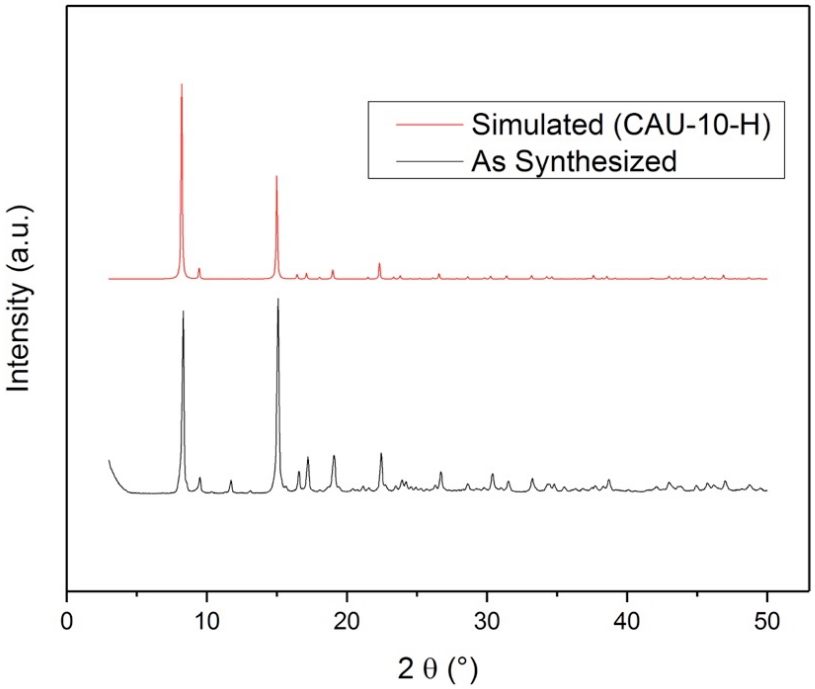


**Figure S2.11.** PXRD of as-synthesized CAU-10(Al)-$CH_3$.

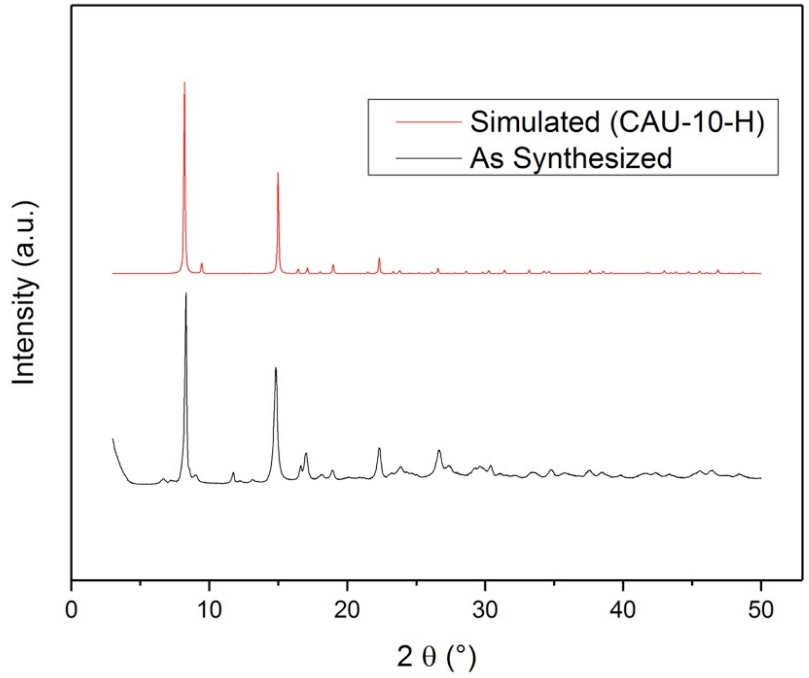


**Figure S2.12.** PXRD of as-synthesized CAU-10(Al)-OH.

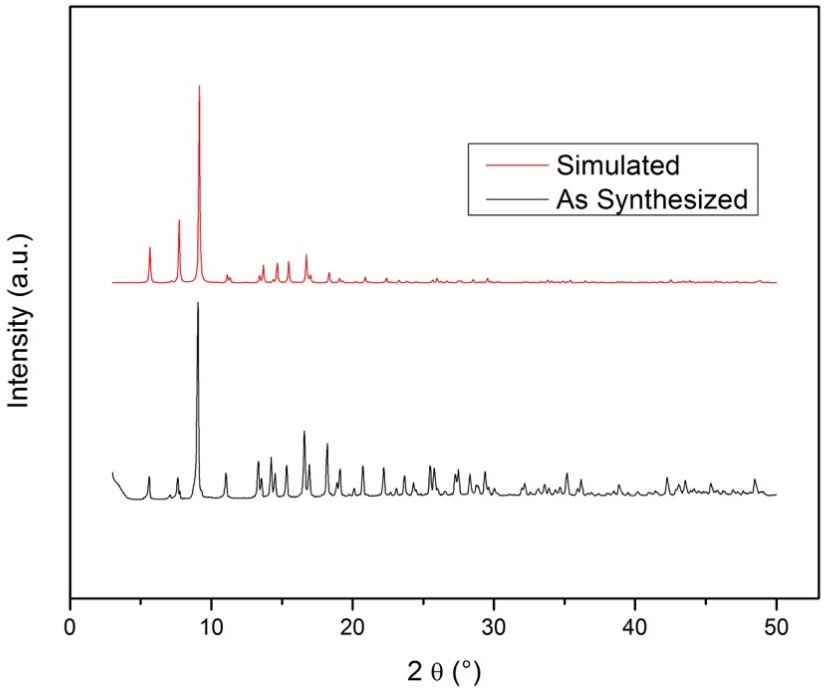


**Figure S2.13.** PXRD of as-synthesized MIL-96(Al).

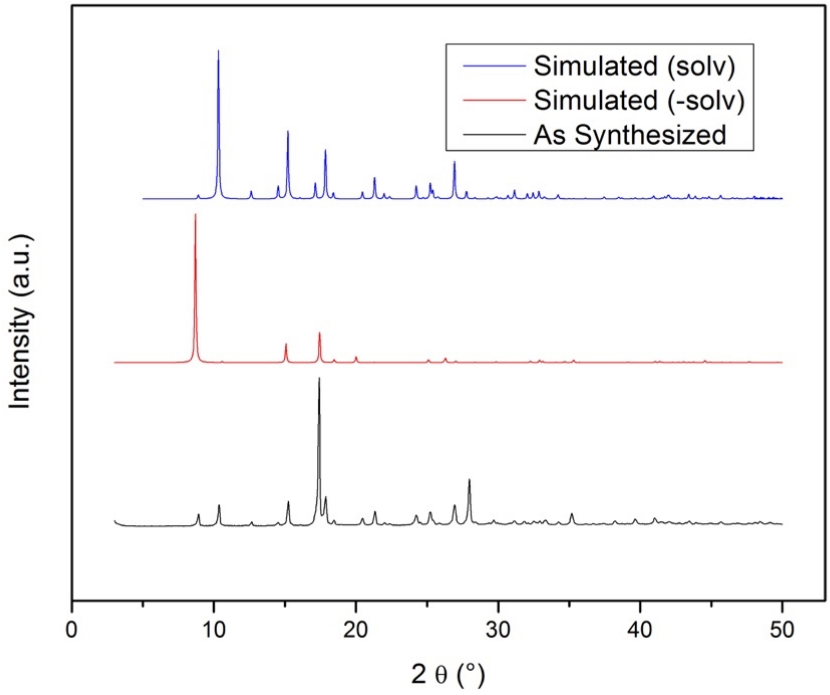


**Figure S2.14.** PXRD of as-synthesized MIL-53(Al). MIL-53(Al) can adopt multiple crystalline conformations based on solvation, simulated patterns of fully solvated and non-solvated are plotted here.

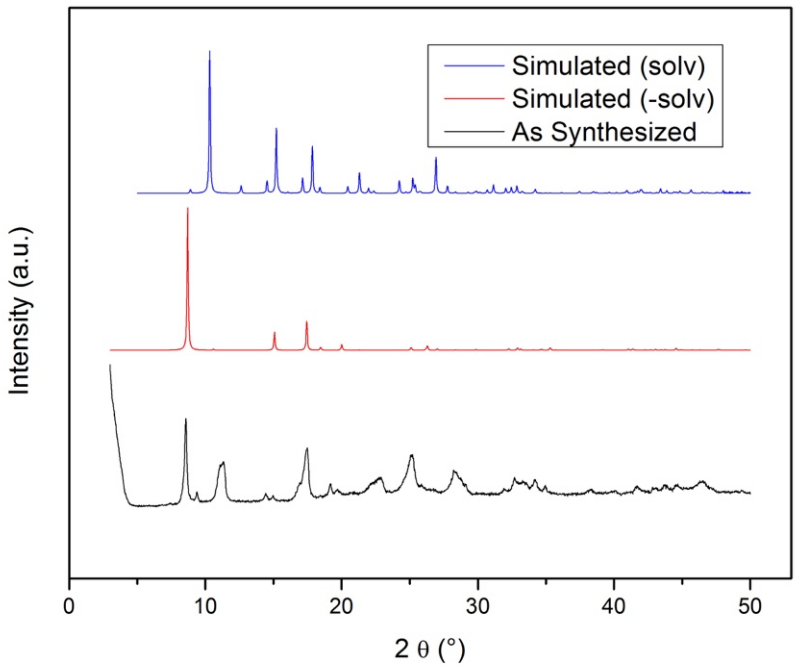


**Figure S2.15.** PXRD of as-synthesized MIL-53(Al)-Br. MIL-53(Al)-Br can adopt multiple crystalline conformations based on solvation, simulated patterns of fully solvated and non-solvated are plotted here.

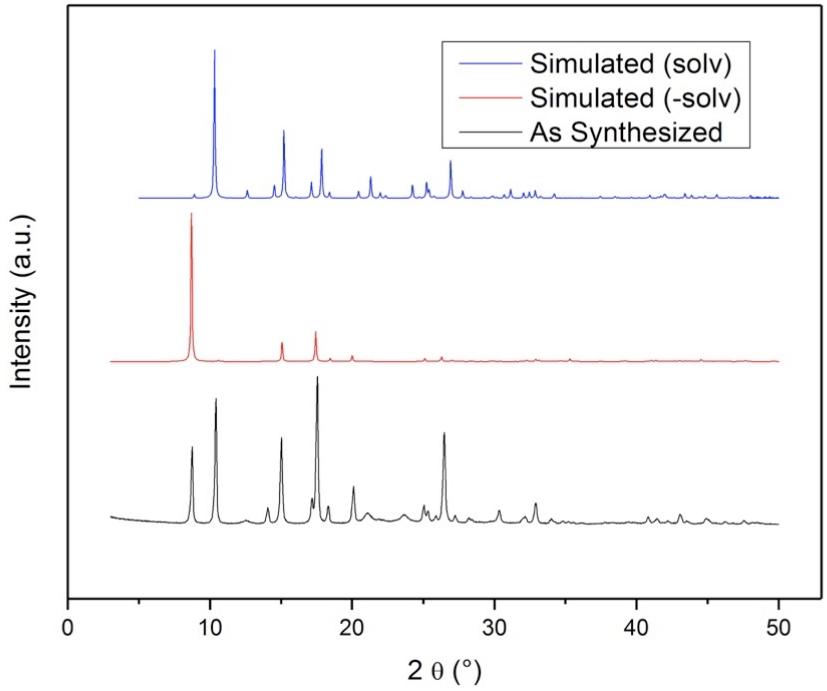


**Figure S2.16.** PXRD of as-synthesized MIL-53(Al)-$NH_2$.

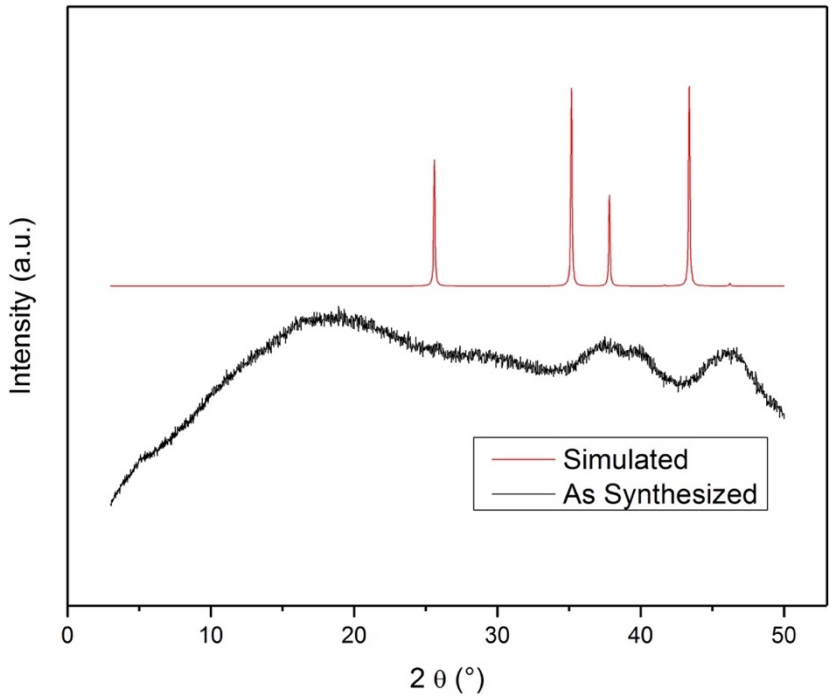


**Figure S2.17.** PXRD of as-purchased $Al_2O_3$.

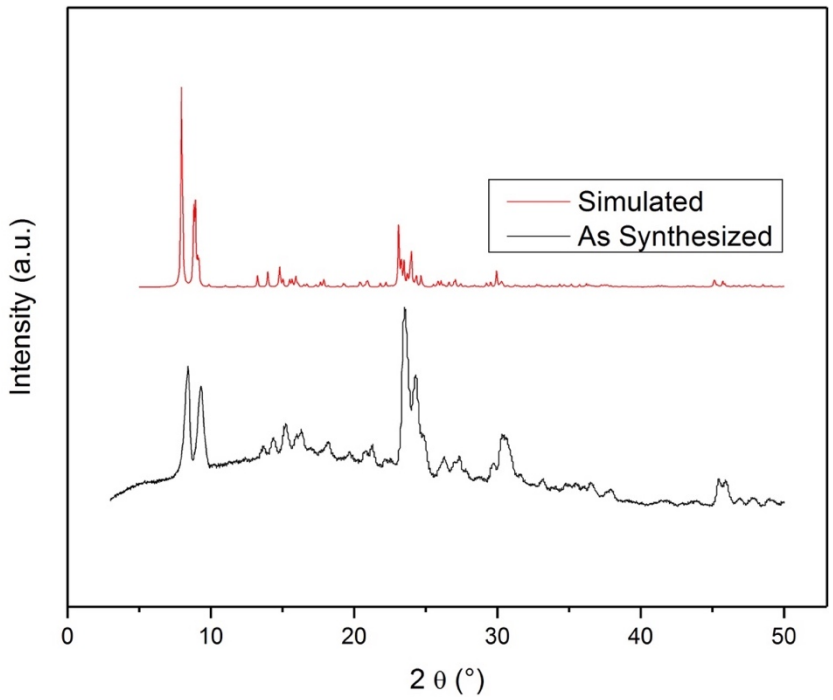


**Figure S2.18.** PXRD of as-purchased Silicalite.

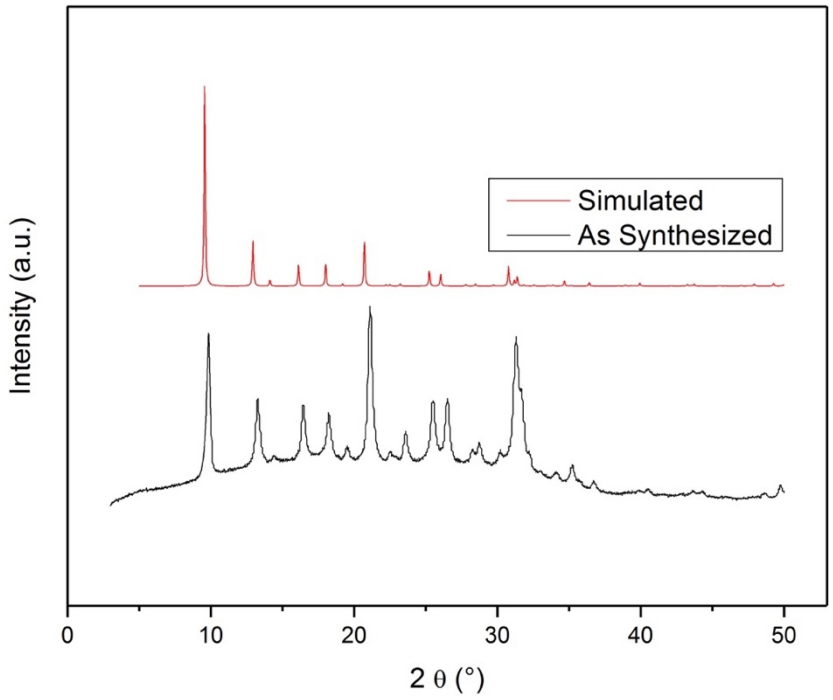


**Figure S2.19.** PXRD of as-purchased SAPO-34.

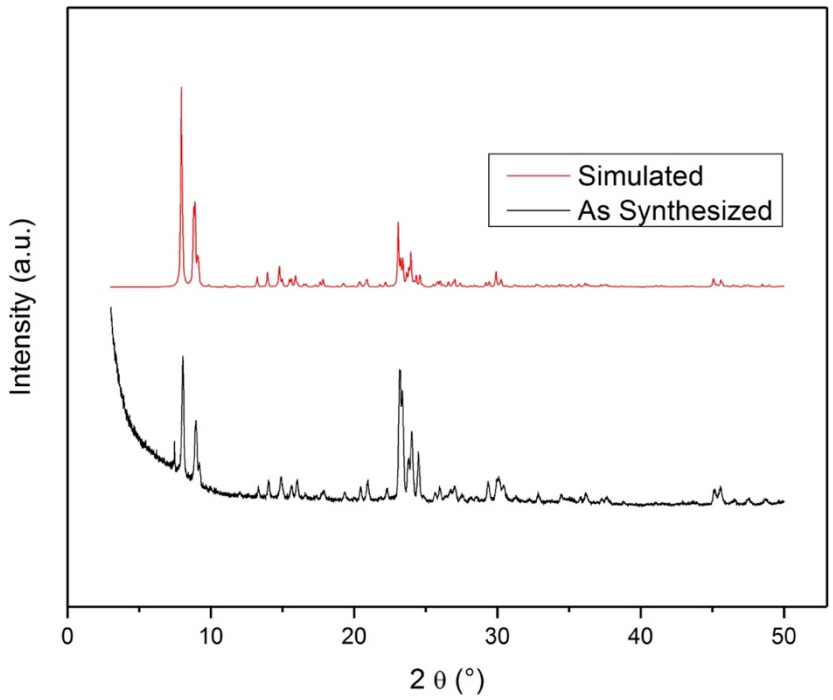


**Figure S2.20.** PXRD of as-purchased H-ZSM-5.

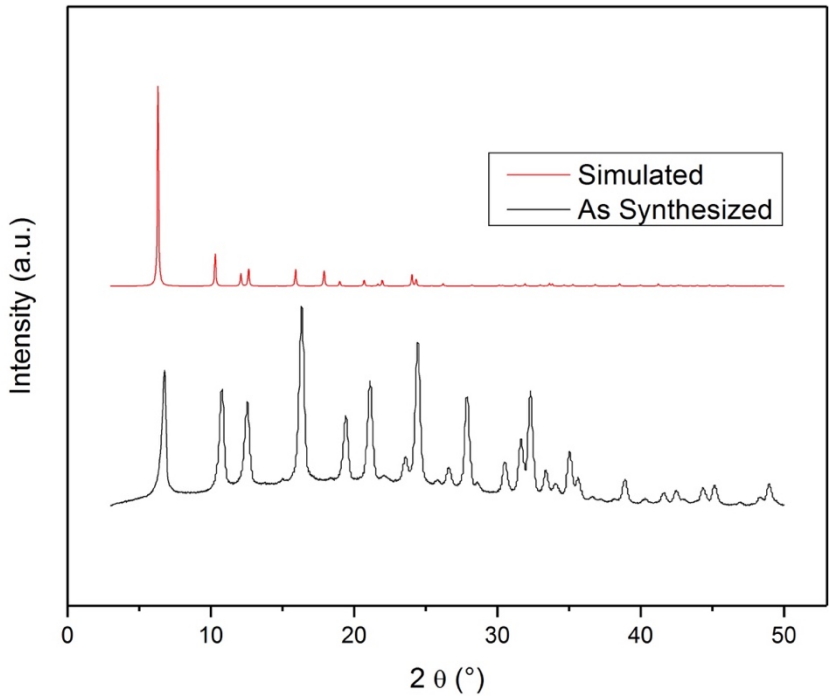


**Figure S2.21.** PXRD of as-purchased HY.

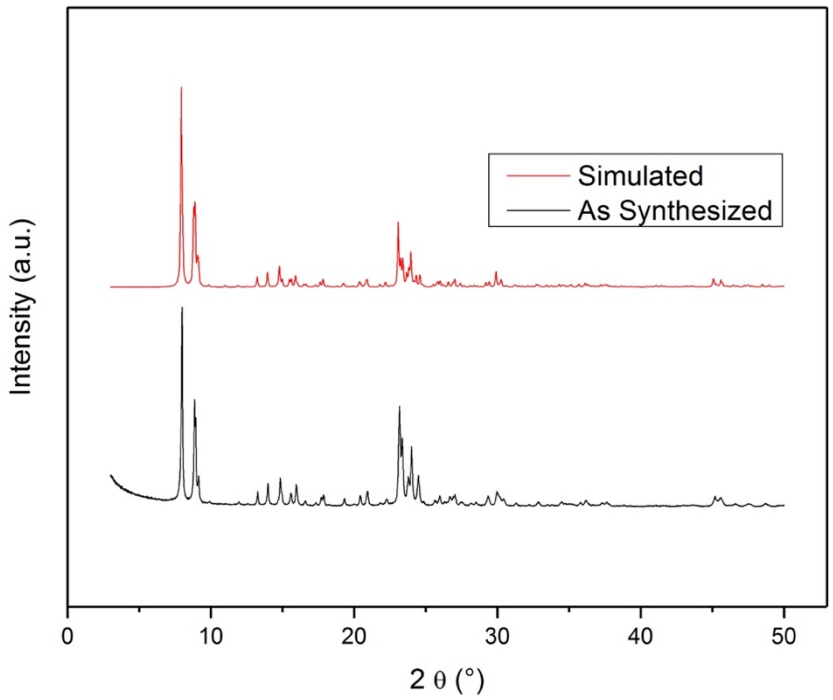


**Figure S2.22.** PXRD of as-purchased Na-ZSM-5.

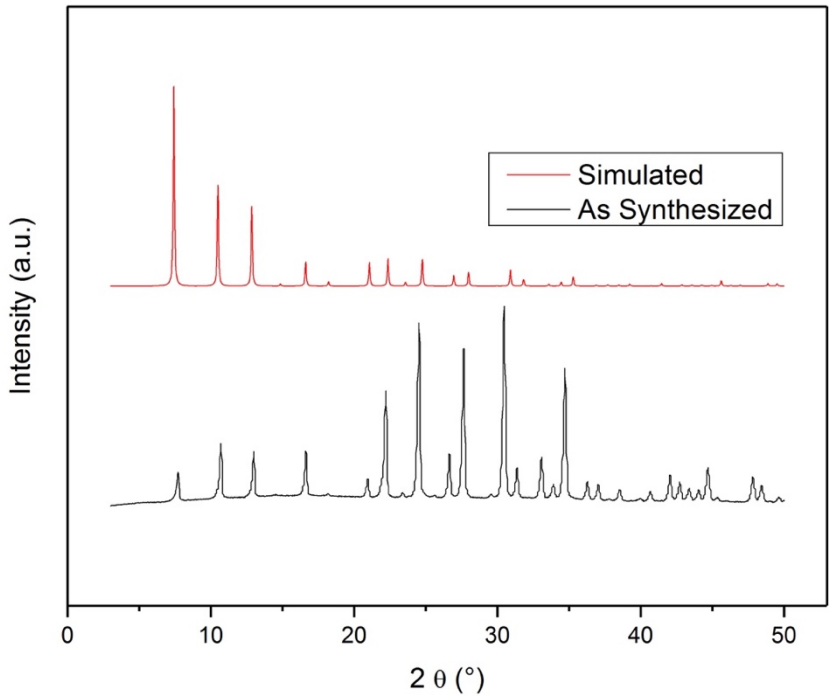


**Figure S2.23.** PXRD of as-purchased Zeolite 4A.

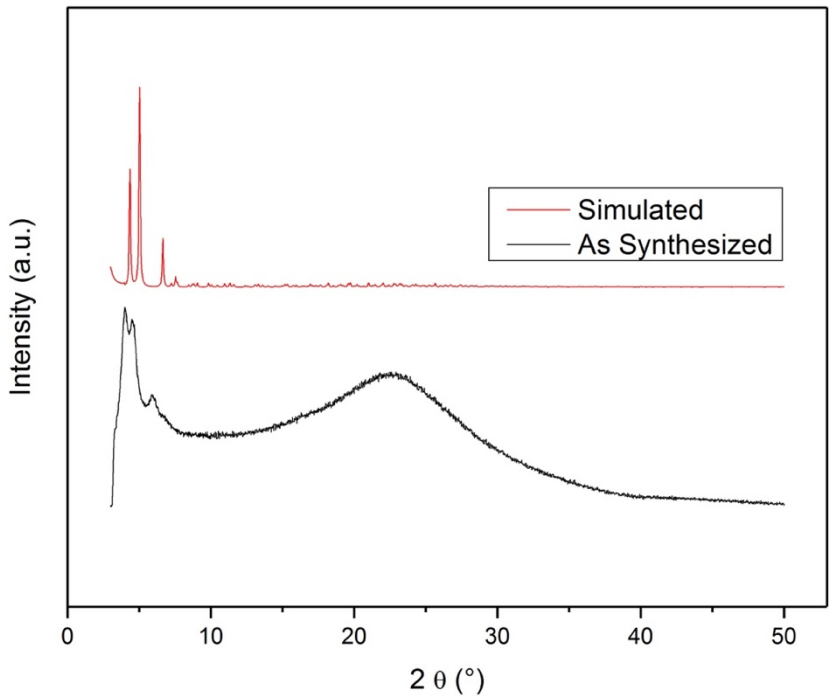


**Figure S2.24.** PXRD of as-purchased MCM-41 (Aldrich).

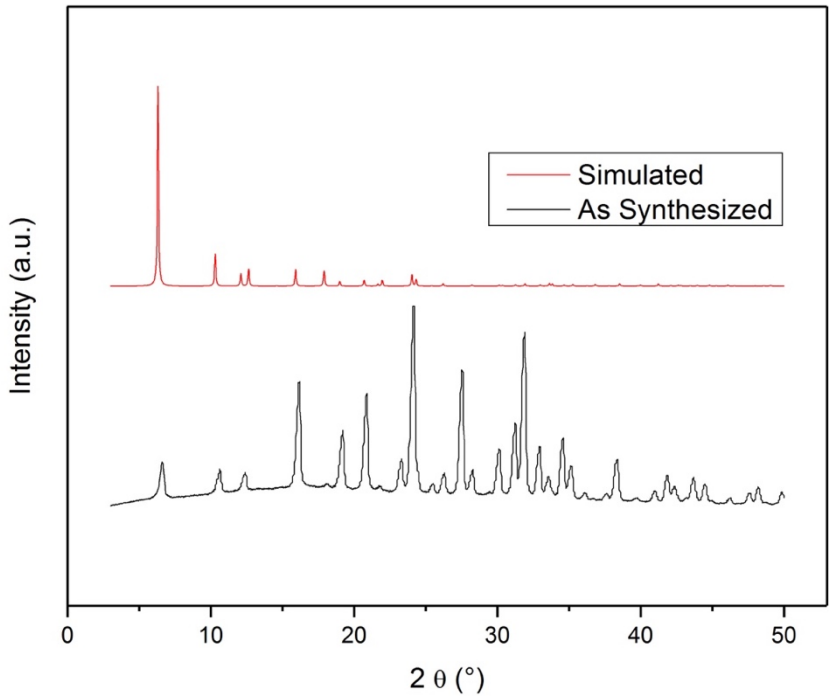


**Figure S2.25.** PXRD of as-purchased Y-54 DR.

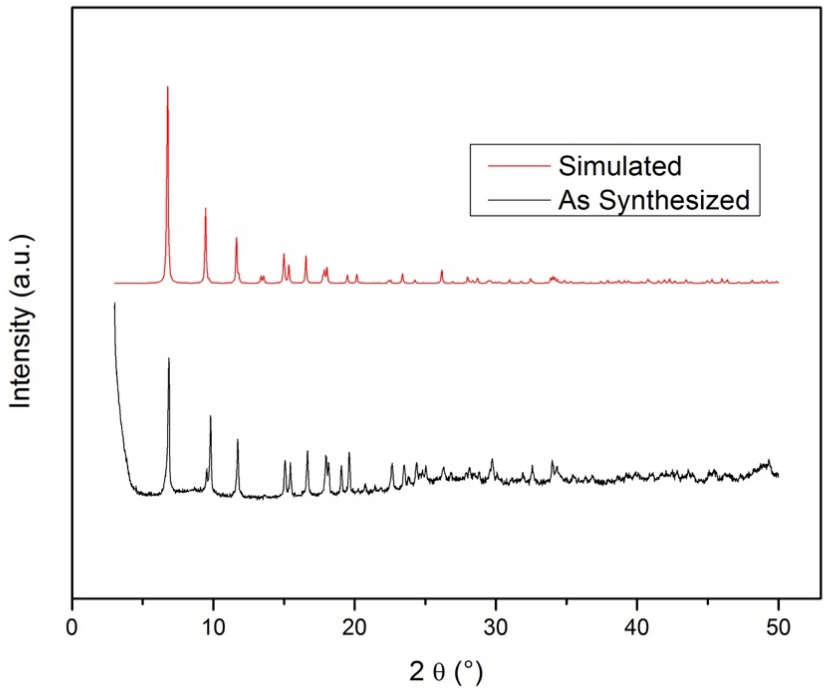


**Figure S2.26.** PXRD of as-synthesized MIL-125(Ti)-$NH_2$.

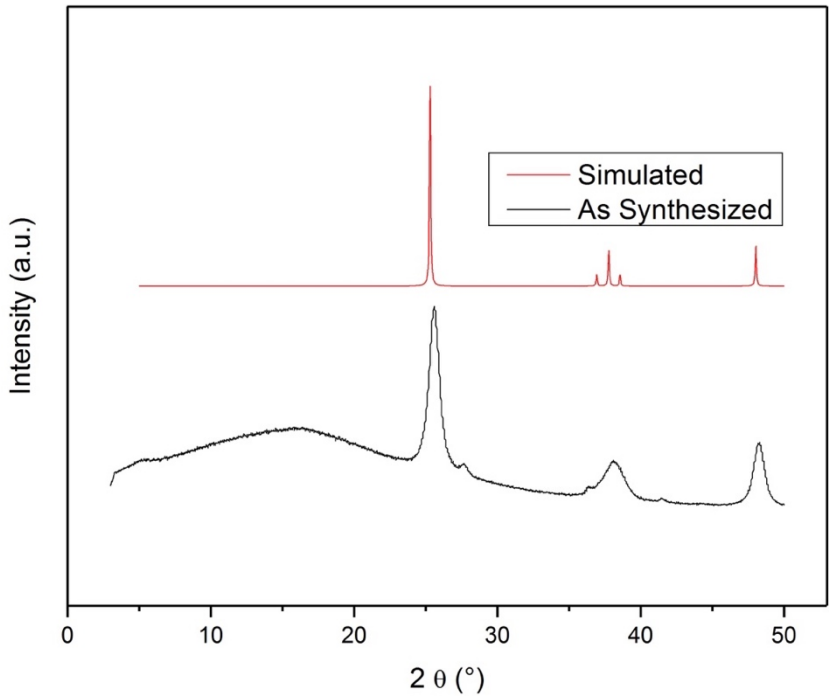


**Figure S2.27.** PXRD of as-synthesized $TiO_2$.

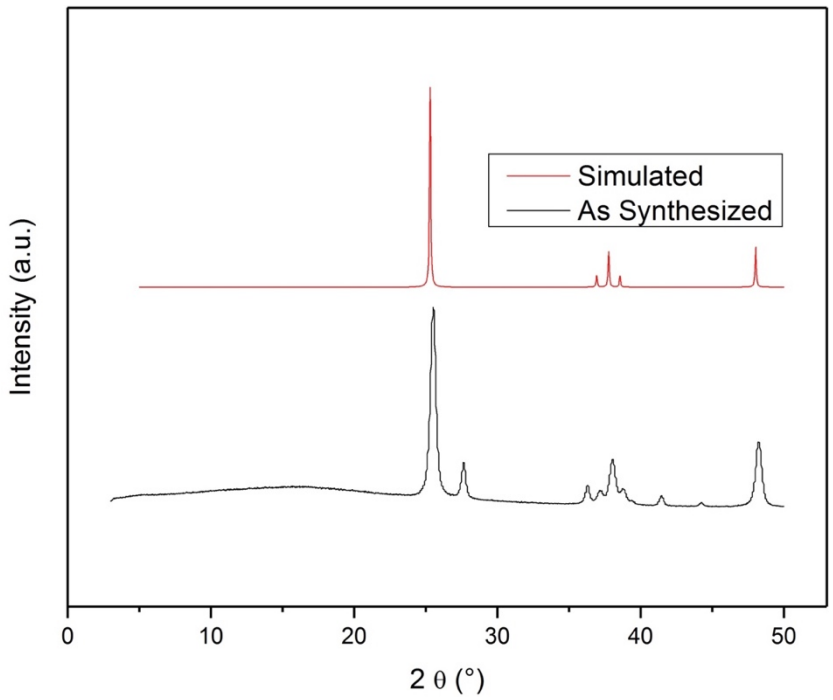


**Figure S2.28.** PXRD of as purchased $TiO_2$ (Aldrich).

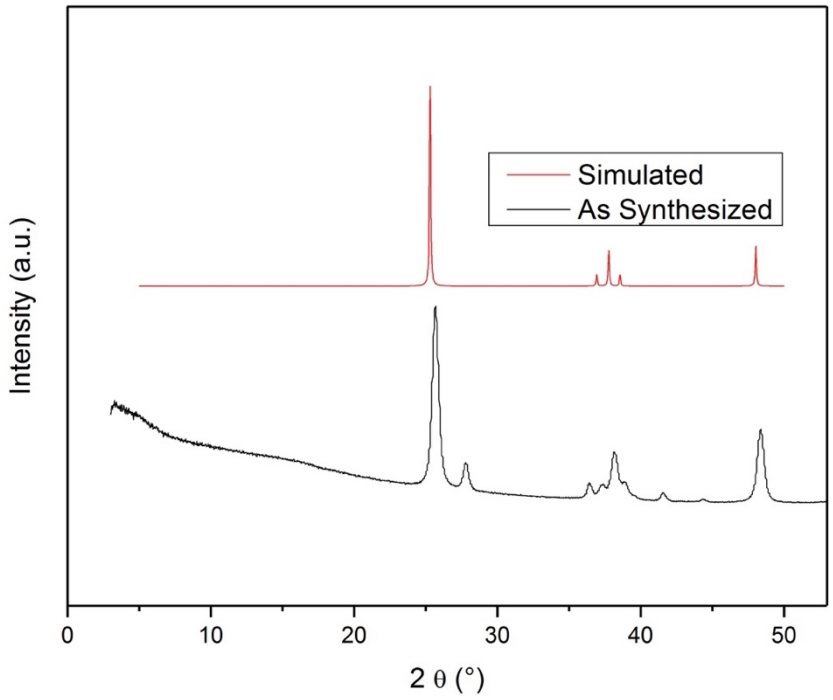


**Figure S2.29.** PXRD of as-purchased $TiO_2$ Anatase (Aldrich).

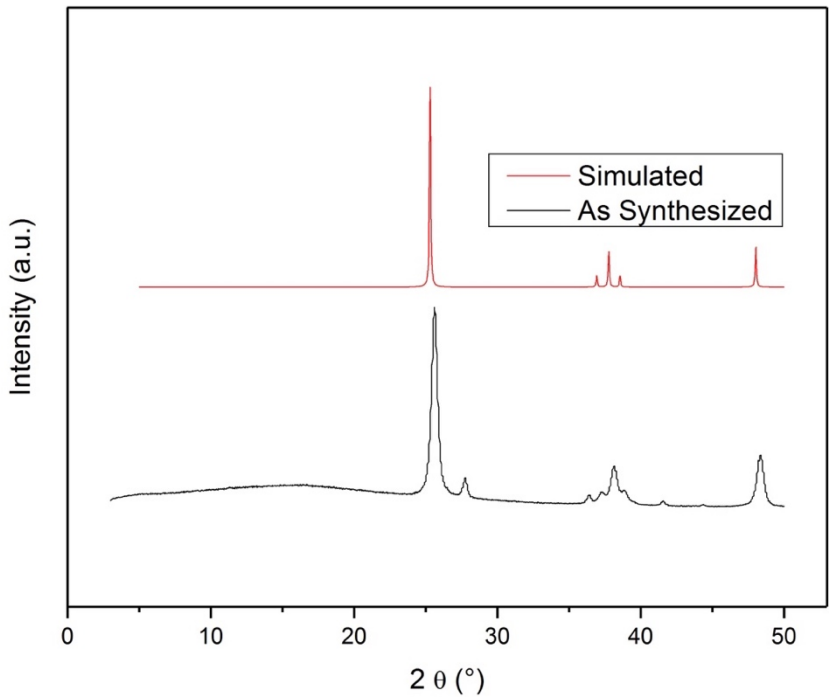


**Figure S2.30.** PXRD of as-purchased $TiO_2$ P25 (Degussa).

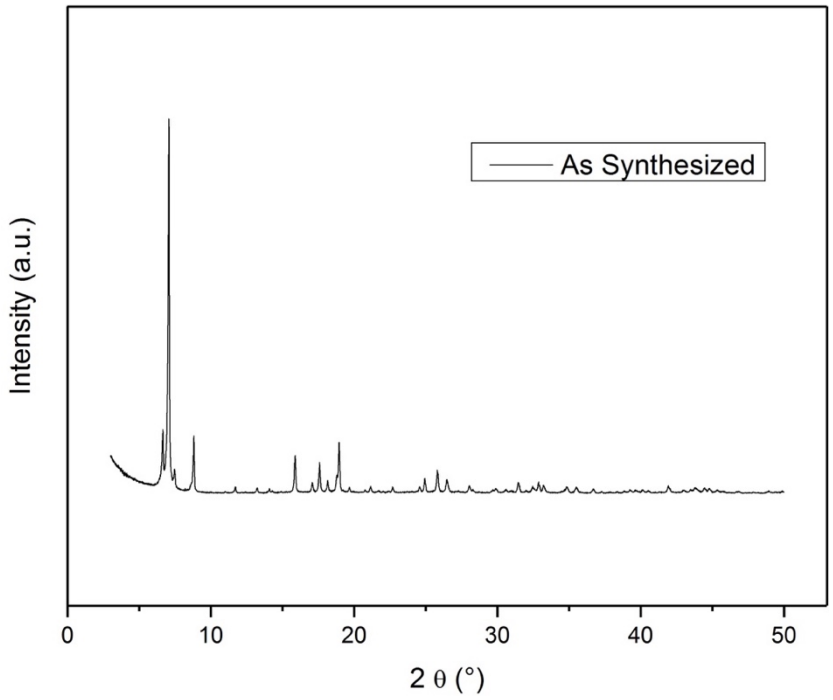


**Figure S2.31.** PXRD of as-synthesized PCN-415.

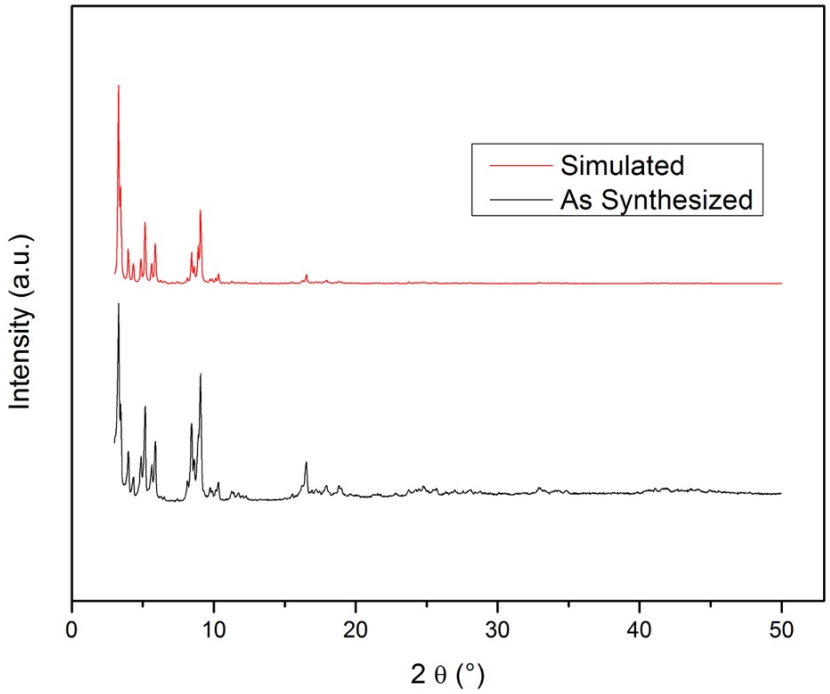


**Figure S2.32.** PXRD of as-synthesized MIL-101(Cr).

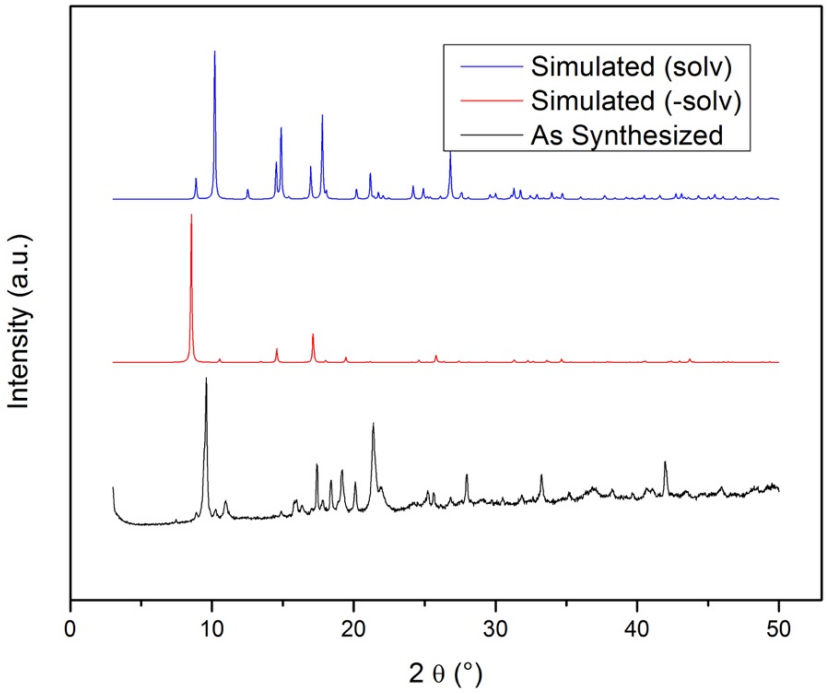


**Figure S2.33.** PXRD of as-synthesized MIL-53(Cr). MIL-53(Cr) can adopt multiple crystalline conformations based on solvation, simulated patterns of fully solvated and non-solvated are plotted here.

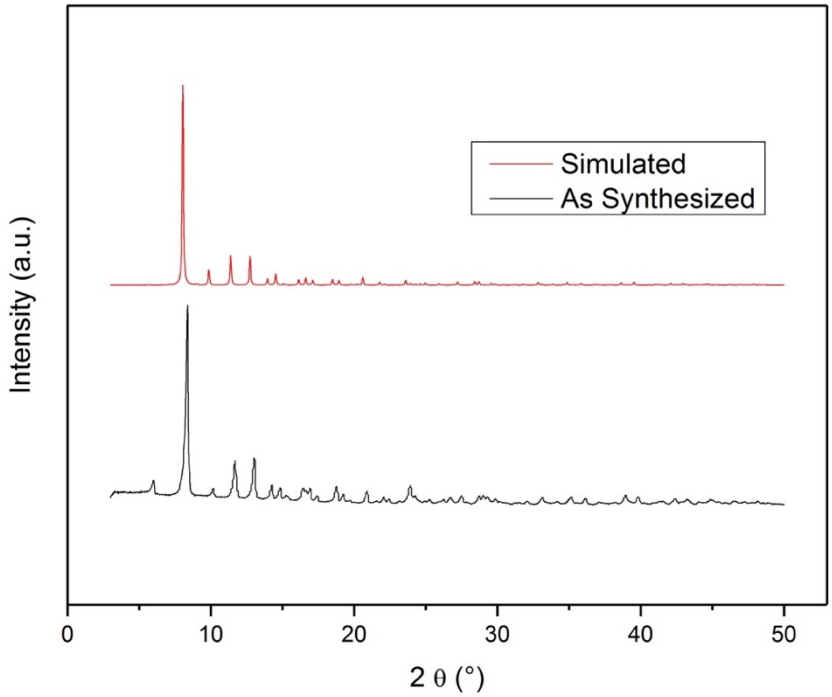


**Figure S2.34.** PXRD of as-synthesized PCN-250(Mn).

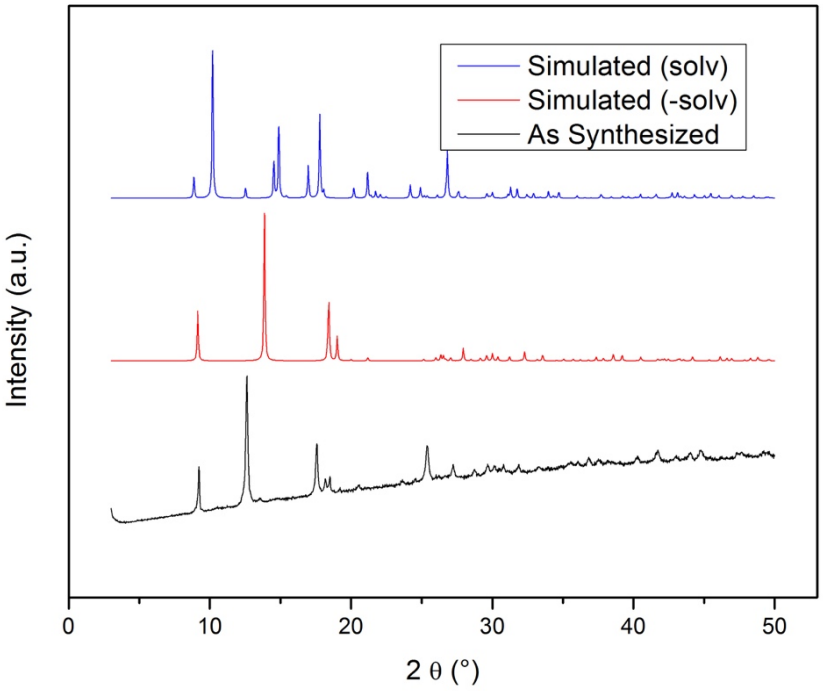


**Figure S2.35.** PXRD of as-synthesized MIL-53(Fe). MIL-53(Fe) can adopt multiple crystalline conformations based on solvation, simulated patterns of fully solvated and non-solvated are plotted here.

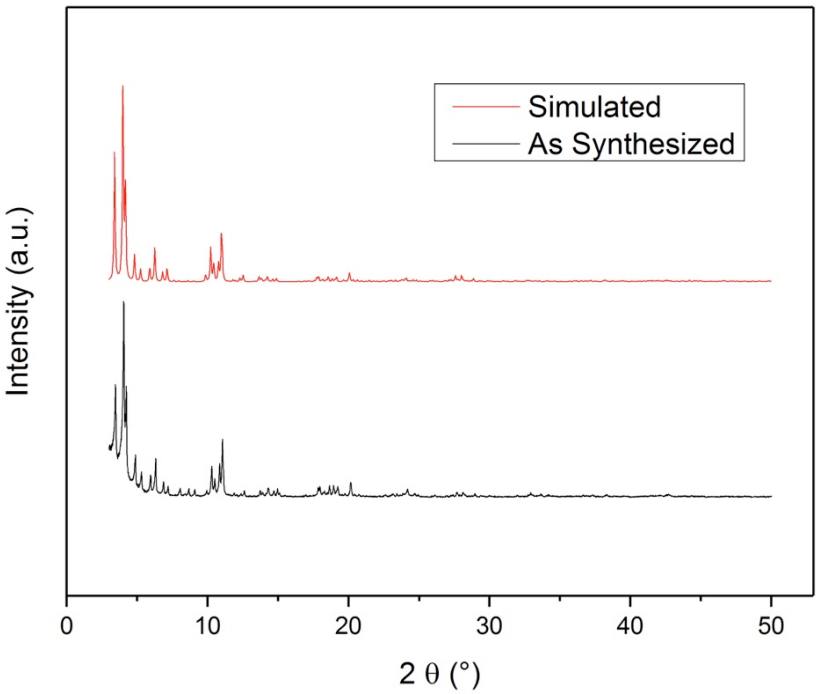


**Figure S2.36.** PXRD of as-synthesized MIL-100(Fe).

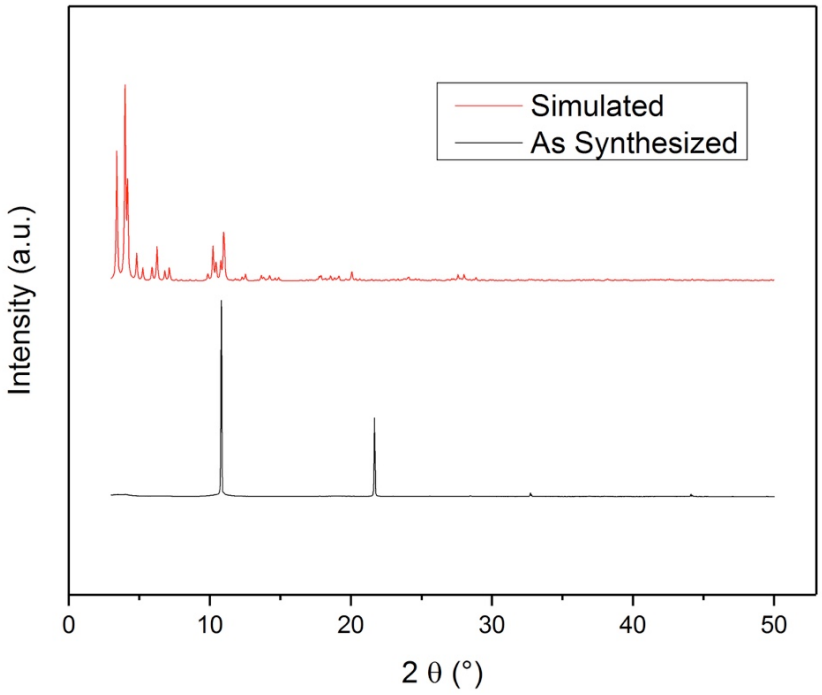


**Figure S2.37.** PXRD of as-purchased MIL-100(Fe) (Aldrich).

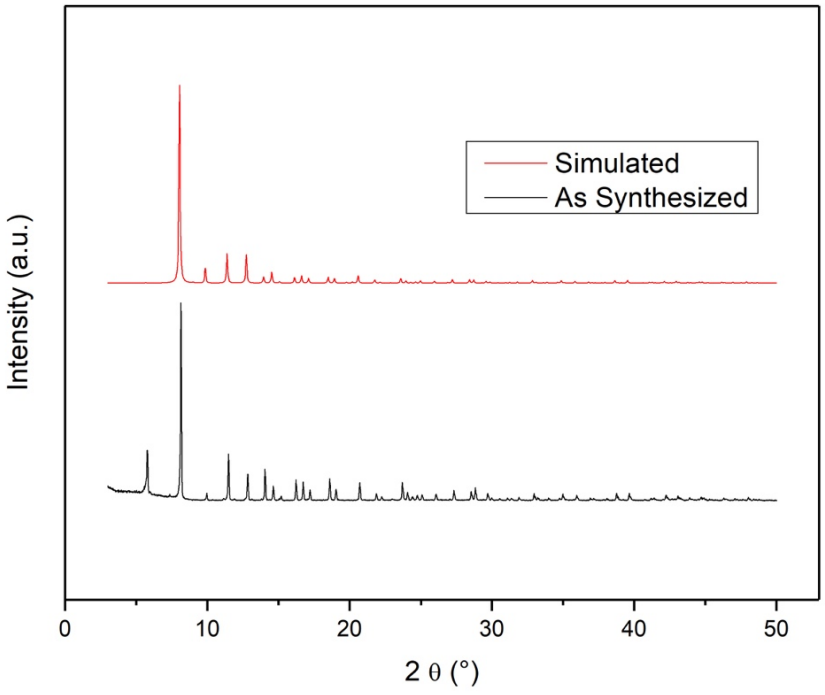


**Figure S2.38.** PXRD of as-purchased PCN-250(Fe) (Strem).

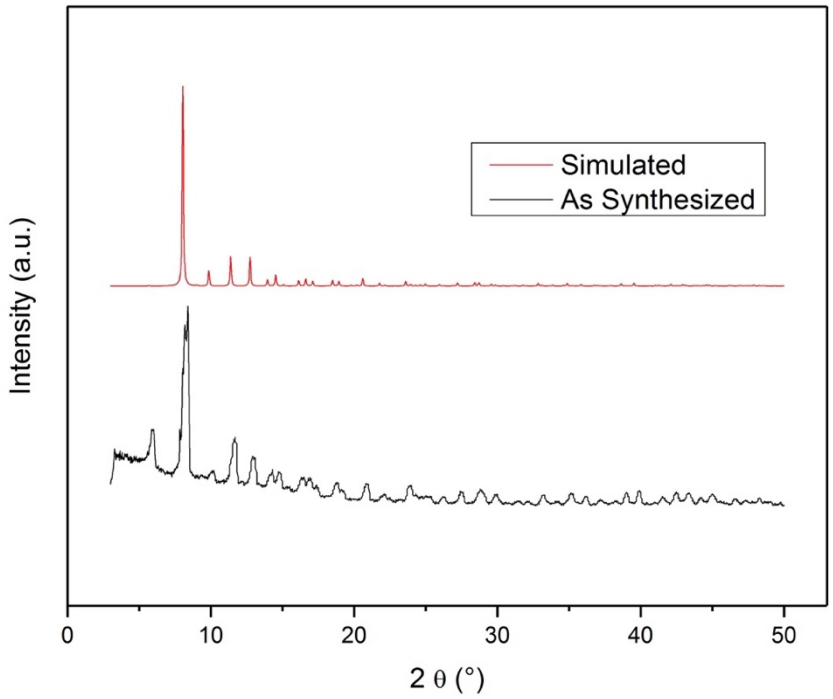


**Figure S2.39.** PXRD of as-synthesized PCN-250(Fe).

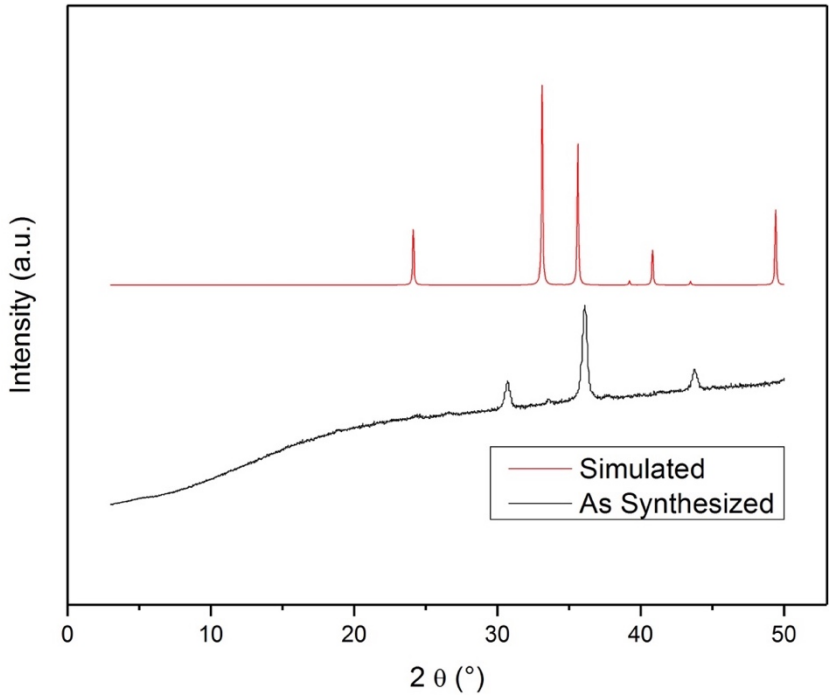


**Figure S2.40.** PXRD of as-purchased $Fe_2O_3$.

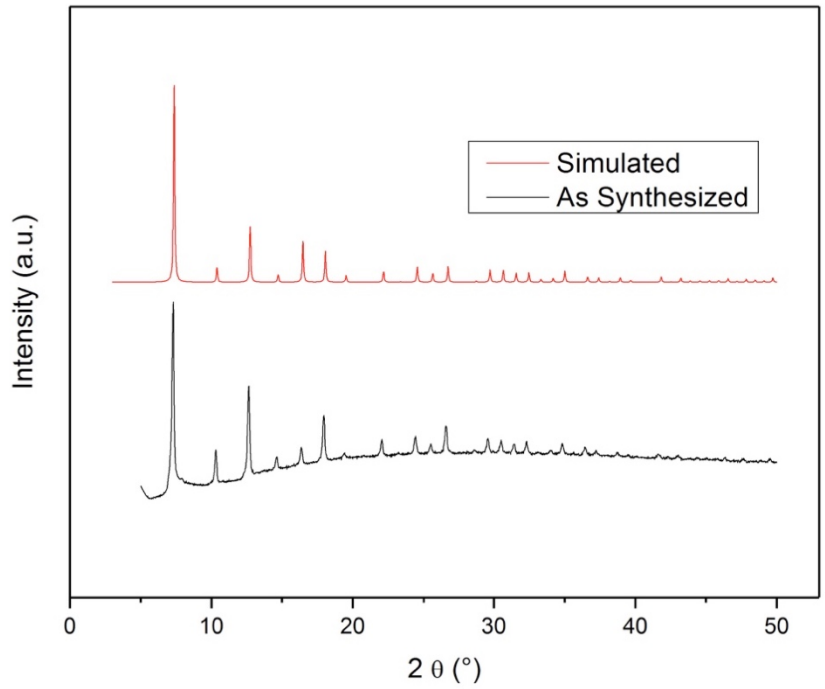


**Figure S2.41.** PXRD of as-synthesized ZIF-67.

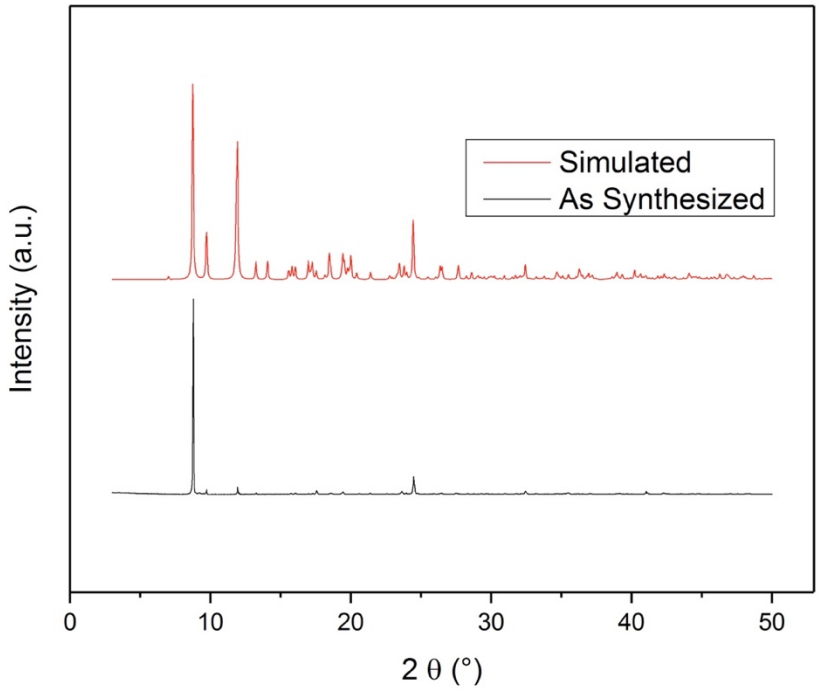


**Figure S2.42.** PXRD of as-synthesized Co-NIC.

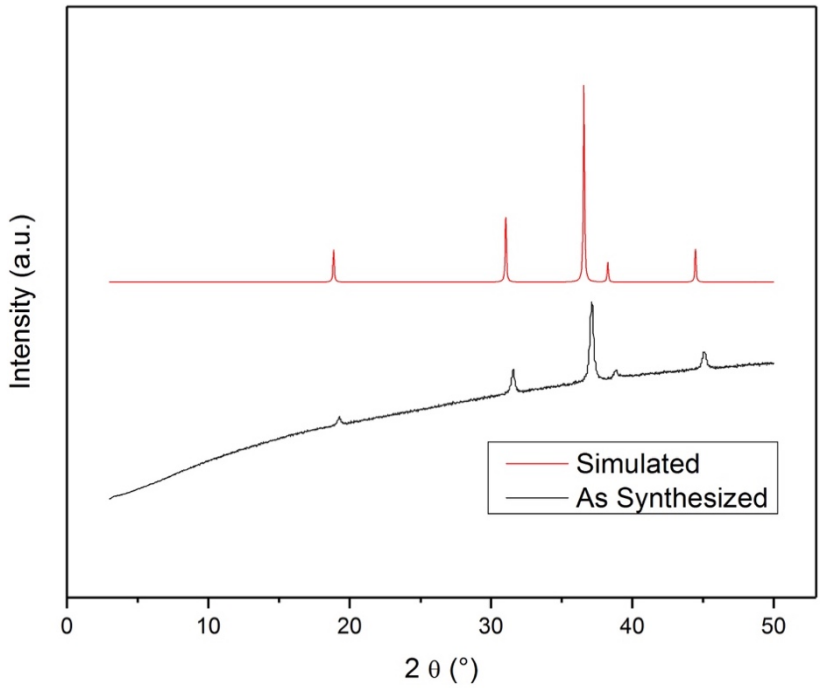


**Figure S2.43.** PXRD of as-purchased $Co_3O_4$.

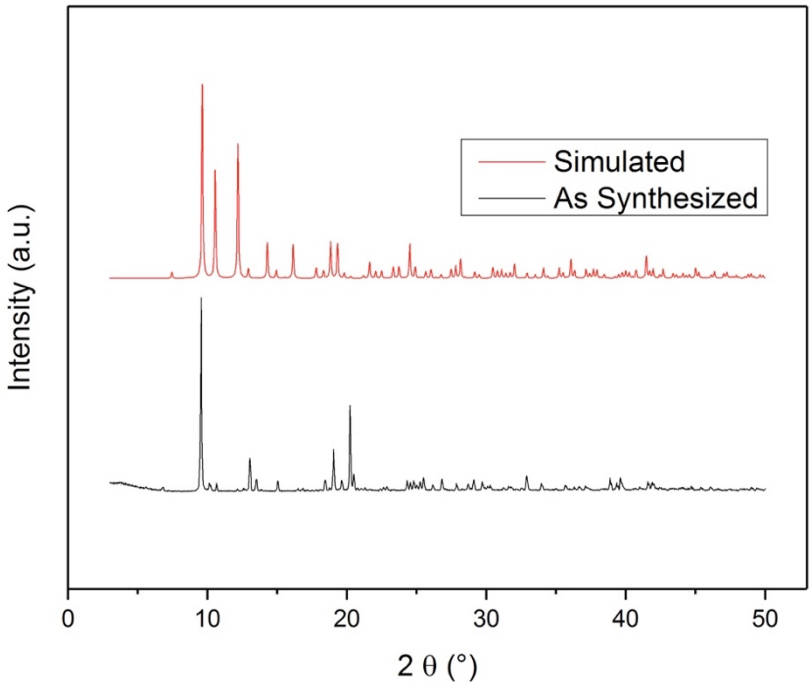


**Figure S2.44.** PXRD of as-synthesized Zn/Co BTEC.

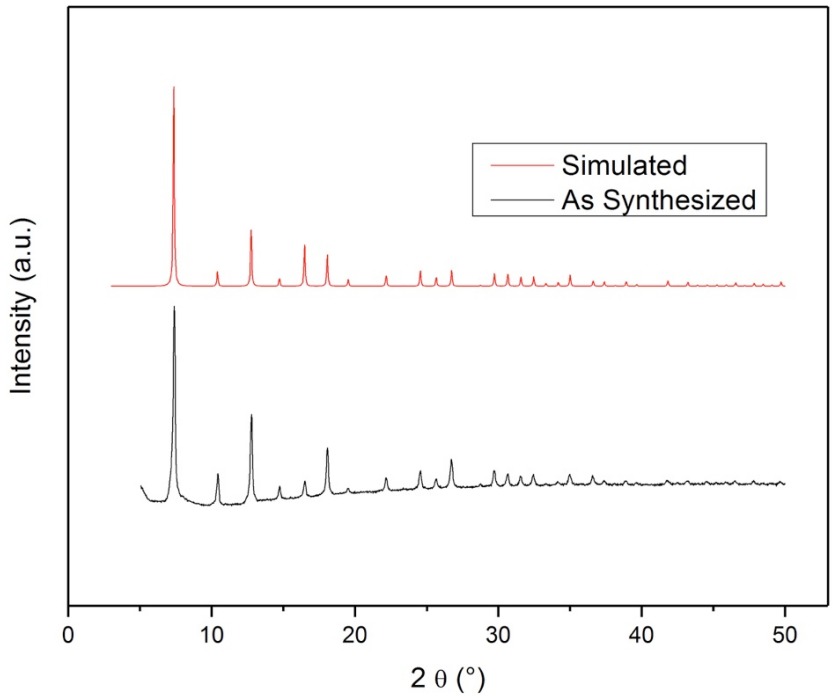


**Figure S2.45.** PXRD of as-synthesized ZIF-8/67(Zn/Co).

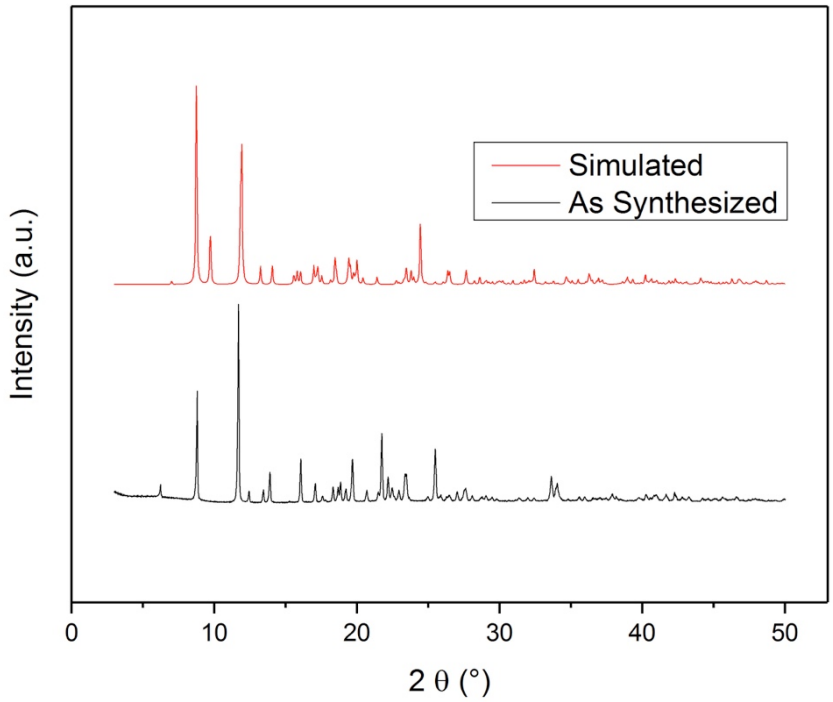


**Figure S2.46.** PXRD of as-synthesized Ni-NIC.

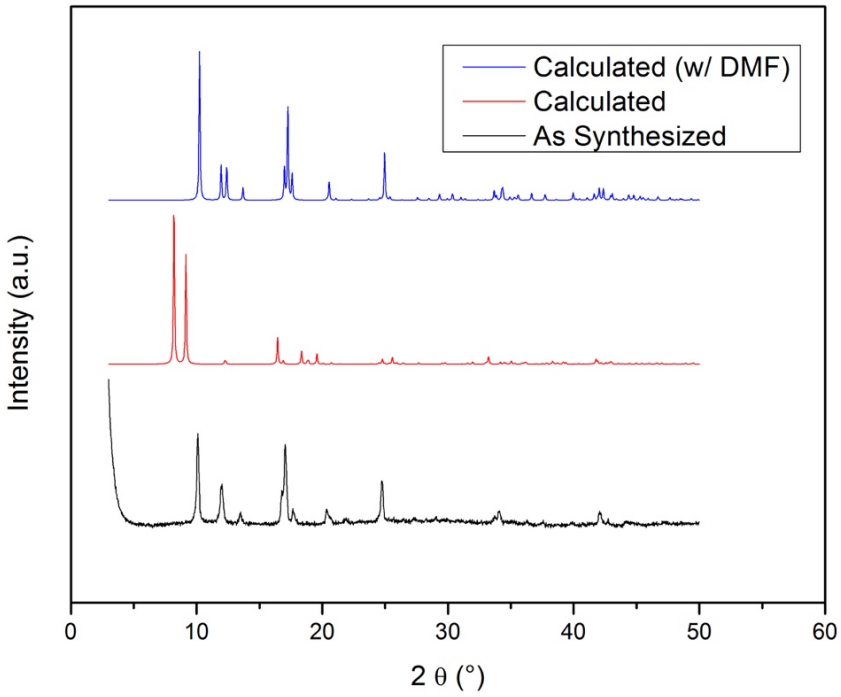


**Figure S2.47.** PXRD of as-synthesized CuBDC. CuBDC can adopt two crystalline conformations, both simulated patterns are plotted here.

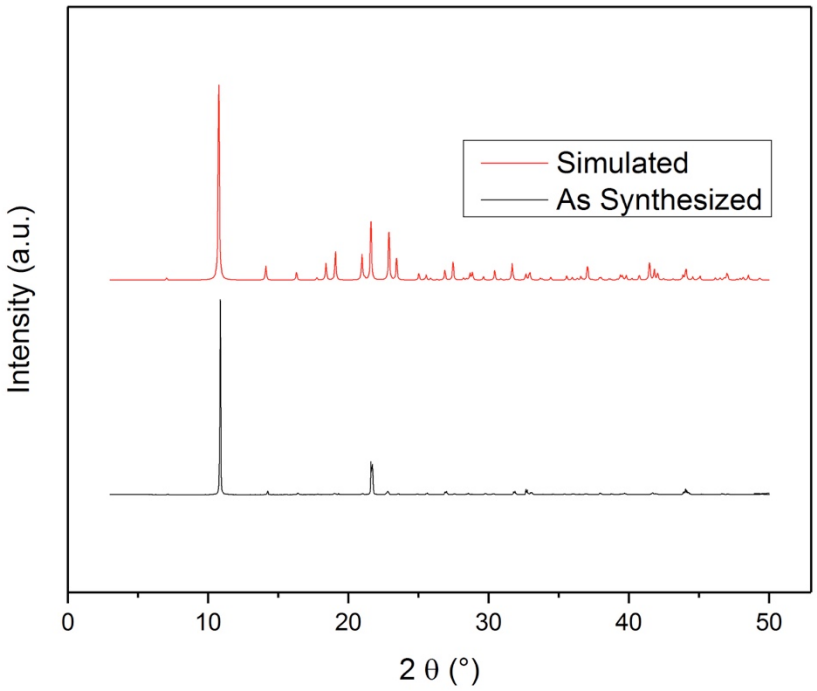


**Figure S2.48.** PXRD of as-synthesized Cu-PCN.

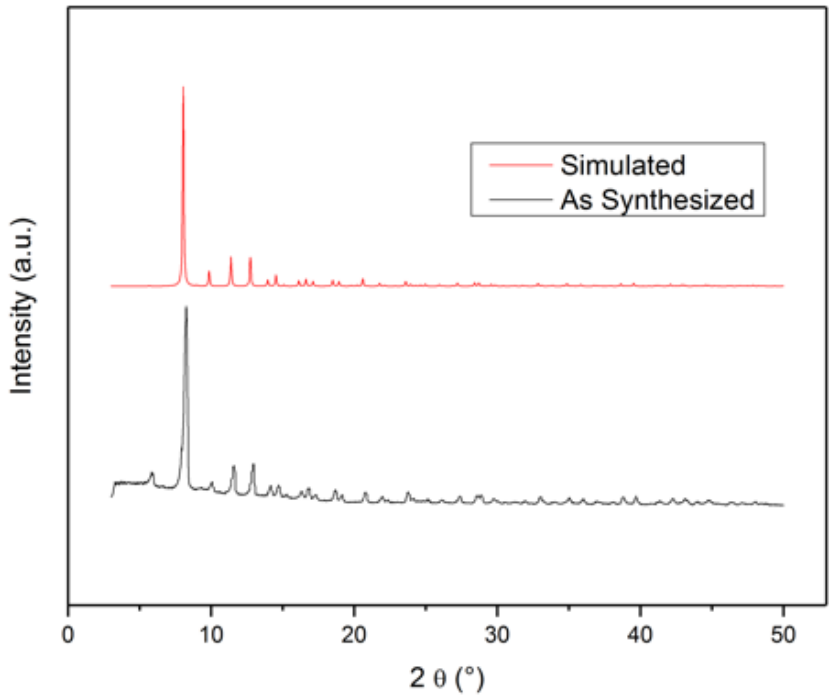


**Figure S2.49.** PXRD of as-synthesized PCN-250(Cu).

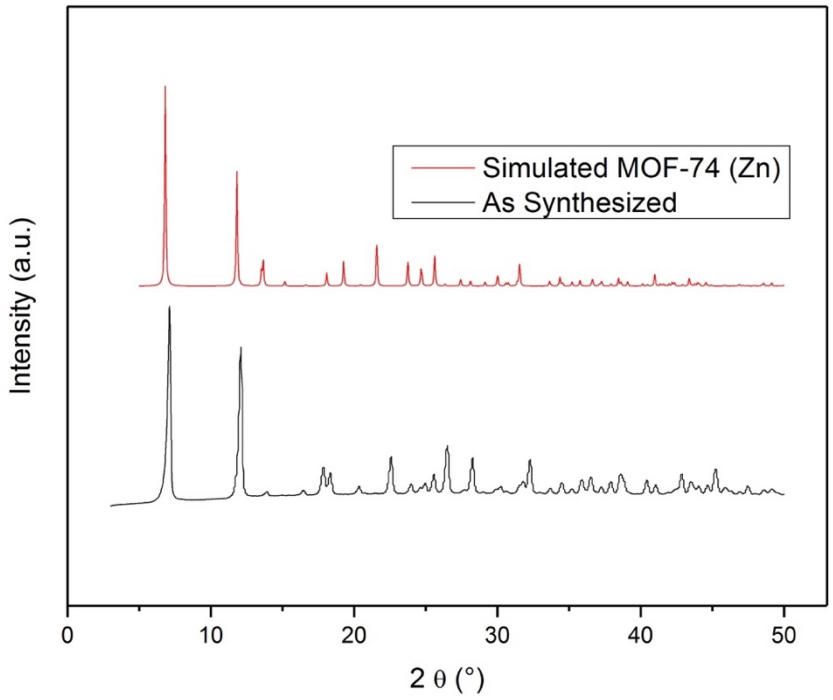


**Figure S2.50.** PXRD of as-synthesized MOF-74(Cu).

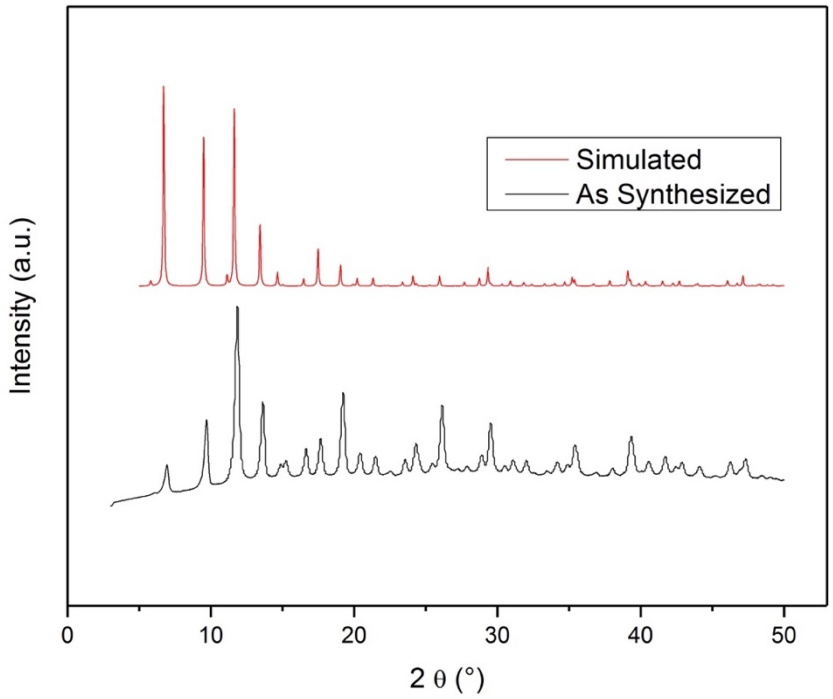


**Figure S2.51.** PXRD of as-synthesized HKUST-1(Cu) (Aldrich).

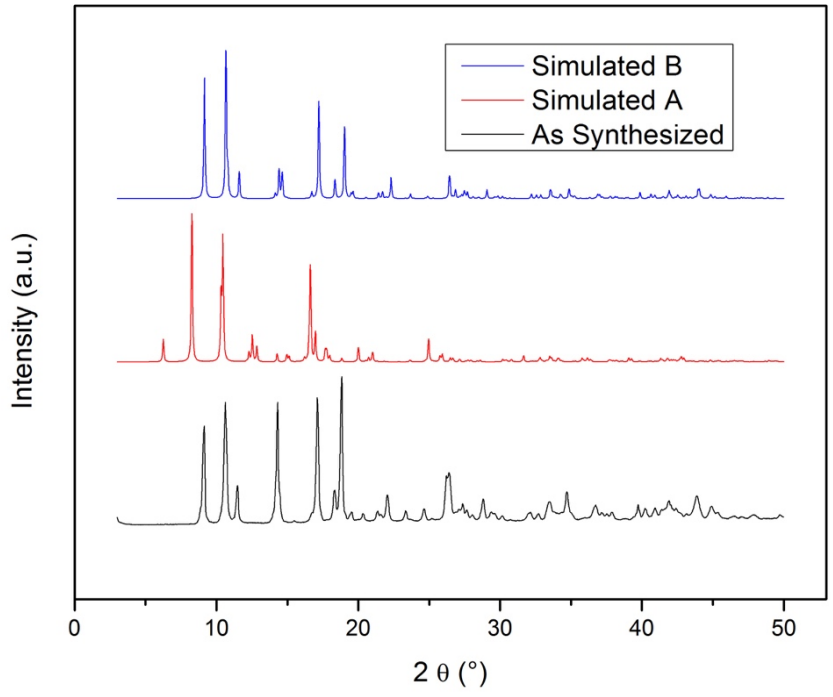


**Figure S2.52.** PXRD of as-synthesized MOF-508. MOF-508 can adopt two crystalline conformations, both simulated patterns are plotted here.

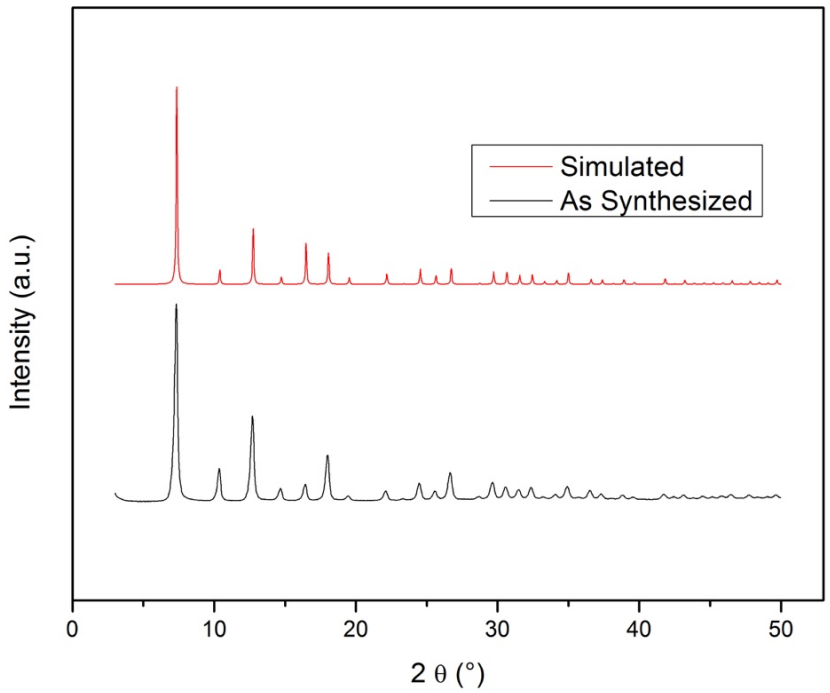


**Figure S2.53.** PXRD of as-synthesized ZIF-8(Zn).

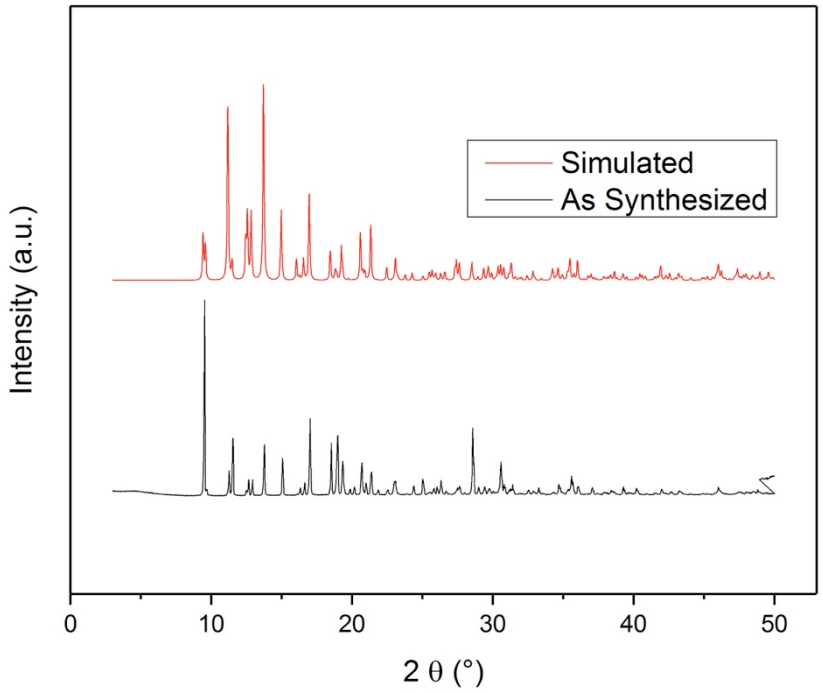


**Figure S2.54.** PXRD of as-synthesized ZIF-4(Zn).

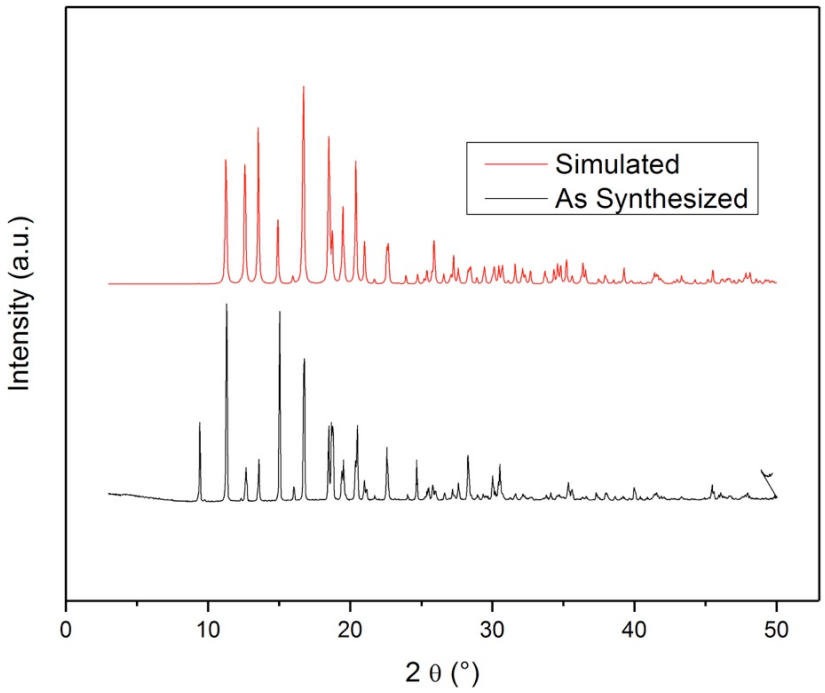


**Figure S2.55.** PXRD of as-synthesized ZIF-62(Zn).

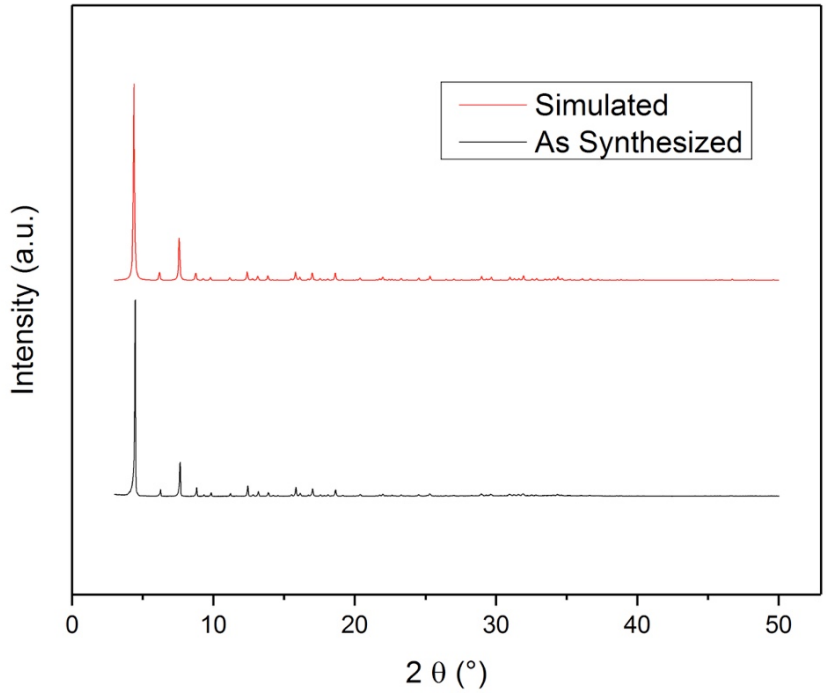


**Figure S2.56.** PXRD of as-synthesized ZIF-71(Zn).

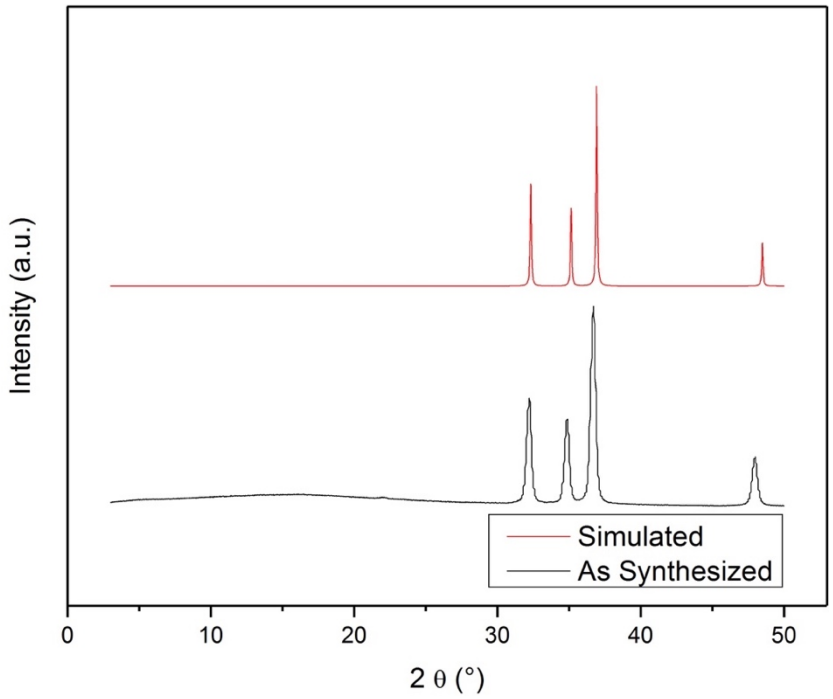


**Figure S2.57.** PXRD of as-purchased ZnO.

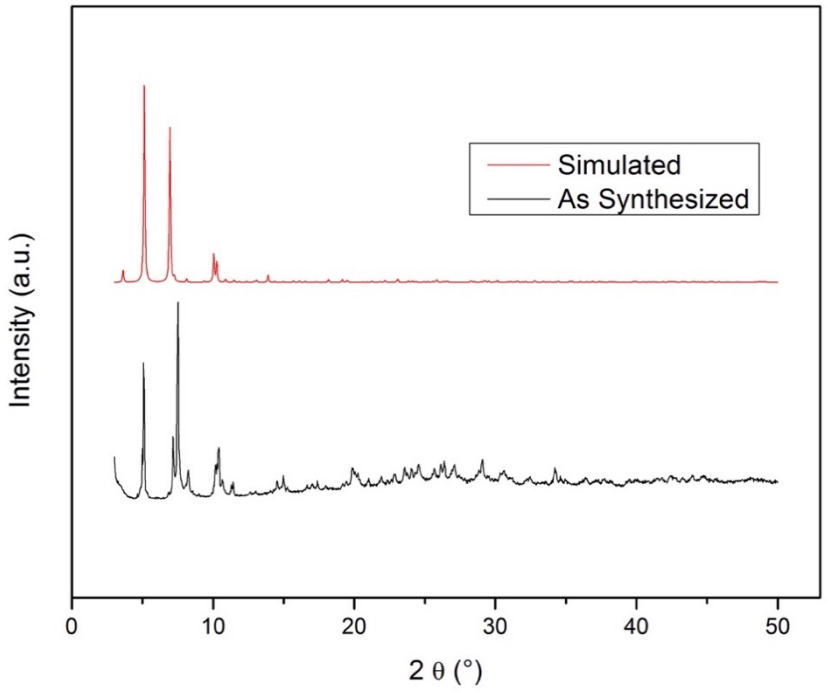


**Figure S2.58.** PXRD of as-synthesized PCN-700(Zr).

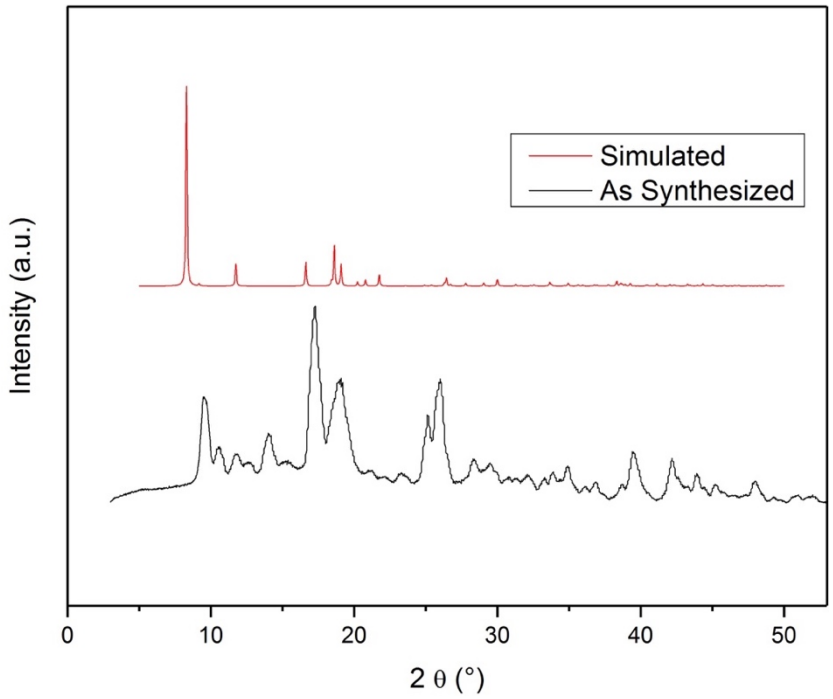


**Figure S2.59.** PXRD of as-synthesized DMOF-1(Zn).

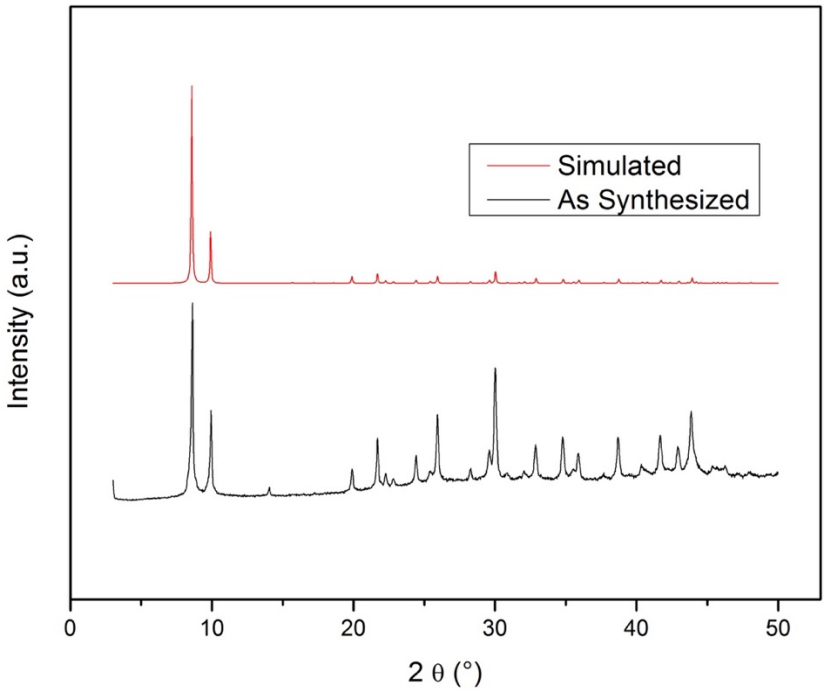


**Figure S2.60.** PXRD of as-synthesized MOF-801(Zr).

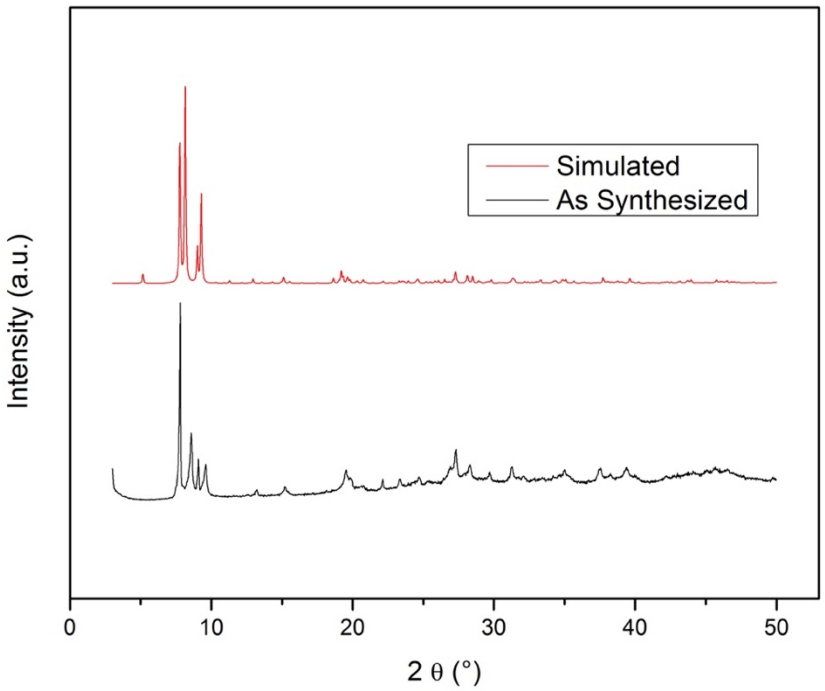


**Figure S2.61.** PXRD of as-synthesized MOF-802(Zr).

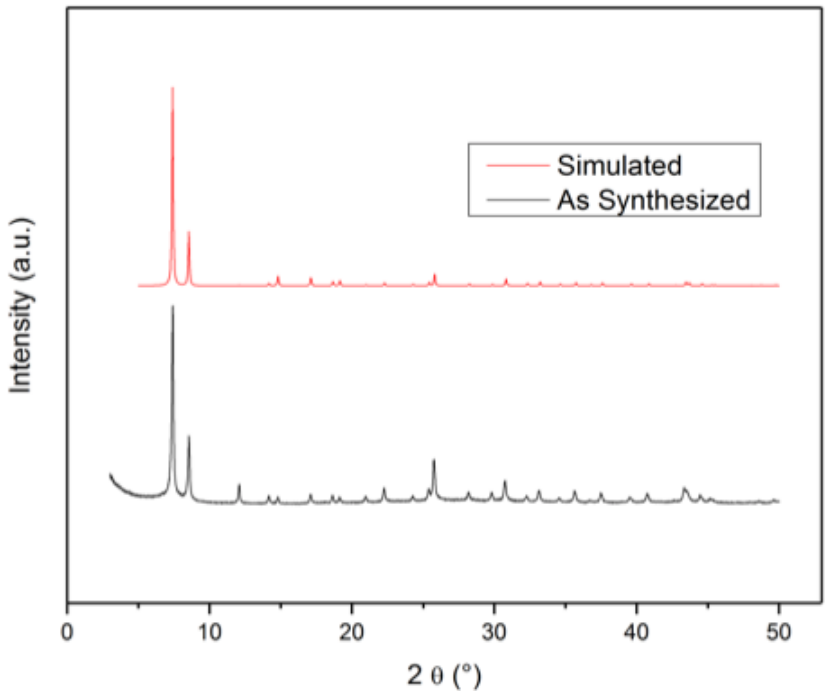


**Figure S2.62.** PXRD of as-synthesized UiO-66(Zr)-$NH_2$ [DMF/AcOH].

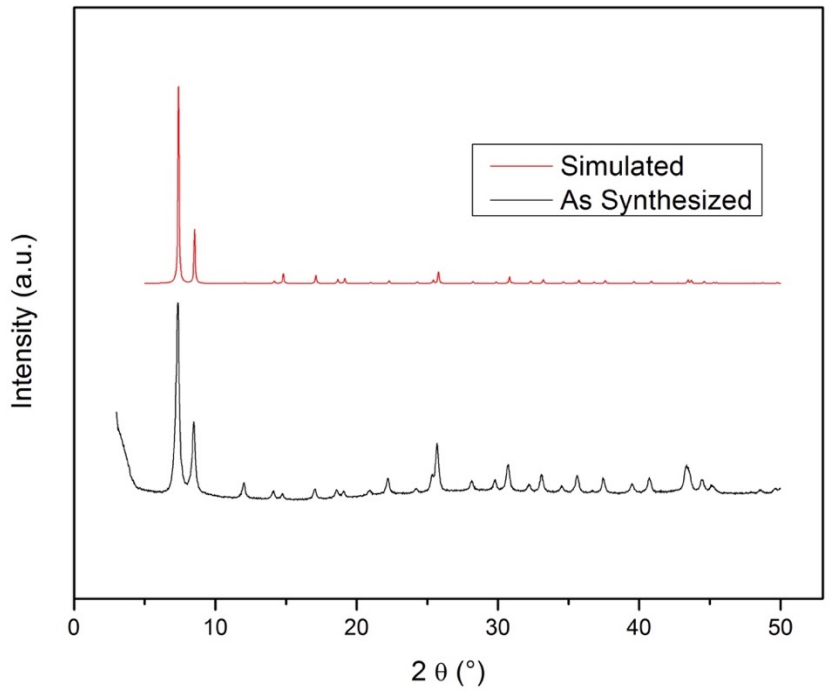


**Figure S2.63.** PXRD of as-synthesized UiO-66(Zr)-$NH_2$ [DMF/HCl].

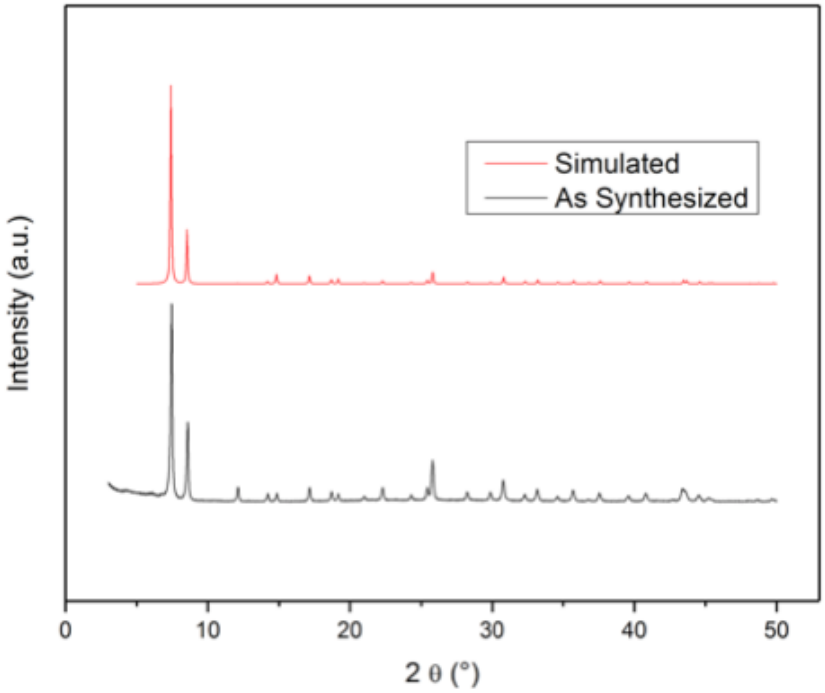


**Figure S2.64.** PXRD of as-purchased UiO-66(Zr)-$NH_2$ (Strem).

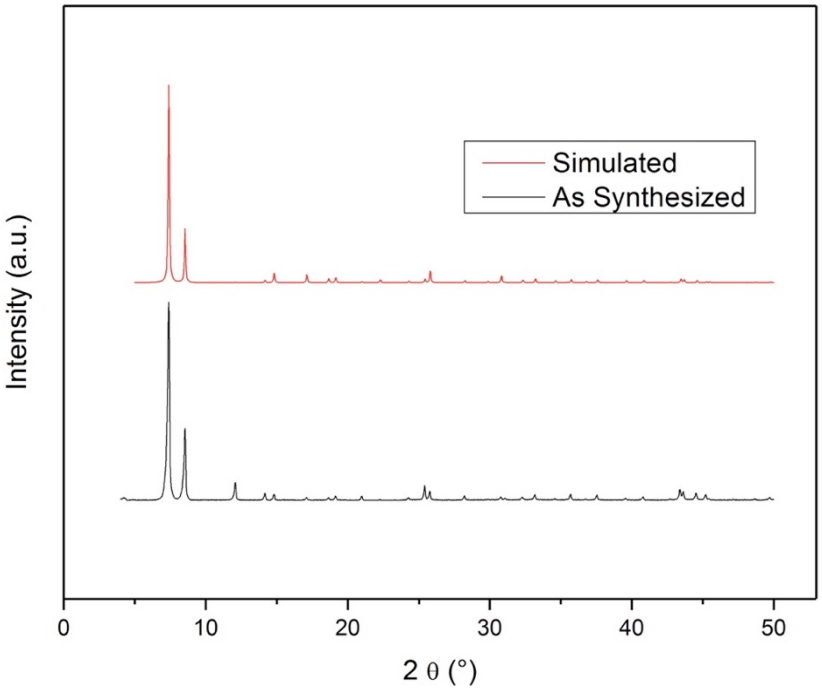


**Figure S2.65.** PXRD of as-synthesized UiO-66-$SO_3H$ [DMF/HCOOH].

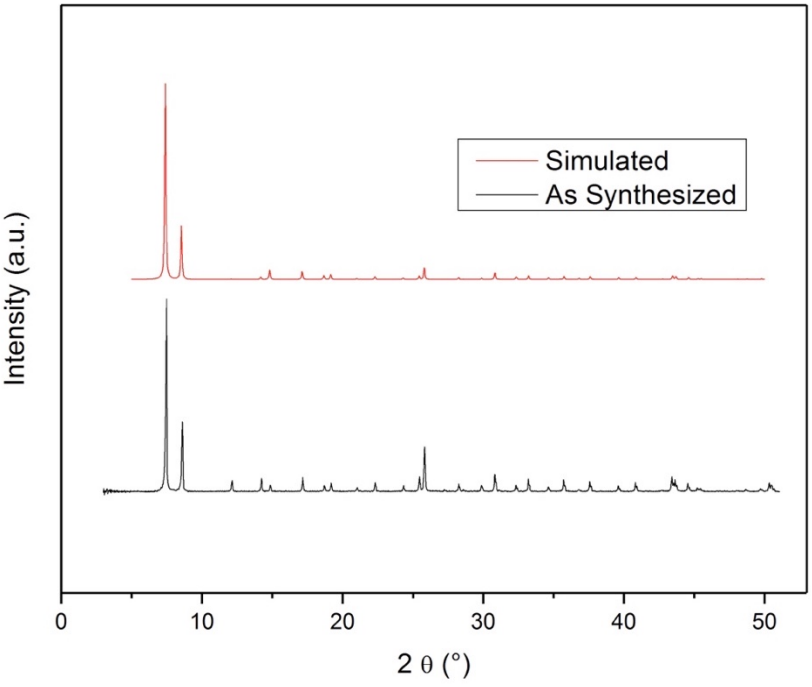


**Figure S2.66.** PXRD of as-synthesized UiO-66(Zr)-COOH [DMF/BzOH].

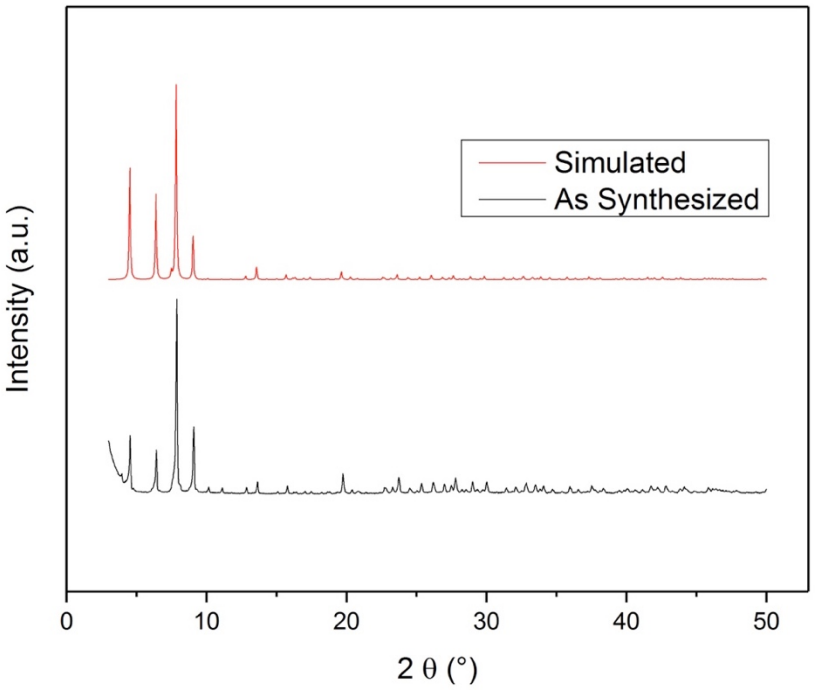


**Figure S2.67.** PXRD of as-synthesized DUT-67(Zr).

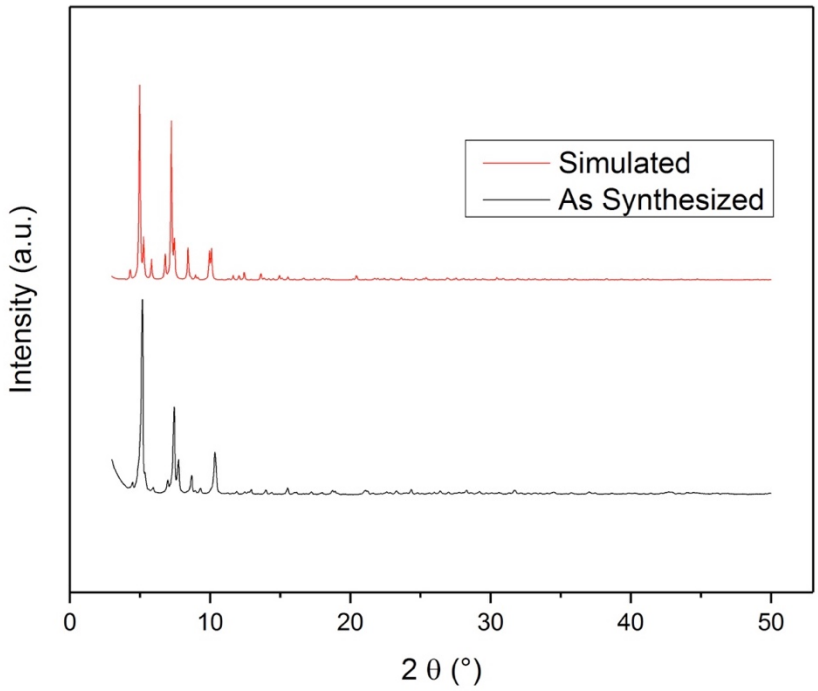


**Figure S2.68**. PXRD of as-synthesized NU-1000(Zr).

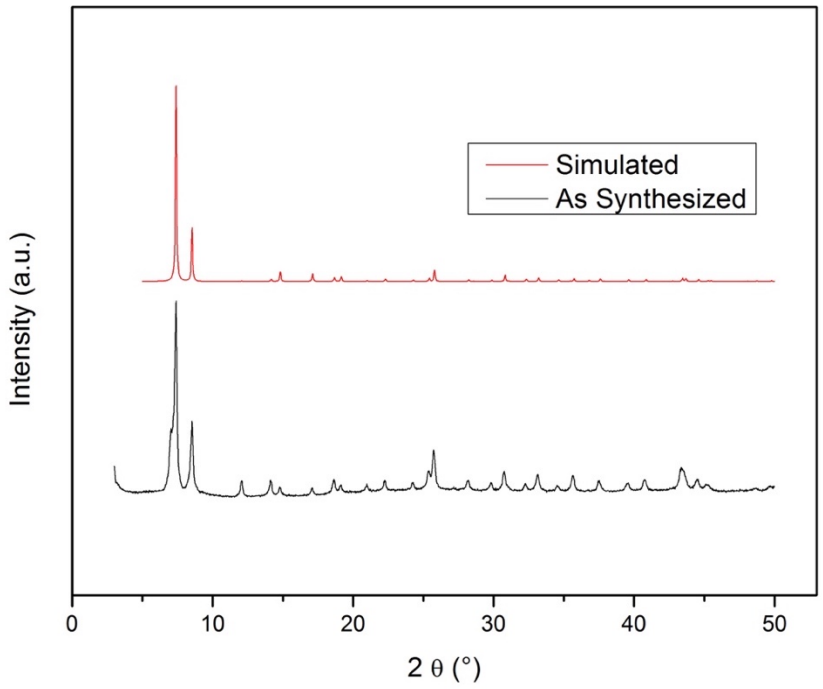


**Figure S2.69.** PXRD of as-synthesized polyUiO-66(Zr).

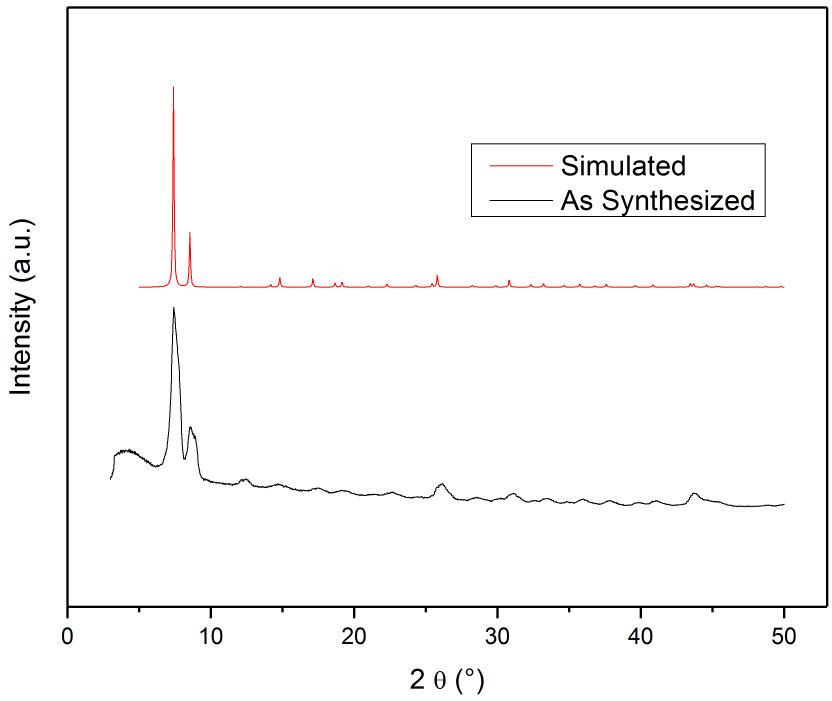


**Figure S2.70.** PXRD of as-synthesized UiO-66(Zr)-$NH_2$-LD.

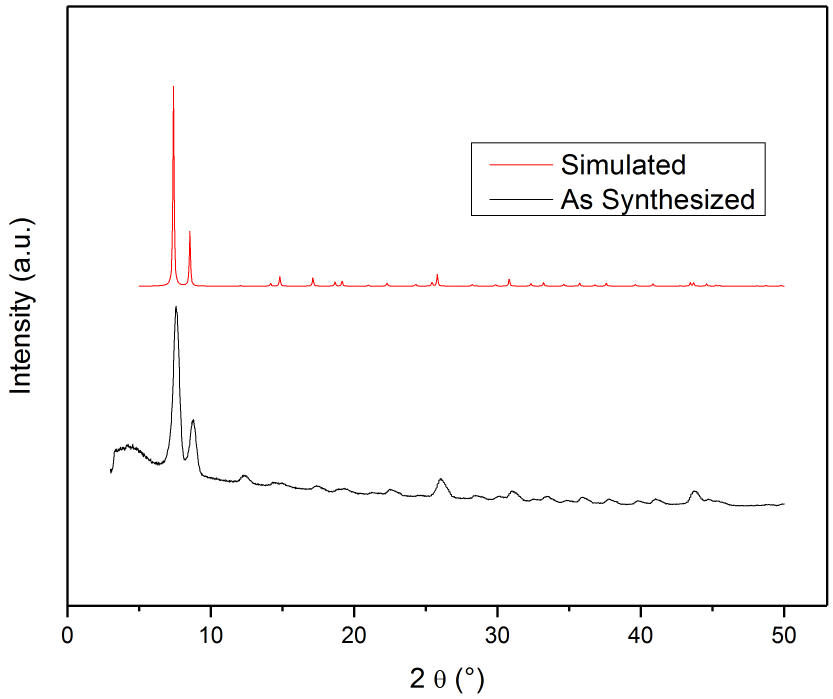


**Figure S2.71.** PXRD of as-synthesized UiO-66(Zr)-$NH_2$-MD.

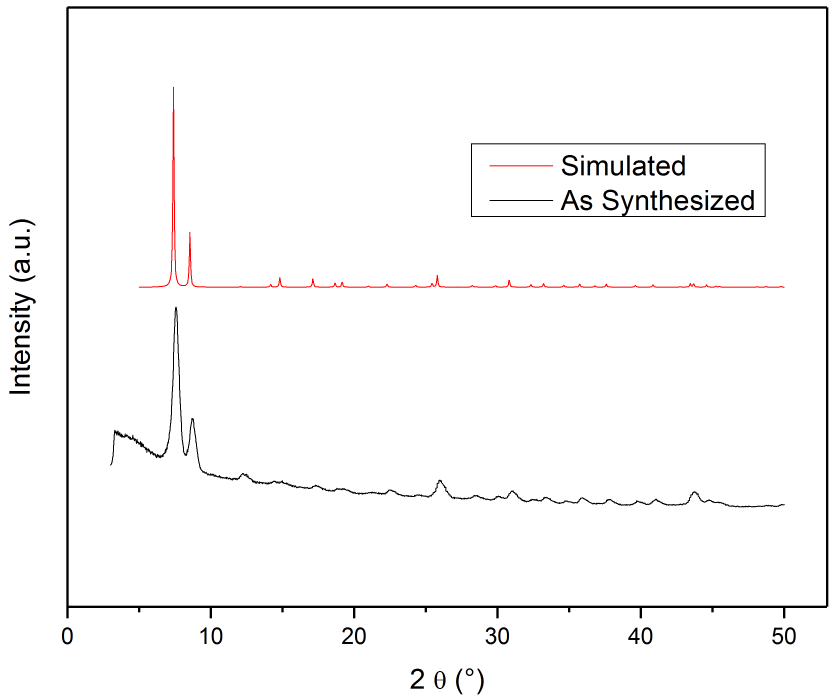


**Figure S2.72.** PXRD of as-synthesized UiO-66(Zr)-$NH_2$-HD.

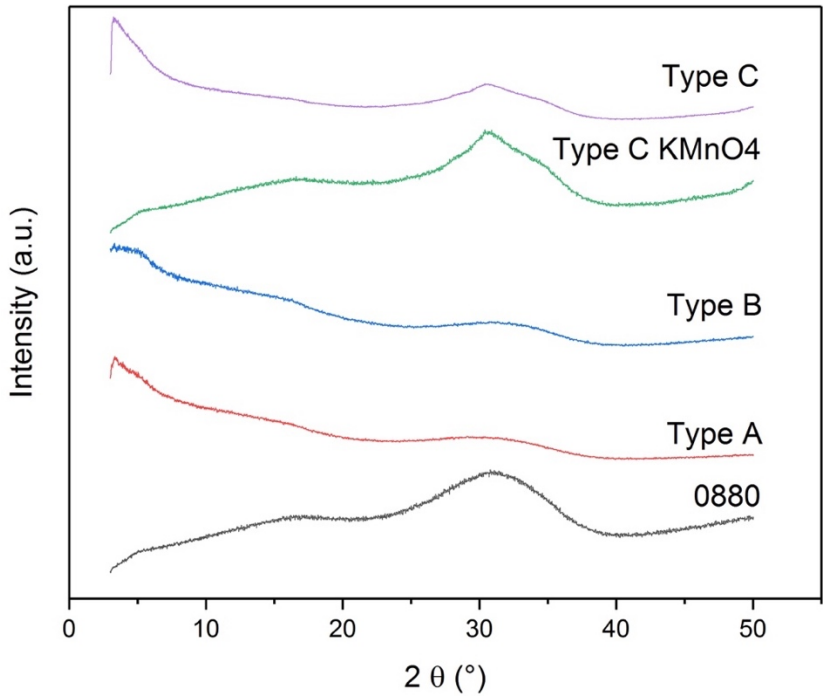


**Figure S2.73.** PXRD of as-purchased $Zr(OH)_2$ materials: 0880, Type A, Type B, Type C-$KMnO_4$, and Type C.

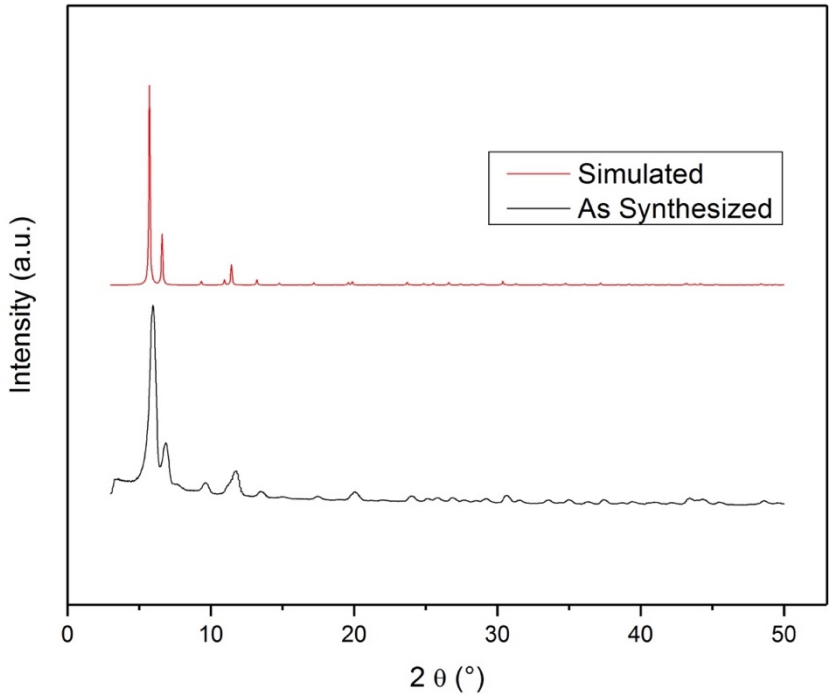


**Figure S2.74.** PXRD of as-synthesized UiO-67(Zr).

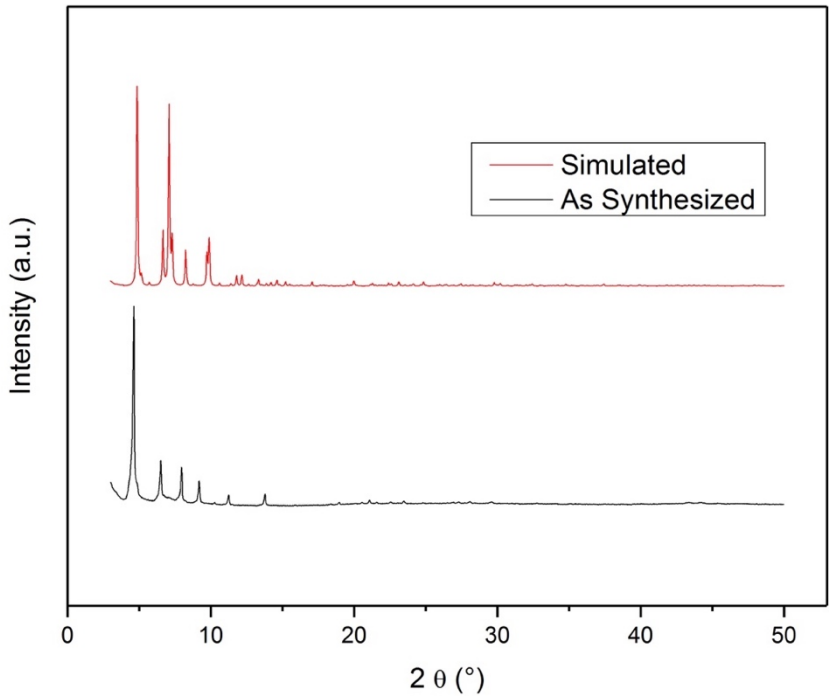


**Figure S2.75.** PXRD of as-synthesized PCN-222(Zr).

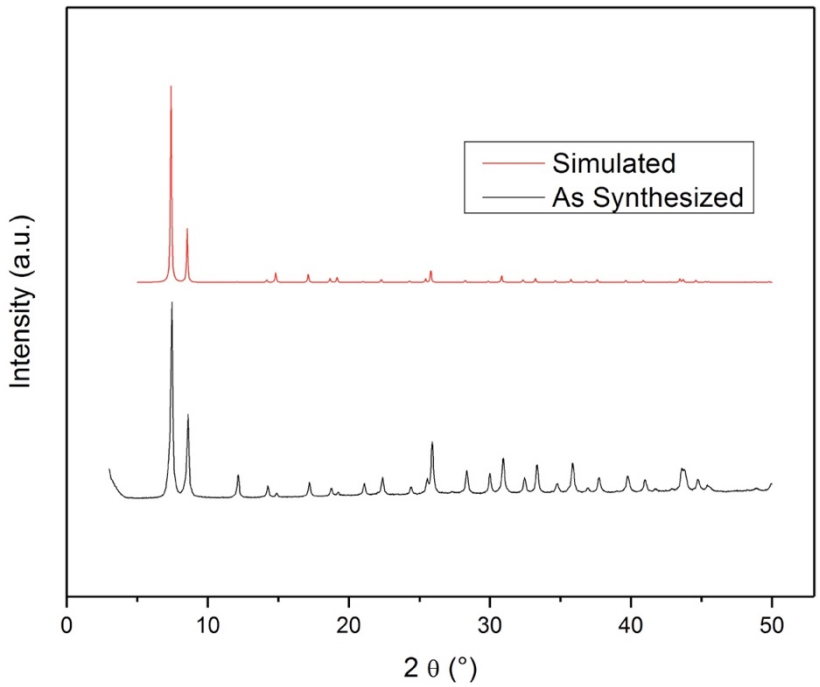


**Figure S2.76.** PXRD of as-synthesized UiO-66(Zr)-$NH_2$ [Acetone/HCl].

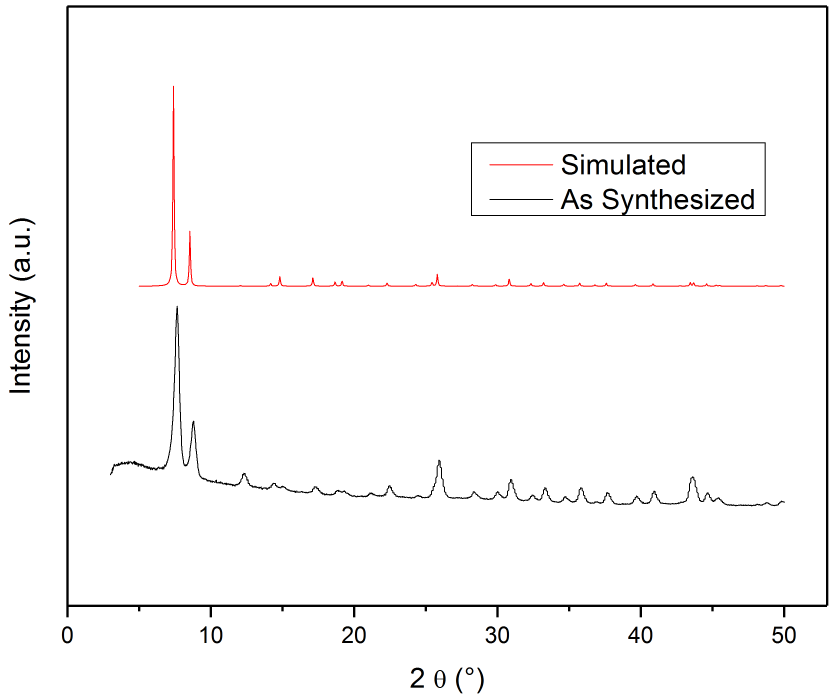


**Figure S2.77.** PXRD of as-synthesized UiO-66(Zr)-$NH_2$ [DMF/HCOOH].

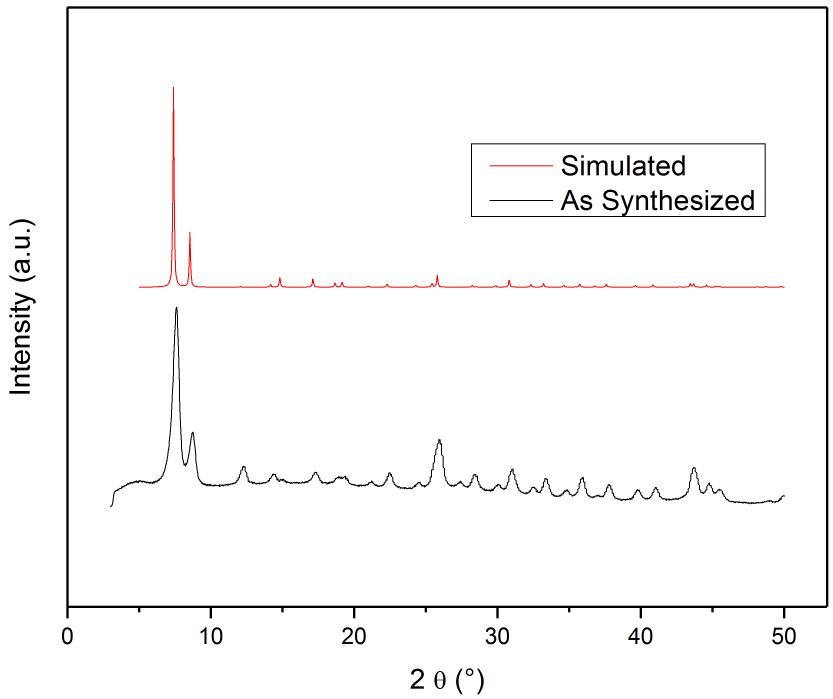


**Figure S2.78.** PXRD of as-synthesized UiO-66(Zr)-$(COOH)_2$ [DMF/HCOOH].

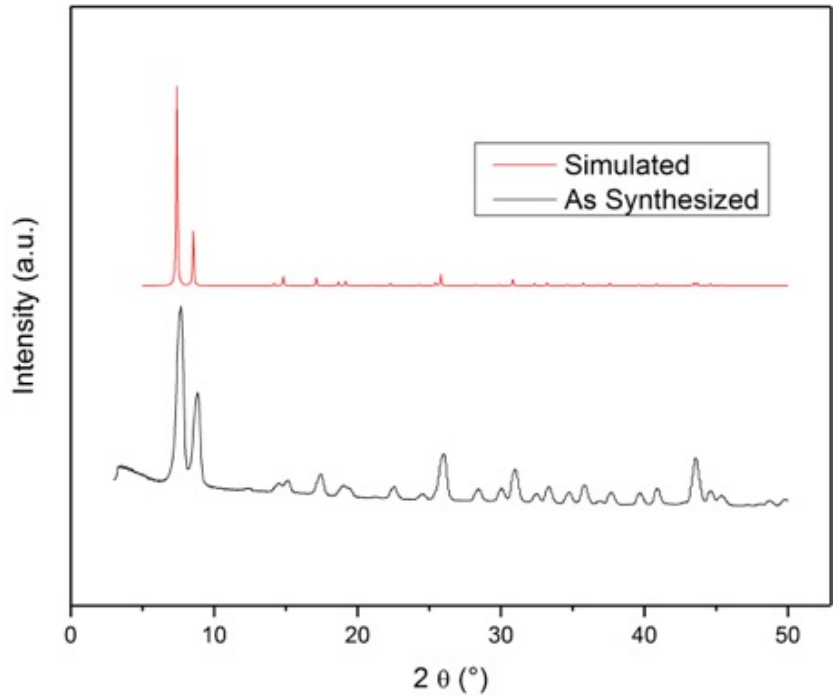


**Figure S2.79.** PXRD of as-synthesized UiO-66(Zr)-$(OH)_2$ [DMF/HCOOH].

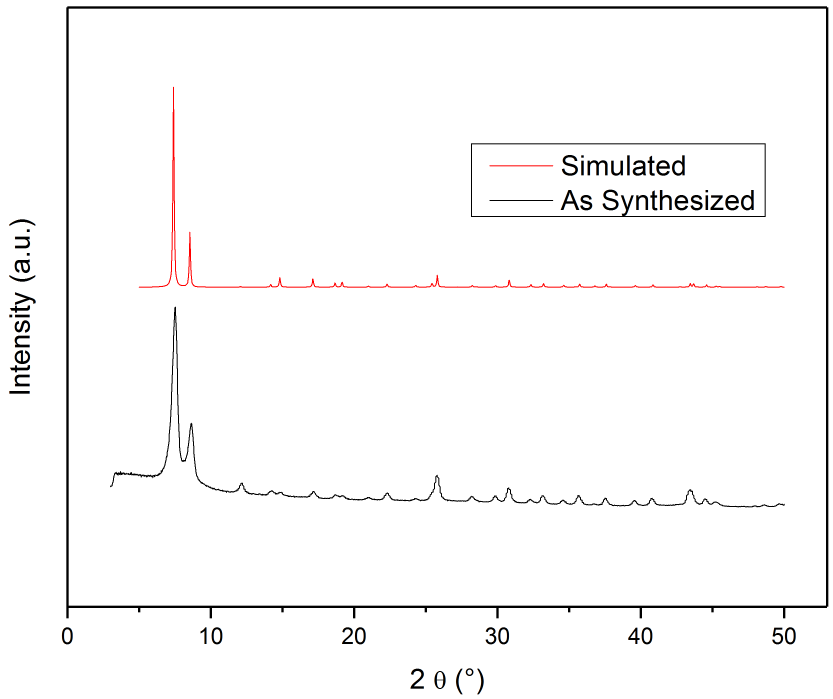


**Figure S2.80.** PXRD of as-synthesized UiO-66(Zr)-OH [DMF/HCOOH].

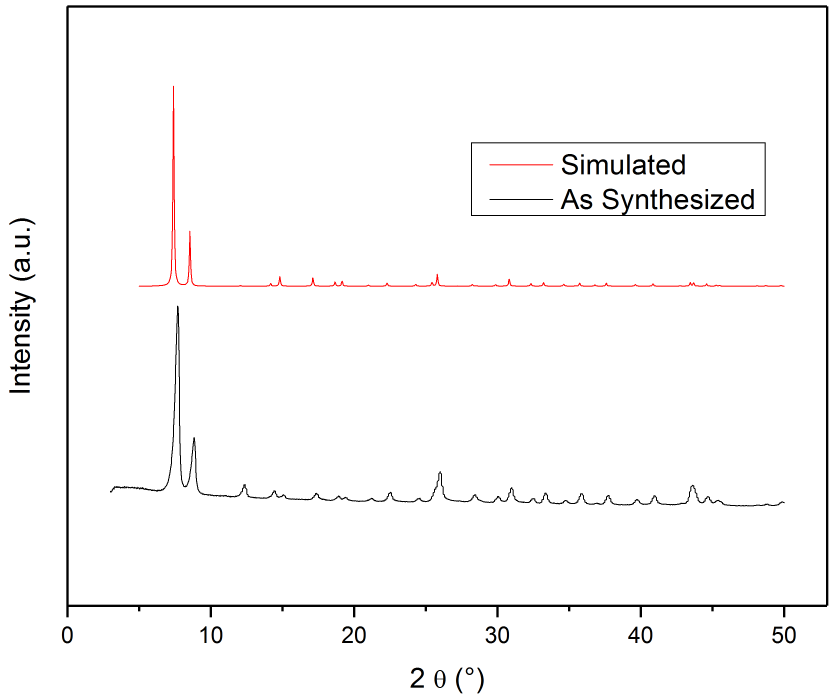


**Figure S2.81.** PXRD of as-synthesized UiO-66(Zr)-$NO_2$ [DMF/HCOOH].

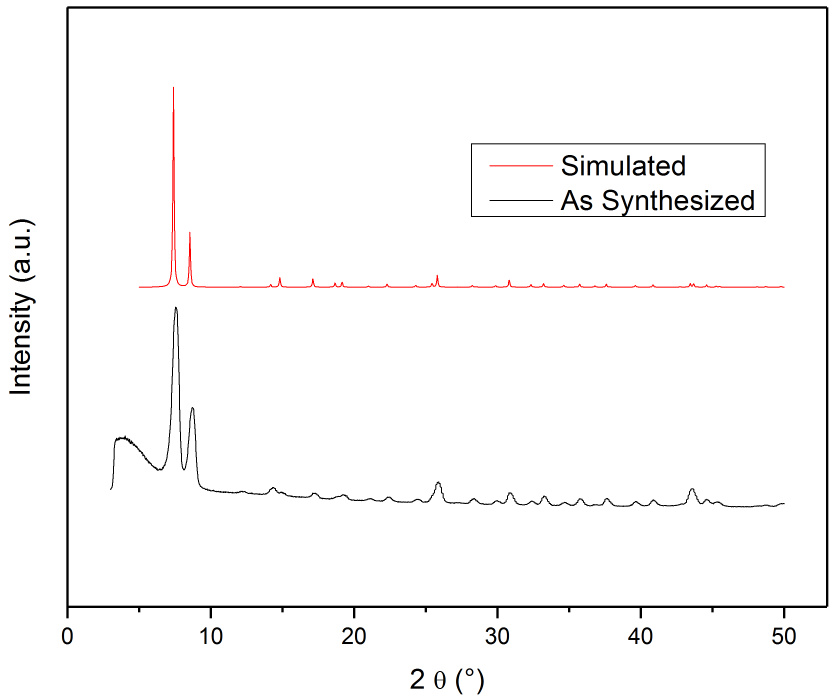


**Figure S2.82.** PXRD of as-synthesized UiO-66(Zr)-$OCF_3$ [DMF/HCOOH].

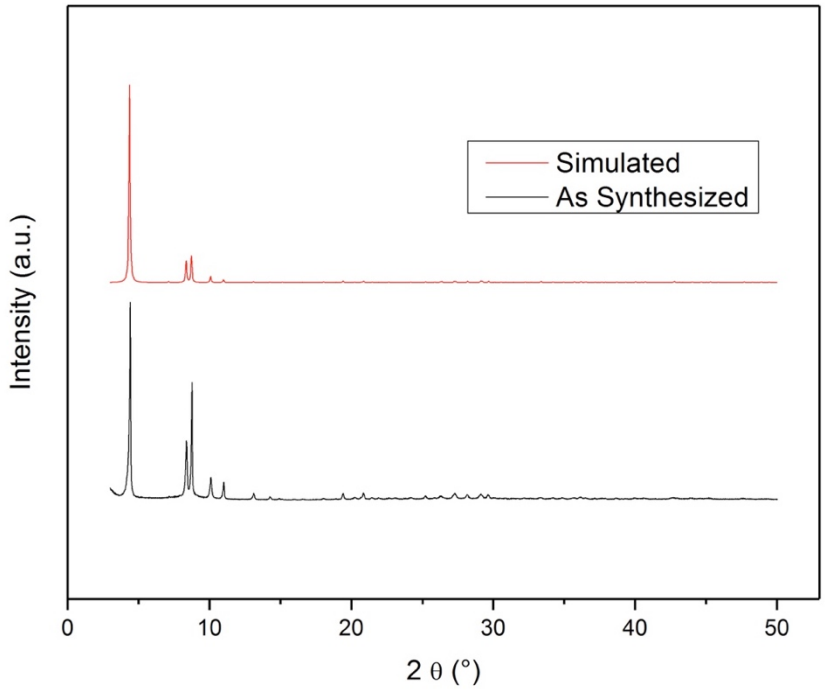


**Figure S2.83.** PXRD of as-synthesized MOF-808(Zr).

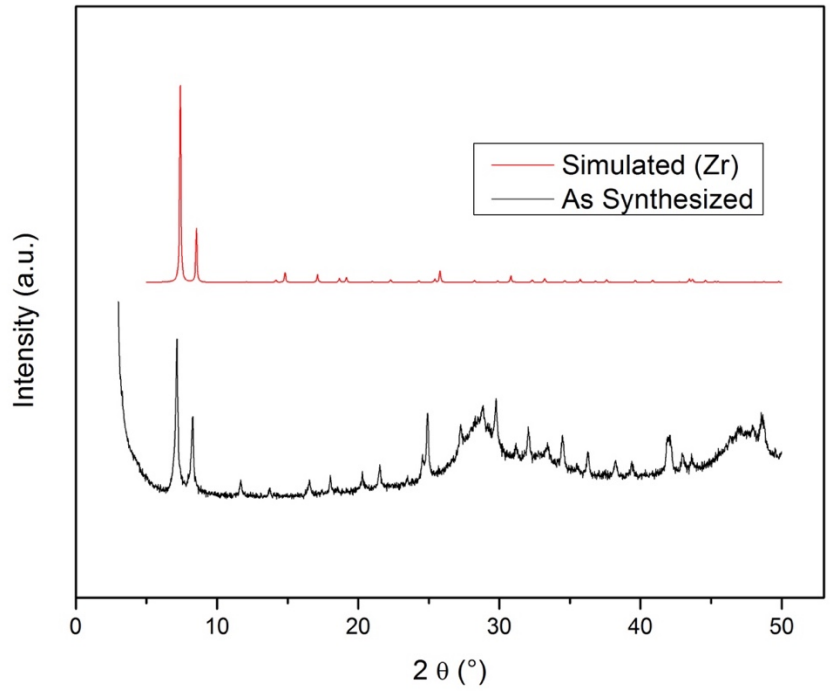


**Figure S2.84.** PXRD of as-synthesized UiO-66(Ce).

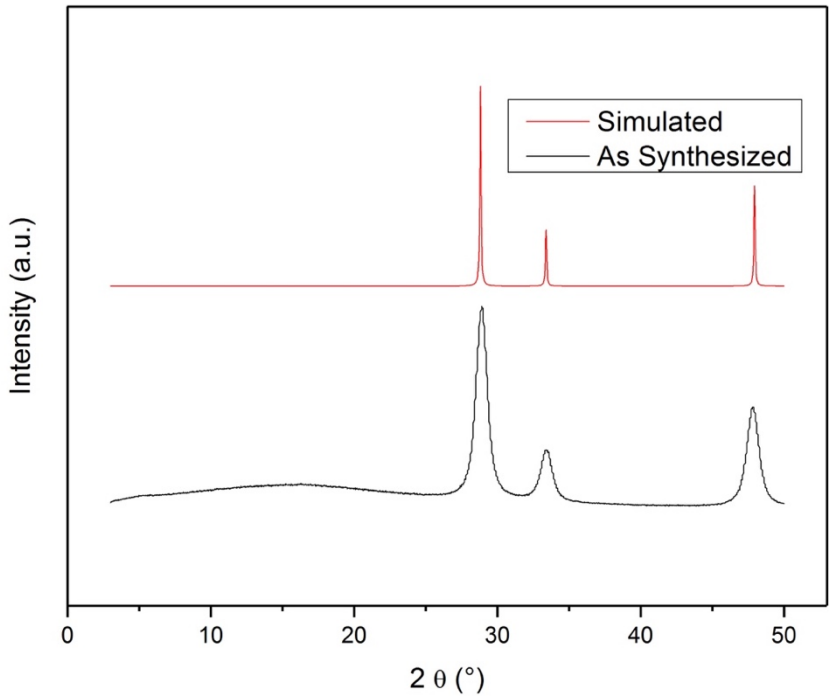


**Figure S2.85.** PXRD of as-purchased $CeO_2$.

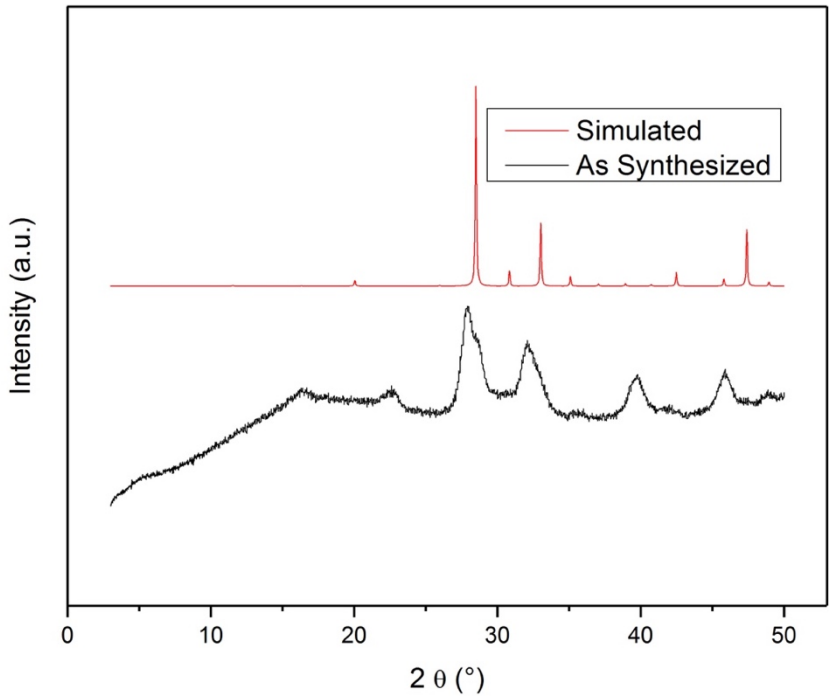


**Figure S2.86.** PXRD of as-purchased $Eu_2O_3$.

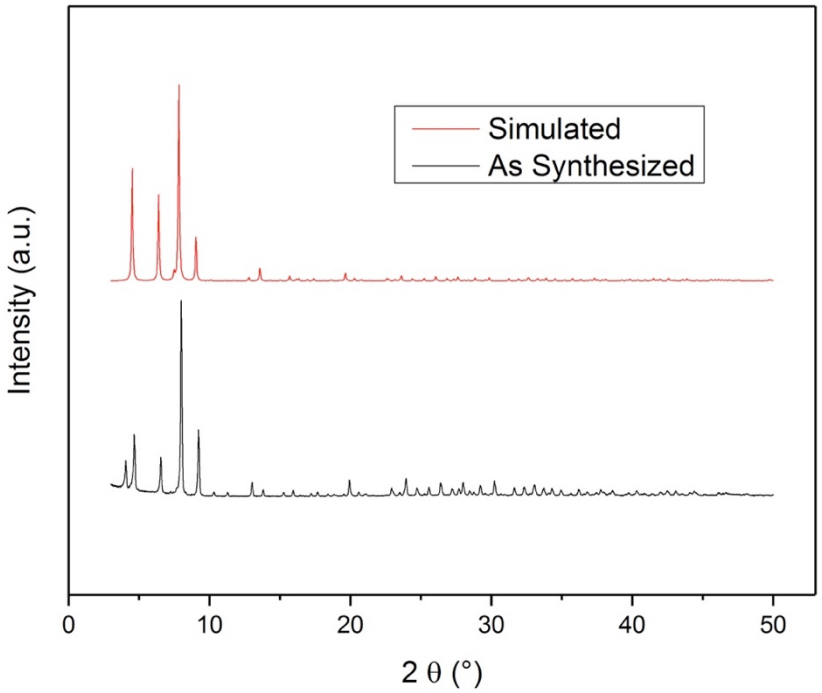


**Figure S2.87.** PXRD of as-synthesized DUT-67(Hf).

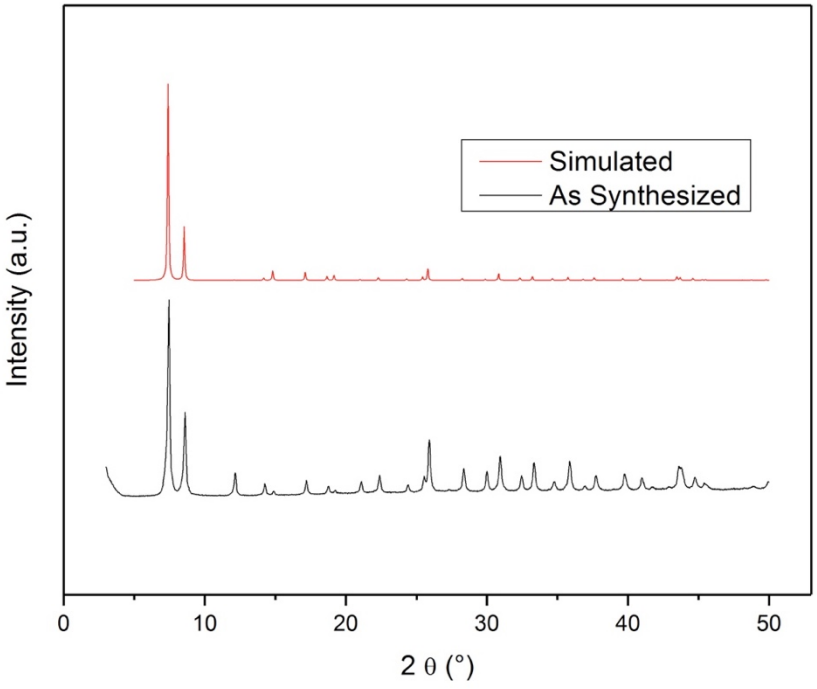


**Figure S2.88.** PXRD of as-synthesized UiO-66(Hf).

## 2.7 Acknowledgements

Chapter 2, in part, is a reprint of the following material “Joseph M. Palomba, Cy V. Credille, Mark Kalaj, Jared B. DeCoste, Gregory W. Peterson, Trenton M. Tovar, and Seth M. Cohen, High-throughput screening of solid-state catalysts for nerve agent degradation, *Chem. Commun.* **2018,** *54*, 5768-5771.” The dissertation author was the primary author this manuscript and gratefully acknowledges the contributions of coauthors. The dissertation author also gratefully acknowledges the editing help of Dr. Kathleen E. Prosser, Dr. Sergio Ayala Jr., Dr. Michael S. Denny Jr., Dr. Jessica C. Moreton, and Mark Kalaj.

## 2.8 References

1. Islamoglu, T.; Chen, Z.; Wasson, M. C.; Buru, C. T.; Kirlikovali, K. O.; Afrin, U.; Mian, M. R.; Farha, O. K., Metal–Organic Frameworks against Toxic Chemicals. *Chem. Rev.* **2020,** *120*, 8130-8160.

2. Peterson, G. W.; Moon, S.-Y.; Wagner, G. W.; Hall, M. G.; DeCoste, J. B.; Hupp, J. T.; Farha, O. K., Tailoring the Pore Size and Functionality of UiO-Type Metal–Organic Frameworks for Optimal Nerve Agent Destruction. *Inorg. Chem.* **2015,** *54*, 9684-9686.

3. Farha, O. K.; Islamoglu, T.; Ortuno, M. A.; Proussaloglou, E.; Howarth, A. J.; Vermeulen, N. A.; Atilgan, A.; Asiri, A. M., Presence vs. proximity: the role of pendant amines in the catalytic hydrolysis of a nerve agent simulant. *Angew. Chem., Int. Ed.* **2018,** *57*, 1949-1953.

4. Katz, M. J.; Moon, S.-Y.; Mondloch, J. E.; Beyzavi, M. H.; Stephenson, C. J.; Hupp, J. T.; Farha, O. K., Exploiting parameter space in MOFs: a 20-fold enhancement of phosphate-ester hydrolysis with UiO-66-NH2. *Chem. Sci.* **2015,** *6*, 2286-2291.

5. Katz, M. J.; Mondloch, J. E.; Totten, R. K.; Park, J. K.; Nguyen, S. T.; Farha, O. K.; Hupp, J. T., Simple and Compelling Biomimetic Metal–Organic Framework Catalyst for the Degradation of Nerve Agent Simulants. *Angew. Chem.* **2014,** *126*, 507-511.

6. Martin, D. P.; Cohen, S. M., Nucleophile recognition as an alternative inhibition mode for benzoic acid based carbonic anhydrase inhibitors. *Chem. Commun.* **2012,** *48*, 5259-5261.

7. Ji-Hu, Z.; Thomas, D. Y. C.; Kevin, R. O., A Simple Statistical Parameter for Use in Evaluation and Validation of High Throughput Screening Assays. *J. Biomol. Screening* **1999,** *4*, 67-73.

8. Ayala, S.; Zhang, Z.; Cohen, S. M., Hierarchical structure and porosity in UiO-66 polyMOFs. *Chem. Commun.* **2017,** *53*, 3058-3061.

9. Katz, M. J.; Klet, R. C.; Moon, S.-Y.; Mondloch, J. E.; Hupp, J. T.; Farha, O. K., One Step Backward Is Two Steps Forward: Enhancing the Hydrolysis Rate of UiO-66 by Decreasing [OH–]. *ACS Catal.* **2015,** *5*, 4637-4642.

10. Dissegna, S.; Epp, K.; Heinz Werner, R.; Kieslich, G.; Fischer Roland, A., Defective Metal‐Organic Frameworks. *Adv. Mater.* **2018,** *30*, 1704501.

11. Liu, Y.; Moon, S.-Y.; Hupp, J. T.; Farha, O. K., Dual-Function Metal–Organic Framework as a Versatile Catalyst for Detoxifying Chemical Warfare Agent Simulants. *ACS Nano* **2015,** *9*, 12358-12364.

12. Yuan, S.; Qin, J. S.; Xu, H. Q.; Su, J.; Rossi, D.; Chen, Y.; Zhang, L.; Lollar, C.; Wang, Q.; Jiang, H. L.; Son, D. H.; Xu, H.; Huang, Z.; Zou, X.; Zhou, H. C., [Ti8Zr2O12(COO)16] Cluster: An Ideal Inorganic Building Unit for Photoactive Metal-Organic Frameworks. *ACS Cent. Sci.* **2018,** *4*, 105-111.

13. Rimoldi, M.; Howarth, A. J.; DeStefano, M. R.; Lin, L.; Goswami, S.; Li, P.; Hupp, J. T.; Farha, O. K., Catalytic Zirconium/Hafnium-Based Metal–Organic Frameworks. *ACS Catal.* **2017,** *7*, 997-1014.

14. Peterson, G. W.; Destefano, M. R.; Garibay, S. J.; Ploskonka, A.; McEntee, M.; Hall, M.; Karwacki, C. J.; Hupp, J. T.; Farha, O. K., Optimizing Toxic Chemical Removal through Defect-Induced UiO-66-NH2 Metal–Organic Framework. *Chem. - Eur. J.* **2017,** *23*, 15913-15916.

15. Rouquerol, J.; Llewellyn, P.; Rouquerol, F., *Is the BET equation applicable to microporous adsorbents?* Elsevier: 2007; Vol. 160, p 49-56.

16. Lu, G.; Cui, C.; Zhang, W.; Liu, Y.; Huo, F., Synthesis and Self-Assembly of Monodispersed Metal-Organic Framework Microcrystals. *Chem. - Asian J.* **2013,** *8*, 69-72.

17. Zwolinski, K. M.; Nowak, P.; Chmielewski, M. J., Towards multifunctional MOFs - transforming a side reaction into a post-synthetic protection/deprotection method. *Chem. Commun.* **2015,** *51*, 10030-10033.

18. Daniel, K. B.; Major Jourden, J. L.; Negoescu, K. E.; Cohen, S. M., Activation of sulfonate ester based matrix metalloproteinase proinhibitors by hydrogen peroxide. *J. Biol. Inorg. Chem.* **2011,** *16*, 313-323.

19. Perez, C.; Li, J.; Parlati, F.; Rouffet, M.; Ma, Y.; Mackinnon, A. L.; Chou, T.-F.; Deshaies, R. J.; Cohen, S. M., Discovery of an Inhibitor of the Proteasome Subunit Rpn11. *J. Med. Chem* **2017,** *60*, 1343-1361.

20. Moon, S.-Y.; Wagner, G. W.; Mondloch, J. E.; Peterson, G. W.; DeCoste, J. B.; Hupp, J. T.; Farha, O. K., Effective, Facile, and Selective Hydrolysis of the Chemical Warfare Agent VX Using Zr6-Based Metal–Organic Frameworks. *Inorg. Chem.* **2015,** *54*, 10829-10833.

21. Mondloch, J. E.; Katz, M. J.; Isley, W. C.; Ghosh, P.; Liao, P. L.; Bury, W.; Wagner, G.; Hall, M. G.; DeCoste, J. B.; Peterson, G. W.; Snurr, R. Q.; Cramer, C. J.; Hupp, J. T.; Farha, O. K., Destruction of chemical warfare agents using metal-organic frameworks. *Nature Mater.* **2015,** *14*, 512-516.

22. Budd, P. M.; Ghanem, B. S.; Makhseed, S.; McKeown, N. B.; Msayib, K. J.; Tattershall, C. E., Polymers of intrinsic microporosity (PIMs): robust, solution-processable, organic nanoporous materials. *Chem. Commun.* **2004**, 230-231.

23. Fateeva, A.; Chater, P. A.; Ireland, C. P.; Tahir, A. A.; Khimyak, Y. Z.; Wiper, P. V.; Darwent, J. R.; Rosseinsky, M. J., A water-stable porphyrin-based metal-organic framework active for visible-light photocatalysis. *Angew. Chem., Int. Ed.* **2012,** *51*, 7440-4.

24. Reinsch, H.; van der Veen, M. A.; Gil, B.; Marszalek, B.; Verbiest, T.; de Vos, D.; Stock, N., Structures, Sorption Characteristics, and Nonlinear Optical Properties of a New Series of Highly Stable Aluminum MOFs. *Chem, Mater.* **2012,** *25*, 17-26.

25. Sindoro, M.; Jee, A. Y.; Granick, S., Shape-selected colloidal MOF crystals for aqueous use. *Chem. Commun.* **2013,** *49*, 9576-8.

26. Ahnfeldt, T.; Gunzelmann, D.; Loiseau, T.; Hirsemann, D.; Senker, J.; Férey, G.; Stock, N., Synthesis and Modification of a Functionalized 3D Open-Framework Structure with MIL-53 Topology. *Inorg. Chem.* **2009,** *48*, 3057-3064.

27. Sohail, M.; Yun, Y.-N.; Lee, E.; Kim, S. K.; Cho, K.; Kim, J.-N.; Kim, T. W.; Moon, J.-H.; Kim, H., Synthesis of Highly Crystalline NH2-MIL-125 (Ti) with S-Shaped Water Isotherms for Adsorption Heat Transformation. *Cryst. Growth Des.* **2017,** *17*, 1208-1213.

28. Férey, G.; Mellot-Draznieks, C.; Serre, C.; Millange, F.; Dutour, J.; Surblé, S.; Margiolaki, I., A Chromium Terephthalate-Based Solid with Unusually Large Pore Volumes and Surface Area. *Science* **2005,** *309*, 2040.

29. Serre, C.; Millange, F.; Thouvenot, C.; Noguès, M.; Marsolier, G.; Louër, D.; Férey, G., Very Large Breathing Effect in the First Nanoporous Chromium(III)-Based Solids: MIL-53 or CrIII(OH)·{O2C–C6H4–CO2}·{HO2C–C6H4–CO2H}x·H2Oy. *J. Am. Chem. Soc.* **2002,** *124*, 13519-13526.

30. Gordon, J.; Kazemian, H.; Rohani, S., Rapid and efficient crystallization of MIL-53(Fe) by ultrasound and microwave irradiation. *Microporous Mesoporous Mater.* **2012,** *162*, 36-43.

31. Horcajada, P.; Salles, F.; Wuttke, S.; Devic, T.; Heurtaux, D.; Maurin, G.; Vimont, A.; Daturi, M.; David, O.; Magnier, E.; Stock, N.; Filinchuk, Y.; Popov, D.; Riekel, C.; Férey, G.; Serre, C., How Linker's Modification Controls Swelling Properties of Highly Flexible Iron(III) Dicarboxylates MIL-88. *J. Am. Chem. Soc.* **2011,** *133*, 17839-17847.

32. Zhang, F.; Shi, J.; Jin, Y.; Fu, Y.; Zhong, Y.; Zhu, W., Facile synthesis of MIL-100(Fe) under HF-free conditions and its application in the acetalization of aldehydes with diols. *Chem. Eng. J.* **2015,** *259*, 183-190.

33. Venna, S. R.; Jasinski, J. B.; Carreon, M. A., Structural Evolution of Zeolitic Imidazolate Framework-8. *J. Am. Chem. Soc.* **2010,** *132*, 18030-18033.

34. Ayyappan, P.; Evans, O. R.; Lin, W., Three-Dimensional Open Frameworks Based on Cobalt(II) and Nickel(II) m-Pyridinecarboxylates. *Inorg. Chem.* **2001,** *40*, 4627-4632.

35. Caskey, S. R.; Matzger, A. J., Selective Metal Substitution for the Preparation of Heterobimetallic Microporous Coordination Polymers. *Inorg. Chem.* **2008,** *47*, 7942-7944.

36. Carson, C. G.; Hardcastle, K.; Schwartz, J.; Liu, X.; Hoffmann, C.; Gerhardt, R. A.; Tannenbaum, R., Synthesis and Structure Characterization of Copper Terephthalate Metal–Organic Frameworks. *Eur. J. Inorg. Chem.* **2009,** *2009*, 2338-2343.

37. Han, S.; Huang, Y.; Watanabe, T.; Dai, Y.; Walton, K. S.; Nair, S.; Sholl, D. S.; Meredith, J. C., High-Throughput Screening of Metal–Organic Frameworks for CO2 Separation. *ACS Comb. Sci.* **2012,** *14*, 263-267.

38. Jasuja, H.; Walton, K. S., Effect of catenation and basicity of pillared ligands on the water stability of MOFs. *Dalton Trans.* **2013,** *42*, 15421-15426.

39. Gustafsson, M.; Zou, X., Crystal formation and size control of zeolitic imidazolate frameworks with mixed imidazolate linkers. *J. Porous Mater.* **2013,** *20*, 55-63.

40. Fei, H. H.; Cahill, J. F.; Prather, K. A.; Cohen, S. M., Tandem Postsynthetic Metal Ion and Ligand Exchange in Zeolitic Imidazolate Frameworks. *Inorg. Chem.* **2013,** *52*, 4011-4016.

41. Yuan, S.; Lu, W.; Chen, Y.-P.; Zhang, Q.; Liu, T.-F.; Feng, D.; Wang, X.; Qin, J.; Zhou, H.-C., Sequential Linker Installation: Precise Placement of Functional Groups in Multivariate Metal–Organic Frameworks. *J. Am. Chem. Soc.* **2015,** *137*, 3177-3180.

42. Furukawa, H.; Gándara, F.; Zhang, Y.-B.; Jiang, J.; Queen, W. L.; Hudson, M. R.; Yaghi, O. M., Water Adsorption in Porous Metal–Organic Frameworks and Related Materials. *J. Am. Chem. Soc.* **2014,** *136*, 4369-4381.

43. Katz, M. J.; Brown, Z. J.; Colon, Y. J.; Siu, P. W.; Scheidt, K. A.; Snurr, R. Q.; Hupp, J. T.; Farha, O. K., A facile synthesis of UiO-66, UiO-67 and their derivatives. *Chem. Commun.* **2013,** *49*, 9449-9451.

44. Biswas, S.; Van Der Voort, P., A General Strategy for the Synthesis of Functionalised UiO-66 Frameworks: Characterisation, Stability and CO2 Adsorption Properties. *Eur. J. Inorg. Chem.* **2013,** *2013*, 2154-2160.

45. Bon, V.; Senkovska, I.; Baburin, I. A.; Kaskel, S., Zr- and Hf-Based Metal–Organic Frameworks: Tracking Down the Polymorphism. *Cryst. Growth Des.* **2013,** *13*, 1231-1237.

46. Ploskonka, A. M.; Marzen, S. E.; DeCoste, J. B., Facile Synthesis and Direct Activation of Zirconium Based Metal–Organic Frameworks from Acetone. *Ind. Eng. Chem. Res.* **2017,** *56*, 1478-1484.

47. Feng, D.; Gu, Z. Y.; Li, J. R.; Jiang, H. L.; Wei, Z.; Zhou, H. C., Zirconium-metalloporphyrin PCN-222: mesoporous metal-organic frameworks with ultrahigh stability as biomimetic catalysts. *Angew. Chem. Int. Ed.* **2012,** *51*, 10307-10.

48. Lammert, M.; Wharmby, M. T.; Smolders, S.; Bueken, B.; Lieb, A.; Lomachenko, K. A.; Vos, D. D.; Stock, N., Cerium-based metal organic frameworks with UiO-66 architecture: synthesis, properties and redox catalytic activity. *Chem. Commun.* **2015,** *51*, 12578-12581.

# Chapter 3: Applications of High-Throughput Screening for Dimethyl-4-nitrophenyl Phosphate Degradation

## 3.1 Introduction

The possibility of screening large libraries of materials for the breakdown of the nerve agent simulant dimethyl-4-nitrophenyl phosphate (DMNP) was introduced and validated in Chapter 2. This work proved not only that HTS is an efficient way to analyze many materials but illustrated the importance of testing conditions and preparation methods for materials on the comparative rates for a given set of solid-state catalysts. As proposed in Chapter 2, the technique of HTS creates opportunity for investigation of materials that would otherwise be discarded or overlooked with traditional time-intensive methods. Chapter 3 presents the application of the HTS developed in Chapter 2 onto a larger set of MOF materials as well as MOF-polymer composites.

Chapter 2 explored a variety of MOFs and confirmed that Zr-MOFs are the top performers even in a larger set of MOFs with various metal centers. To further the concept of increasing chemical space within the constraints of Zr-MOFs, the MOF UiO-66(Zr) was chosen to further study. UiO-66(Zr) is easily synthesized with modified organic ligands[1] and provides a straightforward opportunity to generate a large number of derivatives. As highlighted in Section 1.6, simple linear combinations of ligands can generate a large library of MOFs to screen. Based on success of amino-functionalized ligands in previous studies,[2, 3] a library using five modified terephthalic acid ($H_2$bdc-R) ligands were synthesized in linear combinations to produce 31 new MOFs. Only a high-throughput analysis technique would allow for practical testing of this relatively large set of new MOFs. Section 3.2 reveals that linear combinations of ligands cannot predict the top candidates.

Section 3.3 examines the activity of a sublibrary of MOFs to identify key characteristics for high activity. A series of halogenated terephthalic acid ligands ($H_2$bdc-X) was used to make UiO-66(Zr) derivatives and the MOF with iodine-functionalized ligand proved to have ~4-fold increase in hydrolysis rate. The origin of this effect was attributed to the great increase in polarizability of iodine over the other halogens and its ability to participate in halogen bonding.[4] The effectiveness of screening allows for this type of feature to be isolated and studied quickly.

Polymer-MOF composites have been actively pursued for protection from CWAs as outlined in Section 1.5. Sections 3.4 and 3.5 discuss two MOF-polymer composites that were evaluated by a modified HTS method to demonstrate the usefulness of the technique. Section 3.4 outlines the synthesis and testing of a UiO-66(Zr)-polyamine composite that was synthesized using an interfacial polymerization technique. The simple mixture of an acid chloride and an amine yields a polyamine (like Nylon-6,6) at the interface of an aqueous and organic solvent mixture which can be pulled into a fiber. Although the formation of amide bonds with acid chlorides or anhydrides and UiO-66(Zr)-$NH_2$ had been widely studied,[5, 6] the use of this amide linkage for polyamide formation had not been achieved. The formation of this composite demonstrates the advantage of covalent linkage to the MOF and also provides a new form factor for a functional composite that can hydrolyze nerve agent simulants.

In Section 3.5, the use of a HTS method allowed for the evaluation of simple MOF-polymer mixtures. Solution-cast polymers with MOF filler, termed mixed-matrix membranes (MMMs), have been demonstrated with a number of polymers including

poly(vinylidene fluoride) (PVDF),[7] styrene-butadiene (SBS) copolymers,[8] and poly(ethylene oxide) (PEO).[9, 10] These polymers each have their own mechanical properties and access to the MOF functionality based polymer interaction with MOF. To achieve improved mechanical properties in a low cost, flexible polymer, poly(ethylene-co-vinyl acetate) (EVA) was selected for investigation. Despite a lack of $N_2$ accessible surface area for some of these MMMs under the cryogenic testing conditions, a number of other tests showed the activity of the MOF was retained in MMM composite. Included in this was the application of these composites for nerve agent simulant degradation, where they were successful in degradation at 70 and 80 wt%, albeit lower than PVDF composites at 70 wt%. These results highlight the need to investigate the polymer selection in functional composites and the utility of a HTS method to support the number of samples that can be generated quickly using simple mixtures of MOFs and polymers.

## 3.2 Multivariate MOFs for the Degradation of Nerve Agent Simulant

Previous work using MOFs with combinations of functionalized ligands (termed multivariate (MTV) MOFs) resulted in unexpected improvement in gas selectivity.[11] Inspired by this strategy a library of 31 MOFs was synthesized (5 single-ligand and 26 mixed-ligand) by simple equimolar combinations of 1,4-benzendicarboxylic acid ($H_2$bdc) and four mono-functional 1,4-benzendicarboxylic acids ($H_2$bdc-R) (Figure 3.1). MOFs were named according to which ligands they are composed of; for example, MTV-UiO-66(Zr)-AB contains a 1:1 mixture of $H_2$bdc and $H_2$bdc-$NH_2$ ligands whereas MTV-UiO-66(Zr)-BCE contains a 1:1:1 mixture of $H_2$bdc-$NH_2$, $H_2$bdc-OH, and $H_2$bdc-Br. The

crystallinity and composition of these materials were confirmed by powder X-ray diffraction (PXRD) and $^{1}$H-NMR of digested material.[12]

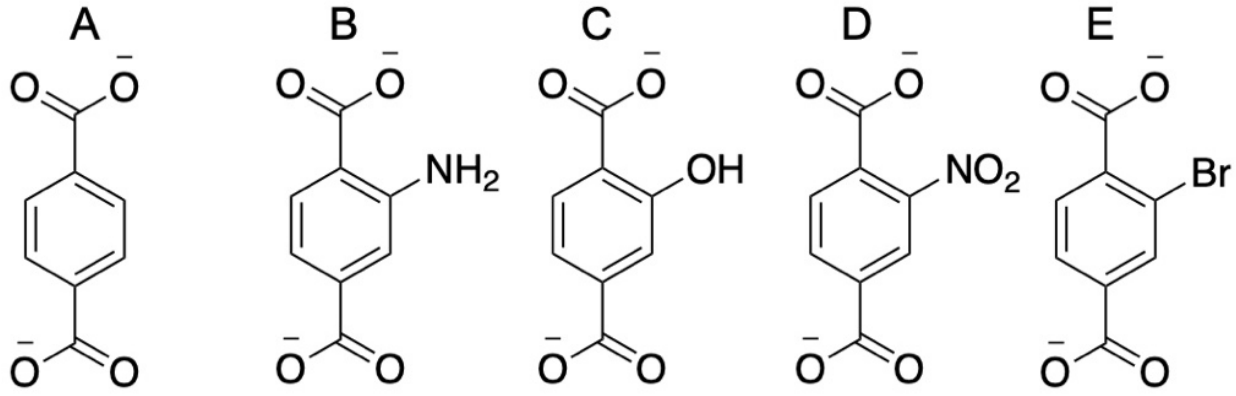


**Figure 3.1.** Five ligands used for synthesis of 31 MTV MOFs with arbitrary A-E labeling shown.

This new library of 31 materials, referred to as MTV-UiO-66(Zr), was tested for the hydrolysis of nerve agent simulant DMNP using the HTS method described in Chapter 2. These materials were screened at pH = 8.0 to better simulate the conditions of field applications and values represent an average of seven samples for improved statistics. In initial studies there was clear increase in hydrolysis rate from MTV-UiO-66(Zr) MOFs and the data analysis protocol was altered to account for the newer, faster catalysts.

Faster hydrolysis rates were first identified in a separate set of 11 mixed ligand $H_2$bdc and $H_2$bdc-$NH_2$ MOFs with in 10 mol% increments from 0% to 100% $H_2$bdc-$NH_2$. To accurately compare initial rates based on pseudo-zero order kinetics, the time regime was investigated. In this example, there is a significant difference (~2-fold) in calculated rate when the time interval for linear rate calculation is 1000-2300 sec vs. 100-700 sec

for materials such as UiO-66(Zr)-$NH_2$(70%) (Figure 3.2). The more accurate rate was taken from earlier time points (100-700 sec) when substrate concentration is much greater than catalyst concentration. At later points the reaction involves higher-order kinetics, as seen by the beginning of a plateau in the UiO-66(Zr)-$NH_2$(70%) absorbance curve in Figure 3.2. For the remainder of studies kinetic rates were calculated with linear slopes from the first 700 sec as it gives more accurate kinetics for both slow and fast catalysts.

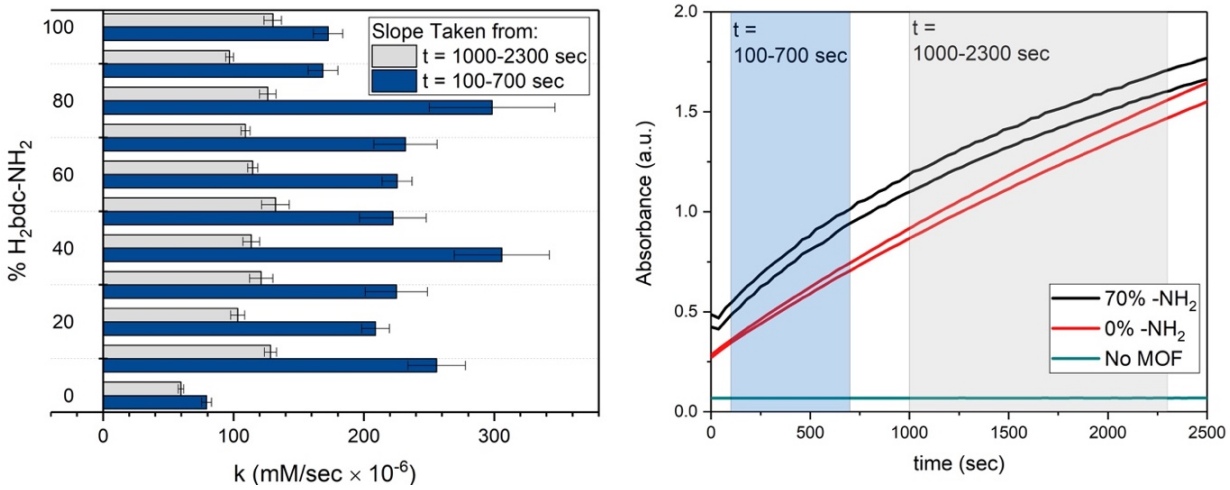


**Figure 3.2.** *Left:* Hydrolysis rates calculated from different time sections of kinetic trace for a series of mixed ligand UiO-66(Zr)-H/$NH_2$ MOFs. *Right:* Example raw data showing the regions selected for calculation of initial rates, this accounts for induction period observed in UiO-66(Zr)-$NH_2$(70%).

Screening of the complete library of 31 MTV-UiO-66(Zr) MOFs showed significantly higher activity for mixed ligand MOFs than MOFs with single ligands. No clear trend was observed based on functional group electron donating or withdrawing ability (Figure 3.3). For example, MTV-UiO-66(Zr)-B MOF and the MTV-UiO-66(Zr)-E

MOF display about 3-fold slower activity than when these ligands are both incorporated into the MTV-UiO-66(Zr)-BE. Interestingly, seven of the top eight MTV-UiO-66(Zr) MOFs contain the $NH_2$-$bdc^{2-}$ linker while the single-ligand UiO-66(Zr)-$NH_2$ (MTV-UiO-66(Zr)-B) is one of the poorest performing MOFs. This result suggests there is a synergistic ligand effect occurring when multiple functional groups are incorporated into a single MOF. MOF particle size was analyzed via scanning electron microscopy (SEM) and the results indicate that activity is not correlated with particle size.[12] The surface area of the MOFs was analyzed via $N_2$ gas sorption and also failed to show a correlation with the DMNP catalysis data; hence enhanced catalysis is not a result of higher BET surface area ($R^2$ = 0.092, Figure S3.1, Table S3.1).[12]

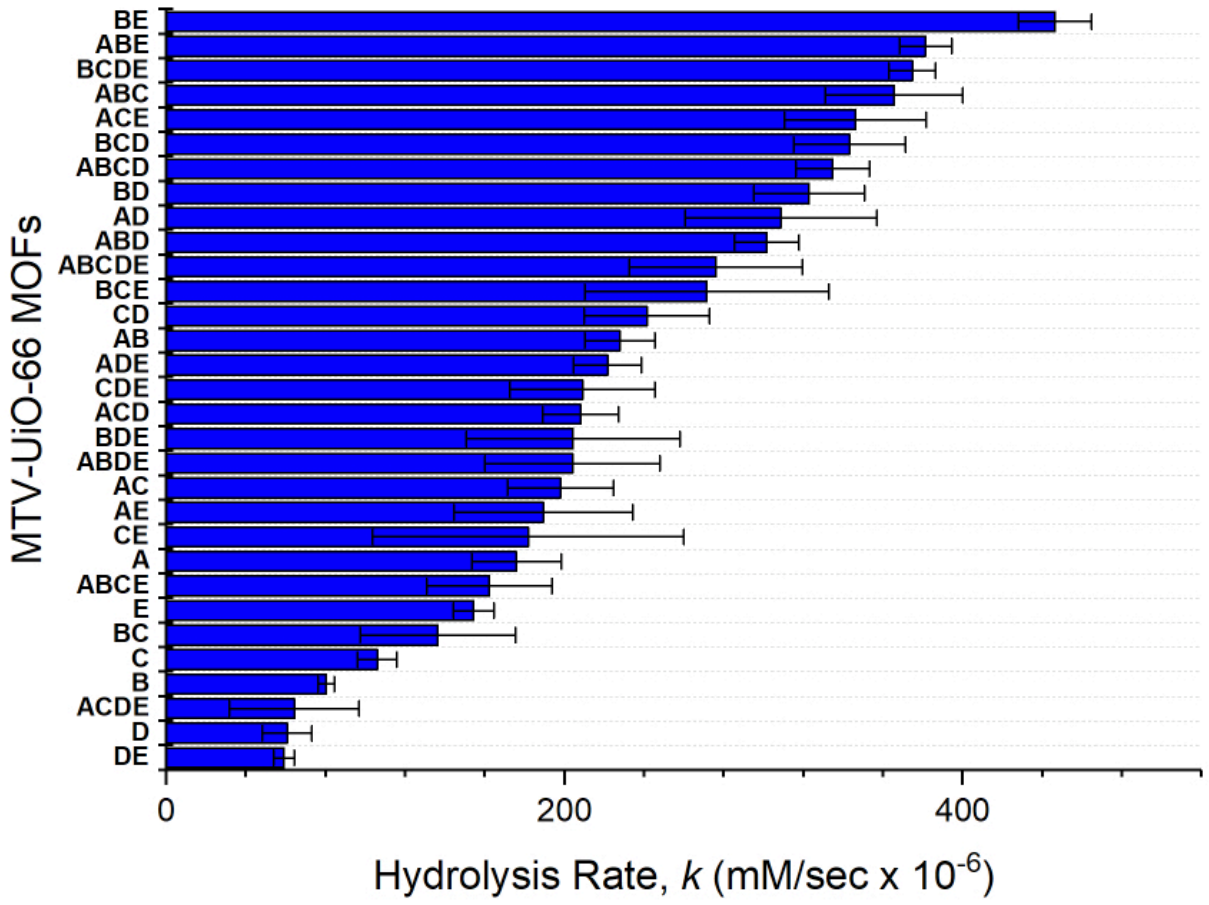


**Figure 3.3**. DMNP Hydrolysis rate (in mM/ sec × $10^{-6}$) of MTV-UiO-66(Zr) MOFs normalized by molecular weight.

Further analysis of MTV-MOF data was conducted to determine if combinations of ligands in MTV-MOFs followed a pattern or were random. It is reasonable to hypothesize that the single-ligand UiO-66(Zr) results may inform the MTV-MOF hydrolysis rates. However, the lack of pattern is made clear when the library is organized by ligand number in Figure 3.4. The relatively low rates of the single-ligand MOFs clearly show that these MOFs could not be used to predict the rates of MTV-MOFs with more than one ligand. However, it is not clear from Figure 3.4, whether rates of MTV-MOFs with two ligands would be good predictors of activity for MTV-MOFs with 3, 4, and 5 ligands. For example,

it is difficult to determine if the rate of MTV-UiO-66(Zr)-AB, MTV-UiO-66-BE, and MTV-UiO-66(Zr)-AE help predict the rate of MTV-UiO-66(Zr)-ABE from visual inspection. However, the average rate of the two-ligand MTV-MOFs is smaller (288 ± 17 mM/sec $\times$ $10^{-6}$) than MTV-UiO-66(Zr)-ABE (381 ± 13 mM/sec $\times$ $10^{-6}$). Similar analysis was done for all MTV-MOFs with 3, 4, and 5 ligands and plotted Figure S3.2. Most of the MOFs tested do not fall on the line, showing that interaction of two ligands in the UiO-66(Zr) is not a linear effect that can explain the differences in rates of MTV-MOFs.

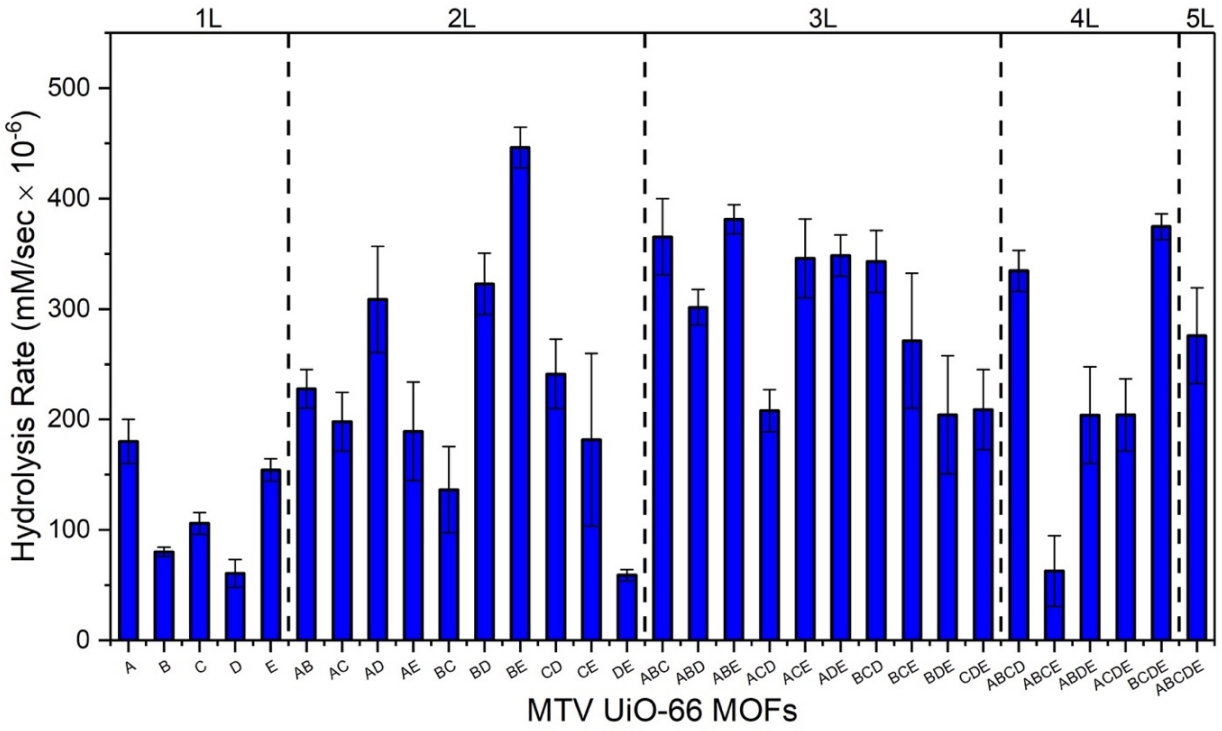


**Figure 3.4.** Library of MTV UiO-66(Zr) MOFs grouped by number of ligands that make up the mixture.

This sublibrary of MOFs illustrates that MOF systems are very complex systems with many variables that are difficult to predict. In this case, use of HTS enabled the discovery of new MTV UiO-66(Zr) MOFs that exceeded previous best materials under these conditions. This represents one of the few combinatorial experimental studies with MOFs and is enabled by the speed of these experiments. To screen all 31 materials seven times each on three 96 well plates would take 1.5 h, versus the 93 h if the materials were screened in triplicate serially for 1 h each. Practically that means materials would be left out and best materials would have been easily missed. In the future it will be important to continue to form combinatorial libraries of materials to screen as much of the chemical space as possible without making assumptions about material performance.

## 3.3 Halogen Bonding Promoted Hydrolysis of Nerve Agent Simulant

The investigation of mixed ligand MOFs showing unexpected improvement in catalytic hydrolysis rates led to attempts at systematic understanding of ligand substitution on reaction rate. Two series of MOFs with mono-functionalized ligands were analyzed, with different Hammet parameters and halogen ligands. As in Section 3.2, the series of differing Hammet parameters did not show any strong correlation (Figure 3.5). However, the halogen series of -F, -Cl, -Br, and -I revealed an interesting discovery. The UiO-66(Zr)-I greatly outperformed the other three halogenated frameworks for the hydrolysis of DMNP at pH = 8 (Figure 3.6, Table S3.2). Even when the amount of I-bdc$^{2-}$ was reduced by half in the MOF, the activity was almost double the unfunctionalized UiO-66(Zr), other halogen UiO-66(Zr) MOFs, and even NU-1000(Zr), one of the best MOFs at pH = 10.

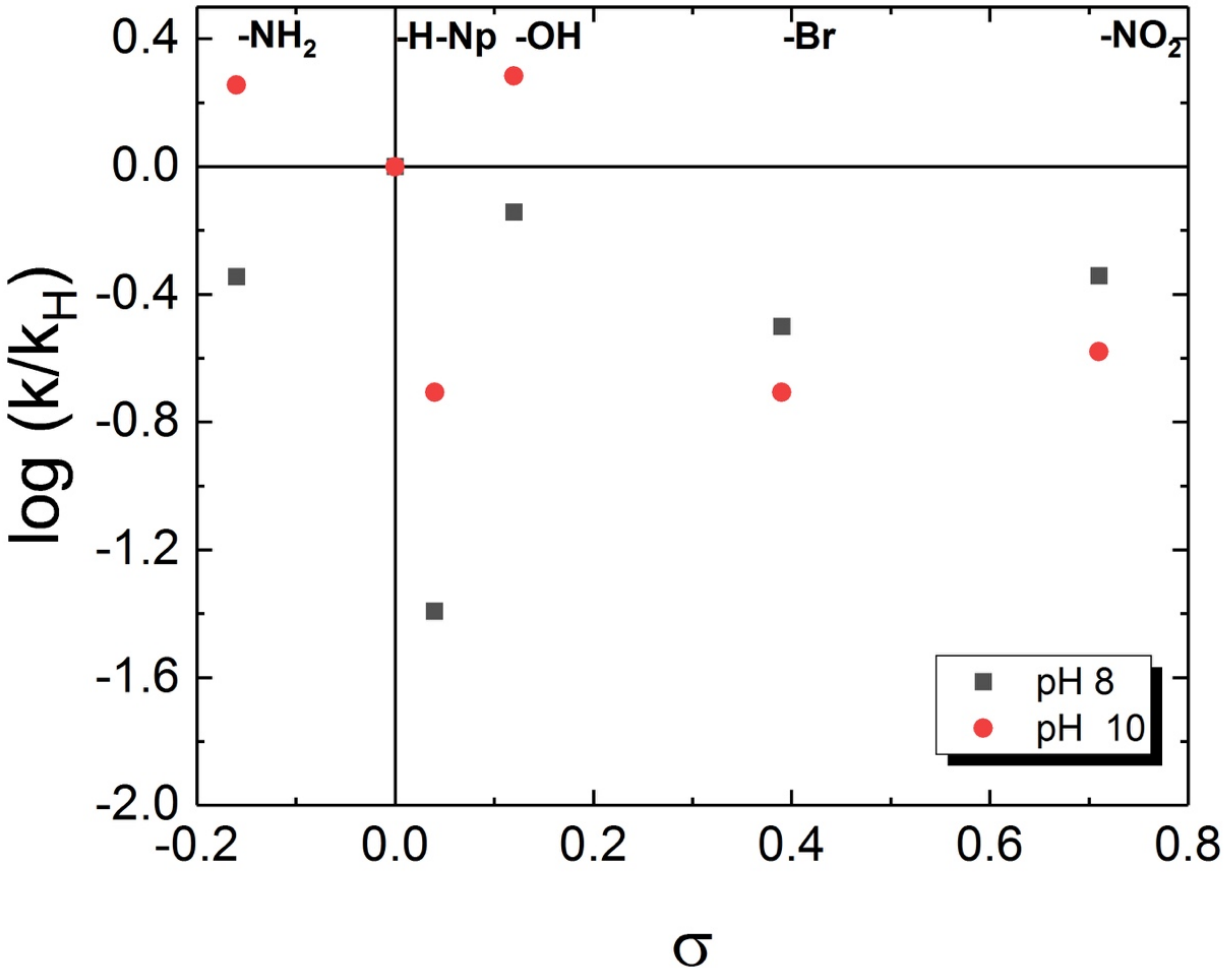


**Figure 3.5.** DMNP hydrolysis rate normalized to UiO-66(Zr) ($k_H$) compared to Hammett parameter ($\sigma$) for functionalized UiO-66(Zr) (-$NH_2$, -Np, -Br, and -$NO_2$) at both pH = 8 and 10, showing no correlation.

This increase in activity that did not follow electronegativity or atomic size trends so other factors like crystallinity, surface area, and defect concentration were investigated. Based on PXRD there was no quantifiable trend between crystallinity and activity, however it should be noted that the ratio of first two reflections is lowest for UiO-66(Zr)-I, typically an indication of low crystallinity.[13] Gravimetric $N_2$ accessible surface also showed no trend in activity and again UiO-66(Zr)-I had the lowest surface area both

by weight and molar, which would typically lead to a less accessible reactive sites.[13] Comparing the particle size using SEM images the five MOFs in the series are all in the same general size regime (50-200 nm).[13] While UiO-66(Zr)-I is slightly smaller in size than the rest and MOF particles have been shown to increase catalytic rates with decreasing size,[14] this small difference in average particle size cannot account for the drastic increase in hydrolysis rate.

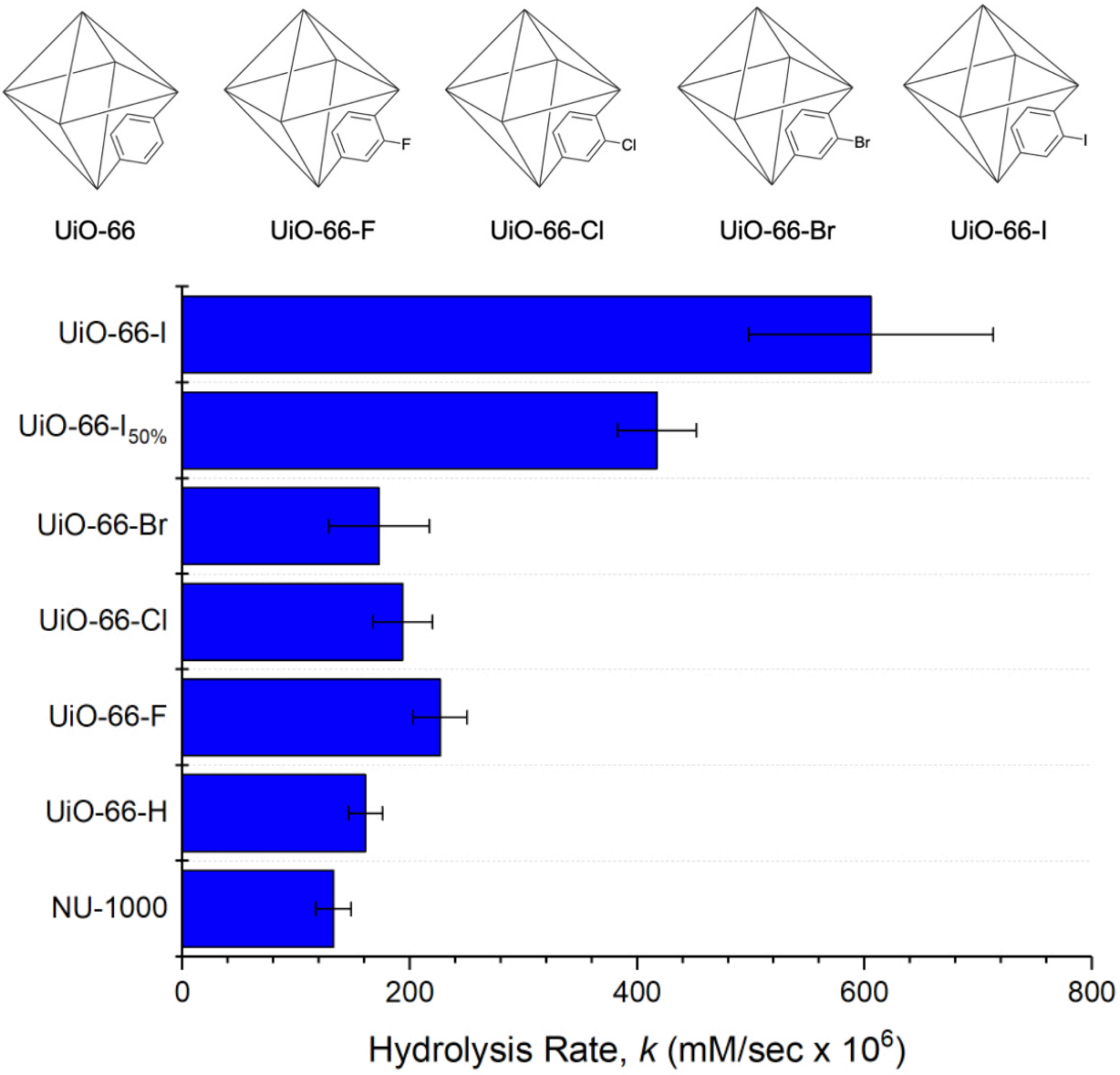


**Figure 3.6.** Representations of UiO-66(Zr) and halogenated UiO-66(Zr) MOFs (*top*) and hydrolysis rates for this series compared to non-halogenated UiO-66(Zr) and NU-1000(Zr) at pH = 8.0 (*bottom*).

The sharp increase in hydrolysis was attributed to halogen bonding between the DMNP and the iodine on the ligand of the MOF. Using a density functional theory (DFT), our collaborators provided us a model of the cluster with and without functional ligand and

found the transition state of the iodine UiO-66(Zr) had a lower barrier by ~9 kcal/mol.[13] This stabilization when the iodine was on substituted adjacent to the active site compared to iodine substituted away from the active site that had similar barrier as non-functionalized UiO-66(Zr). In the transition state structure, the O-I distance between the -OMe group of DMNP and bdc-I of the MOFs was less than the sum of van der Waals radii indicating a halogen bonding interaction between the two groups.[13] This stabilization accounts for the decrease in activation energy and is consistent with other studies showing a significant increase in halogen bonding promoted catalysis with iodine over other halogens.[4, 15]

Despite the lack of quantifiable relationship between ligand functional group and hydrolysis activity across a series, the ability to test all these materials led to the discovery of an outlier in UiO-66(Zr)-I. This material represents the MOF with the highest rate tested in the HTS conditions set forth in Chapter 2 which includes over 100 materials, including 14 single ligands UiO-66(Zr) MOFs and the 26 mixed ligand UiO-66(Zr) MOFs in Section 3.2. This shows that HTS can identify these hits quickly allowing for additional time to analyze the factors that led to hit compounds. Until greater understanding and control over parameters that directly affect MOFs exists, HTS will be useful in application focused research.

## 3.4 MOF-polyamide Composite for Nerve Agent Simulant Hydrolysis

After success with using HTS to identify MOFs for DMNP hydrolysis with HTS, polymer-MOF composites that could also catalyze DMNP hydrolysis were targeted. The

application for these composites being PPE for toxic chemicals, the polyamide polymer (such as Nylon-6,6) was selected as it is ubiquitous in clothing. To incorporate MOF into the polymer material, a postsynthetic polymerization (PSP) technique was employed with UiO-66(Zr)-$NH_2$. The amine group on the MOF ligand was used a binding site for growth of the polymer chain during the synthesis of the polyamide polymer. This technique of PSP works by a series of PSM reactions that results in a polymer that includes the MOF crystal and therefore forms a hybrid that is covalently linked.[16]

To form Nylon-6,6 (PA-66), a simple growth of polyamide chains occurs spontaneously at the interface of aqueous solution containing diamine and organic solution containing diacid chloride, which can be then pulled into a fiber, exposing interface to continue growth of the polymer. By adding UiO-66(Zr)-$NH_2$ to the organic layer, the amine groups are reacted with the acid chloride and can participate in growth of the polymer when reacted with diamine at the interface. This was successfully demonstrated with mixture of adipoyl chloride and UiO-66(Zr)-$NH_2$ in an ethyl acetate solution layer on an aqueous solution containing hexamethylenediamine that was pulled into a polyamide (Figure 3.7). The resulting polyamide fibers have the structure of PA-66 with MOF covalent attached to the polymer chain, termed PA-66-UiO-66(Zr)-$NH_2$.

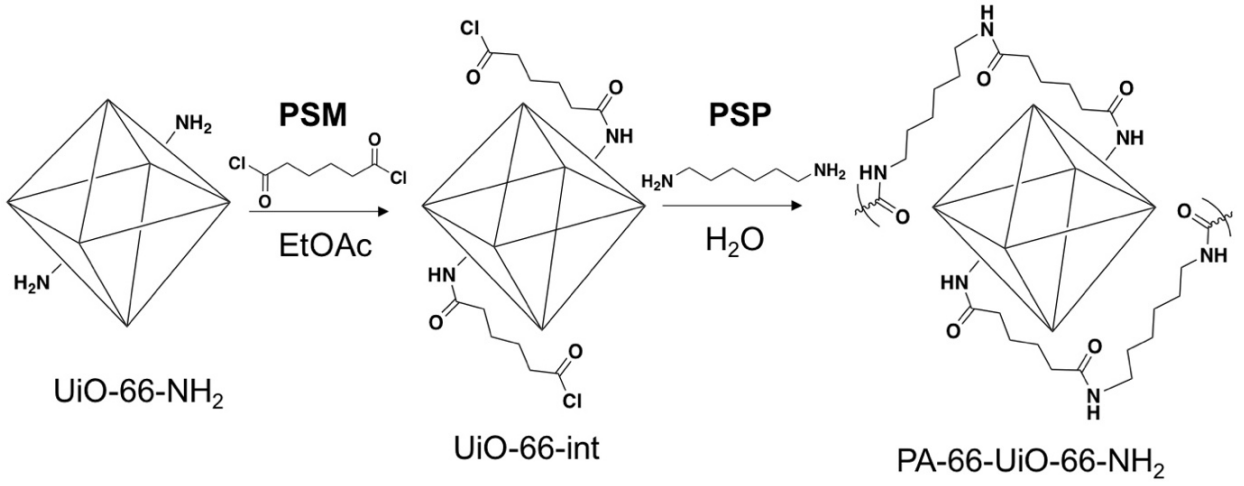


**Figure 3.7.** Scheme showing postsynthetic modification of UiO-66(Zr)-$NH_2$ with acid chloride then the polymerization off the surface of the MOF with diamine.

To indirectly study the covalency of the UiO-66(Zr)-$NH_2$ in the polymer fibers, a set of three control MOFs that would yield non-covalent composites were synthesized for comparison. Figure 3.8 shows this set consisting of unfunctionalized UiO-66(Zr) MOF; UiO-66(Zr)-$NH_2$ MOF treated with hexanoyl chloride resulting in an alkyl amide (UiO-66(Zr)-AM6); and UiO-66(Zr)-$NH_2$ treated with adipoyl chloride resulting in an acid-terminated amide (UiO-66(Zr)-AM6COOH). The control UiO-66(Zr)-AM6COOH best mimics the covalent fibers but was designed with key processing difference: the MOF is subjected to adipoyl chloride, isolated, quenched with methanol, and washed before exposure to PSP conditions. This differs from UiO-66(Zr)-$NH_2$ that is used for covalent composite, where PSM then PSP are carried out in tandem without purification step. In all cases the polymers pulled from the control MOFs resulted in fibers that were less robust and only about 1 ft compared to 3 ft in covalent PA-66-UiO-66(Zr)-$NH_2$ composite.

Without reactive groups to participate in the growing polymer chain, the control MOFs are likely disturbing the interface of the polymerization.[17]

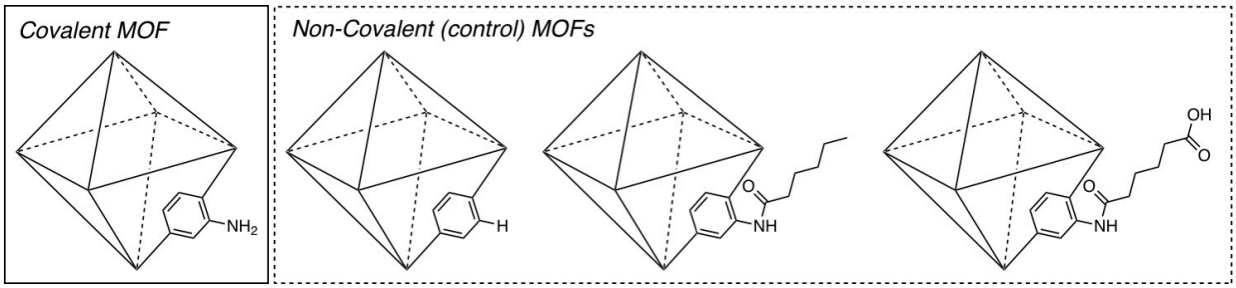


**Figure 3.8.** Representations of MOFs used for PSP composites UiO-66(Zr)-$NH_2$ (*left*) and control tests, UiO-66(Zr), UiO-66(Zr)-AM6, and UiO-66(Zr)-AM6COOH (*right*).

The integration of MOFs into a PA-66 fiber makes them much more suited to application into PPE, but their efficacy as CWA mitigation catalysts must be tested. The PA-66-MOF hybrid materials were screened for catalytic activity against the nerve agent simulant DMNP (Figure 3.9, Figure S3.3). Using the HTS technique developed in Chapter 2, degradation of the DMNP simulant at pH = 8 was monitored for powders of UiO-66(Zr), UiO-66(Zr)-$NH_2$, UiO-66(Zr)-AM6, and UiO-66(Zr)-AM6COOH MOFs. In addition, using the larger wells of a 24-well plate, small segments of composite fibers were assayed for the degradation of DMNP. While these initial rates are not comparable to MOF powders, the fibers are normalized by MOF content and can be compared internally. As shown in Figure 3.9, UiO-66(Zr) and UiO-66(Zr)-AM6 powders are approximately three times more active than the UiO-66(Zr)-$NH_2$ and UiO-66(Zr)-AM6COOH MOFs, which is consistent with UiO-66(Zr) and UiO-66(Zr)-$NH_2$ rates from Chapter 2 and Section 3.2.

Incorporation of the various functionalized MOFs into PA-66 composites had a dramatic effect on the catalytic degradation of DMNP. The covalently attached hybrid material, PA-66-UiO-66(Zr)-$NH_2$, was nearly an order of magnitude more active than any of the non-covalent incorporated PA-66 composites. Further, composite materials were recycled and displayed no loss in catalytic activity toward DMNP degradation through four cycles (Figure S3.4). These results demonstrate that more MOF particles in the PA-66-UiO-66(Zr)-$NH_2$ composite are accessible to catalysis and active than in the nylon-entrapped materials (i.e., PA-66@UiO-66(Zr), PA-66@UiO-66(Zr)-AM6, and PA-66@UiO-66(Zr)-AM6COOH).

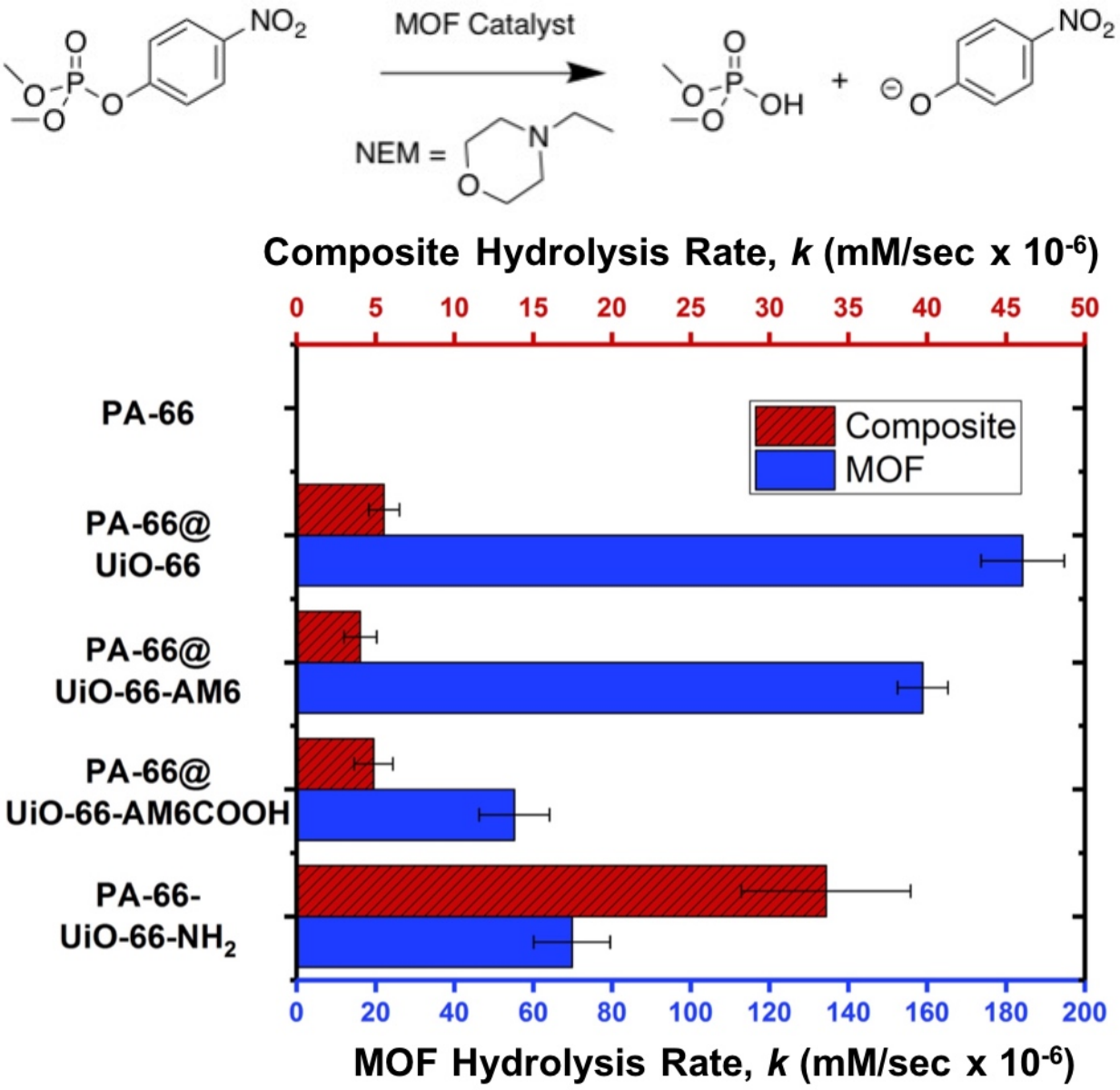


**Figure 3.9.** MOF-catalyzed hydrolysis of DMNP (*top*) and rates of catalytic degradation of DMNP by MOF-PA-66 composites (red, *bottom*) and the MOF the composite was constructed from (blue, *bottom*).

This study shows the covalent integration of MOFs into industrially relevant (e.g., Nylon) polymers can result in useful composites. The ability for these composites to break down nerve agent simulants provides a step in the right direction for the application of

these materials. The development of a rapid screening technique for the fibers allowed for the initial rate to be compared among a series of composites and perform recyclability tests all in triplicate.

## 3.5 MOF-Polymer Membranes for Nerve Agent Simulant Hydrolysis

While PSP MOF-polymer hybrids have the advantage of covalent tethers, there are advantages to physical mixtures of MOFs that can be solution cast into MMMs. For example, poly(ethylene-co-vinyl acetate) (EVA) is a commodity polymer with tunable ratios of monomers provides a low-cost and tunable alternative to both poly(vinylidene fluoride) (PVDF) and polyamides composites. These composites are formed by dissolving EVA in toluene, mixing with MOF (UiO-66(Zr) as a test case) dispersed in ethyl acetate, concentrating this mixture to a viscous ink, and casting the ink into a suitable membrane. Free-standing EVA-UiO-66(Zr) MMMs could be made in various loadings of MOF; 50, 70, and 80 wt% MMMs were chosen for further study. PXRD of formed composite clearly shows UiO-66(Zr)-based reflections and SEM shows that MOF is well mixed throughout the composite.[18]

Expanding upon the high-throughput screening (HTS) protocol developed in Chapter 2 and modified in Section 3.5, the 24-well plate was modified to test MMMs. Unlike powders and fibers examined previously, MMMs required development of a special technique to prevent films from migrating in the well of the multiwell plate and blocking the beam of the absorbance plate reader. A plastic holder was designed and 3D printed to contain a 12×8 mm membrane which could be set into a well (Figure 3.10, Figure S3.5).

This method gave reproducible absorbance curve without beam blocking suitable for this HTS method (Figure S3.6-S3.8).

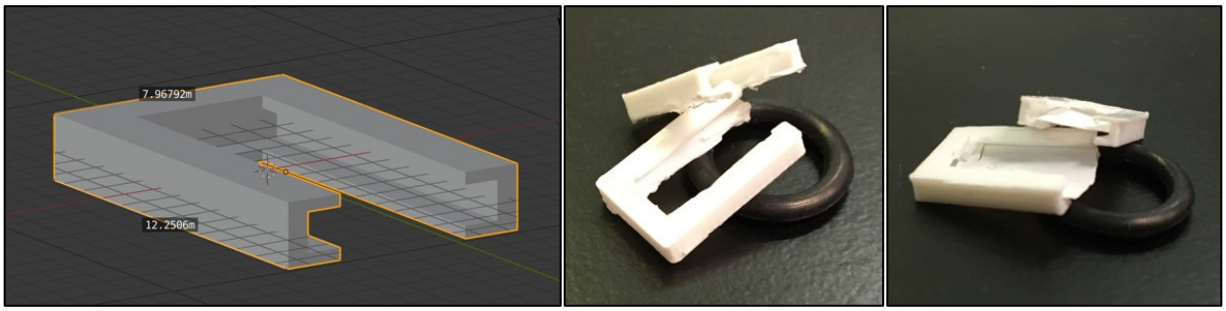


**Figure 3.10.** Render view of holder with dimensions in mm (*left*), empty 3D printed holders (*center*), and MMMs inserted into 3D printed holders for analysis of membranes by HTS (*right*).

Taking advantage of the ability to screen 24 MMMs simultaneously two additional polymer-MOF MMMs were fabricated to compare to EVA MMMs. First, A UiO-66(Zr)/PVDF MMM was chosen as PVDF MMMs had been previously explored for PPE applications,[19] but not for DMNP hydrolysis. PVDF MMMs were chosen because they had good transport properties despite being brittle at high MOF loadings.[7] In addition, a UiO-66(Zr)/PEO MMM was chosen as the polymer is hydrophilic compared to the hydrophobic PVDF and EVA polymers. PEO MMMs were also chosen because reported pore-filling[20] would likely limit the access to catalytic MOF in composite, lowering the hydrolysis rate.

The HTS was run on three replicates each of composite, with MMMs of the three different polymers: EVA-based MMMs at both 70 wt% UiO-66(Zr) and 80 wt% UiO-66(Zr), 80 wt% UiO-66(Zr)/PEO MMMs, and 70 wt% UiO-66(Zr)/PVDF MMMs (Figure 3.11,

Table S3.3). The experiments show that PVDF-based MMMs outperform EVA and PEO MMMs, but all of the MMMs are capable of decomposing the CWA simulant. The polymer infiltration of the PEO MMM resulted in lower hydrolysis rate than PVDF MMM as hypothesized, despite being higher loading than the PVDF MMM (80 wt% vs. 70 wt%, respectively). Without further study it is difficult to identify the source of the lower rate for UiO-66(Zr)/EVA MMMs relative to PEO and PVDF MMMs. Importantly, the polymer used to form the MMM clearly affects the overall reaction rate, and as such, is an important consideration for future design and implementation of these catalytic composites.

That stated, catalytic activity is only one factor for developing a composite for application in protective equipment. For example, when the MMMs tested were subjected to significant physical handling, the 70 wt% MOF/PVDF MMMs were prone to cracking due to brittleness. Similarly, the PEO MMMs swell significantly in aqueous solution and have delicate edges prone to tearing. In contrast, at 80 wt% UiO-66(Zr) in EVA, the MMMs retained excellent flexibility and maintained structural integrity through a series of qualitative handling tests such as rolling, folding, bending, and twisting. Both the reactivity and stability of these materials must be considered and optimized for future advancement of new materials for MOF-based protective equipment.

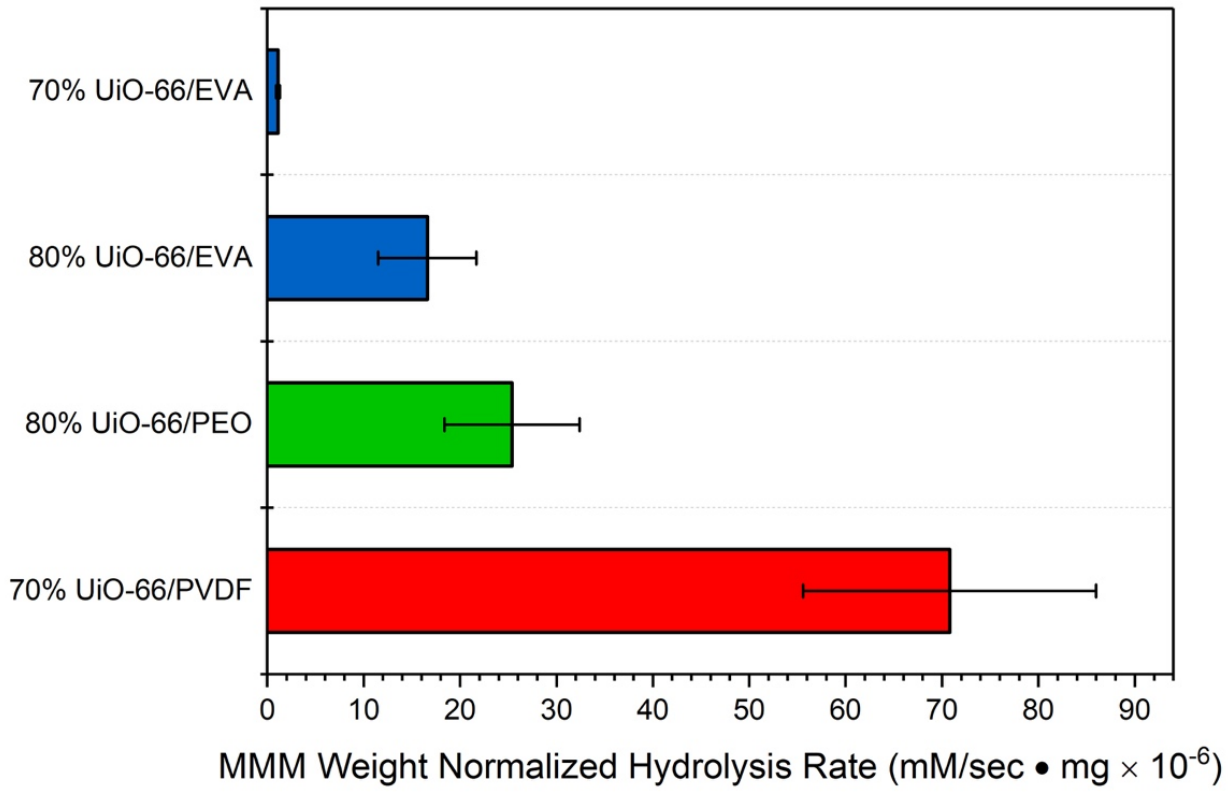


**Figure 3.11.** Hydrolysis rates of DMNP for MMMs with different polymers. Rates were averaged for three membranes and normalized for weight of the composite.

## 3.6 Conclusions

The use of HTS to evaluate MOFs and MOF-polymer composites is robust. Sections 3.2 and 3.3 build on the methodology developed in Chapter 2 to show the breadth and depth of study possible with the simple HTS. The evaluation of MOF-polymer fibers and MMMs in Sections 3.4 and 3.5 shows the potential to use HTS on MOF-polymer composites. In all cases the technique removes the barrier that previously existed for comparing large sample sets for DMNP hydrolysis. The time savings in catalytic rate evaluation allows for more time for synthesis of materials and investigation into fundamental principles that determine hydrolysis rates.

## 3.7 Appendix: Supporting Information

**General Materials and Methods.** Starting materials were purchased and used from commercially available suppliers (Sigma-Aldrich, Acros Organics, Matrix Scientific, and others) without further purification.

**$N_2$ Sorption Analysis.** Approximately 50 mg of sample were placed in a tare-weighed sample tube and degassed at 105 °C on a Micromeritics ASAP 2020 Adsorption Analyzer until the outgas rate was <5 mmHg (12-48 h). Post-degas, the sample tube was weighed, and then $N_2$ sorption isotherm data was collected at 77 K on a Micromeritics ASAP 2020 Adsorption Analyzer using a volumetric technique. BET areas were then determined from analysis of the Rouquerol[21] plots of the isotherm data, using 4-10 data points each.

## Experimental - Multivariate MOFs for the Degradation of Nerve Agent Simulant

**DMNP Hydrolysis Experiments.** DMNP hydrolysis was measured using a modified version of procedure from Chapter 2. All catalytic monitoring was carried out using a BioTek Synergy H4 plate reader using single wavelength absorbance mode. 20 and 40 mM of *N*-ethylmorpholine buffer was prepared from deionized water adjusted to pH = 8.0. A plot of absorbance of *p*-nitrophenol at varying concentrations was measured yielding a calibration curve with a slope of 3.48 Abs/mM. MOF samples were prepared by weighing 6 mg of MOF powder and diluting this powder in 10 mL of deionized water.

These solutions were rigorously sonicated and vortexed (>3× of each) and diluted in half with 40 mM buffer solution yielding 300 μg/mL MOF in 20 mM buffer solution. Assays with MOF powders were carried out in Olympus Plastics clear, flat-bottom 96-well plates. Each well was prepared with 100 μL total volume containing: 95 μL MOF suspension in buffer and 5 μL substrate (25 mM DMNP in $CH_3OH$; 1.25 mM total concentration; 0.125 μmol). Upon the addition of substrate using a multi-channel pipette, hydrolysis was monitored by the change in absorbance ($\lambda_{max}$ = 407 nm) over 15 min at 24 °C, with 3 sec shaking of the plate, every 10 sec. The absorbance was monitored from the 30 to 360 sec time period. Rates for MOF samples are an average of seven replicates. Hydrolysis rates were adjusted to account for the increased mass of the various species such that a direct comparison could be made across all materials in this study.

## Experimental - Halogen Bonding Promoted Hydrolysis of Nerve Agent Simulant

**Synthesis of UiO-66(Zr)-type MOFs**. Zirconium(IV) chloride (0.26 mmol; 61 mg) and terephthalic acid, 2-fluoroterephthalic acid, 2-chloroterephthalic acid, 2-bromoterephthalic acid, or 2-iodoterephthalic acid (0.26 mmol; 43 mg, 48 mg, 52 mg, 64 mg, or 76 mg, respectively) were dissolved in 15 mL DMF with 0.45 mL glacial acetic acid in a 20 mL vial with Teflon-lined cap. The vial was then placed in a 120 °C oven for 24 h. After cooling to ambient temperature, the particles were collected by centrifugation (fixed-angle rotor, 6000 rpm, 5 min), followed by washing with 3×10 mL DMF and 3×10 mL

$CH_3OH$. The particles were then soaked in $CH_3OH$ for 3 d with solvent changed daily, before being dried under vacuum at room temperature.

**DMNP Hydrolysis Experiments.** DMNP hydrolysis was measured using a modified version of procedure from Chapter 2. All catalytic monitoring was carried out using a BioTek Synergy H4 plate reader using single wavelength absorbance mode. 20 and 40 mM of *N*-ethylmorpholine buffer was prepared from deionized water adjusted to pH = 8.0. A plot of absorbance of *p*-nitrophenol at varying concentrations was measured yielding a calibration curve with a slope of 3.48 Abs/mM. MOF samples were prepared by weighing 6 mg of MOF powder and diluting this powder in 10 mL of deionized water. These solutions were rigorously sonicated and vortexed (>3× of each) and diluted in half with 40 mM buffer solution yielding 300 µg/mL MOF in 20 mM buffer solution. Assays with MOF powders were carried out in Olympus Plastics clear, flat-bottom 96-well plates. Each well was prepared with 100 µL total volume containing: 95 µL MOF suspension in buffer and 5 µL substrate (25 mM DMNP in $CH_3OH$; 1.25 mM total concentration; 0.125 µmol). Upon the addition of substrate using a multi-channel pipette, hydrolysis was monitored by the change in absorbance ($\lambda_{max}$ = 407 nm) over 15 min at 24 °C, with 3 sec shaking of the plate, every 10 sec. The absorbance was monitored from the 30 to 360 sec time period. Rates for MOF samples are an average of seven replicates. Hydrolysis rates were adjusted to account for the increased mass of the various species such that a direct comparison could be made across all materials in this study. Rates were calculated to account for the substantial difference in moles of MOF catalyst between samples (due to the increased mass of the halogenated MOFs) such that a direct comparison could be

made across all materials in this study. For example, UiO-66(Zr) has a molecular mass of 1628 g/mol, whereas UiO-66(Zr)-I has a molecular mass of 2383 g/mol. The difference in number of moles per sample well was account for as shown in Table S3.2.

## Experimental - MOF-polyamide Composite Capable of Nerve Agent Simulant Hydrolysis

**PA-66 MOF Fabrication.** A series of MOF-PA composites were prepared by this method and the materials were characterized to assess the integrity of the MOF component after fabrication. In a typical preparation, a quantity of UiO-66(Zr)-$NH_2$ (0.27 mmol, 80 mg) was dispersed in 20 mL ethyl acetate with ultrasonication for 20 min. Adipoyl chloride (3.4 mmol, 0.63 g, 0.50 mL) was then added to this dispersion and further sonicated for 10 min (time was varied for specific studies). Upon addition of the adipoyl chloride, a reaction is evident by a color change of the MOF particles to a paler shade of yellow. A series of samples were prepared containing UiO-66(Zr) and UiO-66(Zr)-$NH_2$ quantities ranging from 5 mg to 100 mg of MOF.

Separately, a solution of HMDA (3.45 mmol, 0.400 g, 0.45 mL) in 20 mL $H_2O$ was prepared and layered into a 100-mL beaker as the bottom layer. The ethyl acetate dispersion was then carefully layered on top of the aqueous layer. Polymerization occurred at the interface of the two layers and the PA-MOF product was slowly pulled from the interface, forming a continuous fiber. The product was removed until fiber formation became discontinuous, indicated a depletion of the monomer feedstocks. The

product was washed with water and dried at 70 °C overnight, then dried under vacuum at room temperature for 24 h.

**DMNP Hydrolysis Experiments.** DMNP hydrolysis was measured using a modified version of procedure from Chapter 2. All catalytic monitoring was carried out using a BioTek Synergy H4 plate reader using single wavelength absorbance mode. 20 and 40 mM of *N*-ethylmorpholine buffer was prepared from deionized water adjusted to pH = 8.0. A plot of absorbance of *p*-nitrophenol at varying concentrations was measured yielding a calibration curve with a slope of 3.48 Abs/mM. MOF samples were prepared by weighing 6 mg of MOF powder and diluting this powder in 10 mL of deionized water. These solutions were rigorously sonicated and vortexed (>3× of each) and diluted in half with 40 mM buffer solution yielding 300 µg/mL MOF in 20 mM buffer solution. Assays with MOF powders were carried out in Olympus Plastics clear, flat-bottom 96-well plates. Each well was prepared with 100 µL total volume containing: 95 µL MOF suspension in buffer and 5 µL substrate (25 mM DMNP in $CH_3OH$; 1.25 mM total concentration; 0.125 µmol). Upon the addition of substrate using a multi-channel pipette, hydrolysis was monitored by the change in absorbance ($\lambda_{max}$ = 407 nm) over 15 min at 24 °C, with 3 sec shaking of the plate, every 10 sec. Reported activities for MOF-only samples are an average slope of seven replicates.

MOF-polymer composite testing was carried out with minor modifications to MOF powder screen due physical parameters of fibers. Fibers of each composite were cut to 3.0 ± 0.2 mg segments and placed into well of a Grenier Bio-one Cellstar 24-well plate. Each well was prepared with 1.02 mL total volume containing: a single 3 mg fiber, 1 mL

20 mM buffer, and 20 µL substrate (25 mM DMNP in methanol; 0.39 mM total concentration; 0.5 µmol). DMNP hydrolysis was monitored in the same way as above for MOF powders. Reported activities for MOF-polymer composites are an average slope of six replicates.

## Experimental - MOF-Polymer Physical Mixtures for Hydrolysis of Nerve Agent Simulant

**EVA-based MMM Fabrication.** Approximately 200-300 mg of UiO-66(Zr) were dispersed in ethyl acetate solution (5 mL) via sonication. The EVA polymer used in this study (Sigma Aldrich) contains 40% vinyl acetate (VA) monomer and 60% ethylene monomer. EVA amounts corresponding to 50-80 wt% of the projected total MMM contents were dissolved in 1 mL of toluene, then the MOF and polymer solutions were mixed and sonicated. The fluid ink was then subjected to rotary evaporation to remove the ethyl acetate and concentrate the ink to a honey-like viscosity. The ink was then mixed with a vortex mixer and sonication bath briefly to ensure homogeneity. The ink was allowed to sit for 15 min to permit bubbles to escape the solution. Using the draw-down method, the MOF-polymer solution was transferred to a substrate of Bytac©-coated glass and then cast with a MTI Corporation MSK-AFA-II automatic thick film coater using an adjustable doctor blade set to a height of 500 µm at a speed of 25 mm/second. The cast films were then cured at 55 °C on a hotplate under a thin-neck glass funnel, for 1 h. After cooling, the films were removed from the substrate with tweezers. Although the

technique is inherently scalable, most MMMs fabricated were composed of a total of 200-300 mg of combined MOF and polymer components and were roughly $3 \times 5$ in$^2$ in size.

**MMM 'Holder' Fabrication.** In order to keep the membranes from floating to the surface of the well or blocking the beam of the absorbance spectrometer, MMM holders were fabricated using a 3D printer. Rectangular holders with slits were designed using Blender (open-source 3D rendering software) and printed with a Prusa i3 MK3 3D printer using polylactic acid (PLA) as the polymer. MMMs were cut to fit into the holders and slid into the groove: Figure 3.10 and Figure S3.5 show the holders and how they were placed in the 24-well plate with O-ring to secure them. PEO MMMs swelled in solution and were more mobile, so a rubber band was added for additional security in the holder (Figure S3.5).

**Screening of MMMs for DMNP Hydrolysis.** Membranes (~12 mm $\times$ 8 mm) were inserted into 3D printed plastic holders and placed in individual wells of an Olympus Plastics clear, flat-bottom 24-well assay plate. In order to avoid beam blockage, a small rubber O-ring was used to keep the membrane in place along the wall of the well. Buffer solution (2 mL 20 mM *N*-ethylmorpholine, pH = 8.0) was added to each well. A solution of dimethyl-4-nitrophenyl phosphate (DMNP, 20 $\mu$L of 25 mM in MeOH) was added and appearance of *p*-nitrophenoxide was monitored at $\lambda_{max}$ = 407 nm every 12 sec for 30 min. Slopes were calculated from the linear region of each plot (typically at 500-800 seconds) and normalized by the mass of membrane in the holder.

## Supplemental Tables

**Table S3.1.** BET surface areas and DMNP hydrolysis rates for selected MTV-UiO-66(Zr) MOFs.

| Name | BET Surface Area ($m^2/g$) | DMNP Hydrolysis Rate ($mM/sec \times 10^{-6}$) |
|---|---|---|
| MTV-UiO-66(Zr)-A | 1055 | 180 |
| MTV-UiO-66(Zr)-B | 1010 | 80 |
| MTV-UiO-66(Zr)-C | 411 | 106 |
| MTV-UiO-66(Zr)-D | 1086 | 61 |
| MTV-UiO-66(Zr)-E | 927 | 154 |
| MTV-UiO-66(Zr)-AB | 1477 | 228 |
| MTV-UiO-66(Zr)-BD | 599 | 323 |
| MTV-UiO-66(Zr)-BE | 572 | 446 |
| MTV-UiO-66(Zr)-ABE | 808 | 381 |
| MTV-UiO-66(Zr)-ABCD | 898 | 335 |
| MTV-UiO-66(Zr)-BCDE | 815 | 375 |

**Table S3.2.** Molar mass and hydrolysis rates for MOFs in Section 3.3.

| MOF | Molar Mass of MOF (*g/mol*) | Mole ratio to UiO-66(Zr) Standard | Experimental Rate[a] (*k*, $mM/sec \times 10^{-6}$) | Molar Mass Corrected Rate (*k*, $mM/sec \times 10^{-6}$) |
|---|---|---|---|---|
| NU-1000 | 1624 | 1.00 | 133 | 133 |
| UiO-66(Zr) | 1628 | 1.00 | 161 | 161 |
| UiO-66(Zr)-F | 1736 | 0.94 | 213 | 226 |
| UiO-66(Zr)-Cl | 1835 | 0.89 | 172 | 194 |
| UiO-66(Zr)-Br | 2101 | 0.77 | 134 | 173 |
| UiO-66(Zr)-$I_{50\%}$ | 2016 | 0.81 | 337 | 417 |
| UiO-66(Zr)-I | 2383 | 0.68 | 413 | 605 |

[a] equal mass of MOF used in each experiment.

**Table S3.3.** DMNP hydrolysis rates and standard deviations for MOF MMMs based on three replicates for each. Rates are normalized by the mass of the individual MMMs and by cut area (roughly 12 mm × 8 mm).

| Sample | Average DMNP Rate (per mass) (mM $sec^{-1}$ $mg^{-1} \times 10^{-6}$) | Std. Dev. | Average DMNP Rate (per area) (mM $sec^{-1}$ $\times$ $10^{-6}$) | Std. Dev. |
|---|---|---|---|---|
| 70% UiO-66(Zr)/ EVA MMM | 1.1 | 0.1 | 7.9 | 0.7 |
| 80% UiO-66(Zr)/ EVA MMM | 16.6 | 3.0 | 70.6 | 3.0 |
| 80% UiO-66(Zr)/ PEO MMM | 25.4 | 7.0 | 61.6 | 18.2 |
| 70% UiO-66(Zr)/ PVDF MMM | 70.8 | 15.2 | 262 | 7 |

## Supplemental Figures

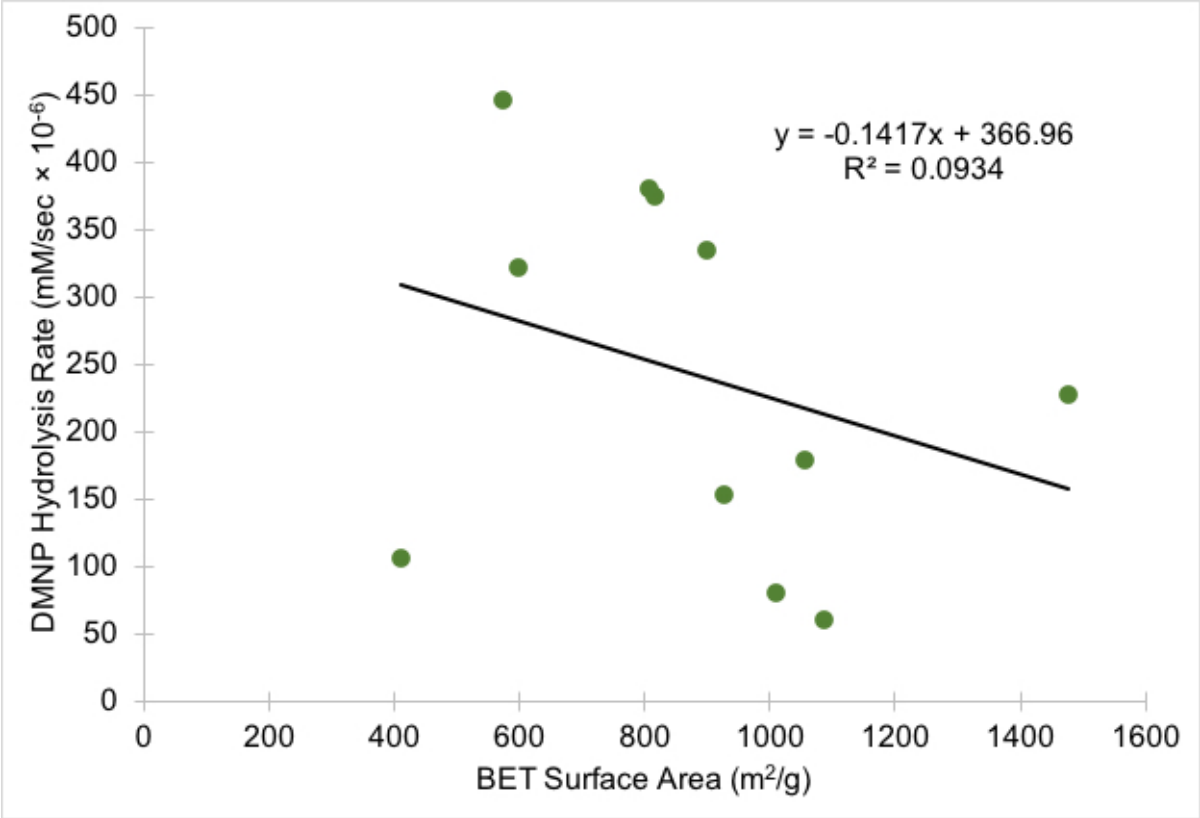


**Figure S3.1.** Correlation of BET surface area and hydrolysis of DMNP of selected MTV-UiO-66(Zr) MOFs.

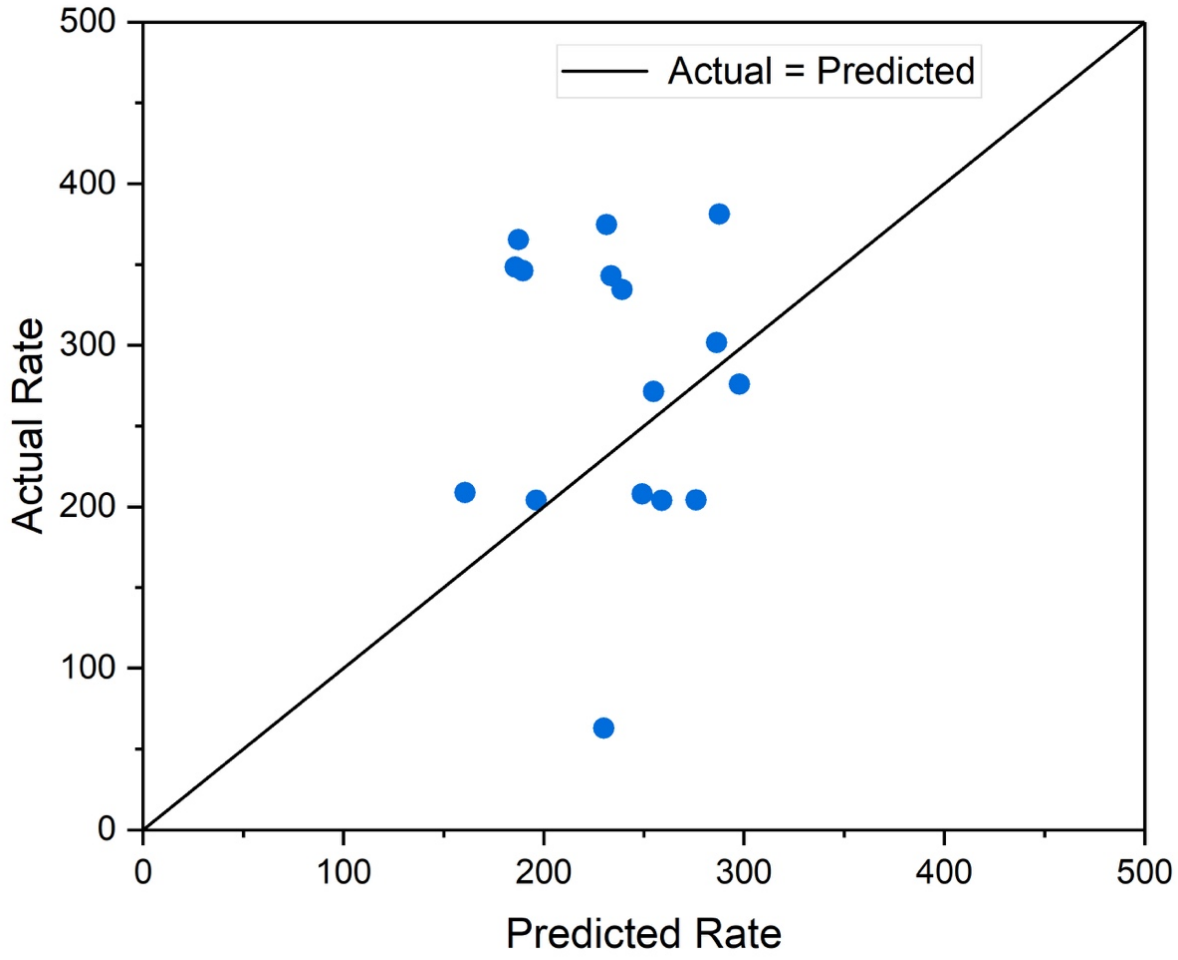


**Figure S3.2.** Rates of MTV-MOFs with 3, 4, 5 mixed ligands from HTS assay compared to the rate predicted by average rate of component two ligand MTV-MOFs.

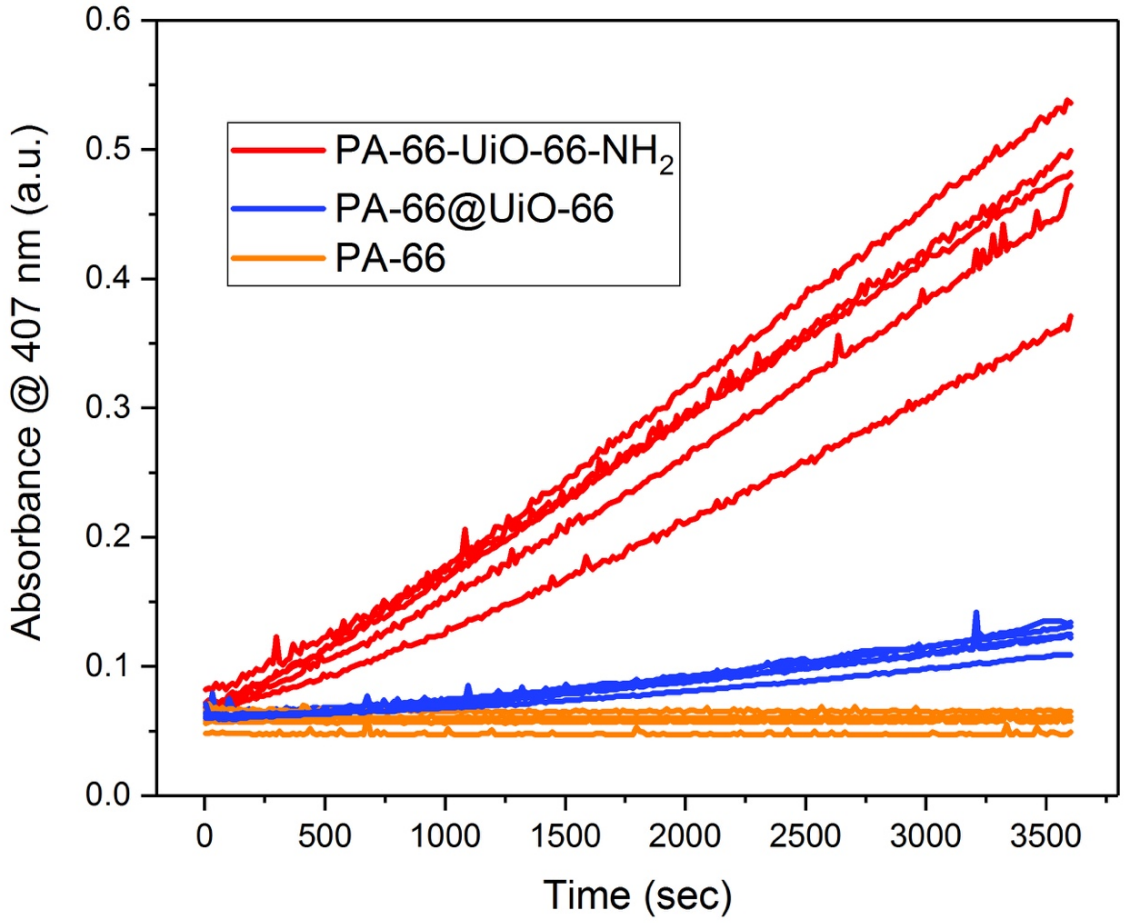


**Figure S3.3.** Absorbance (407nm) vs time (sec) monitoring the conversion of DMNP to *p*-nitrophenoxide for PA-66, PA-66@UiO66(Zr), and PA-66-UiO-66(Zr)-$NH_2$. All slopes are calculated from 10 min to 50 min and averaged per the procedure above. Representative individual trials for PA-66, PA-66@UiO-66(Zr), and PA-66-UiO-66(Zr)-$NH_2$ are shown for comparison.

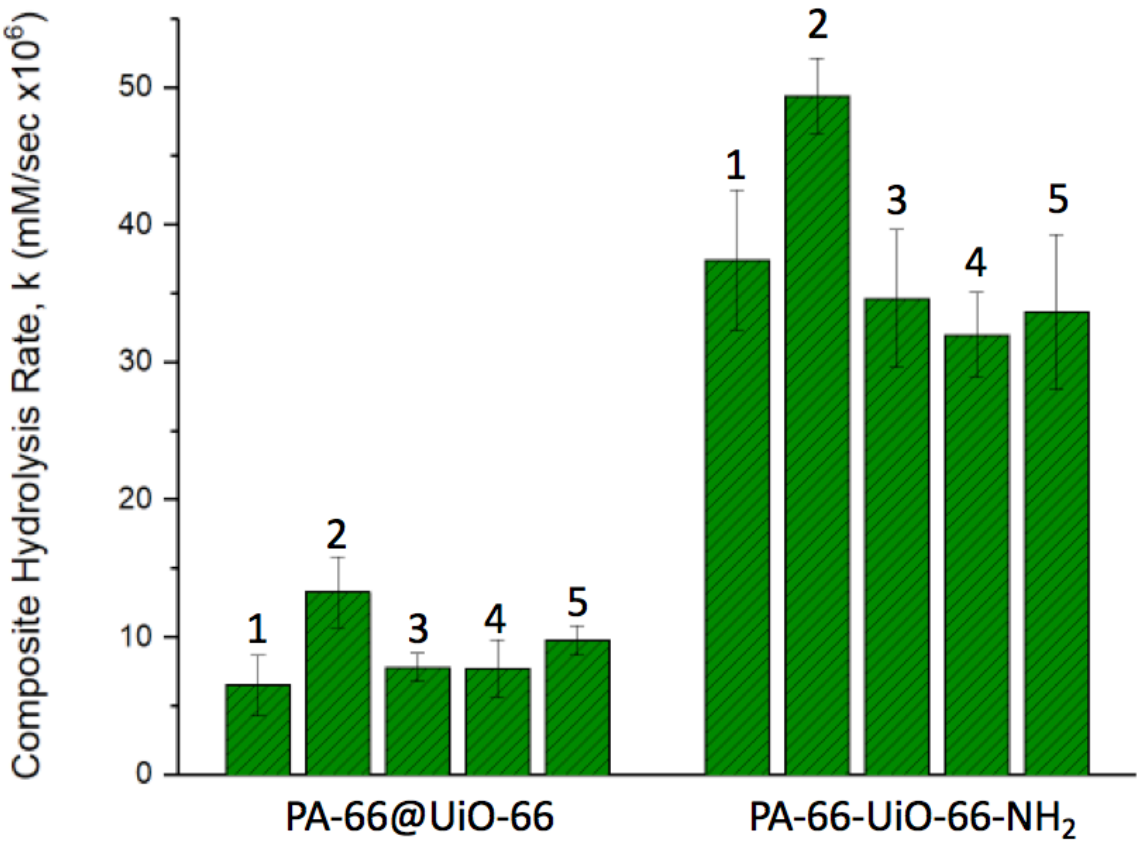


**Figure S3.4.** Rate of catalytic degradation of recycled PA-66-MOF composites at pH = 8 measured using HTS method. Composite materials were washed thoroughly in water and methanol (3× each) with sonication and then dried under vacuum at room temperature overnight between each DMNP hydrolysis experiment.

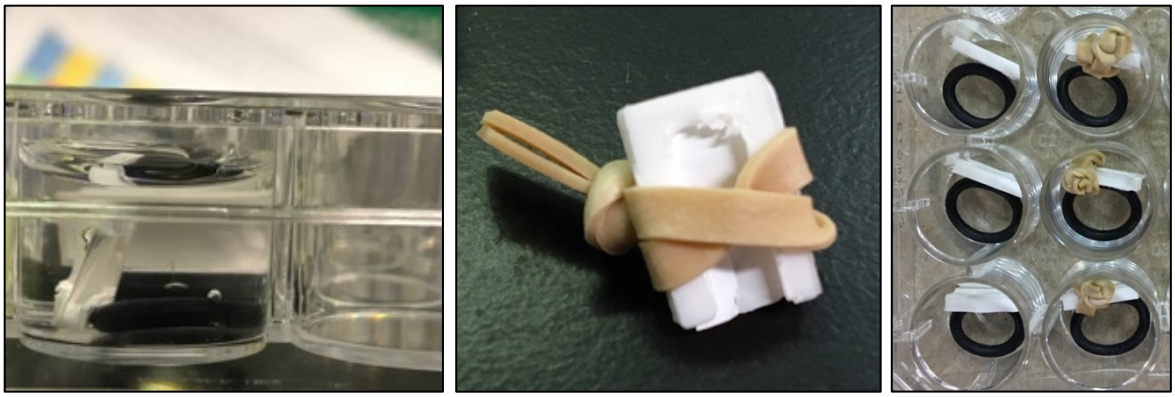

**Figure S3.5.** Photographs of membrane holder in well with buffer (*left*), holder with PEO membrane and rubber band (*center*), and top view of holders in wells with o-rings (*right*).

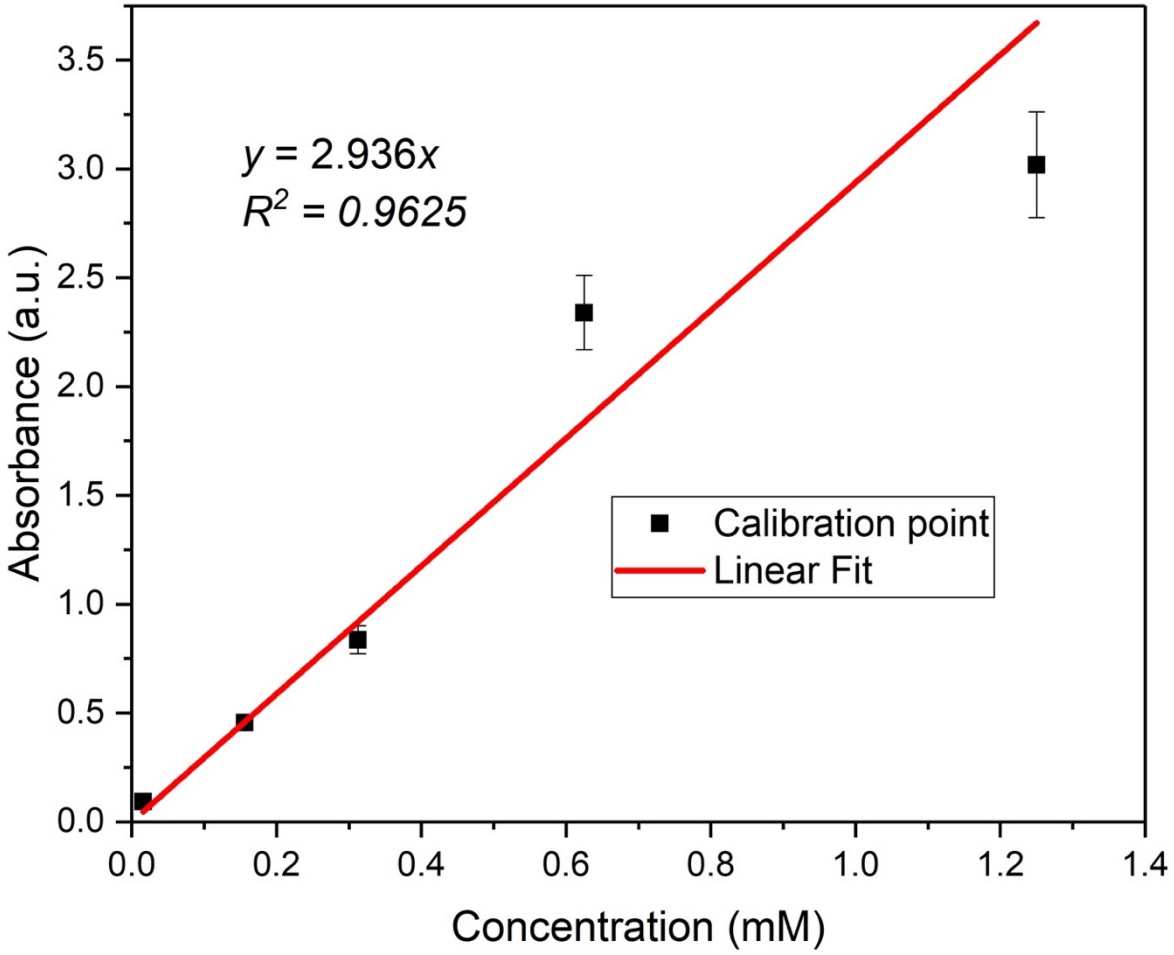


**Figure S3.6.** Calibration curve of *p*-nitrophenoxide in 20 mM NEM buffer at pH = 8.0 for 24-well plate in plate reader.

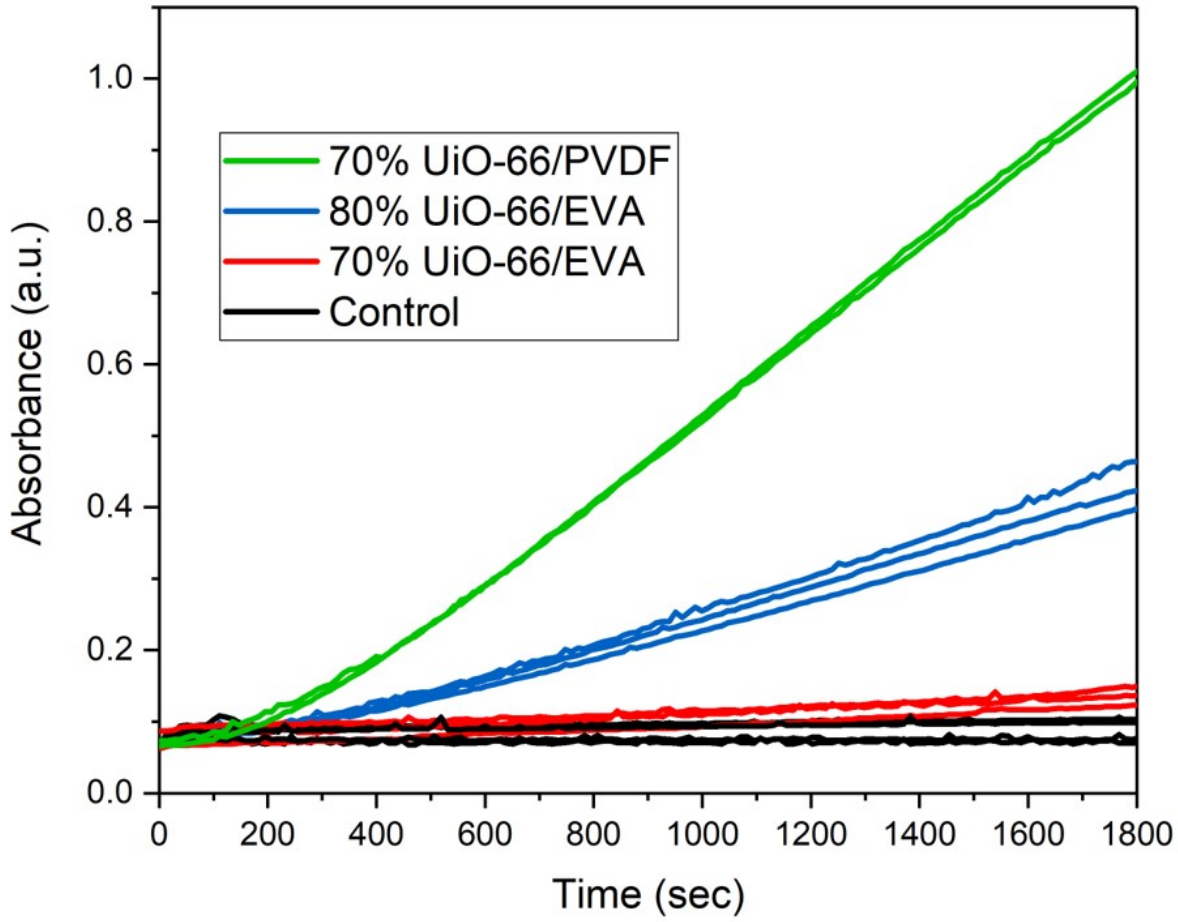


**Figure S3.7.** UV-Vis readout of absorbance at $\lambda_{max}$ of DMNP, indicating turnover rates for various polymers and MOF loadings studied. Clear, replicable differences depending on the identity of the polymer are seen in turnover rates and amounts.

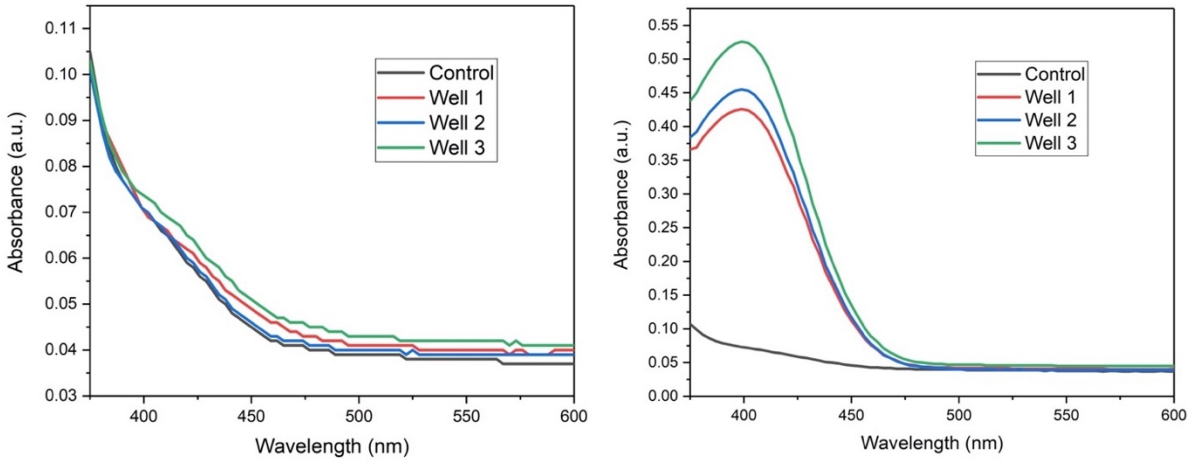


**Figure S3.8.** Full UV-Vis spectra of several wells containing assay conditions and MMMs, demonstrating turnover of DMNP to the yellow *p*-nitrophenoxide product.

## 3.8 Acknowledgements

Chapter 3, in part, is a reprint of the following materials as listed: “Mark Kalaj, Joseph M. Palomba, Kyle C. Bentz, Seth M. Cohen, Multiple functional groups in UiO-66 improve chemical warfare agent simulant degradation *Chem. Commun.,* **2019***, 55,* 5367-5370;” “Mark Kalaj, Mohammad R. Momeni, Kyle C. Bentz, Kyle S. Barcus, Joseph M. Palomba, Francesco Paesani, Seth M. Cohen, Halogen bonding in UiO-66 frameworks promotes superior chemical warfare agent simulant degradation *Chem. Commun.,* **2019***, 55,* 3481-3484;” “Mark Kalaj, Michael S. Denny Jr., Kyle C. Bentz, Joseph M. Palomba, Seth M. Cohen, Nylon–MOF Composites through Postsynthetic Polymerization” *Angew. Chem. Int. Ed.,* **2019**, *58*, 2336;” “Jessica C. Moreton, Joseph M. Palomba, Seth M. Cohen, Liquid-Phase Applications of Metal–Organic Framework Mixed-Matrix Membranes Prepared from Poly(ethylene-co-vinyl acetate) *ACS Appl. Polym. Materials* **2020,** *2*, 2063-2069.” The dissertation author was a coauthor of these manuscripts and

gratefully acknowledges the contributions of coauthors. The dissertation author also gratefully acknowledges the editing help of Dr. Kathleen E. Prosser, Ryjul W. Stokes, Dr. Sergio Ayala Jr., and Mark Kalaj.

## 3.9 References

1. Garibay, S. J.; Cohen, S. M., Isoreticular synthesis and modification of frameworks with the UiO-66 topology. *Chem. Commun.* **2010,** *46*, 7700-7702.

2. Islamoglu, T.; Ortuño, M. A.; Proussaloglou, E.; Howarth, A. J.; Vermeulen, N. A.; Atilgan, A.; Asiri, A. M.; Cramer, C. J.; Farha, O. K., Presence versus Proximity: The Role of Pendant Amines in the Catalytic Hydrolysis of a Nerve Agent Simulant. *Angew. Chem., Int. Ed.* **2018,** *57*, 1949-1953.

3. Katz, M. J.; Moon, S.-Y.; Mondloch, J. E.; Beyzavi, M. H.; Stephenson, C. J.; Hupp, J. T.; Farha, O. K., Exploiting parameter space in MOFs: a 20-fold enhancement of phosphate-ester hydrolysis with UiO-66-NH2. *Chem. Sci.* **2015,** *6*, 2286-2291.

4. Jungbauer, S. H.; Huber, S. M., Cationic Multidentate Halogen-Bond Donors in Halide Abstraction Organocatalysis: Catalyst Optimization by Preorganization. *J. Am. Chem. Soc.* **2015,** *137*, 12110-12120.

5. Tanabe, K. K.; Wang, Z.; Cohen, S. M., Systematic Functionalization of a Metal–Organic Framework via a Postsynthetic Modification Approach. *J. Am. Chem. Soc.* **2008,** *130*, 8508-8517.

6. Hintz, H.; Wuttke, S., Solvent-Free and Time Efficient Postsynthetic Modification of Amino-Tagged Metal–Organic Frameworks with Carboxylic Acid Derivatives. *Chem. Mater.* **2014,** *26*, 6722-6728.

7. Denny Jr, M. S.; Cohen, S. M., In Situ Modification of Metal–Organic Frameworks in Mixed-Matrix Membranes. *Angew. Chem., Int. Ed.* **2015,** *54*, 9029-9032.

8. Moreton, J. C.; Denny, M. S.; Cohen, S. M., High MOF loading in mixed-matrix membranes utilizing styrene/butadiene copolymers. *Chem. Commun.* **2016,** *52*, 14376-14379.

9. Semino, R.; Moreton, J. C.; Ramsahye, N. A.; Cohen, S. M.; Maurin, G., Understanding the origins of metal–organic framework/polymer compatibility. *Chem. Sci.* **2018,** *9*, 315-324.

10. Duan, P.; Moreton, J. C.; Tavares, S. R.; Semino, R.; Maurin, G.; Cohen, S. M.; Schmidt-Rohr, K., Polymer Infiltration into Metal–Organic Frameworks in Mixed-Matrix Membranes Detected in Situ by NMR. *J. Am. Chem. Soc.* **2019,** *141*, 7589-7595.

11. Deng, H.; Doonan, C. J.; Furukawa, H.; Ferreira, R. B.; Towne, J.; Knobler, C. B.; Wang, B.; Yaghi, O. M., Multiple Functional Groups of Varying Ratios in Metal-Organic Frameworks. *Science* **2010,** *327*, 846.

12. Kalaj, M.; Palomba, J. M.; Bentz, K. C.; Cohen, S. M., Multiple functional groups in UiO-66 improve chemical warfare agent simulant degradation. *Chem. Commun.* **2019,** *55*, 5367-5370.

13. Kalaj, M.; Momeni, M. R.; Bentz, K. C.; Barcus, K. S.; Palomba, J. M.; Paesani, F.; Cohen, S. M., Halogen bonding in UiO-66 frameworks promotes superior chemical warfare agent simulant degradation. *Chem. Commun.* **2019,** *55*, 3481-3484.

14. Dhakshinamoorthy, A.; Alvaro, M.; Hwang, Y. K.; Seo, Y.-K.; Corma, A.; Garcia, H., Intracrystalline diffusion in Metal Organic Framework during heterogeneous catalysis: Influence of particle size on the activity of MIL-100 (Fe) for oxidation reactions. *Dalton Trans.* **2011,** *40*, 10719-10724.

15. Gliese, J.-P.; Jungbauer, S. H.; Huber, S. M., A halogen-bonding-catalyzed Michael addition reaction. *Chem. Commun.* **2017,** *53*, 12052-12055.

16. Zhang, Y.; Feng, X.; Li, H.; Chen, Y.; Zhao, J.; Wang, S.; Wang, L.; Wang, B., Photoinduced Postsynthetic Polymerization of a Metal–Organic Framework toward a Flexible Stand-Alone Membrane. *Angew. Chem., Int. Ed.* **2015,** *54*, 4259-4263.

17. Kalaj, M.; Denny Jr, M. S.; Bentz, K. C.; Palomba, J. M.; Cohen, S. M., Nylon–MOF Composites through Postsynthetic Polymerization. *Angew. Chem., Int. Ed.* **2019,** *58*, 2336-2340.

18. Moreton, J. C.; Palomba, J. M.; Cohen, S. M., Liquid-Phase Applications of Metal–Organic Framework Mixed-Matrix Membranes Prepared from Poly(ethylene-co-vinyl acetate). *ACS Appl. Polym. Mater.* **2020,** *2*, 2063-2069.

19. DeCoste, J. B.; Denny, J. M. S.; Peterson, G. W.; Mahle, J. J.; Cohen, S. M., Enhanced aging properties of HKUST-1 in hydrophobic mixed-matrix membranes for ammonia adsorption. *Chem. Sci.* **2016,** *7*, 2711-2716.

20. Duan, P.; Moreton, J. C.; Tavares, S. R.; Semino, R.; Maurin, G.; Cohen, S. M.; Schmidt-Rohr, K., Polymer Infiltration into Metal–Organic Frameworks in Mixed-Matrix Membranes Detected in Situ by NMR. *J. Am. Chem. Soc.* **2019,** *141*, 7589-7595.

21. Rouquerol, J.; Llewellyn, P.; Rouquerol, F., *Is the BET equation applicable to microporous adsorbents?* Elsevier: 2007; Vol. 160, p 49-56.

# Chapter 4: High-Throughput Screening of Metal-Organic Frameworks for Targeted Breakdown of V-series Nerve Agents

## 4.1 Introduction

Chapters 2 and 3 detailed the expansion in breadth and understanding of MOF catalysts for the hydrolysis of nerve agent simulant DMNP. In most cases the ability to hydrolyze the P-O bond of DMNP does not match the ability of the catalyst to hydrolyze P-F, P-S, or P-C bonds of many nerve agents.[1-4] This is highlighted by two recent studies with Zr-MOFs noting the lack of correlation between simulant and nerve agent reactivity.[5, 6] For these catalytic materials to be applied to PPE,[7] they must be effective for a wide range of nerve agents. The goal of this study is to find simulants that have reactivity trends that match nerve agents.

This chapter focuses on the development a high-throughput assay to assess catalysts for a simulant with the same liable bond for hydrolysis as the nerve agent. As a first step towards goal of better aligning MOF discovery for simulant and agent hydrolysis, the nerve agent (*O*-ethyl *S*-[2-(diisopropylamino)ethyl] methylphosphonothioate) (VX, Figure 4.1) found in use as recently as 2017 was selected.[8] This agent was selected as it has distinct hydrolysis chemistry (P-S bond cleavage) and reactivity trends from G-series nerve agents with Zr-MOFs.[5, 9] The P-S cleavage in the productive hydrolysis of VX can be directly replicated with the simulant *O*,*O*-diethyl *S*-phenyl phosphorothioate (DEPPT, Figure 4.1) that also possesses a P-S bond.[10] This is in contrast to hydrolysis of the P-O bond in DMNP that has been used as an analog for the hydrolysis of P-F bonds in G-series nerve agents like (*RS*)-propan-2-yl methylphosphonofluoridate (GB, Figure 4.1).

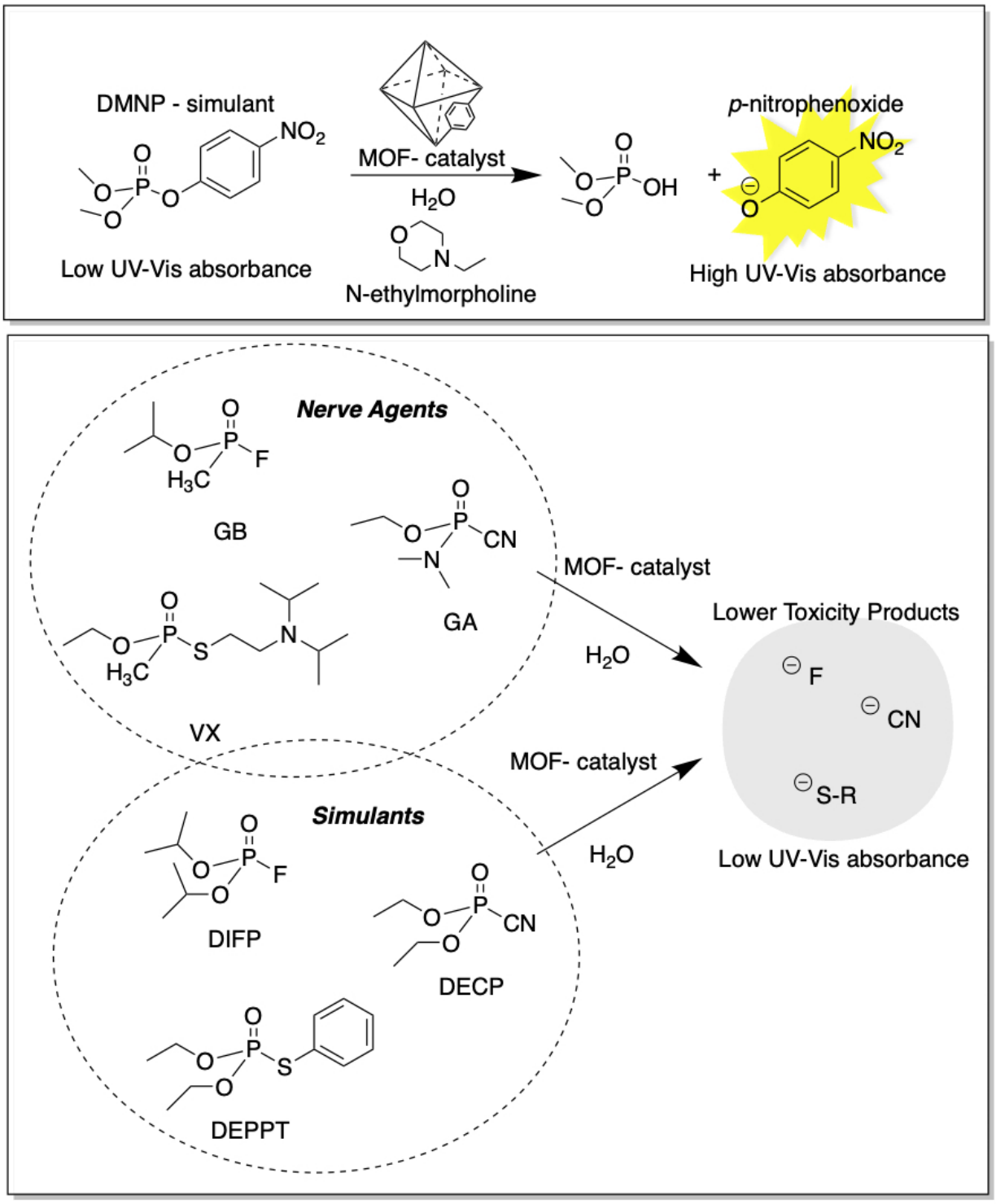


**Figure 4.1.** *Top:* DMNP hydrolysis resulting in colored product. *Bottom:* Nerve agent and simulant hydrolysis resulting in non-colored products.

Figure 4.1 highlights the advantage of using DMNP as a simulant as hydrolysis produces a colored product, making assay design simple. Nerve agents and other simulants with target bond for hydrolysis (P-F, P-C, and P-S, Figure 4.1) result in non-colored products, making an absorbance-based assay challenging. Based on the success of identifying new MOFs using and absorbance-based HTS in Chapters 2 and 3, it was important to develop a suitable HTS assay for the P-S bond simulant, DEPPT. While the hydrolysis of the phosphorothioester bond results in a free thiol which is colorless, thiols can be easily detected by reporter complexes. 5,5-dithiobis-(2-nitrobenzoic acid) (DTNB, Figure 4.2) is a reporter molecule common to biochemical assays[11, 12] and was reported as a detection molecule in tandem with MOFs for quantifying VX contamination on surfaces.[13] Using DTNB a new HTS assay that allows for detection of P-S bond hydrolysis was developed.

DTNB was utilized to make an assay suitable for a 96-well plate reader for DEPPT that is analogous to those presented in Chapters 2 and 3. The results of DEPPT HTS were compared to DMNP HTS results and the differences between the two simulants is significant. A selection of MOFs from the HTS were then compared VX hydrolysis tested with a medium-throughput absorbance-based assay that also used DTNB as a reporter molecule. The results of this comparison screen revealed the lack of strong correlation between either simulant, DMNP or DEPPT, and VX nerve agent, but together the simulants were able to identify hits for VX. Finally, this faster reporter-based absorbance assay was compared to the predominant $^{31}$P NMR assay as validation of the technique.[3, 14, 15]

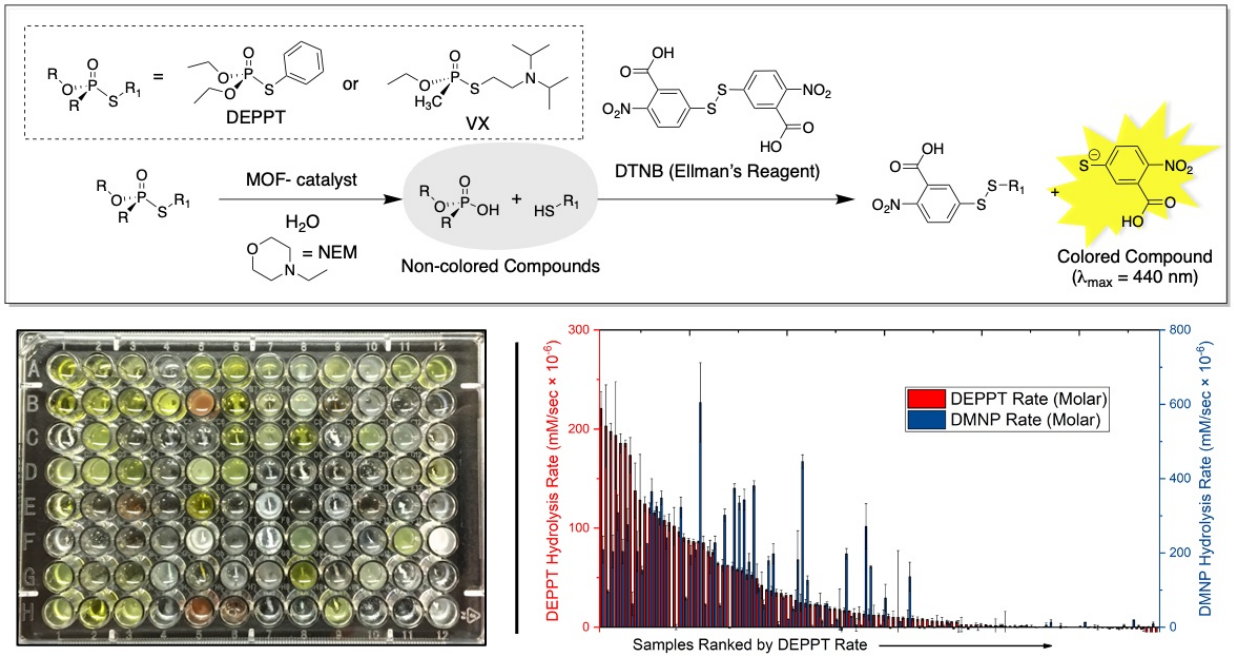


**Figure 4.2.** *Top*: General scheme for HTS assay using DTNB as a reporter molecule to allow for detection of P-S hydrolysis. *Bottom*: 96-well plate with a unique MOF in each well after DEPPT HTS and results from screening of both DEPPT and DMNP HTS.

## 4.2 Development of DEPPT-DTNB HTS Assay

The overall scheme for DEPPT HTS assay is shown in Figure 4.2, where plate reader is used to detect 3-carboxy-4-nitrobenzenethiolate at 440 nm. Thiophenol, the DEPPT hydrolysis product, was used to calibrate the proposed assay setup (Figure 4.3) by monitoring the reaction with DTNB to obtain a linear absorbance response at both pH = 8.0 and 7.4 (Figures 4.4 and 4.5). The assay is not suitable at pH = 7.0 or pure water due to insolubility of thiophenol leading to lack of linear absorbance response when reacted with DTNB (Figures S4.1 and S4.2). The linear response of thiophenol monitoring with DTNB showed that DMNP can effectively detect the hydrolysis product of

DEPPT under the assay conditions, and these calibration curves were used to calculate the concentration of thiol hydrolysis product over time (Equation 4.1).

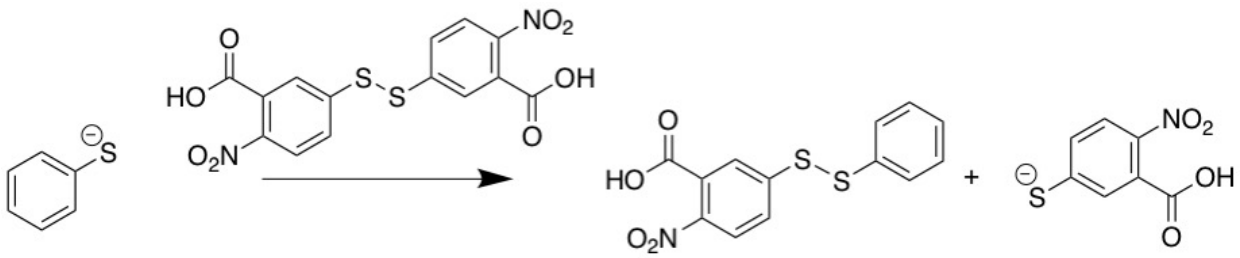


**Figure 4.3.** Reaction of thiophenol with DTNB, for detection of free thiol, used for calibration curves.

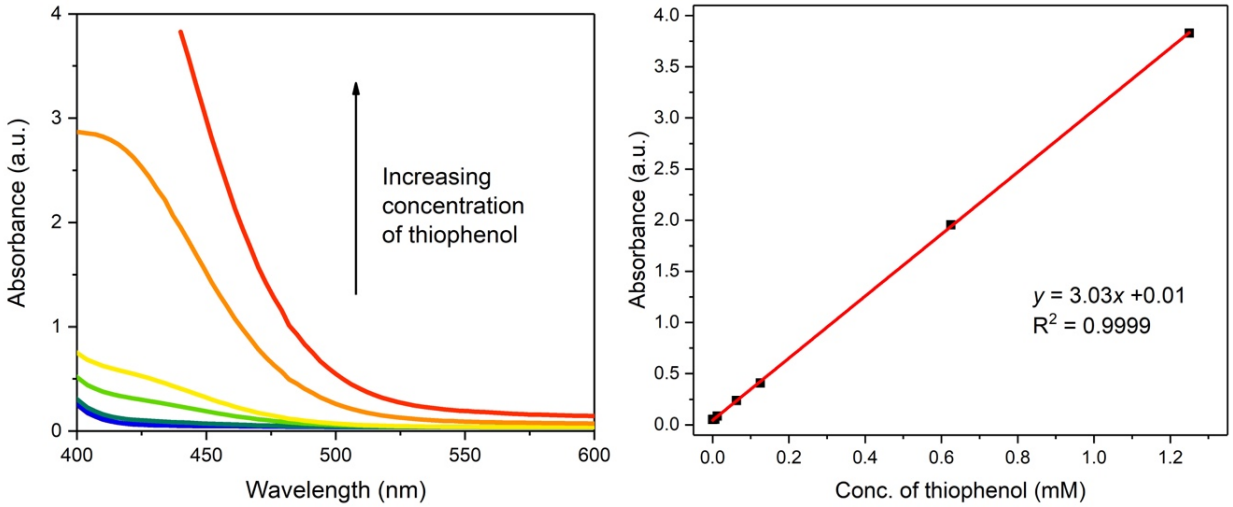


**Figure 4.4.** Absorbance curves (*left*) and calibration curve (*right*) for DTNB combined with thiophenol at various concentrations in pH = 8.0 NEM buffer.

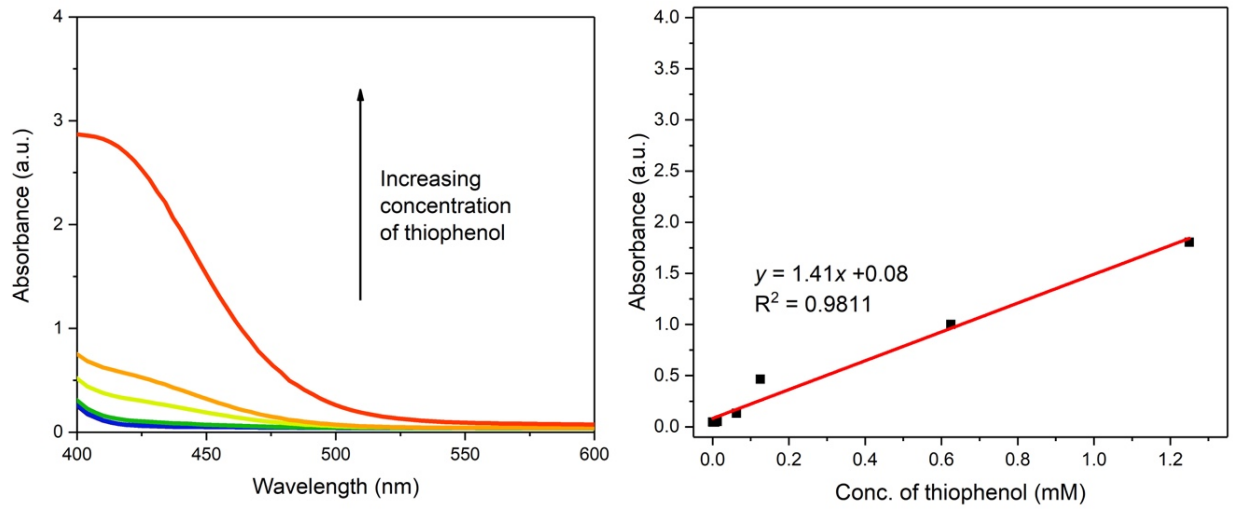


**Figure 4.5.** Absorbance curves (*left*) and calibration curve (*right*) for DTNB combined with thiophenol at various concentrations in pH = 7.4 NEM buffer.

$$\frac{Initial\ Rate\ \left(\frac{Abs}{sec}\right)}{slope\ of\ calibration\ curve\ \left(\frac{Abs}{mM}\right)} = k\ \left(\frac{mM}{sec}\right)$$

**Equation 4.1.** Hydrolysis rate of DEPPT by MOF catalyst (*k*) based on assay slope (initial rate) and slope of calibration curve using thiophenol (Figures 4.3 and 4.4).

With DTNB as a reporter molecule, a 96-well plate assay was devised based on the previously developed HTS approach (Chapter 2), with optimization of the concentration of MOF and simulant to minimize background effects. Initial testing used a series of MOFs previously identified as hits and controls with DMNP as simulant (Figure S4.3). The robustness of the assay was tested via a Z-test for a series of four MOFs with different reactivity. Commonly used for biochemical assays, the Z-test is a measure of the separation of signal and background and quantifies the strength of an assay.[16] By running a large number of replicate wells of a series of MOFs and controls, the signal and

background averages can be calculated. Using the statistical parameter Z-factor (the assay quality was assessed (see Chapter 2).

UiO-66(Zr), UiO-66(Zr)-H/$NH_2$/OH/$NO_2$/Br, UiO-66(Zr)-Cl, and UiO-66(Zr)-OH/Br were repeated 32 times and resulting Z-factors were 0.79, 0.61, 0.52, and -1.41, respectively (See Figure 4.6 and Figure S4.4). Assays with Z-factor scores greater than 0.5 are considered “excellent assays” and scores below 0 (negative values) are not able to be assayed because signal and background overlap. These results indicate that for samples that hydrolyze DEPPT, the assay can be reliably repeated, the data are separated from background, and conclusions about relative rates can be drawn. For samples with low turnover of DEPPT and high standard deviation, like UiO-66(Zr)-OH/Br, the Z-test confirms this material as not active for hydrolysis (Figure S4.4). The Z-test provides statistical evidence that the assay performs well for UiO-66(Zr), UiO-66(Zr)-H/$NH_2$/OH/$NO_2$/Br, and UiO-66(Zr)-Cl (Z-factor >0.5) and that UiO-66(Zr)-OH/Br can be confidently excluded (Z-factor = -1.41).

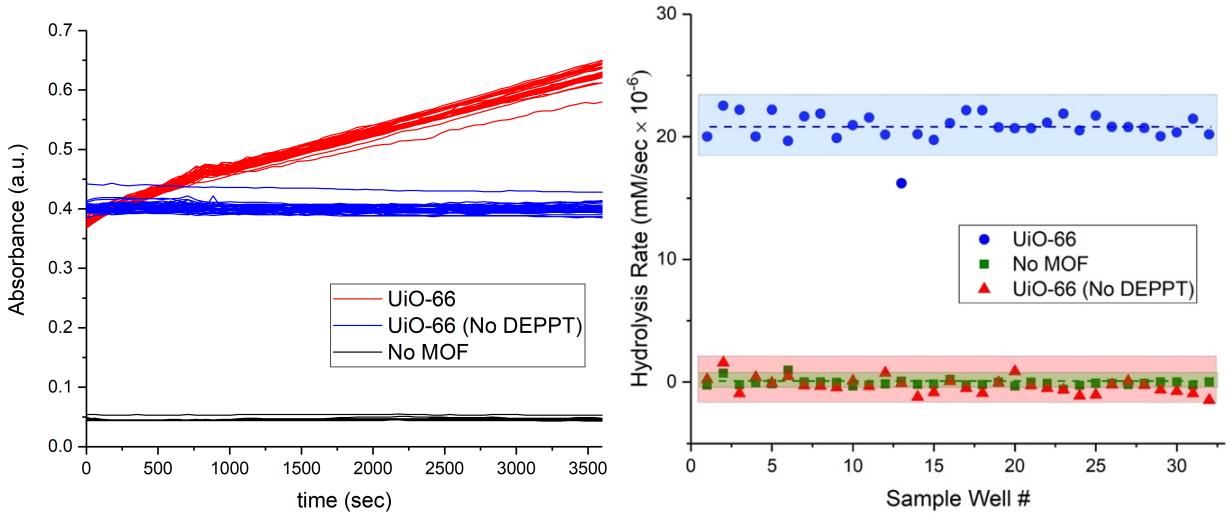


**Figure 4.6.** Absorbance traces (*left*) and hydrolysis rates (*right*) of DEPPT HTS for UiO-66, UiO-66 without DEPPT control, and No MOF control. The tests were performed 32 wells each for reproducibility testing and Z-factor calculations.

The versatility of the assay was explored by altering the pH of the buffer and testing a selection of MOFs. This was done in an effort to analyze the effectiveness of materials near neutral pH. A linear concentration response of reporter molecule was found down to pH = 7.4, but at lower pH (7.0 and pure water) thiophenol was insoluble, preventing its reaction with DTNB (Figures S4.1 and S4.2). The HTS assay was performed on a subset of MOFs at pH = 7.4 and were compared to their rates at pH = 8.0 (Figure 4.7). Consistent with previous results, the rates of reaction at the two pH values differed substantially, highlighting the significance of analyzing materials as close to real world conditions as possible.[17, 18] The ability to screen these materials easily under different reaction conditions (e.g., at multiple pH values) demonstrates how HTS allows for exploration of more variables to understand and optimize simulant (and potentially agent) hydrolysis. In this chapter the library of materials was screened at pH = 8.0 for direct comparison to

DMNP hydrolysis at pH = 8.0, because the *p*-nitrophenoxide indicator product is not soluble at pH = 7.4.

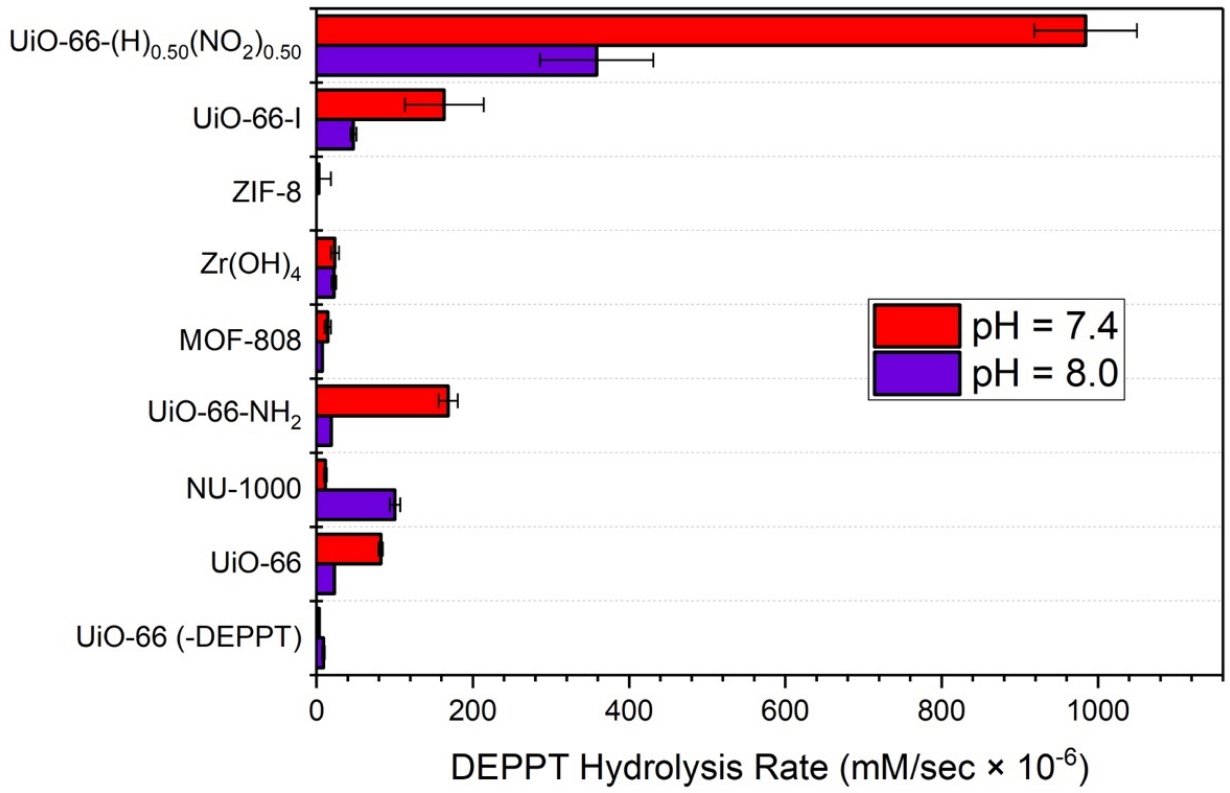


**Figure 4.7.** Comparison of DEPPT hydrolysis rates at pH = 8.0 and 7.4 of selected MOFs.

## 4.3 Library screening against DEPPT

A library of 117 MOFs, metal oxides, zeolites, and related materials were screened for hydrolysis of DEPPT (Table S4.1 and Figure S4.5). Results from this screen were normalized to the molecular weight of each material so activity is compared on a per mole basis. The results of this library screen show that Zr(IV)-based MOFs are the most active materials from this library for the catalytic hydrolysis of DEPPT, which is consistent with established mechanism for phosphate ester hydrolysis by MOFs (Table S4.1, Figure

S4.5-S4.10).[19] To guard against false positives caused by material settling in wells and scattering light, visual inspection of well color change was compared to rate; non-yellow wells were subjected to additional control testing without simulant (see Appendix and Table S4.2).

The 20 most active materials identified were a series of UiO-66 materials with mixtures of functionalized ligands (Figure S4.6). This result highlights the ability of this method to screen large numbers of simple derivatives of an active material. In addition, when these data are compared to the hydrolysis rates for the same 20 MOFs with DMNP, there is no correlation in activity ($R^2$ = 0.0032, Figure 4.8). This indicates that the distinction between hydrolysis rates of the P-S bond simulant, DEPPT, and P-O bond simulant, DMNP, merits further mechanistic investigation.

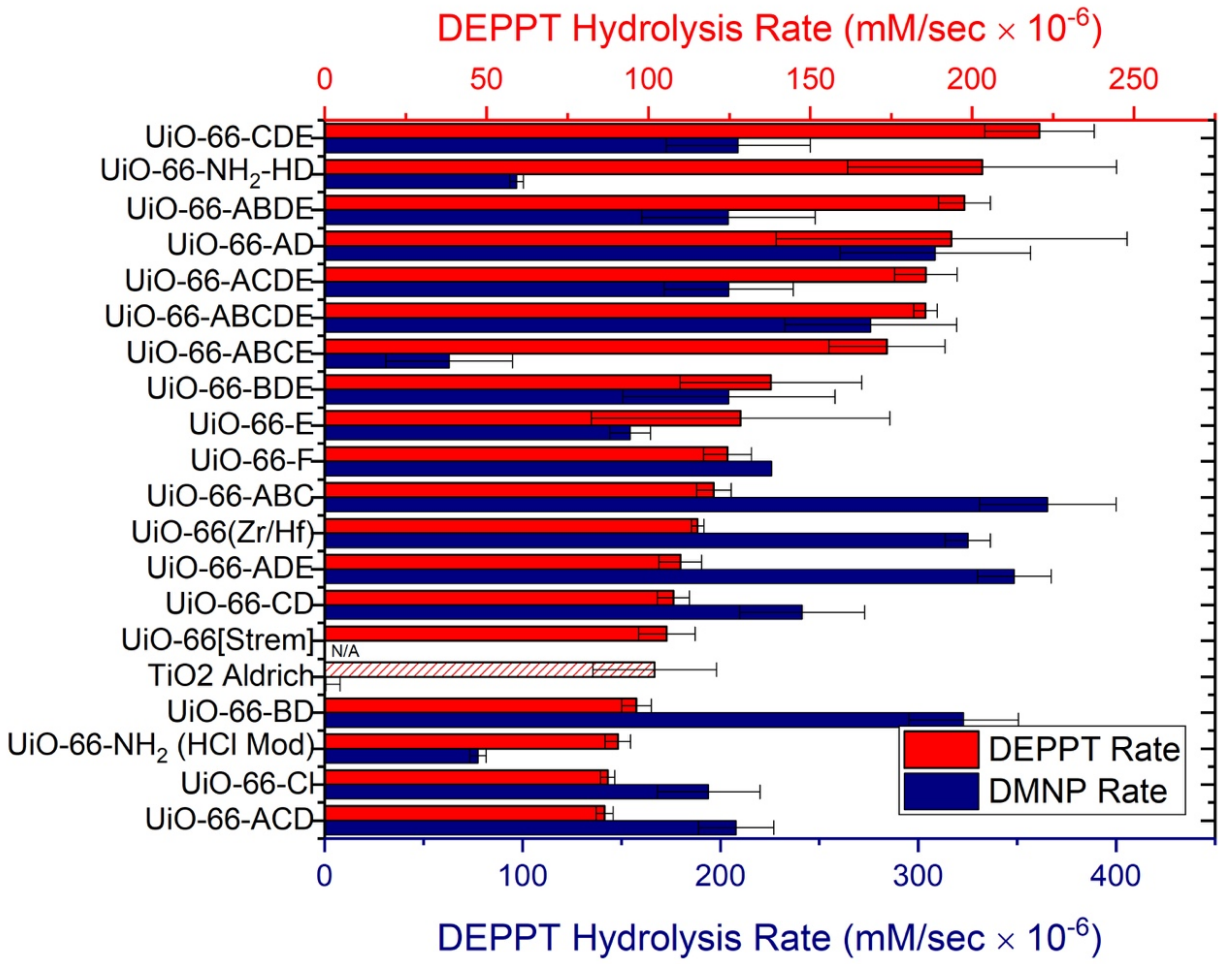


**Figure 4.8.** Top 20 MOFs from DEPPT HTS, with DMNP hydrolysis rate for comparison. $R^2$ value for correlation is 0.0032. $TiO_2$ (Aldrich) is highlighted as a striped bar as it was determined to be a false positive with controls (see Appendix).

Examining the data for the entire library for the hydrolysis of DEPPT versus DMNP, there is clear distinction between the simulants through the entire data set. This is further highlighted by a scatter plot of DEPPT (y-axis) versus DMNP (x-axis) activity in Figure 4.9 (Table S4.3). The scatter plot shows there is no strong correlation between DEPPT and DMNP hydrolysis (correlation $R^2 = 0.3587$). The plot also identifies outliers like UiO-66-H/$NH_2$/OH/Br and UiO-66-I, which are top hits for DEPPT and DMNP, respectively. These outliers readily hydrolyze one simulant but are >3-times slower for the other

simulant underscoring the significance of screening with multiple simulants. As stated above, the most significant difference in the two simulants is the hydrolyzed phosphorothioester or phosphoester bond, respectively DEPPT and DMNP. Therefore, by using a simulant with a P-S bond, this HTS assay should be a better predictive tool for developing materials to degrade V-series agents that contain P-S bonds. Combining the data from these screens can provide a starting place to design and optimize a material to hydrolyze both P-S and P-O bonds efficiently.

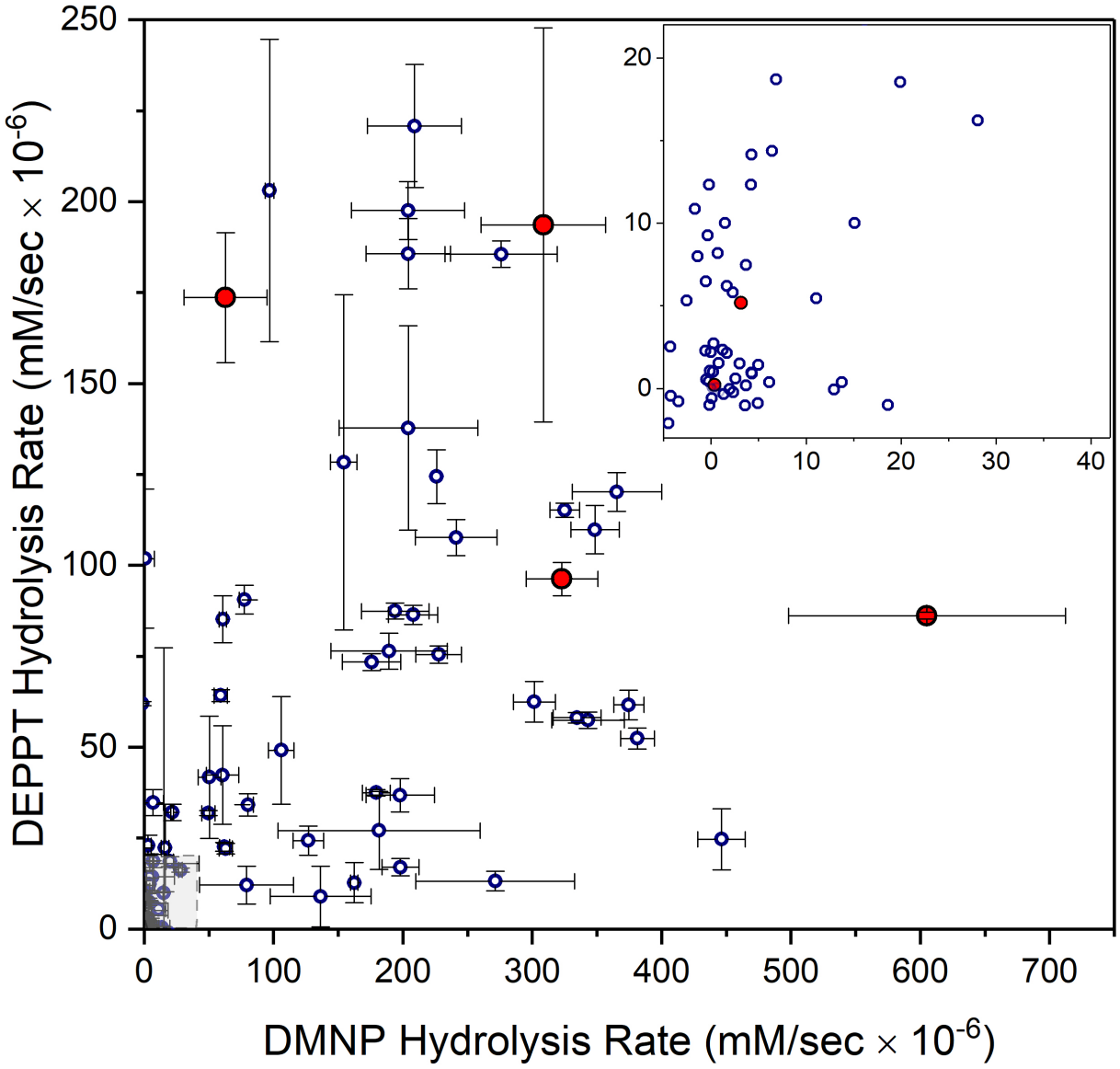


**Figure 4.9.** Library of materials tested with both DEPPT and DMNP hydrolysis rates shown for each material, points are average and error bars show one standard deviation. The six MOFs used for VX screening are highlighted in red. *Inset:* Magnification of the region of samples with low activity (gray box in main figure). The majority of DMNP hydrolysis rates shown were collected in Chapters 2 and 3.

## 4.4 Evaluation of MOF Subsets

Based on the results of HTS screening against DEPPT, hydrolysis of VX was monitored to determine the degree of correlation between simulant and agent. Six

materials identified as low, medium, and high activity for P-S bond hydrolysis with DEPPT were selected for a specialized absorbance spectroscopy assay using VX. This set also represents MOFs with a range of activity toward DMNP, such as UiO-66(Zr)-H/$NH_2$/OH/Br, which has low activity for DMNP hydrolysis and would be overlooked for VX testing based on the DMNP results alone (Figure 4.10, Figure S4.7-S4.13, and Table S4.4).

A six-cuvette absorbance spectrometer was used to screen the six selected MOFs in triplicate with VX using a volume-adapted method. This method works on the same concept as the HTS, with DTNB acting as the reporter for VX hydrolysis product 2-(diisopropylamino)ethane-1-thiol (DESH). Using this method, only the productive hydrolysis of the P-S bond of VX into its non-toxic products, ethyl methylphosphonic acid (EMPA) and DESH, is monitored, because P-O cleavage would result in toxic *S*-2-(diisopropylamino)ethyl *O*-hydrogen methylphosphonothioate (EA-2192) and ethanol, both not detected by DTNB. To validate the HTS results performed in an absorbance plate reader, the same six MOFs were tested using DEPPT in a conventional absorbance spectrometer; the results from the plate reader and spectrometer were identical (Figures S4.9 and S4.10).

The hydrolysis rates as determined by absorbance spectroscopy show that neither DEPPT nor DMNP is a perfect simulant for VX (Figure 4.10). DEPPT hydrolysis identifies the top candidates for VX hydrolysis, but overpredicts (i.e., incorrectly ranks) the activity of UiO-66(Zr)-H/$NO_2$. The DMNP HTS results also do not perfectly correlate to the VX data, but the DMNP data do identify additional hits (UiO-66(Zr)-I) for VX. Overall, the

HTS results suggests that the use of both simulants, DEPPT and DMNP, may be best used in tandem to identify the most promising candidates for agent testing. It is possible that evaluating a larger number of materials with VX would show a greater differentiation between the predictive ability of DEPPT and DMNP.

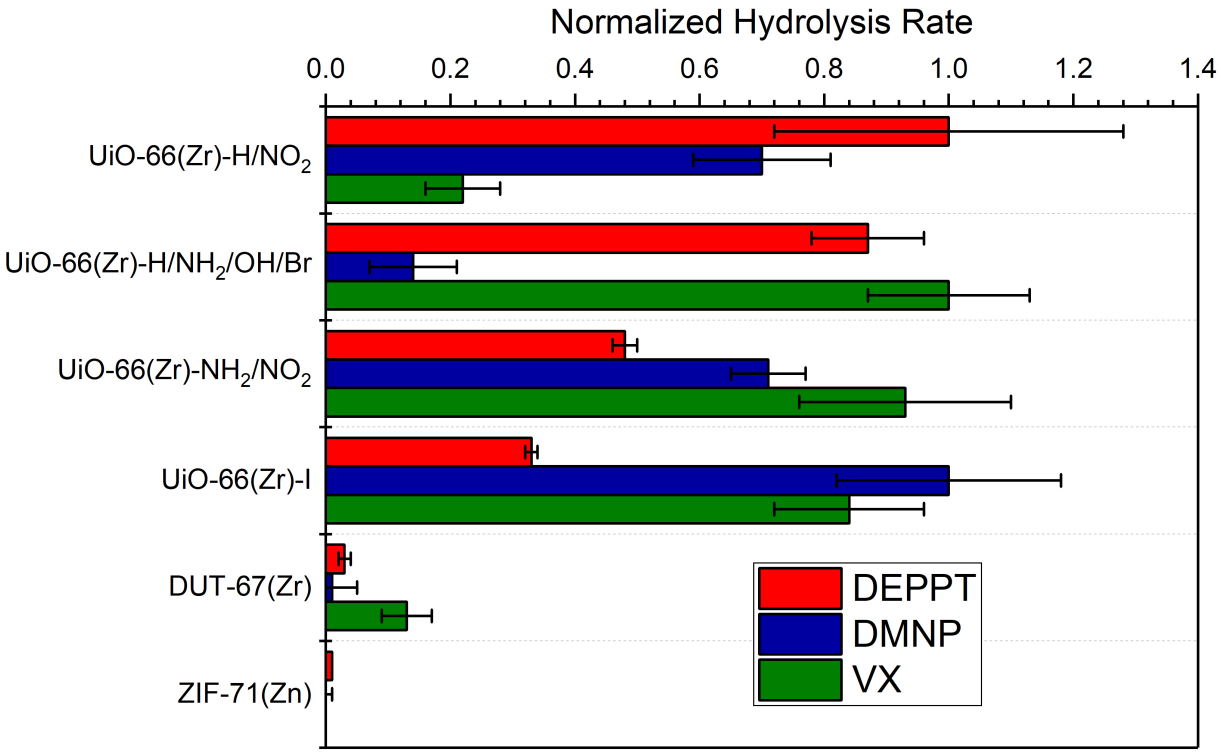


**Figure 4.10.** Normalized hydrolysis rates with standard deviations for DEPPT and DMNP from HTS assay compared to hydrolysis rates for VX absorbance assay.

$^{31}$P NMR was employed as an orthogonal assay to confirm results from the absorbance spectroscopy screen with MOFs with high, medium, and low activities: UiO-66(Zr)-H/$NH_2$/OH/Br (Figure 4.11, UiO-66(Zr)-H/$NO_2$ (Figure 4.12), and DUT-67(Zr) (Figure S4.11), respectively. Figures 4.13 shows the conversion of VX in NEM buffer (40 mM, pH = 8.0) to EMPA (monitored by $^{31}$P NMR) and DESH, which shows that VX is

hydrolyzed faster by UiO-66(Zr)-H/$NH_2$/OH/Br than UiO-66(Zr)-H/$NO_2$ consistent with VX absorbance assay data. The DUT-67(Zr) is the lowest rate of the set which is consistent with simulant HTS and VX absorbance assay. Importantly, in all cases VX hydrolysis by MOFs was confirmed to be selective for P-S cleavage producing EMPA, instead of P-O cleavage that results in toxic product EA-2192 (Figure 4.11, Figure 4.12, and Figure S4.11). From a materials development perspective, this confirms that DEPPT can be used for initial evaluation to narrow and optimize catalysts to degrade nerve agents, without having to do exhaustive testing with these dangerous, restricted chemicals.

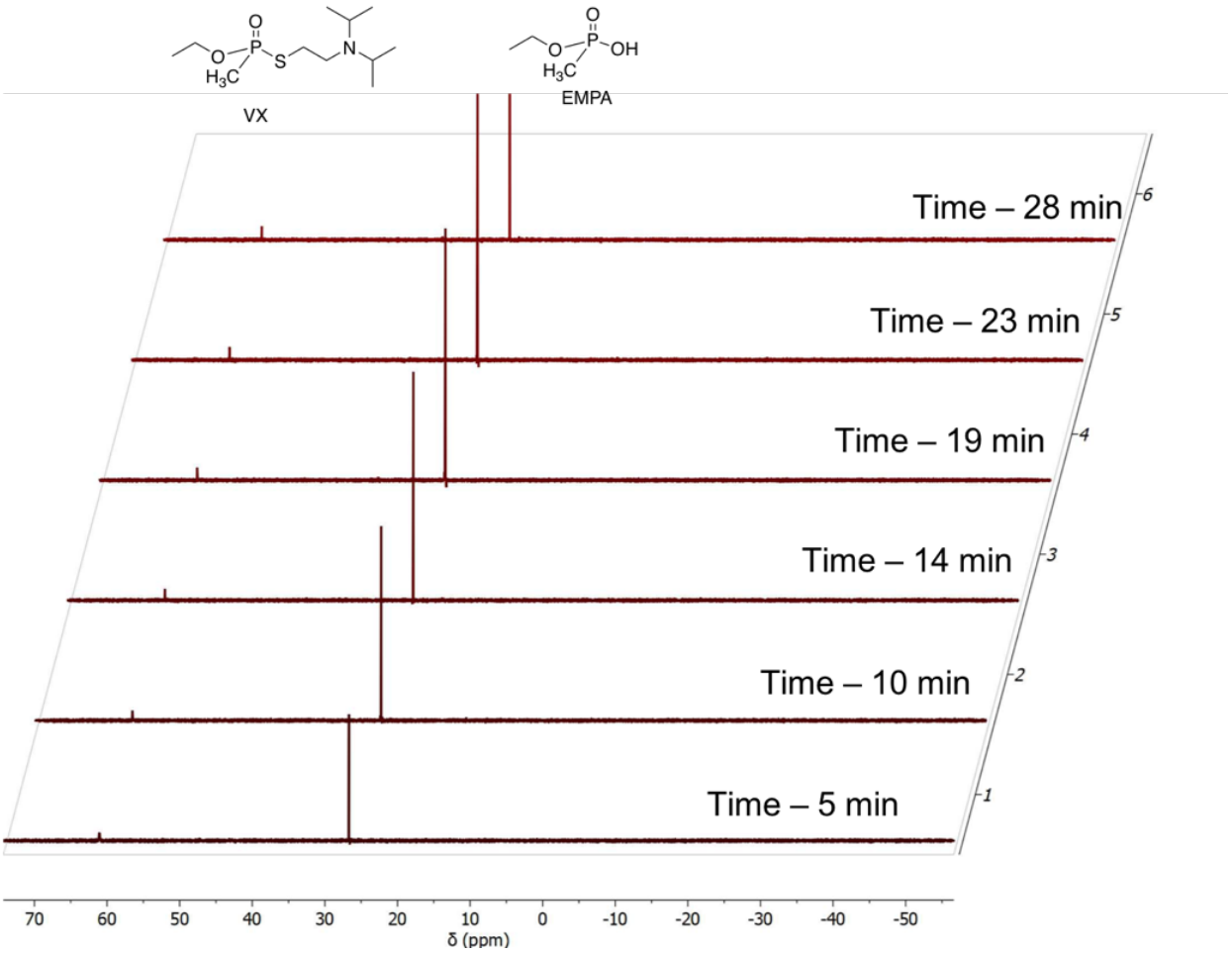


**Figure 4.11.** $^{31}P$ spectra of VX hydrolysis to EMPA by UiO-66(Zr)-H/$NH_2$/OH/Br for first 14 min of experiment. Note: None of the toxic byproduct S-2-(diisopropylamino)ethyl O-hydrogen methylphosphonothioate (EA-2192, NMR Shift 43.1) was detected.

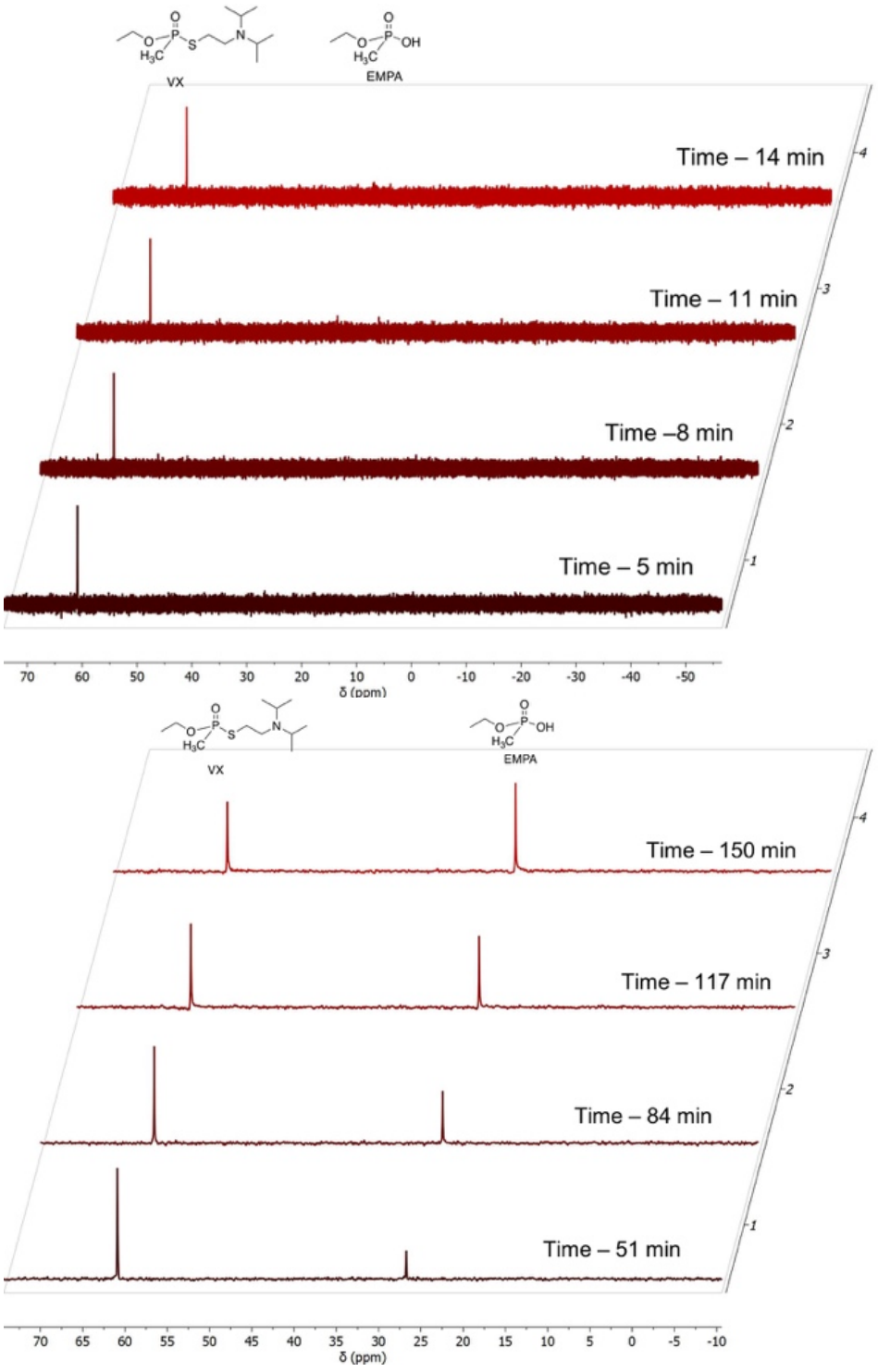


**Figure 4.12.** $^{31}$P spectra of VX hydrolysis to EMPA by DUT-67(Zr) for first 14 min (*top*) and 150 min (*bottom*) of experiment. *Note*: None of toxic byproduct *S*-2-(diisopropylamino)ethyl *O*-hydrogen methylphosphonothioate (EA-2192, NMR Shift 43.1) was detected.

Prior to VX absorbance assay collection, $^{31}P$ NMR tests were run with a small amount of DTNB with MOF and VX to test if DTNB could detect DESH, the hydrolysis product of VX. Upon addition of VX to the solution containing the DUT-67(Zr), the solution immediately turned yellow (Figure S4.13), proving that DTNB could serve as a reporter molecule for DESH, even in low concentrations. This simple proof-of-concept combined with the use of a reporter in VX absorbance spectroscopy studies underscores the significance of this HTS methodology and that it could be implemented for HTS of VX and related P-S agents in future work. The ability to efficiently monitor the rates of six MOFs for VX using a reporter and compare the rates to simulant serves as a major step forward in bridging the gap for chemical understanding of warfighter protection.

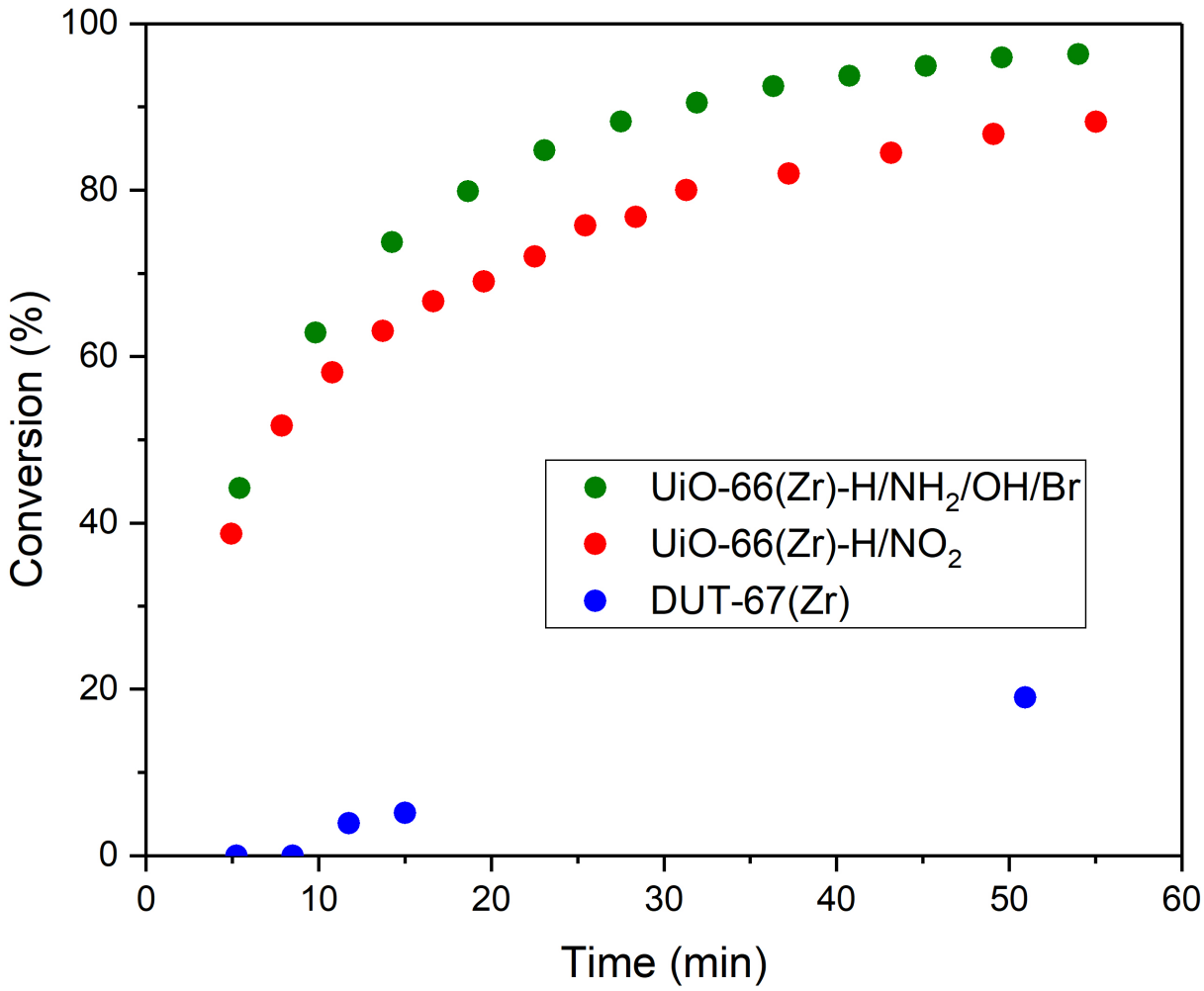


**Figure 4.13.** Percent conversion of VX to EMPA monitored by $^{31}$P NMR for three MOFs: UiO-66(Zr)-H/$NH_2$/OH/Br, UiO-66(Zr)-H/$NO_2$, and DUT-67(Zr).

## 4.5 Conclusions

The use of a reporter molecule allowed for the development of high-throughput and medium-throughput screens for DEPPT and VX, respectively. The volume of data produced by these methods and those developed in Chapter 2 allowed for more progress towards the goal of identifying materials for organophosphate hydrolysis. While the use of a single simulant has proved not to be informative for agent hydrolysis in previous

reports and in this work, the use of multiple simulants may be the most suitable for academic institutions.

In addition, the proof-of-concept for medium-throughput screening of VX proves that agents can be adapted for use in HTS. In the future, the screening of MOF materials and their upstream polymer composites against nerve agents instead of simulants with HTS provides a way to narrow down to the important materials. This saving of time allows for both in depth analysis of parameters that may affect the chemically different nerve agents and minimizes bias in selecting the best material and formulation.

## 4.6 Appendix: Supporting Information

**General Materials and Methods.** All solvents and starting materials were purchased from chemical suppliers and used without further purification (Sigma Aldrich, Alfa Aesar, EMD, and TCI). Some materials (MOFs, metal oxides, and zeolites) used in HTS were purchased from suppliers and used without further purification.

**Powder X-ray Diffraction (PXRD).** PXRD data was collected at room temperature on a Bruker D8 Advance diffractometer running at 40 kV, 40 mA for Cu Kα ($\lambda$ = 1.5418 Å), with primary slit of 1 mm, a scan speed of 0.5 sec/step, a step size of 0.01° in 2θ, and a 2θ range of 3-50° at room temperature.

### Experimental

**Synthetic Procedures.** MOFs purchased from suppliers were used without further purification. All MOFs regardless of synthesis conditions were subjected to

overnight activation at 50 °C in a vacuum oven under active vacuum. MOF crystallinity was accessed via powder X-ray diffraction.

**Synthesis of mixed metal UiO-66(Zr/Hf).** MOFs were synthesized according to literature procedure,[1] but with an equimolar mixture $ZrCl_4$ and $HfCl_4$ as metal sources.

**Synthesis of mixed metal MOF-808(Zr/Hf).** MOFs were synthesized according to literature procedure,[2] but with an equimolar mixture $ZrCl_4$ and $HfCl_4$ as metal sources.

**Preparation of *N*-ethylmorpholine Buffers.** To prepare 20 mM *N*-ethylmorpholine buffer, 0.5 mL (4.0 mmol) of *N*-ethylmorpholine was added to 200 mL of di$H_2O$ with stirring and the pH was monitored. The 20 mM *N*-ethylmorpholine solution produced a pH of 10.4. To adjust to the desired pH (7.0, 7.4, or 8.0), ~1 M HCl was added dropwise while continuously monitoring the pH.

**Thiophenol Calibration Curves.** A dilution series of thiophenol with concentrations from 25.0 to 0.025 mM were made in $CH_3OH$. 5 µL of these thiophenol solutions were added to mixtures of 95 µL of 20 mM *N*-ethyl morpholine (NEM) buffer adjusted to pH = 8.0 or 7.4 and 5 µL of 50 mM 5,5-dithiobis-(2-nitrobenzoic acid) (DTNB) in $CH_3OH$. This was prepared in individual wells of a 96-well clear-bottom polystyrene plate, and absorbance at 440 nm was monitored and plotted for each concentration. A linear fit was used to determine the effective extinction coefficient.

**Control Testing for DEPPT Assay.** Control wells were prepared with UiO-66(Zr) suspended in pH = 8.0 *N*-ethylmorpholine solution containing DTNB and DEPPT separately. A third control was prepared with no DTNB, no DEPPT and no MOF. Over the course of the assay, there was minimal change in absorbance for all three controls,

indicating there is little background hydrolysis without MOF and reaction of DTNB with MOF.

**DEPPT HTS Assay Development.** A series of MOFs previously studied with DMNP HTS assay with different activity (15 MOFs) were screened to identify suitable assay conditions. The change in absorbance was also monitored at 550 nm as a reference. Over the 30 min course of the assay, some MOFs had an increase at 440 nm but not at 550 nm indicating that they could hydrolyze DEPPT (Figure S5). Some MOFs settled in the bottom of the well over the course of the assay causing an increase in absorbance, which was shown both at 440 and 550 nm, an example is Y-ImDC showing similar rate for both wavelengths and is therefore a false positive (Figure S4.3).

**DEPPT Post Assay Control Testing.** To evaluate false positives, a visual inspection was performed on all assay plates, wells without a color change were flagged. Those with significant slope, >10 mM/sec $\times$ $10^{-6}$, were retested under the same conditions as DEPPT HTS, but with DEPPT solution replaced with pure $CH_3OH$, these samples were labeled “No DEPPT” and reported in Table S2.

**HTS assay for DEPPT.** In individual wells of a clear-bottom 96-well plate (Olympus Plastics), 90 µL of MOF stock suspension (250 µL of 12 mg/mL MOF in $H_2O$, 150 µL of 40 mM *N*-ethyl morpholine (NEM) buffer adjusted to pH = 8.0 or 7.4, and 150 µL of $H_2O$) were added. To each well, 5 µL of 10 mM 5,5-dithiobis-(2-nitrobenzoic acid) (DTNB) solution in $CH_3OH$ was added. To initiate the reaction, 5 µL of 50 mM *O*,*O*-diethyl *S*-phenyl phosphorothioate (DEPPT) solution in $CH_3OH$ was added to each well using a multichannel pipet. Absorbance at 440 nm was monitored every 34 sec for 50 min with

shaking (2 sec) between each reading. Hydrolysis rates were calculated from an average initial slope from the linear region (typically 200-800 sec) of absorbance vs. time trace. Each 96-well plate included four wells of each MOF for statistical analysis.

**DEPPT Serial Absorbance Assay.** MOF solution was prepared in a 1.5 mL centrifuge tube with: 250 µL of 1.2 mg/mL MOF suspension (in $H_2O$), 400 µL of $H_2O$, 400 µL of 40 mM N-ethylmorpholine solution (in $H_2O$), and 50 µL of 10 mM DTNB solution (in $CH_3OH$). Experiment was initiated with 50 µL of 50 mM DEPPT (in $CH_3OH$) added to centrifuge tube with above solutions, solution mixed, and 1 mL added to cuvette. A spectral scan was taken from 375-600 nm with a scan every 44 sec for 45 min. Data shown in Figure S4.10.

**Hydrolysis of VX monitored by Absorbance Spectroscopy.** Caution! Nerve agents (VX) are extremely toxic compounds and experiments should only be conducted by trained personnel in a laboratory that is permitted to use such agents. VX assays were conducted as described above for DEPPT (pH = 8.0) with the substitution of VX for DEPPT and the use of a Jasco V-730 spectrophotometer for measurements. Absorbance readings were obtained every 23 sec. The cuvette volume was 1.5 mL and assays were conducted with continuous stirring at 400 rpm. VX was of >95% purity as determined by $^{31}P$ NMR and mass spectroscopy.

**Hydrolysis of VX monitored by $^{31}P$ NMR.** Caution! Nerve agents (VX) are extremely toxic compounds and experiments should only be conducted by trained personnel in a laboratory that is permitted to use such agents. Hydrolysis of VX to ethyl methylphosphonic acid (EMPA) was monitored in situ using $^{31}P$ NMR. MOF (1.5 µmol)

and DTNB (1 mg, 2.5 μmol) were dispersed in 1 mL of 40 mM, pH 8.0 NEM solution in 9:1 di$H_2O$/$D_2O$ mixture and sonicated for 1-2 min to break up MOF particle aggregates. This suspension was transferred to an NMR tube and VX (3.9 μL, 14.7 μmol) was added to the tube followed by shaking. The reaction mixture was placed into the NMR instrument and spectra were taken immediately (first time point at 1 min). Each spectrum was the average of 32 scans and the time point was recorded at the end of each spectrum. Percent conversion was calculated by relative integration of VX peak (62.5 ppm) and ethyl methylphosphonic acid (EMPA) peak (28.3 ppm).

## Supplemental Tables

**Table S4.1.** Hydrolysis rates (average of four wells in mM/sec × $10^{-6}$) and their standard deviations (σ) for DEPPT and DMNP based on HTS assay. Color indicates relative rates for each simulant (dark green is highest, red is lowest). Unless otherwise indicated, DMNP hydrolysis is reproduced from referenced literature. Rates have been adjusted for molecular weight of MOF. Rounded brackets () indicate metal; curly brackets { } indicate modulator used in synthesis; [ ] indicate suppliers (where applicable). In the case of UiO-66 MOFs synthesized from multiple functionalized terephthalic acid, the designation A, B, C, D, and E represent an equimolar contribution of -H, -$NH_2$, -OH, -$NO_2$, and -Br, respectively, functionalized terephthalic acid ligand in the MOF structure (See Chapter 3).

| Name | DEPPT Rate (Molar) | σ | DMNP Rate (Molar) | σ | Citation |
|---|---|---|---|---|---|
| UiO-66(Zr)-CDE | 220.8 | 16.9 | 208.9 | 36.4 | [5] |
| UiO-66-$NH_2$-High Defects | 203.1 | 41.6 | 96.9 | 3.4 | [4] |
| UiO-66(Zr)-ABDE | 197.6 | 8.0 | 204.0 | 43.8 | [5] |
| UiO-66(Zr)-AD | 193.6 | 54.2 | 308.6 | 48.1 | [5] |
| UiO-66(Zr)-ACDE | 185.7 | 9.7 | 204.1 | 32.6 | [5] |
| UiO-66(Zr)-ABCDE | 185.6 | 3.6 | 275.9 | 43.4 | [5] |
| UiO-66(Zr)-ABCE | 173.6 | 17.9 | 62.9 | 32.0 | [5] |
| UiO-66(Zr)-BDE | 137.8 | 28.1 | 204.3 | 53.6 | [5] |
| UiO-66(Zr)-E | 128.4 | 46.1 | 154.3 | 10.2 | [5,6] |
| UiO-66(Zr)-F | 124.4 | 7.4 | 226.0 | 0.0 | [6] |
| UiO-66(Zr)-ABC | 120.2 | 5.3 | 365.5 | 34.6 | [5] |
| UiO-66(Zr/Hf) | 115.2 | 1.9 | 325.1 | 11.5 | This work[1] |
| UiO-66(Zr)-ADE | 109.8 | 6.6 | 348.5 | 18.6 | [5] |
| UiO-66(Zr)-CD | 107.7 | 5.0 | 241.3 | 31.6 | [5] |
| UiO-66(Zr) [Strem] | 105.6 | 8.7 | | | Strem |
| $TiO_2$ [Aldrich] | 101.9 | 19.1 | 0.7 | 7.1 | [4] |
| UiO-66(Zr)-BD | 96.2 | 4.6 | 322.8 | 27.7 | [5] |
| UiO-66-$NH_2$ {HCl} | 90.5 | 3.9 | 77.4 | 4.2 | [4] |
| UiO-66(Zr)-Cl | 87.4 | 2.2 | 194.0 | 26.0 | [6] |
| UiO-66(Zr)-ACD | 86.4 | 2.6 | 208.0 | 19.0 | [5] |
| UiO-66(Zr)-I | 86.2 | 1.0 | 605.0 | 107.0 | [6] |

| | | | | | |
|---|---|---|---|---|---|
| UiO-66(Zr)-$NH_2$-Med Defects | 85.2 | 6.4 | 60.8 | 2.8 | [4] |
| UiO-66(Zr)-AE | 76.5 | 4.9 | 189.3 | 44.9 | [5] |
| UiO-66(Zr)-AB | 75.5 | 2.4 | 227.7 | 17.6 | [5] |
| UiO-66(Zr)-DE | 64.2 | 1.6 | 59.1 | 5.2 | [5] |
| UiO-66(Zr)-ABD | 62.5 | 5.6 | 301.6 | 16.1 | [5] |
| $TiO_2$ | 62.0 | 0.6 | -1.4 | 0.8 | [4] |
| UiO-66(Zr)-BCDE | 61.6 | 4.1 | 374.6 | 11.7 | [5] |
| UiO-66(Zr)-ABCD | 58.1 | 1.4 | 334.6 | 18.6 | [5] |
| UiO-66(Zr)-BCD | 57.4 | 2.3 | 343.1 | 28.2 | [5] |
| UiO-66(Zr)-A {HOAc} | 53.2 | 4.7 | 175.8 | 22.5 | [5] |
| UiO-66(Zr)-ABE | 52.4 | 2.9 | 381.3 | 13.2 | [5] |
| UiO-66(Zr)-C | 49.1 | 14.8 | 105.9 | 9.9 | [5] |
| UiO-66(Zr)-D | 42.3 | 13.5 | 60.6 | 12.5 | [5] |
| UiO-67(Zr) | 37.5 | 0.9 | 179.5 | 10.8 | [4] |
| UiO-66(Zr)-AC | 36.8 | 4.5 | 197.9 | 26.6 | [5] |
| Zeolite 4A | 34.8 | 3.6 | 6.9 | 7.9 | [4] |
| UiO-66(Zr)-B | 34.2 | 3.1 | 80.2 | 4.1 | [5] |
| UiO-66(Zr)-$SO_3H$ | 32.1 | 2.3 | 21.7 | 1.0 | [4] |
| UiO-66(Zr) {HCl} | 31.9 | 0.7 | 49.7 | 5.1 | [4] |
| UiO-66(Zr)-CE | 27.1 | 10.7 | 181.7 | 78.1 | [5] |
| UiO-66(Zr)-BE | 24.7 | 8.4 | 446.3 | 18.3 | [5] |
| $Mg(OH)_2$ | 23.0 | 2.8 | 3.0 | 2.5 | [4] |
| UiO-66(Zr)-$NH_2$ (acetone) | 22.6 | 1.2 | 62.1 | 3.8 | [4] |
| NU-1000(Zr) | 22.3 | 12.0 | 16.2 | 3.0 | [4] |
| UiO-66(Zr) (acetone) | 22.2 | 1.4 | 63.1 | 5.2 | [4] |
| DUT-67(Hf) | 18.7 | 1.8 | 6.9 | 0.5 | [4] |
| Y-54 DR | 18.5 | 1.4 | 19.9 | 2.9 | [4] |
| Basolite F100 | 18.1 | 20.6 | -8.2 | 50.7 | [4] |
| MOF-808(Hf/Zr) | 17.0 | 2.4 | 198.0 | 14.3 | This work[2] |
| MOF-808(Zr) | 16.2 | 0.6 | 28.1 | 1.4 | [4] |
| ZnO | 14.4 | 4.4 | 6.4 | 16.9 | [4] |
| UiO-66(Zr)-$NH_2$-Low Defects | 14.2 | 6.5 | 4.2 | 2.4 | [4] |
| UiO-66(Zr)-BCE | 13.2 | 2.7 | 271.4 | 61.3 | [4] |

| | | | | | |
|---|---|---|---|---|---|
| MOF-808(Hf) | 12.7 | 5.5 | 162.3 | 2.8 | This work[2] |
| MIL-53(Al)-Br | 12.3 | 10.0 | -0.2 | 0.8 | [4] |
| HKUST-1(Cu) [Aldrich] | 12.3 | 1.6 | 4.2 | 3.9 | [4] |
| pek-MOF-1(Y) | 12.1 | 5.2 | 79.2 | 36.3 | This work[7] |
| Al-PMOF | 10.9 | 2.4 | -1.7 | 1.6 | [4] |
| $Zr(OH)_4$ Type C | 10.0 | 6.2 | 1.5 | 0.2 | [4] |
| PCN-415 | 10.0 | 67.4 | 15.1 | 0.6 | [4] |
| MCM-41 Aldrich | 9.3 | 1.3 | -0.4 | 1.0 | [4] |
| UiO-66(Zr)-BC | 8.9 | 8.4 | 136.4 | 39.0 | [5] |
| Cu-PCN | 8.8 | 2.7 | -0.1 | 0.2 | [4] |
| Tb-BTC | 8.2 | 2.3 | 0.7 | 2.8 | This work[8] |
| MIL-100(Fe) | 8.0 | 1.0 | -1.4 | 1.8 | [4] |
| MOF-801(Zr) | 7.5 | 0.4 | 3.7 | 0.5 | [4] |
| MOF-508(Zn) | 6.5 | 2.4 | -0.5 | 1.0 | [4] |
| MIL-88B(Fe) | 6.2 | 5.8 | 1.7 | 2.0 | [4] |
| MIL-100(Al) | 5.8 | 4.0 | 2.3 | 3.0 | [4] |
| PCN-700(Zr) | 5.4 | 1.7 | 11.1 | 5.4 | [4] |
| Na-ZSM-5 | 5.3 | 0.4 | -2.6 | 2.8 | [4] |
| DUT-67(Zr) | 5.2 | 1.3 | 3.1 | 15.2 | [4] |
| Y-BTC | 2.7 | 7.1 | 0.3 | 1.4 | This work[8] |
| SAPO-34 | 2.5 | 0.3 | -4.3 | 1.6 | [4] |
| Er-BTC | 2.3 | 0.1 | 1.2 | 0.7 | This work[8] |
| $Eu_2O_3$ | 2.3 | 2.1 | -0.6 | 7.6 | [4] |
| MIL-53(Fe) | 2.2 | 1.4 | 0.0 | 0.1 | [4] |
| DMOF-1(Zn) | 2.1 | 0.7 | 1.7 | 2.3 | [4] |
| H-ZSM-5 | 1.5 | 0.6 | 0.8 | 1.3 | [4] |
| UiO-66(Zr)-COOH | 1.5 | 7.0 | 3.0 | 0.0 | [4] |
| Dy-BTC | 1.4 | 1.5 | 5.0 | 2.9 | This work[8] |
| $TiO_2$ Degussa $P_{25}$ | 1.1 | 14.8 | -0.1 | 0.2 | [4] |
| CAU-10(Al)-OH | 1.0 | 1.2 | 0.2 | 1.4 | [4] |
| $Zr(OH)_4$ 0880 | 1.0 | 0.1 | 4.2 | 0.6 | [4] |
| $Zr(OH)_4$ Type C $KMnO_4$ | 0.9 | 0.4 | 4.3 | 2.5 | [4] |

| | | | | | |
|---|---|---|---|---|---|
| CAU-10(Al)-$NH_2$ | 0.6 | 0.1 | 2.6 | 3.0 | [4] |
| MOF-74(Cu) | 0.5 | 0.1 | -0.5 | 0.8 | [4] |
| MIL-53(Cr) | 0.4 | 0.0 | -0.2 | 0.0 | [4] |
| $Fe_2O_3$ | 0.4 | 0.4 | 6.1 | 5.4 | [4] |
| pek-MOF-1(Tb) | 0.4 | 0.3 | 13.8 | 6.2 | This work[7] |
| ZIF-71(Zn) | 0.2 | 0.1 | 0.4 | 0.7 | [4] |
| CAU-10(Al)-$CH_3$ | 0.2 | 0.2 | 3.7 | 6.3 | [4] |
| MIL-96(Al) | 0.1 | 0.1 | 0.6 | 1.4 | [4] |
| $Al_2O_3$ | 0.1 | 0.1 | 0.0 | 0.0 | [4] |
| ZIF-62(Zn) | 0.0 | 0.0 | 0.1 | 0.2 | [4] |
| PCN-250(Fe) | 0.0 | 0.3 | 2.0 | 1.4 | [4] |
| UiO-66-$NH_2$(Zr) [Strem] | -0.1 | 0.1 | 12.9 | 0.8 | [4] |
| PCN-250(Mn) | -0.2 | 0.5 | 0.9 | 0.9 | [4] |
| PCN-250(Cu) | -0.2 | 0.1 | 2.3 | 4.2 | [4] |
| Silicate | -0.3 | 2.1 | 1.3 | 0.4 | [4] |
| No MOF-Control | -0.4 | 0.1 | | | This work |
| $Co_3O_4$ | -0.5 | 0.2 | -4.2 | 0.9 | [4] |
| Ni-NIC | -0.6 | 0.3 | 0.1 | 0.1 | [4] |
| $Zr(OH)_4$ Type A | -0.8 | 0.8 | -3.4 | 2.8 | [4] |
| $Zr(OH)_4$ Type B | -0.9 | 0.6 | 4.9 | 2.9 | [4] |
| MIL-53(Al)-$NH_2$ | -1.0 | 0.3 | -0.2 | 0.1 | [4] |
| PCN-224 | -1.0 | 0.6 | 18.6 | 1.8 | [4] |
| MOF-802(Zr) | -1.0 | 0.7 | 3.6 | 1.9 | [4] |
| PIM-1 | -2.1 | 0.1 | -4.5 | 6.6 | [4] |
| MIL-101(Cr) | -13.8 | 3.8 | 0.5 | 1.9 | [4] |
| $CeO_2$ | -14.8 | 14.5 | 9.3 | 4.8 | [4] |
| $TiO_2$ Anatase [Aldrich] | -25.0 | 4.6 | -0.8 | 0.6 | [4] |

**Table S4.2.** Hydrolysis rates (average of four wells in mM/sec $\times 10^{-6}$) and their standard deviations ($\sigma$) for DEPPT and No DEPPT Control based on same HTS assay conditions. Color indicates relative rates for each simulant (dark green is highest, red is lowest). These samples were identified visually as wells with no liquid color change (except for DUT-67(Zr) included as a control with color change). The No DEPPT rates are high enough in all cases (except HKUST-1 and DUT-67(Zr)) to confirm these samples as false positives.

| **Name** | **DEPPT Rate** | ***σ*** | **No DEPPT Rate** | ***σ*** |
|---|---|---|---|---|
| $TiO_2$ [Aldrich] | 101.86 | 19.12 | 64.93 | 30.82 |
| MIL-53(Al)-Br | 69.35 | 56.27 | -29.48 | 40.44 |
| $TiO_2$ | 62.00 | 0.58 | -7.74 | 8.15 |
| Cu-PCN | 35.18 | 10.54 | 28.07 | 5.55 |
| Zeolite 4A | 34.76 | 3.60 | 9.59 | 2.37 |
| Tb-BTC | 34.65 | 9.80 | 45.27 | 11.54 |
| HKUST-1(Cu) [Aldrich] | 32.81 | 4.39 | 6.63 | 1.90 |
| MOF-508 | 28.93 | 10.65 | 7.57 | 8.73 |
| $Mg(OH)_2$ | 22.97 | 2.83 | 17.08 | 0.95 |
| MIL-100(Fe) | 20.56 | 2.54 | 27.55 | 22.32 |
| Al-PMOF | 20.36 | 4.51 | overflow | overflow |
| Y-54 DR | 18.54 | 1.41 | 9.47 | 1.92 |
| MIL-100(Al) | 17.29 | 11.93 | 38.81 | 16.69 |
| MIL-53(Fe) | 14.90 | 9.31 | 119.01 | 44.03 |
| DUT-67(Zr) | 6.16 | 1.60 | 0.56 | 0.48 |

**Table S4.3.** Hydrolysis rates (average of four wells in mM/sec × $10^{-6}$) and their standard deviations (σ) for DEPPT and DMNP based on HTS assay for MOF based on mass. Molecular weights and ratio to UiO-66(Zr) were used to calculate values in Table S1.

| Name | DEPPT | *σ* | DMNP | *σ* | Formula[a] | MW (g/mol) | Ratio to UiO-66(Zr) |
|---|---|---|---|---|---|---|---|
| UiO-66-$NH_2$-HD | 192.4 | 39.4 | 91.8 | 3.2 | $Zr_6O_6$(BDC-$NH_2$)$_6$ | 1718.0 | 0.95 |
| UiO-66-CDE | 191.3 | 14.7 | 208.9 | 36.4 | $Zr_6O_6$(BDC-OH)$_2$(BDC-$NO_2$)$_2$(BDC-Br)$_2$ | 1878.7 | 0.87 |
| UiO-66-AD | 180.3 | 50.5 | 308.6 | 48.1 | $Zr_6O_6$(BDC)$_3$(BDC-$NO_2$)$_3$ | 1748.0 | 0.93 |
| UiO-66-ABDE | 175.9 | 7.1 | 204.0 | 43.8 | $Zr_6O_6$(BDC)$_{1.5}$(BDC-$NH_2$)$_{1.5}$(BDC-$NO_2$)$_{1.5}$(BDC-Br)$_{1.5}$ | 1828.8 | 0.89 |
| UiO-66-ABCDE | 167.1 | 3.2 | 275.9 | 43.4 | $Zr_6O_6$(BDC)$_{1.2}$(BDC-$NH_2$)$_{1.2}$(BDC-OH)$_{1.2}$(BDC-$NO_2$)$_{1.2}$(BDC-Br)$_{1.2}$ | 1807.8 | 0.90 |
| UiO-66-ACDE | 165.2 | 8.6 | 204.1 | 32.6 | $Zr_6O_6$(BDC)$_{1.5}$(BDC-OH)$_{1.5}$(BDC-$NO_2$)$_{1.5}$(BDC-Br)$_{1.5}$ | 1830.3 | 0.89 |
| UiO-66-ABCE | 157.6 | 16.3 | 62.9 | 32.0 | $Zr_6O_6$(BDC)$_{1.5}$(BDC-$NH_2$)$_{1.5}$(BDC-OH)$_{1.5}$(BDC-Br)$_{1.5}$ | 1792.8 | 0.91 |
| UiO-66-BDE | 119.5 | 24.3 | 204.3 | 53.6 | $Zr_6O_6$(BDC-$NH_2$)$_2$(BDC-$NO_2$)$_2$(BDC-Br)$_2$ | 1876.7 | 0.87 |
| UiO-66-ABC | 117.0 | 5.2 | 365.5 | 34.6 | $Zr_6O_6$(BDC)$_2$(BDC-$NH_2$)$_2$(BDC-OH)$_2$ | 1673.1 | 0.97 |
| UiO-66-F | 116.7 | 6.9 | 226.0 | | $Zr_6O_6$(BDC-F)$_6$ | 1736.0 | 0.94 |
| UiO-66 [Strem] | 105.6 | 8.7 | | | $Zr_6O_6$(BDC)$_6$ | 1628.0 | 1.00 |
| UiO-66-E | 99.5 | 35.7 | 154.3 | 10.2 | $Zr_6O_6$(BDC-Br)$_6$ | 2101.0 | 0.77 |
| UiO-66(Zr/Hf) | 99.2 | 1.7 | 280.0 | 11.5 | $Zr_3Hf_3O_6$(BDC)$_6$ | 1889.8 | 0.86 |

| | | | | | | | |
|---|---|---|---|---|---|---|---|
| UiO-66-CD | 97.6 | 4.5 | 241.3 | 31.6 | $Zr_6O_6(BDC\text{-}OH)_3(BDC\text{-}NO_2)_3$ | 1796.0 | 0.91 |
| UiO-66-ADE | 89.9 | 5.4 | 348.5 | 18.6 | $Zr_6O_6(BDC)_2(BDC\text{-}NO_2)_2(BDC\text{-}Br)_2$ | 1988.1 | 0.82 |
| UiO-66-BD | 87.4 | 4.1 | 322.8 | 27.7 | $Zr_6O_6(BDC\text{-}NH_2)_3(BDC\text{-}NO_2)_3$ | 1793.0 | 0.91 |
| UiO-66-$NH_2$ {HCl} | 85.8 | 3.7 | 73.4 | 3.9 | $Zr_6O_6(BDC\text{-}NH_2)_6$ | 1718.0 | 0.95 |
| UiO-66-ACD | 81.6 | 2.5 | 208.0 | 19.0 | $Zr_6O_6(BDC)_2(BDC\text{-}OH)_2(BDC\text{-}NO_2)_2$ | 1722.6 | 0.95 |
| UiO-66-NH2-MD | 80.7 | 6.1 | 57.6 | 2.7 | $Zr_6O_6(BDC\text{-}NH_2)_6$ | 1718.0 | 0.95 |
| UiO-66-Cl | 77.5 | 1.9 | 194.0 | 26.0 | $Zr_6O_6(BDC\text{-}Cl)_6$ | 1834.7 | 0.89 |
| UiO-66-AB | 73.4 | 2.3 | 227.7 | 17.6 | $Zr_6O_6(BDC)_3(BDC\text{-}NH_2)_3$ | 1673.0 | 0.97 |
| MIL-53(Al)-Br | 69.4 | 56.3 | -1.3 | 4.4 | Al(OH)(BDC-Br) | 289.0 | 5.63 |
| UiO-66-AE | 66.8 | 4.3 | 189.3 | 44.9 | $Zr_6O_6(BDC)_3(BDC\text{-}Br)_3$ | 1864.5 | 0.87 |
| UiO-66-ABD | 59.1 | 5.3 | 301.6 | 16.1 | $Zr_6O_6(BDC)_2(BDC\text{-}NH_2)_2(BDC\text{-}NO_2)_2$ | 1720.6 | 0.95 |
| UiO-66-I | 58.9 | 0.7 | 605.0 | 107.0 | $Zr_6O_6(BDC\text{-}I)_6$ | 2383.4 | 0.68 |
| UiO-66-ABCD | 54.6 | 1.3 | 334.6 | 18.6 | $Zr_6O_6(BDC)_{1.5}(BDC\text{-}NH_2)_{1.5}(BDC\text{-}OH)_{1.5}(BDC\text{-}NO_2)_{1.5}$ | 1734.5 | 0.94 |
| UiO-66-BCDE | 54.2 | 3.6 | 374.6 | 11.7 | $Zr_6O_6(BDC\text{-}NH_2)_{1.5}(BDC\text{-}OH)_{1.5}(BDC\text{-}NO_2)_{1.5}(BDC\text{-}Br)_{1.5}$ | 1852.8 | 0.88 |
| UiO-66-BCD | 53.4 | 2.1 | 343.1 | 28.2 | $Zr_6O_6(BDC\text{-}NH_2)_2(BDC\text{-}OH)_2(BDC\text{-}NO_2)_2$ | 1752.3 | 0.93 |
| UiO-66-A | 53.2 | 4.7 | 175.8 | 22.5 | $Zr_6O_6(BDC)_6$ | 1628.0 | 1.00 |

| | | | | | | | |
|---|---|---|---|---|---|---|---|
| UiO-66-DE | 52.7 | 1.4 | 59.1 | 5.2 | $Zr_6O_6(BDC\text{-}NO_2)_3(BDC\text{-}Br)_3$ | 1984.5 | 0.82 |
| UiO-66-ABE | 47.5 | 2.6 | 381.3 | 13.2 | $Zr_6O_6(BDC)_2(BDC\text{-}NH_2)_2(BDC\text{-}Br)_2$ | 1797.5 | 0.91 |
| UiO-66-C | 46.4 | 14.0 | 105.9 | 9.9 | $Zr_6O_6(BDC\text{-}OH)_6$ | 1724.0 | 0.94 |
| UiO-67 | 37.5 | 0.9 | 179.5 | 10.8 | $Zr_6O_6(BPDC)_6$ | 2087.6 | 1.00 |
| UiO-66-D | 36.9 | 11.8 | 60.6 | 12.5 | $Zr_6O_6(BDC\text{-}NO_2)_6$ | 1868.0 | 0.87 |
| UiO-66-AC | 35.7 | 4.4 | 197.9 | 26.6 | $Zr_6O_6(BDC)_3(BDC\text{-}OH)_3$ | 1676.0 | 0.97 |
| UiO-66-ACE | 35.4 | 3.2 | 346.0 | 35.7 | $Zr_6O_6(BDC)_2(BDC\text{-}OH)_2(BDC\text{-}Br)_2$ | 1799.5 | 0.90 |
| Cu-PCN | 35.2 | 10.5 | -0.4 | 0.8 | $Cu_2(PCN)_2(H_2O)_2$ | 409.3 | 3.98 |
| Tb-BTC | 34.6 | 9.8 | 3.1 | 12.1 | $Tb(BTC)(H_2O)$ | 384.1 | 4.24 |
| HKUST-1 [Aldrich] | 32.8 | 4.4 | 11.2 | 10.3 | $Cu_3(BTC)_2$ | 610.9 | 2.66 |
| UiO-66-B | 32.4 | 2.9 | 80.2 | 4.1 | $Zr_6O_6(BDC\text{-}NH_2)_6$ | 1718.0 | 0.95 |
| UiO-66 {HCl} | 31.9 | 0.7 | 49.7 | 5.1 | $Zr_6O_6(BDC)_6$ | 1628.0 | 1.00 |
| MOF-508 | 28.9 | 10.6 | -2.4 | 4.3 | Zn(BDC)(BPY) | 363.7 | 4.48 |
| UiO-66-$SO_3H$ | 24.7 | 1.7 | 16.6 | 0.8 | $Zr_6O_6(BDC\text{-}SO_3H)_6$ | 2120.5 | 0.77 |
| UiO-66-CE | 23.1 | 9.1 | 181.7 | 78.1 | $Zr_6O_6(BDC\text{-}OH)_3(BDC\text{-}Br)_3$ | 1912.5 | 0.85 |
| UiO-66 (acetone) | 22.2 | 1.4 | 63.1 | 5.2 | $Zr_6O_6(BDC)_6$ | 1628.0 | 1.00 |
| UiO-66-$NH_2$ (acetone) | 21.4 | 1.1 | 58.8 | 3.6 | $Zr_6O_6(BDC\text{-}NH_2)_6$ | 1718.0 | 0.95 |
| UiO-66-BE | 21.1 | 7.2 | 446.3 | 18.3 | $Zr_6O_6(BDC\text{-}NH_2)_3(BDC\text{-}Br)_3$ | 1909.5 | 0.85 |
| MIL-100(Fe) | 20.6 | 2.5 | -3.7 | 4.7 | $Fe_3OX(BTC)_2$, X=OH, F, Cl | 633.2 | 2.57 |
| Al-PMOF | 20.4 | 4.5 | -3.2 | 3.0 | $(AlOH)_2(TCPP)$ | 868.7 | 1.87 |

| | | | | | | | |
|---|---|---|---|---|---|---|---|
| MOF-808(Zr) | 19.3 | 0.7 | 33.4 | 1.7 | $Zr_6O_4(OH)_4(BTC)_2(HCOO)_6$ | 1369.0 | 1.19 |
| MIL-100(Al) | 17.3 | 11.9 | 6.8 | 8.9 | $Al_3OX(BTC)_2$, X=OH, F, Cl | 546.4 | 2.98 |
| MOF-808(Hf/Zr) | 17.0 | 2.4 | 198.3 | 14.3 | $Zr_3Hf_3O_4(OH)_4(BTC)_2(HCOO)_6$ | 1625.5 | 1.00 |
| NU-1000 | 16.7 | 9.0 | 12.1 | 2.3 | $Zr_6(OH)_{16}(TBAPY)_2$ | 2176.8 | 0.75 |
| DUT-67(Hf) | 16.1 | 1.5 | 5.9 | 0.4 | $Hf_6O_6(OH)_2(TDC)_4$ | 1889.6 | 0.86 |
| MIL-53(Fe) | 14.9 | 9.3 | 0.0 | 0.3 | Fe(OH)(BDC) | 239.0 | 6.81 |
| Y-BTC | 14.0 | 36.6 | 1.4 | 7.2 | $Y(BTC)(H_2O)$ | 314.0 | 5.18 |
| MIL-88B(Fe) | 13.5 | 12.7 | 3.6 | 4.4 | $Fe_3O(BDC)_3(H_2O)_2(X)$, X=OH, Cl | 747.4 | 2.18 |
| UiO-66-$NH_2$-LD | 13.4 | 6.1 | 4.0 | 2.3 | $Zr_6O_6(BDC\text{-}NH_2)_6$ | 1718.0 | 0.95 |
| Basolite F100 | 12.3 | 14.0 | -5.6 | 34.6 | Fe(OH)(BTC) | 2387.2 | 0.68 |
| pek-MOF-1(Y) | 12.1 | 5.2 | 79.2 | 36.3 | $[Y_9(OH)_{12}(O)_2(H2O)_9][(Y_6(OH)_8(C_7H_4FO_2)_2(HCO_2)_2(C_3H_7NO)_{0.67}(H_2O)_4)_3(C_{15}H_7O_6)_{12}]$ | 8073.3 | 1.00 |
| UiO-66-BCE | 11.7 | 2.4 | 271.4 | 61.3 | $Zr_6O_6(BDC\text{-}NH_2)_2(BDC\text{-}OH)_2(BDC\text{-}Br)_2$ | 1829.2 | 0.89 |
| MOF-808(Hf) | 10.9 | 4.7 | 139.6 | 2.4 | $Hf_6O_4(OH)_4(BTC)_2(HCOO)_6$ | 1893.0 | 0.86 |
| Er-BTC | 9.7 | 0.5 | 5.1 | 3.0 | $Er(BTC)(H_2O)$ | 392.4 | 4.15 |
| MOF-801 | 8.8 | 0.5 | 4.3 | 0.6 | $Zr_6O_4(OH)_4(FUM)_6$ | 1375.8 | 1.18 |
| Yb-BTC | 8.7 | 0.9 | | | $Yb(BTC)(H_2O)$ | 398.2 | 4.09 |
| UiO-66-BC | 8.5 | 7.9 | 136.4 | 39.0 | $Zr_6O_6(BDC\text{-}NH_2)_3(BDC\text{-}OH)_3$ | 1721.0 | 0.95 |
| DMOF-1 | 6.8 | 2.2 | 5.3 | 7.4 | $Zn_2(BDC)_2(DABCO)$ | 509.8 | 3.19 |
| DUT-67(Zr) | 6.2 | 1.6 | 3.7 | 18.2 | $Zr_6O_6(OH)_2(TDC)_4$ | 1366.0 | 1.19 |
| Dy-BTC | 5.9 | 6.4 | 20.9 | 12.1 | $Dy(BTC)(H_2O)$ | 387.6 | 4.20 |
| PCN-415(Ti/Zr) | 4.8 | 32.4 | 7.3 | 0.3 | $Ti_8Zr_2O_{12}(BDC)_{16}$ | 3383.2 | 0.48 |

| | | | | | | | |
|---|---|---|---|---|---|---|---|
| PCN-700 | 4.4 | 1.4 | 8.9 | 4.4 | $Zr_6O_8(OH)_8(Me_2\text{-}BPDC)_4$ | 2023.3 | 0.80 |
| CAU-10-OH | 4.0 | 4.6 | 0.9 | 5.4 | Al(OH)(ISO-OH) | 408.3 | 3.99 |
| MIL-53(Cr) | 2.9 | 0.1 | -1.5 | 0.3 | Cr(OH)(BDC) | 235.1 | 6.92 |
| MOF-74(Cu) | 2.7 | 0.3 | -2.6 | 3.9 | $Cu_2$(DOBDC) | 323.9 | 5.03 |
| CAU-10-$NH_2$ | 2.4 | 0.5 | 10.4 | 11.9 | Al(OH)(ISO-$NH_2$) | 406.3 | 4.01 |
| UiO-66-COOH | 1.3 | 6.0 | 2.6 | 0.0 | $Zr_6O_6$(BDC-COOH)$_6$ | 1904.2 | 0.85 |
| ZIF-71(Zn) | 1.0 | 0.3 | 1.8 | 3.4 | Zn(IM-$Cl_2$)$_2$ | 339.3 | 4.80 |
| CAU-10-$CH_3$ | 0.7 | 1.0 | 14.9 | 25.3 | Al(OH)(ISO-$CH_3$) | 404.3 | 4.03 |
| pek-MOF-1(Tb) | 0.4 | 0.3 | 13.8 | 6.2 | $[Tb_9(OH)_{12}(O)_2(H_2O)_9][(Tb_6(OH)_8(C_7H_4FO_2)_2(HCO_2)_2(C_3H_7NO)_{0.67}(H_2O)_4)_3(C_{15}H_7O_6)_{12}]$ | 9963.8 | 1.00 |
| ZIF-62 | 0.1 | 0.1 | 0.7 | 1.7 | $Zn(IM)_{1.75}(BIM)_{0.25}$ | 214.1 | 7.61 |
| MIL-96(Al) | 0.1 | 0.1 | 0.4 | 1.1 | $Al_{12}O(OH)_{18}(H_2O)_3(Al_2(OH)_4)$(BTC)$_6$ | 2065.9 | 0.79 |
| PCN-250(Fe) | 0.0 | 0.2 | 1.3 | 0.9 | $Fe_3(O)(H_2O)_3$(ABTEC)$_6$ | 2387.2 | 0.68 |
| UiO-66-$NH_2$ [Strem] | -0.1 | 0.1 | 12.3 | 0.7 | $Zr_6O_6$(BDC-$NH_2$)$_6$ | 1718.0 | 0.95 |
| PCN-250(Mn) | -0.2 | 0.3 | 0.6 | 0.6 | $Mn_3(O)(H_2O)_3$(ABTEC)$_6$ | 2384.4 | 0.68 |
| PCN-250(Cu) | -0.2 | 0.1 | 1.6 | 2.8 | $Cu_3(O)(H_2O)_3$(ABTEC)$_6$ | 2410.3 | 0.68 |
| No MOF | -0.4 | 0.1 | | | - | | 1.00 |
| MOF-802(Zr) | -1.1 | 0.7 | 3.7 | 2.0 | $Zr_6O_4(OH)_4(PZDC)_5(HCOO)_2(H_2O)_2$ | 1585.9 | 1.03 |
| Ni-NIC | -1.5 | 0.8 | 0.1 | 0.3 | $Ni_2$(NIC)$_4(H_2O)$ | 628.3 | 2.59 |
| MIL-53(Al)-$NH_2$ | -7.2 | 2.1 | -1.1 | 0.9 | Al(OH)(BDC-$NH_2$) | 225.1 | 7.23 |

| | | | | | | | |
|---|---|---|---|---|---|---|---|
| MIL-101(Cr) | -31.7 | 8.7 | 1.1 | 4.4 | $Cr_3F(H_2O)_2O(BDC)_3$ | 709.4 | 2.29 |

[a] Ligand Abbreviations: (ISO) = isophthalic acid; (BTC) = benzene-1,3,5-tricarboxylic acid; (BDC) = benzene-1,4-dicarboxylic acid; (ABTEC) = azobenzene tetracarboxylic acid; (MEIM) = 2-methyl-1*H*-imidazole; (NIC) = nicotinic acid; (BTEC) = 1,2,4,5-Benzenetetracarboxylic acid; (PCN) = 4-pyridinecarboxylic acid; (DOBDC) = 2,5-dihydroxyterephthalic acid; (BPY) = 4,4′–bipyridyl; (IM) = 1*H*-imidazole; (BIM) = 1*H*-benzo[*d*]imidazole; (IM-Cl2) = 3,4-dichloro-1*H*-imidazole; (DABCO) = 1,4-diazabicyclo[2.2.2]octane; ($Me_2$-BPDC) = 2,2'-dimethyl-[1,1'-biphenyl]-4,4'-dicarboxylic acid; (FUM) = fumaric acid; (PZDC) = 1*H*-pyrazole-3,5-dicarboxylic acid; (TDC) = 2,5-Thiophenedicarboxylic acid; (TBAPY) = 1,3,6,8-tetrakis(p-benzoate)pyrene; (BPDC) = [1,1'-biphenyl]-4,4'-dicarboxylic acid; (TCPP) = meso-tetra(4-carboxyl-phenyl)porphyrin

**Table S4.4.** Hydrolysis rates (mM/sec $\times$ $10^{-6}$) with standard deviations ($\boldsymbol{\sigma}$) for DEPPT, DMNP, and VX for six selected MOFs.

| **MOF** | **DEPPT Rate** | $\boldsymbol{\sigma}$ | **DMNP Rate** | $\boldsymbol{\sigma}$ | **VX Rate** | $\boldsymbol{\sigma}$ |
|---|---|---|---|---|---|---|
| UiO-66(Zr)-H/$NO_2$ | 180.3 | 50.5 | 287.5 | 44.8 | 301.4 | 77.0 |
| UiO-66(Zr)-H/$NH_2$/OH/Br | 157.6 | 16.3 | 57.1 | 29.0 | 1395.3 | 178.5 |
| UiO-66(Zr)-$NH_2$/$NO_2$ | 87.4 | 4.1 | 293.1 | 25.2 | 1302.6 | 243.8 |
| UiO-66(Zr)-I | 58.9 | 0.7 | 413.2 | 73.1 | 1165.6 | 167.2 |
| DUT-67(Zr) | 6.2 | 1.6 | 3.7 | 18.2 | 185.3 | 55.6 |
| ZIF-71(Zn) | 1.0 | 0.3 | 1.8 | 3.4 | <1 | - |

## Supplemental Figures

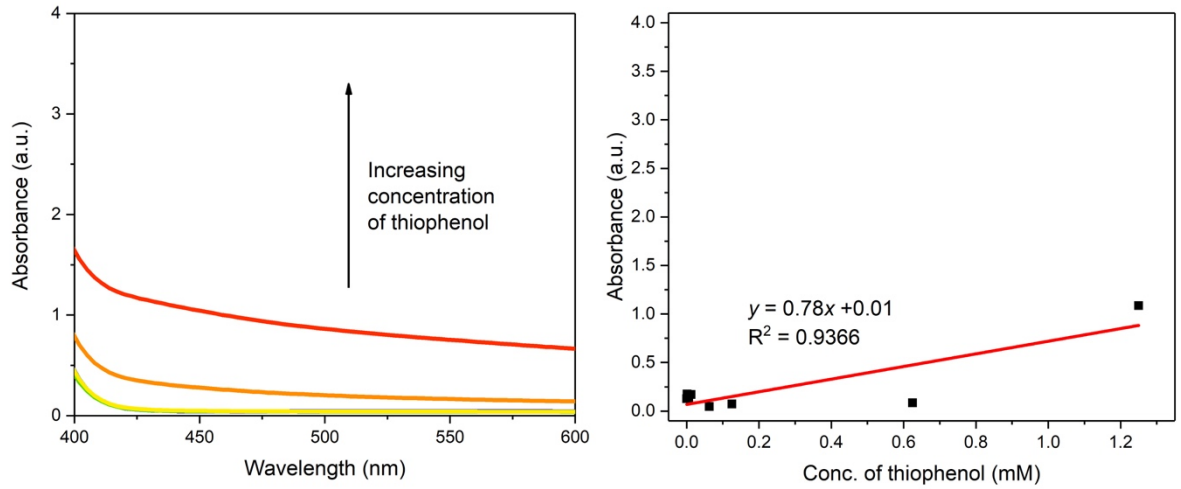


**Figure S4.1.** Absorbance curves (*left*) and calibration curve (*right*) for DTNB reacted with thiophenol at various concentrations in pH = 7.0 NEM buffer. Loss of linearity is due to lack of solubility of thiophenol at this pH.

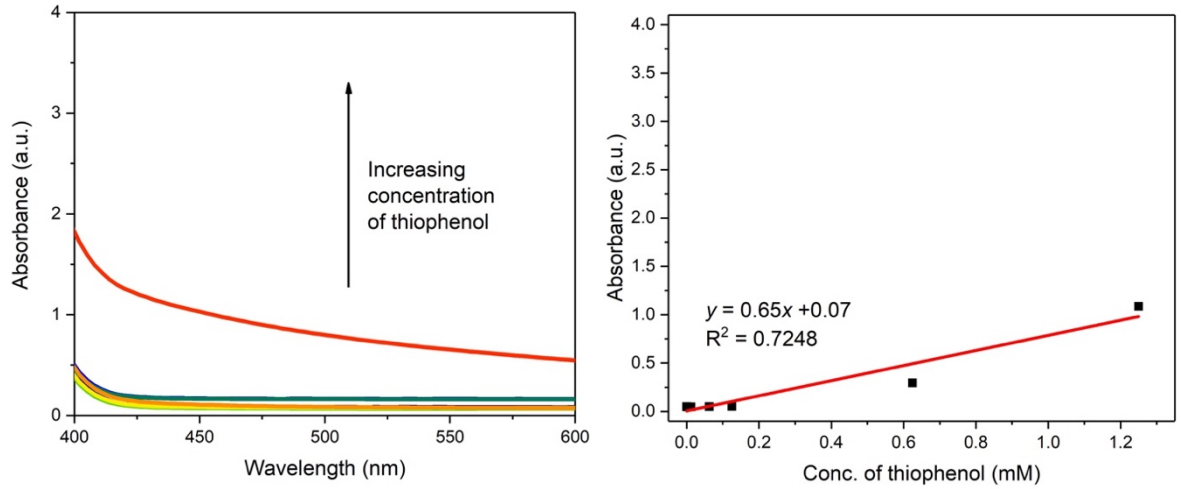


**Figure S4.2.** Absorbance curves (*left*) and calibration curve (*right*) for DTNB reacted with thiophenol at various concentrations in pure water. Loss of linearity is due to lack of solubility of thiophenol at this pH.

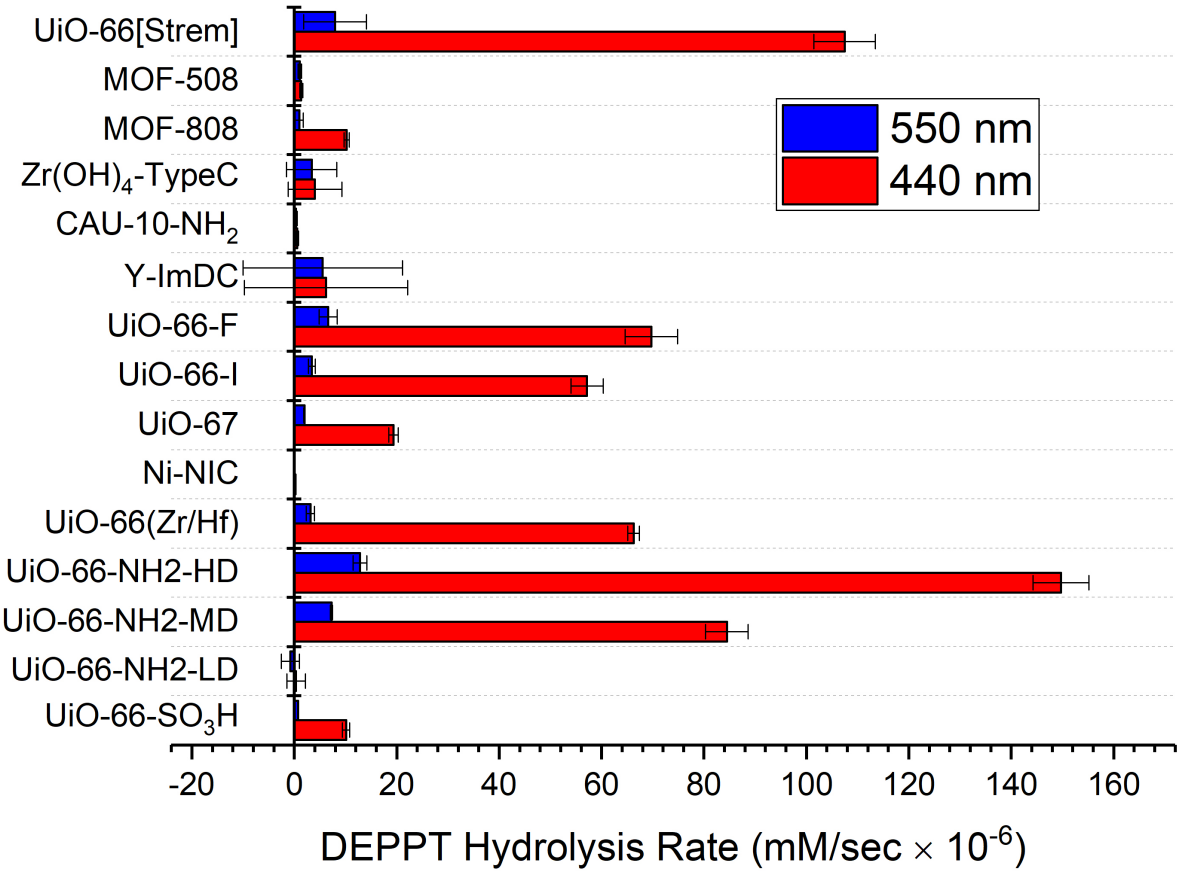


**Figure S4.3.** Hydrolysis rates calculated from change in absorbance at 440 nm and 550 nm for a subset of MOFs to rule out the change in absorbance-based MOF settling in well.

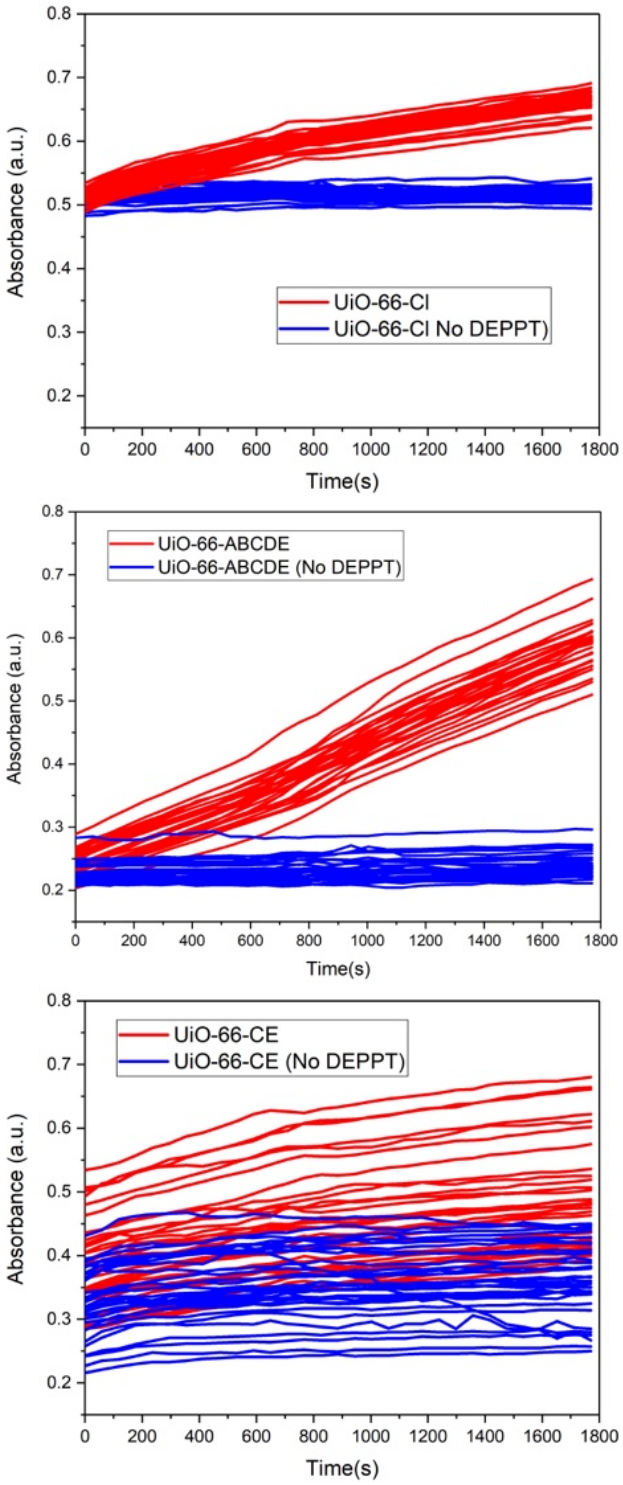


**Figure S4.4.** Absorbance traces for DEPPT HTS of UiO-66(Zr)-Cl (*top*), UiO-66(Zr)-ABCDE (*center*), and UiO-66(Zr)-CE (*bottom*), 32 wells each, for reproducibility testing and Z-factor calculation.

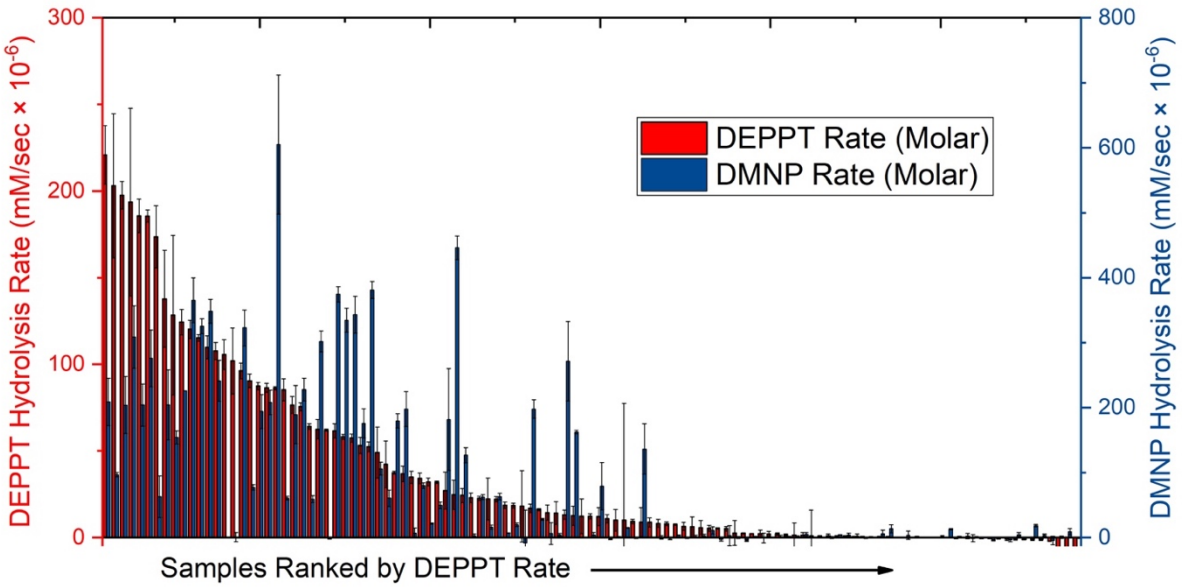


**Figure S4.5.** Full library of MOFs with both DEPPT (red) and DMNP (blue) hydrolysis rates sorted by DEPPT rate.

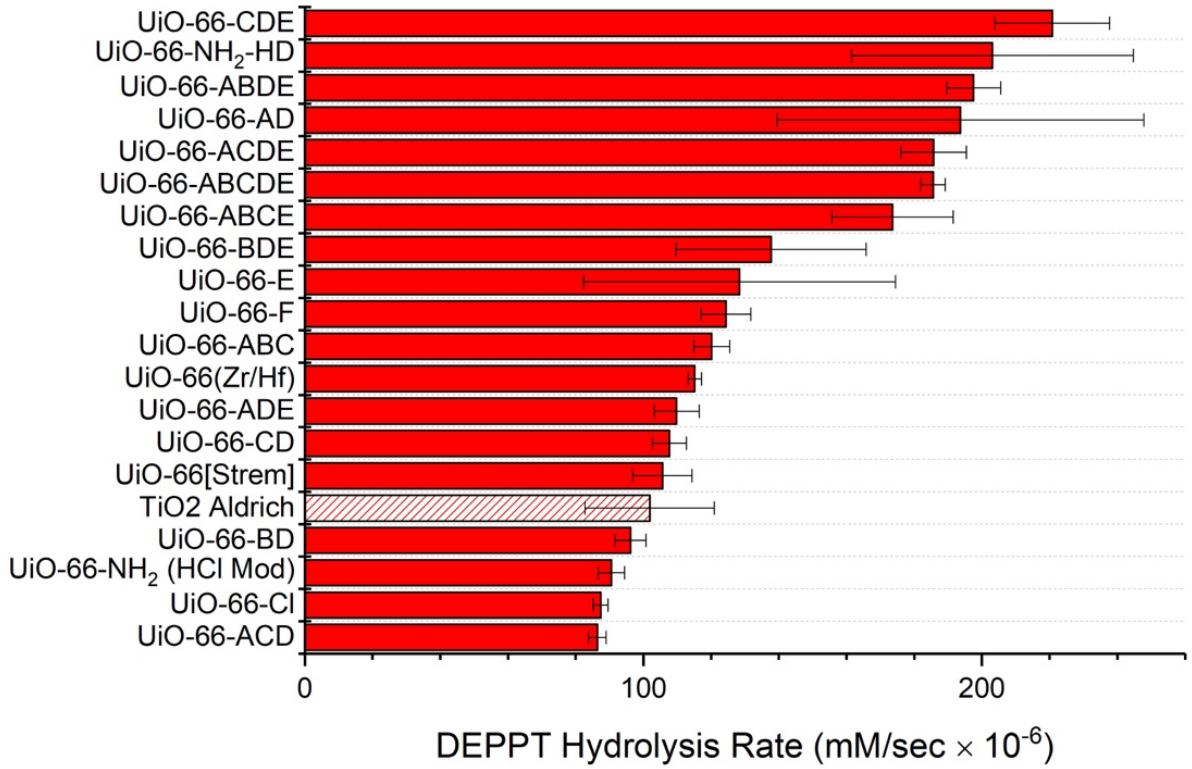


**Figure S4.6.** Top 20 MOFs from HTS ranked by DEPPT hydrolysis rate. $TiO_2$ (Aldrich) is highlighted in striped bar as it was determined to be a false positive with controls (see Table S2).

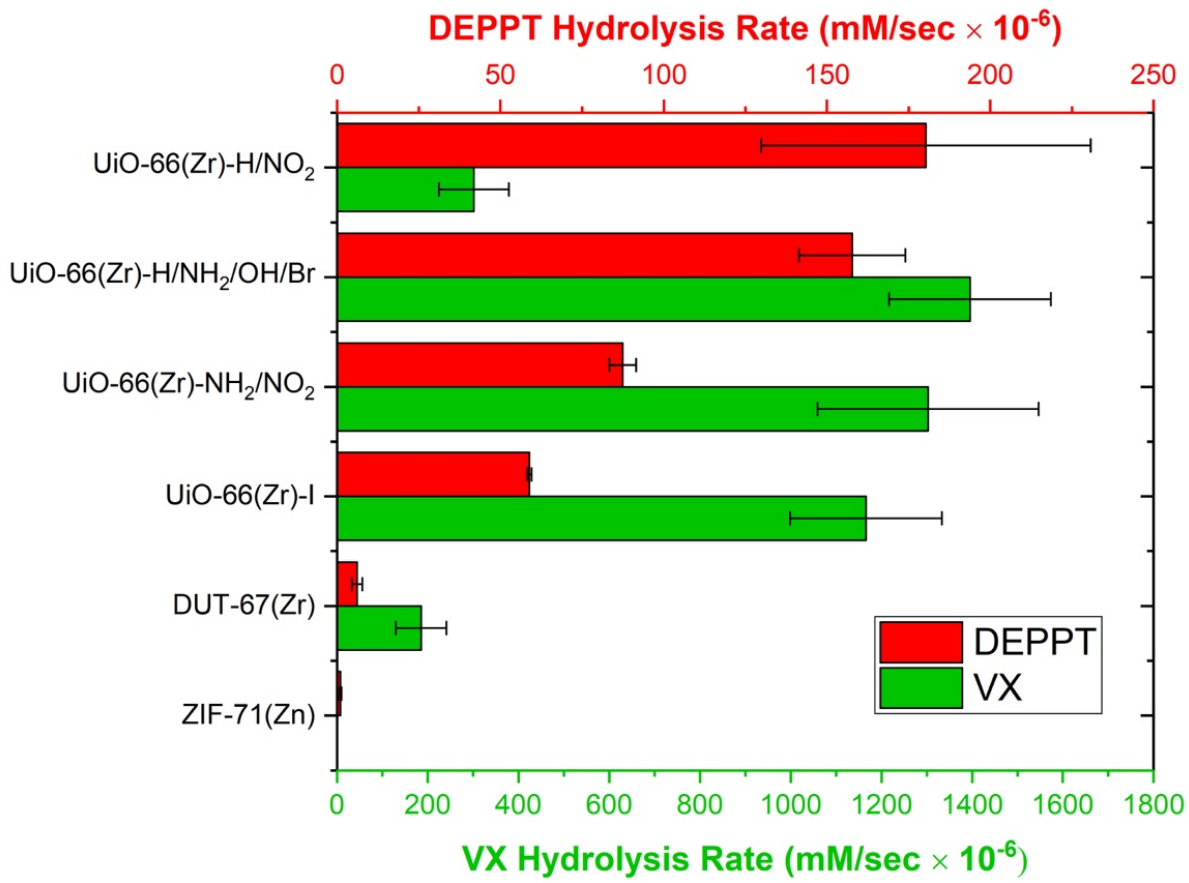


**Figure S4.7.** Comparison of DEPPT HTS hydrolysis rates with those from VX hydrolysis rates. VX rates are average of 3 tests.

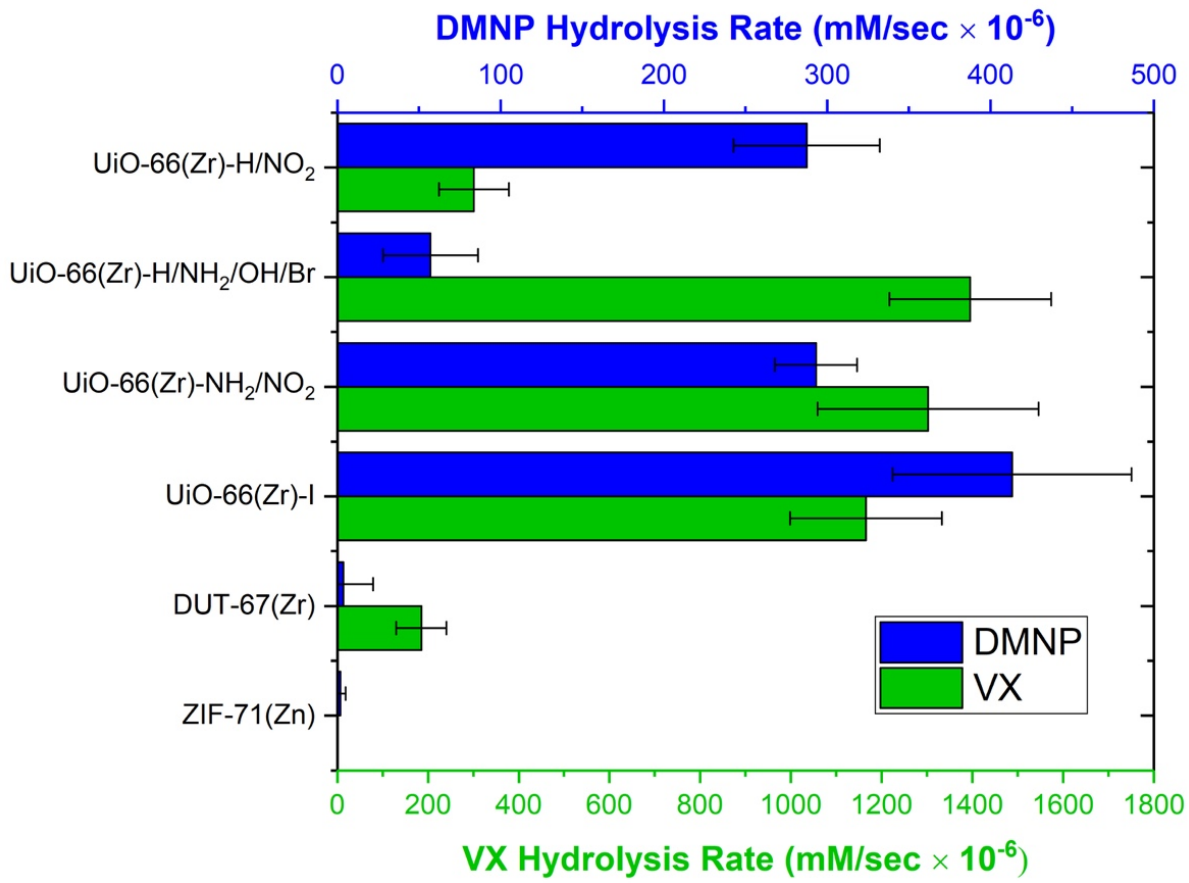


**Figure S4.8.** Comparison of DMNP HTS hydrolysis rates with those from VX hydrolysis rates. VX rates are average of 3 tests.

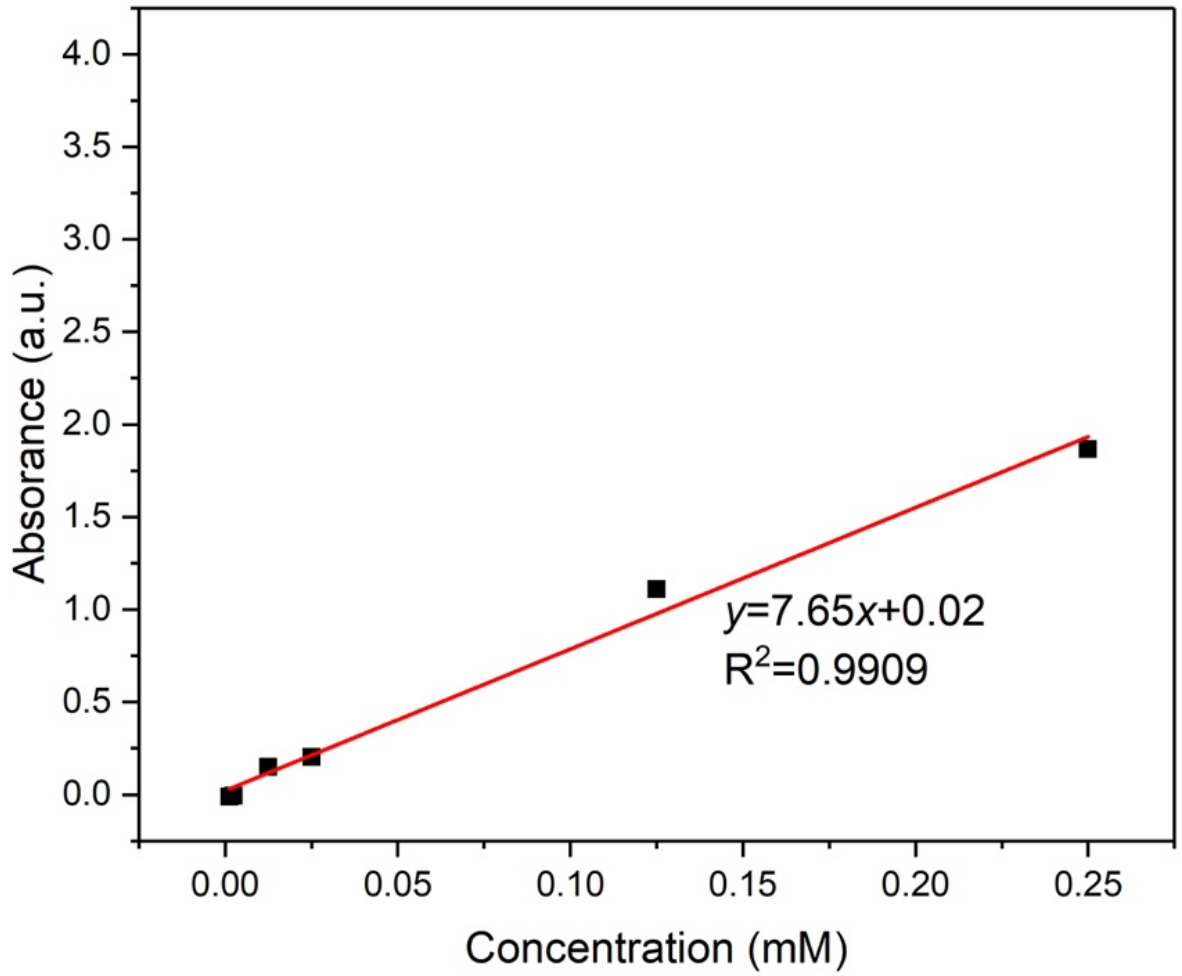


**Figure S4.9**. Calibration curve for detection of thiophenol by DTNB in serial absorbance spectroscopy experiments (pH = 8.0).

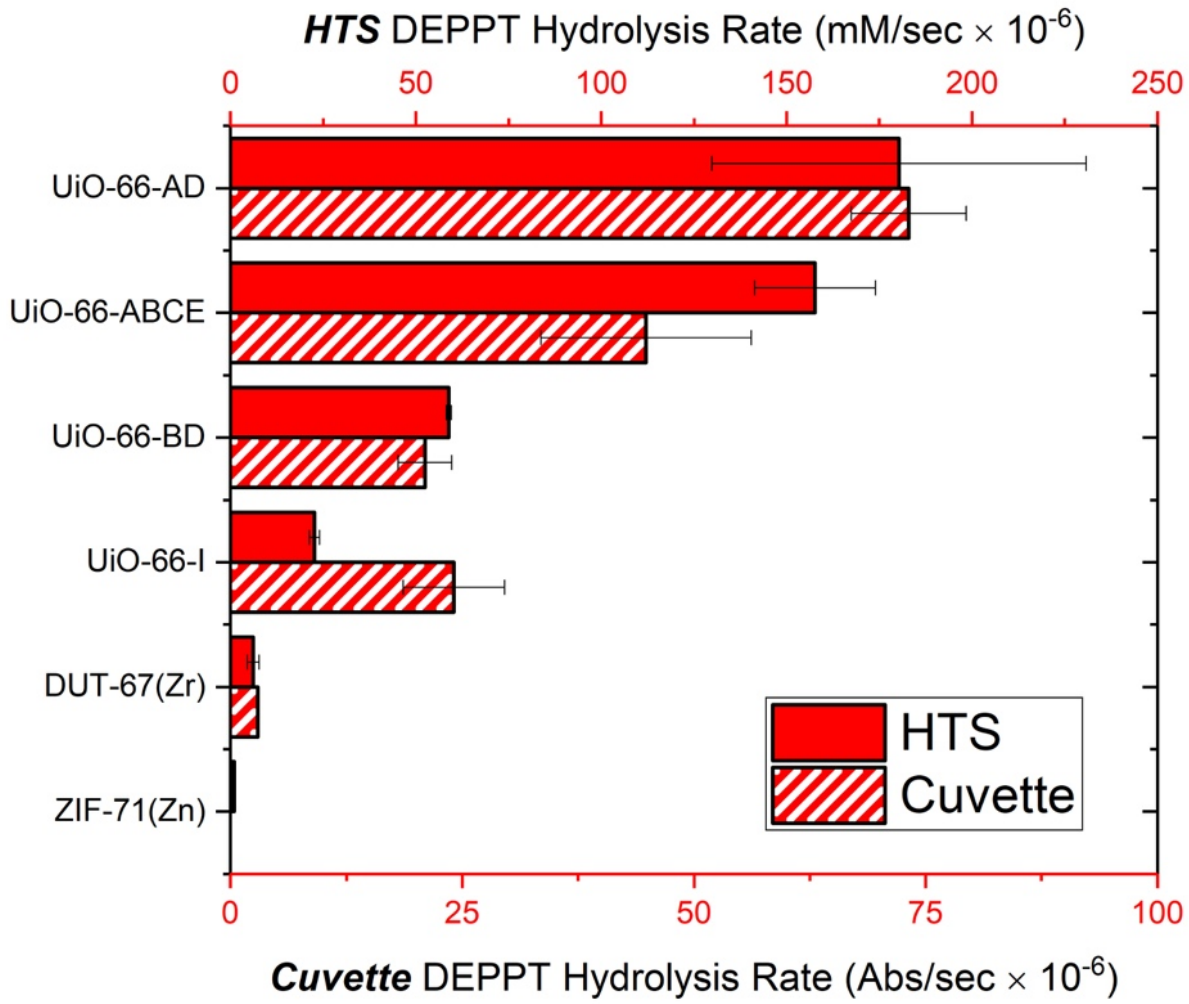


**Figure S4.10.** Hydrolysis rates of selected MOFs from HTS and adapted serial absorbance spectroscopy methods for DEPPT hydrolysis monitoring.

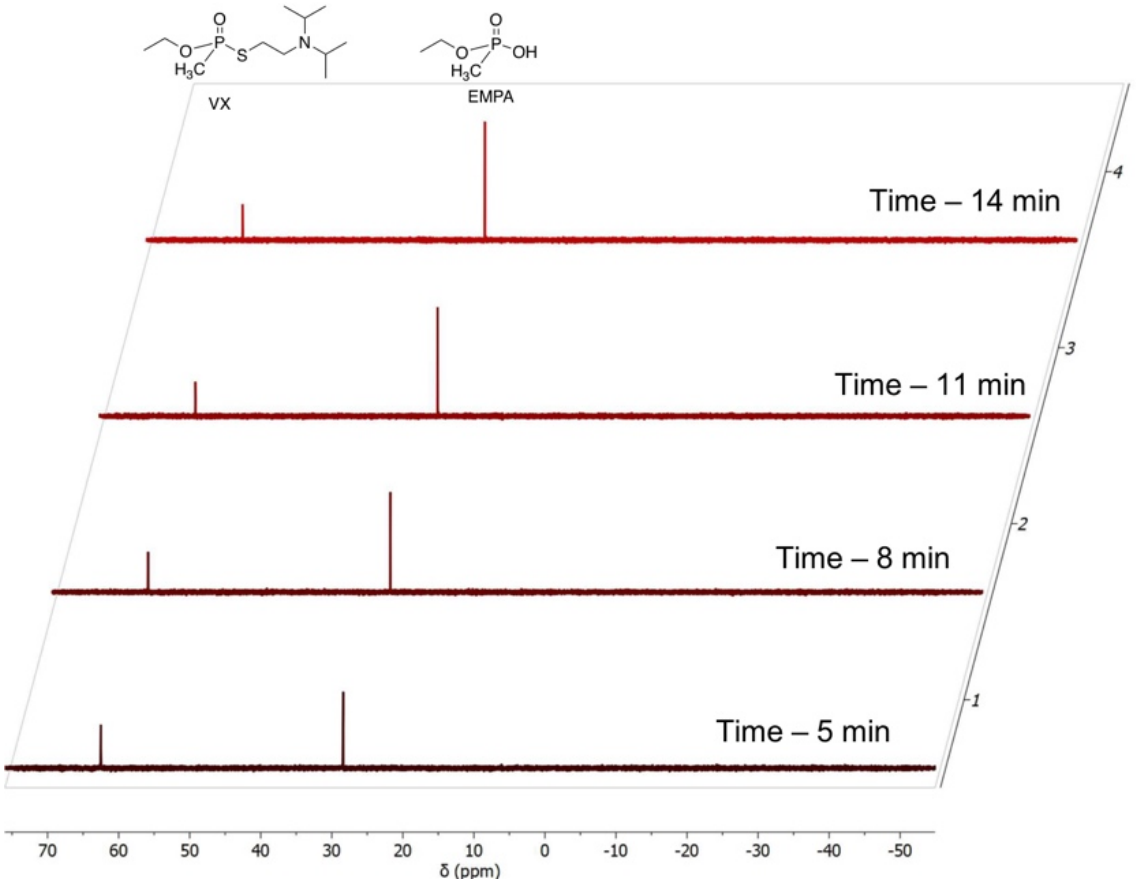


**Figure S4.11.** $^{31}P$ spectra of VX hydrolysis to EMPA by UiO-66(Zr)-H/$NO_2$ for first 14 min of experiment. *Note*: None of toxic byproduct *S*-2-(diisopropylamino)ethyl *O*-hydrogen methylphosphonothioate (EA-2192, NMR Shift 43.1) was detected.

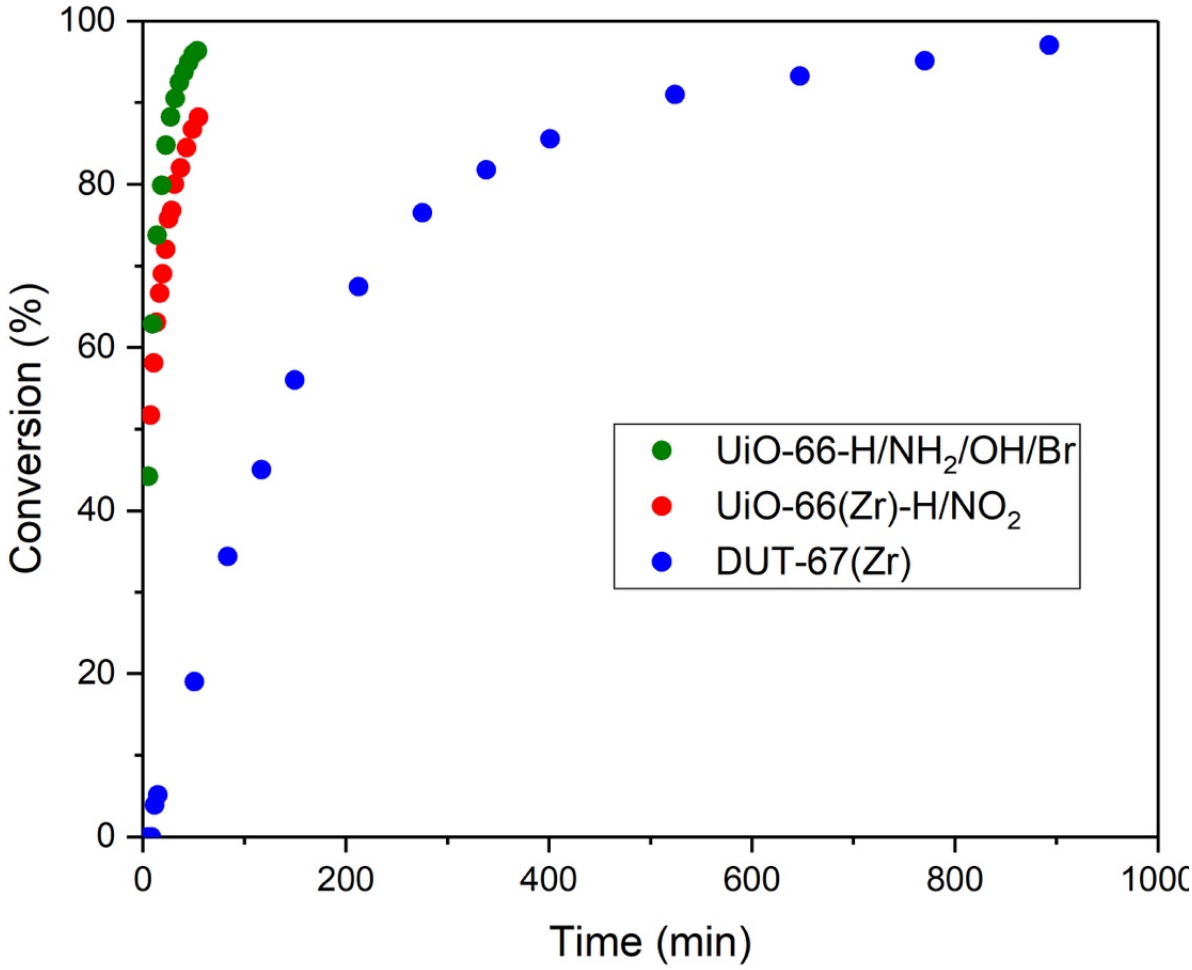


**Figure S4.12.** Percent conversion of VX to ethyl methylphosphonic acid (EMPA) monitored by $^{31}P$ NMR over time for two MOFs: UiO-66(Zr)-H/$NO_2$ and DUT-67(Zr) over a 900 min time scale.

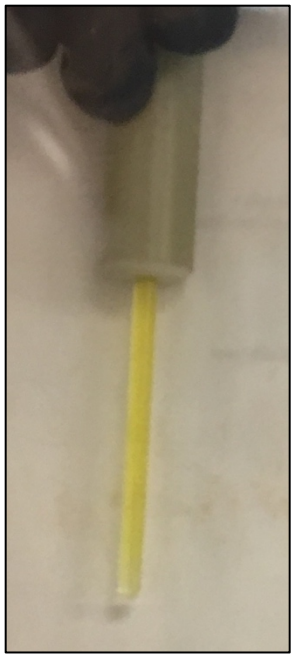

**Figure S4.13.** Photograph of NMR tube of DUT-67(Zr) sample after addition of VX before first scan showing color change due to free thiol reaction with DTNB.

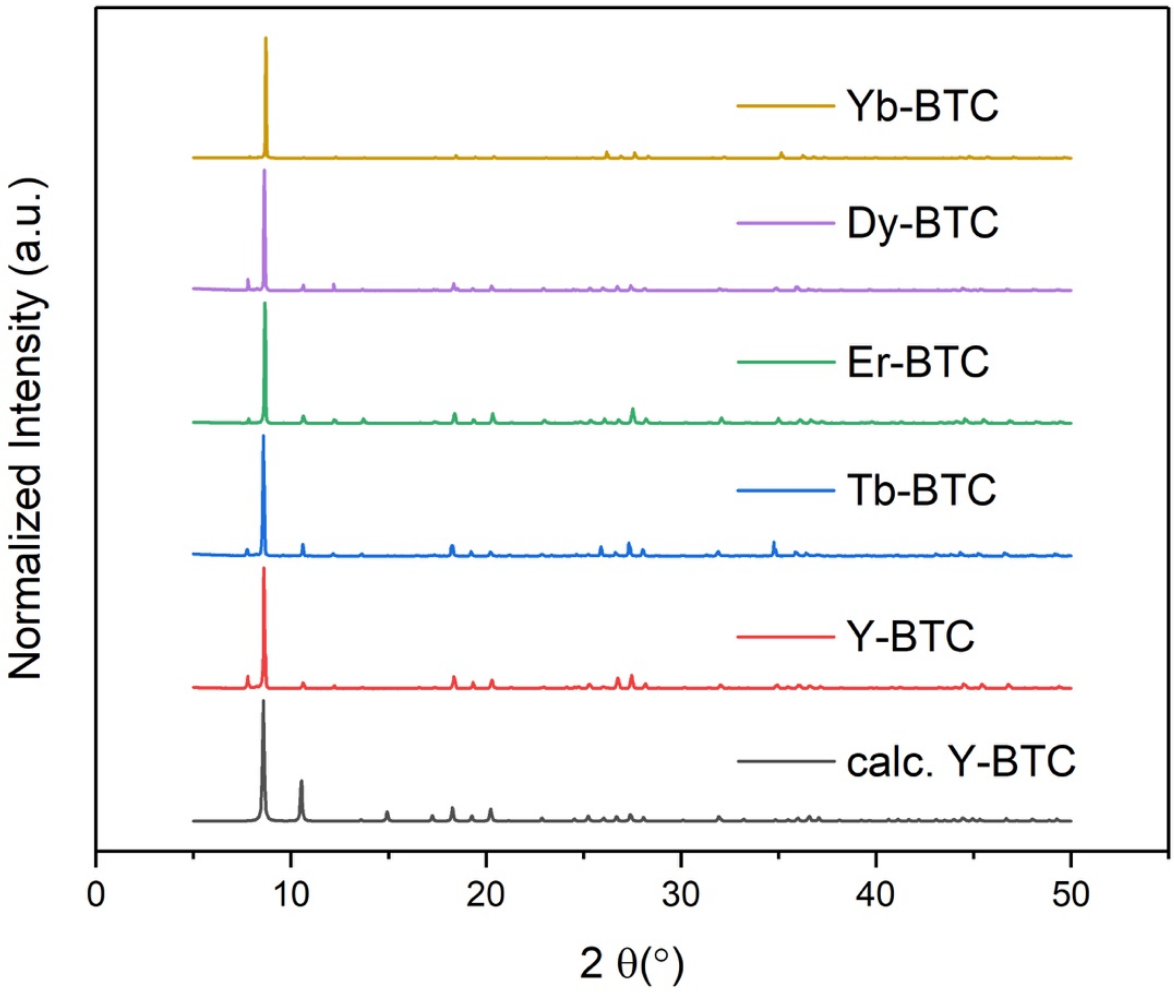


**Figure S4.14.** PXRD of as-synthesized Dy-BTC, Er-BTC, Tb-BTC, and Y-BTC.

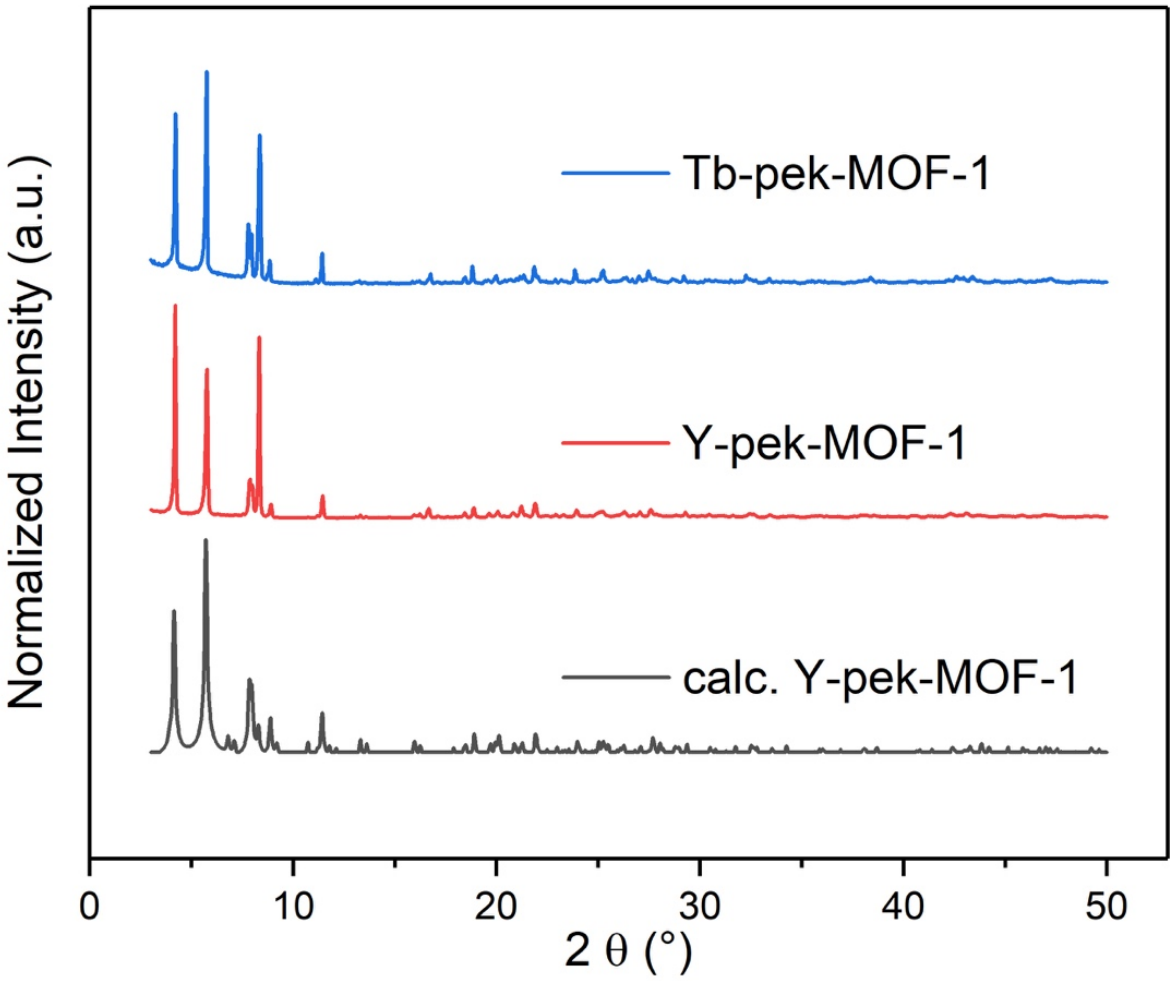


**Figure S4.15.** PXRD of as-synthesized Tb-pek-MOF-1 and Y-pek-MOF-1.

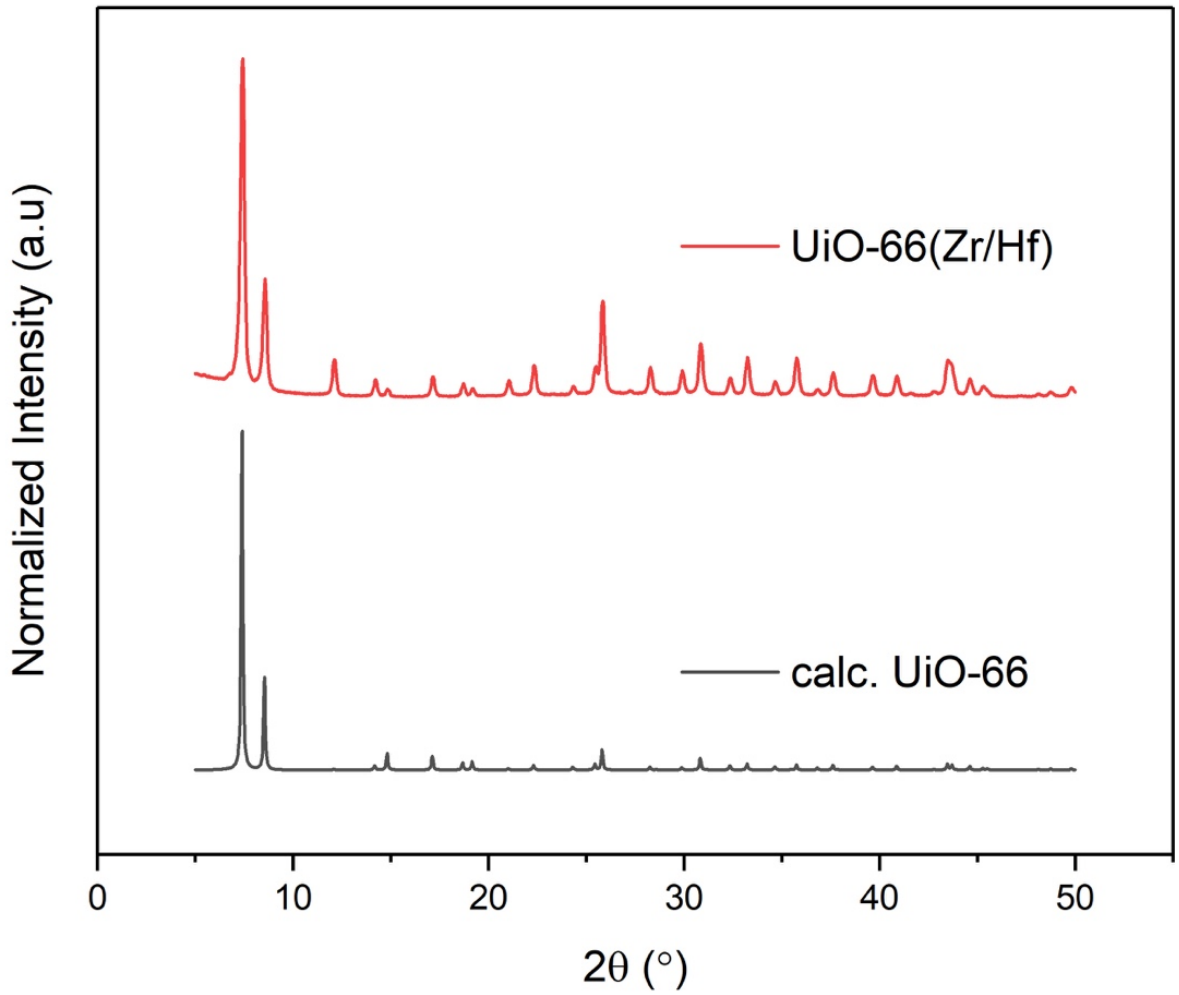


**Figure S4.16.** PXRD of as synthesized UiO-66(Zr/Hf).

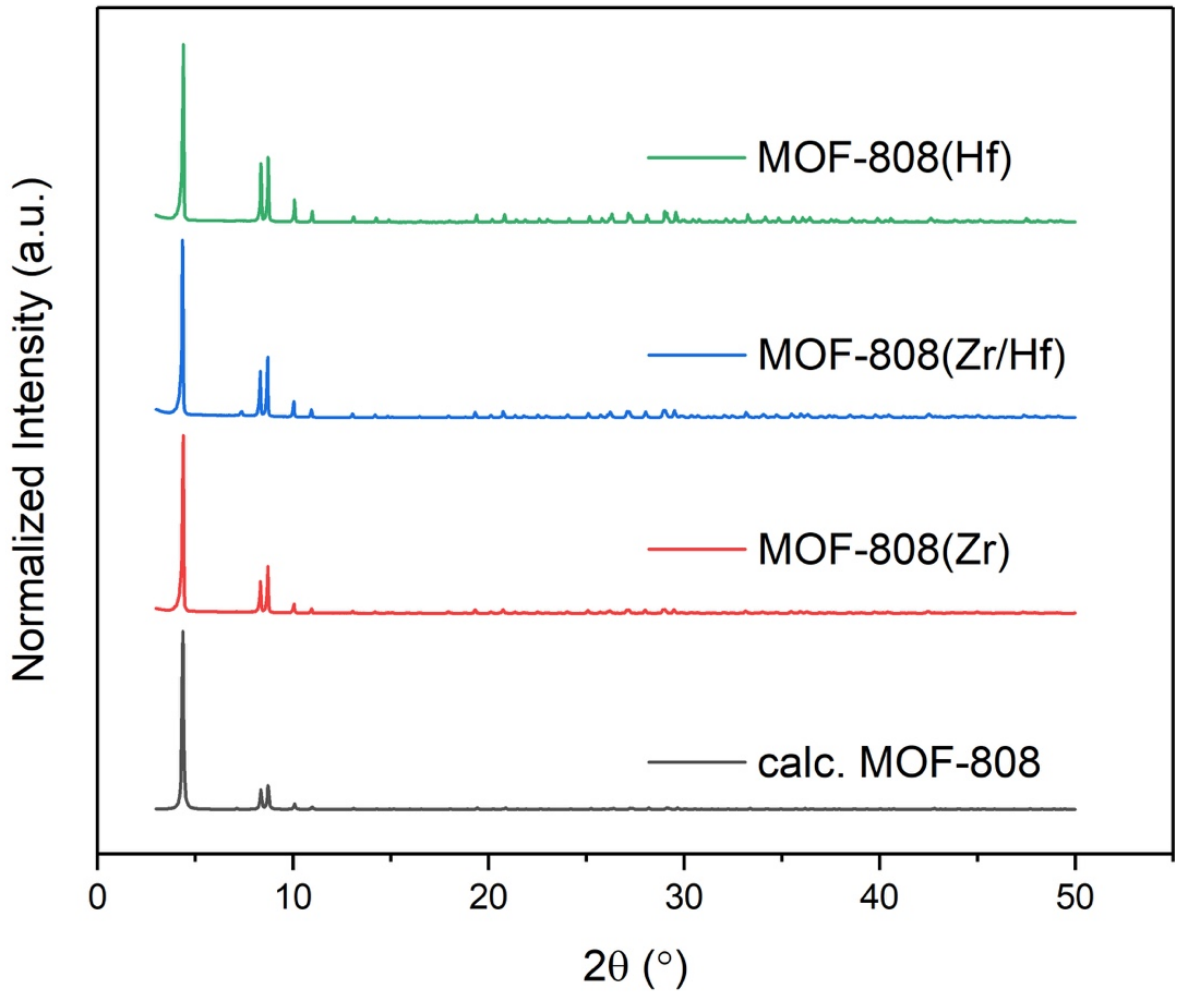


**Figure S4.17.** PXRD of as synthesized MOF-808(Zr), MOF-808(Zr/Hf), and MOF-808(Hf).

## 4.7 Acknowledgements

Chapter 4, in part, is a reprint of the following material "Joseph M. Palomba, Steven P. Harvey, Mark Kalaj, Brian R. Pimentel, Jared B. DeCoste, Gregory W. Peterson, and Seth M. Cohen, High-Throughput Screening of MOFs for Breakdown of V-Series Nerve Agents *ACS Appl. Mater. Interfaces* **2020,** *12*, 14672-14677." The dissertation author was the primary author of this manuscript and gratefully acknowledges the contributions

of coauthors. The dissertation author also gratefully acknowledges the editing help of Kathleen E. Prosser and Jessica C. Moreton.

## 4.8 References

1. Islamoglu, T.; Chen, Z.; Wasson, M. C.; Buru, C. T.; Kirlikovali, K. O.; Afrin, U.; Mian, M. R.; Farha, O. K., Metal–Organic Frameworks against Toxic Chemicals. *Chem. Rev.* **2020,** *120*, 8130-8160.

2. Liu, Y.; Howarth, A. J.; Vermeulen, N. A.; Moon, S.-Y.; Hupp, J. T.; Farha, O. K., Catalytic degradation of chemical warfare agents and their simulants by metal-organic frameworks. *Coordin. Chem. Rev.* **2017,** *346*, 101-111.

3. Moon, S.-Y.; Wagner, G. W.; Mondloch, J. E.; Peterson, G. W.; DeCoste, J. B.; Hupp, J. T.; Farha, O. K., Effective, Facile, and Selective Hydrolysis of the Chemical Warfare Agent VX Using Zr6-Based Metal–Organic Frameworks. *Inorg. Chem.* **2015,** *54*, 10829-10833.

4. Peterson, G. W.; Destefano, M. R.; Garibay, S. J.; Ploskonka, A.; McEntee, M.; Hall, M.; Karwacki, C. J.; Hupp, J. T.; Farha, O. K., Optimizing Toxic Chemical Removal through Defect-Induced UiO-66-NH2 Metal–Organic Framework. *Chem. - Eur. J.* **2017,** *23*, 15913-15916.

5. de Koning, M. C.; van Grol, M.; Breijaert, T., Degradation of Paraoxon and the Chemical Warfare Agents VX, Tabun, and Soman by the Metal–Organic Frameworks UiO-66-NH2, MOF-808, NU-1000, and PCN-777. *Inorg. Chem.* **2017,** *56*, 11804-11809.

6. Ploskonka, A. M.; DeCoste, J. B., Insight into organophosphate chemical warfare agent simulant hydrolysis in metal-organic frameworks. *J. Hazard. Mater.* **2019,** *375*, 191-197.

7. Kalaj, M.; Bentz, K. C.; Ayala, S.; Palomba, J. M.; Barcus, K. S.; Katayama, Y.; Cohen, S. M., MOF-Polymer Hybrid Materials: From Simple Composites to Tailored Architectures. *Chem. Rev.* **2020,** *120*, 8267-8302.

8. Paddock, R. C.; Sang-Hun, C. Kim Jong-nam Was Killed by VX Nerve Agent, Malaysians Say *New York Times* [Online], 2017. (accessed Dec. 10. 2020).

9. Kirlikovali, K. O.; Chen, Z.; Islamoglu, T.; Hupp, J. T.; Farha, O. K., Zirconium-Based Metal–Organic Frameworks for the Catalytic Hydrolysis of Organophosphorus Nerve Agents. *ACS Appl. Mater. Interfaces* **2020,** *12*, 14702-14720.

10. Tsang, J. S. W.; Neverov, A. A.; Brown, R. S., La3+-catalyzed methanolysis of O,O-diethyl S-(p-nitrophenyl) phosphorothioate and O,O-diethyl S-phenyl phosphorothioate. Millions-fold acceleration of the destruction of V-agent simulants. *Org. Biomol. Chem.* **2004,** *2*, 3457-3463.

11. Ellman, G. L., Tissue sulfhydryl groups. *Arch. Biochem. Biophys.* **1959,** *82*, 70-77.

12. Winther, J. R.; Thorpe, C., Quantification of thiols and disulfides. *Biochim. Biophys. Acta, Gen. Subj.* **2014,** *1840*, 838-846.

13. de Koning, M. C.; Peterson, G. W.; van Grol, M.; Iordanov, I.; McEntee, M., Degradation and Detection of the Nerve Agent VX by a Chromophore-Functionalized Zirconium MOF. *Chem. Mater.* **2019,** *31*, 7417-7424.

14. Gil-San-Millan, R.; López-Maya, E.; Platero-Prats, A. E.; Torres-Pérez, V.; Delgado, P.; Augustyniak, A. W.; Kim, M. K.; Lee, H. W.; Ryu, S. G.; Navarro, J. A. R., Magnesium Exchanged Zirconium Metal–Organic Frameworks with Improved Detoxification Properties of Nerve Agents. *J. Am. Chem. Soc.* **2019,** *141*, 11801-11805.

15. Lu, A. X.; McEntee, M.; Browe, M. A.; Hall, M. G.; DeCoste, J. B.; Peterson, G. W., MOFabric: Electrospun Nanofiber Mats from PVDF/UiO-66-NH2 for Chemical Protection and Decontamination. *ACS Appl. Mater. Interfaces* **2017,** *9*, 13632-13636.

16. Zhang, J.-H.; Chung, T. D. Y.; Oldenburg, K. R., A Simple Statistical Parameter for Use in Evaluation and Validation of High Throughput Screening Assays. *J. Biomol. Screen.* **1999,** *4*, 67-73.

17. Palomba, J. M.; Credille, C. V.; Kalaj, M.; DeCoste, J. B.; Peterson, G. W.; Tovar, T. M.; Cohen, S. M., High-throughput screening of solid-state catalysts for nerve agent degradation. *Chem. Commun.* **2018,** *54*, 5768-5771.

18. Katz, M. J.; Klet, R. C.; Moon, S.-Y.; Mondloch, J. E.; Hupp, J. T.; Farha, O. K., One Step Backward Is Two Steps Forward: Enhancing the Hydrolysis Rate of UiO-66 by Decreasing [OH–]. *ACS Catal.* **2015,** *5*, 4637-4642.

19. Plonka, A. M.; Wang, Q.; Gordon, W. O.; Balboa, A.; Troya, D.; Guo, W.; Sharp, C. H.; Senanayake, S. D.; Morris, J. R.; Hill, C. L.; Frenkel, A. I., In Situ Probes of Capture and Decomposition of Chemical Warfare Agent Simulants by Zr-Based Metal Organic Frameworks. *J. Am. Chem. Soc.* **2017,** *139*, 599-602.

# Chapter 5: Metal-Organic Framework Polymer Hybrids Designed for Mechanically Robust Personal Protective Equipment

## 5.1 Introduction

Chapters 2, 3, and 4 focused on the development of HTS methods for the discovery of MOF catalysts and MOF-polymer composites for nerve agent simulant degradation. As noted in Chapter 3, MOFs in their powder, microcrystalline, or crystalline form are not immediately useful in personal protective equipment (PPE) and require integration with polymers to be formed into useful composites.[1] Work on integration of MOFs into polymer composites has been explored using a variety of techniques, including atomic layer deposition-coated (ALD) nanofibers,[2, 3] mixed-matrix membranes (MMMs),[4-6] electrospun nanofibers,[7-9] and postsynthetic polymerization (PSP).[10] Many of these reports have been proof-of-concept studies focused on achieving composites that maintain the CWA protection. The next generation of MOF-polymer composites must also possess mechanical properties necessary for the physical demands put on the material by the wearer.

This chapter describes the discovery of MOF-polymer hybrids that have improved mechanical properties and utilizes HTS methods to screen and compare a series of composites. Spandex was selected as a strong, flexible polymer to target for MOF composites as it could be incorporated into a variety of PPE such as suits, gloves, or masks. A simple spandex-like polyurethane urea (PUU) polymer was synthesized with suitable molecular weight for both mechanical properties and solution processability. The resulting MOF/PUU composites are strong and ductile with up to 50 wt% MOF and show good performance as nerve agent simulant hydrolysis catalysts. The processability of

these composites was demonstrated by their successful fabrication into MMMs, fibers, and electrospun mats.

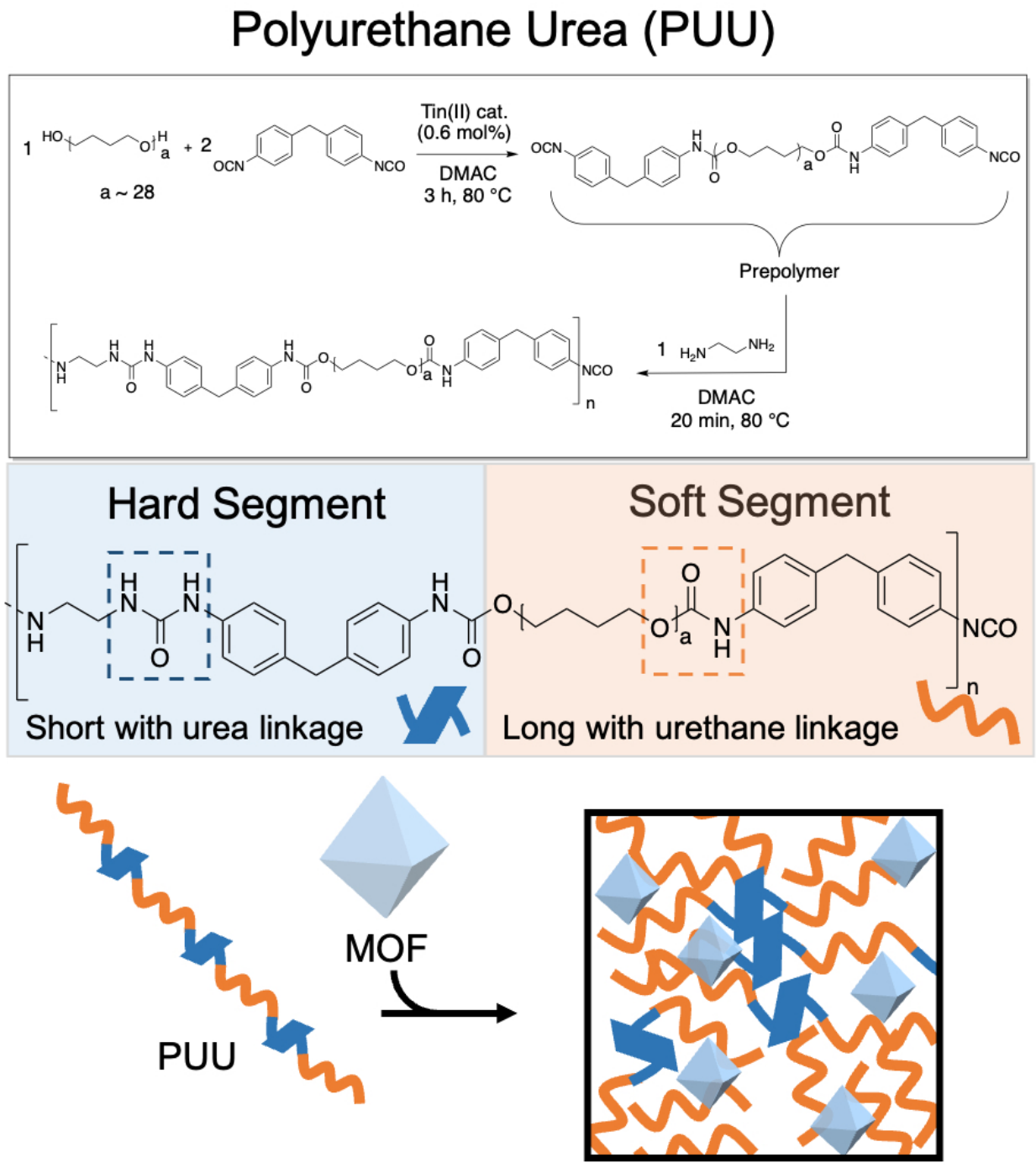


**Figure 5.1.** *Top*: Synthetic scheme of polyurethane urea (PUU) (DMAC = *N*,*N*-dimethylacetamide). *Middle:* Overview of PUU polymer segments. *Bottom*: Scheme representing MOF-PUU composites.

## 5.2 MOF/ PUU Composites

To emulate mechanical properties of a commercial spandex polymer, a solution processable polyurethane urea (PUU) was synthesized. Narrow dispersity polytetrahydrofuran with a $M_w$ of 2000 g/mol (polyTHF$_{2000}$, $Đ$ = 1.34, Figure S5.1) was mixed with 4,4'-methylene diphenyl diisocyanate in a 1:2 ratio to afford prepolymer (Figure 5.1). This prepolymer was then combined with one equivalent of ethylene diamine to chain extend the prepolymer into the final block polymer. The final PUU polymer had a number average molecular weight ($M_n$) of ~80,000 g/mol relative to polystyrene standards (Figure 5.1, Figure S5.1, Table S5.1). The polymer formed rubbery masses, but when dissolved in *N*,*N*-dimethylacetamide (DMAC) it could be cast into clear, flexible films that were stretchable in all directions and could be extended multiple times their initial length (Figure S5.2).

Encouraged by the physical properties of the pure PUU polymer films, MOF-polymer MMMs were made through casting UiO-66(Zr) based inks of various wt% (20-50 wt%). The MOF was well dispersed in the resulting translucent films (thickness 60-100 µm, Table S5.2) as evidenced by scanning electron microscope (SEM) images of 40 and 50 wt% MMMs and PXRD of all MMMs (Figure 5.2, Figures S5.3-S5.5). These materials also could be twisted, folded, or stretched in all directions without breaking or cracking, clearly adopting many of mechanical properties of the parent polymer.

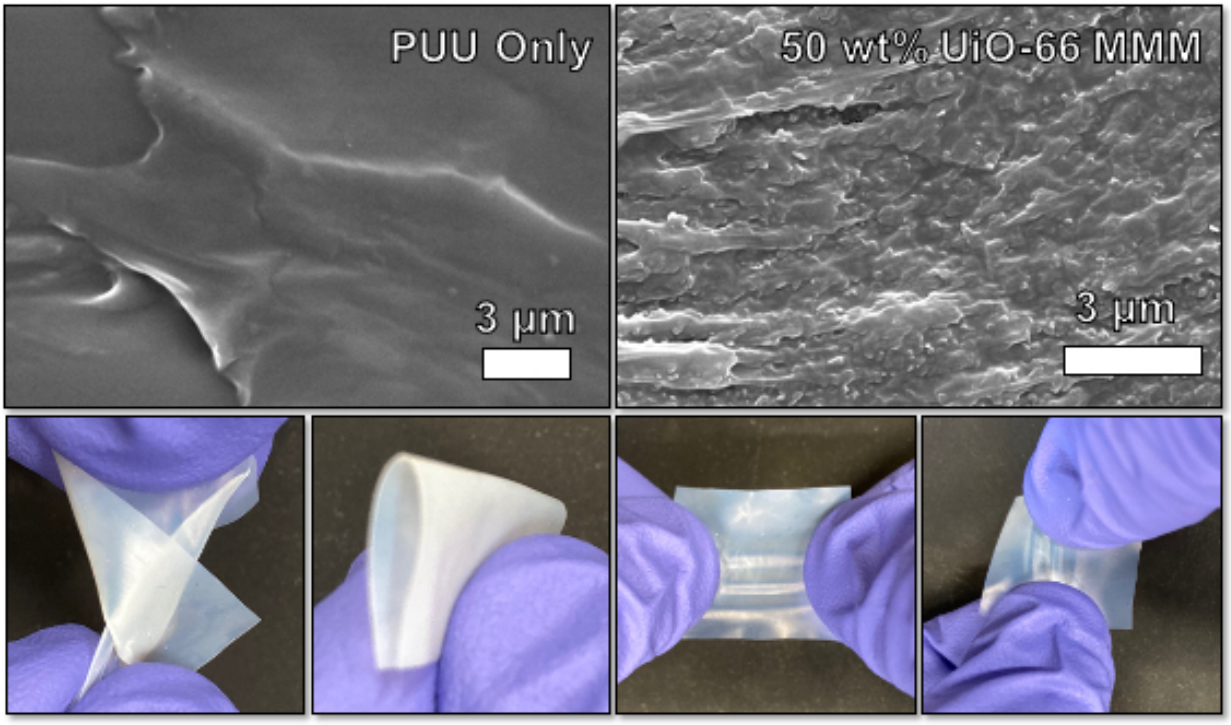


**Figure 5.2.** *Top:* Cross-section SEM images of a pure PUU film (*left*) and 50 wt% UiO-66/PUU MMM (*right*). *Bottom:* Photographs of 50 wt% UiO-66 being twisted, folded, and stretched.

Three ligand-modified UiO-66(Zr) MOFs were synthesized with 2-amino-1,4-benzenedicarboxylate ($NH_2$-$bdc^{2-}$), 2-nitro-1,4-benzenedicarboxylate ($NO_2$-$bdc^{2-}$), and naphthalene-1,4-dicarboxylate (Napth-$bdc^{2-}$) for use in preparing PUU composites. Incorporation of the UiO-66(Zr)-$NH_2$, UiO-66(Zr)-$NO_2$, and UiO-66(Zr)-Naph into 50 wt% composites was successful despite the differences in the functional groups on the ligands of these MOFs (Figure S5.2 and Figures S5.6-S5.8). This shows general PUU polymer compatibility for incorporating different functionalized MOFs, which is important as new MOFs are identified for PPE applications.

The composites were found to have no BET surface area as prepared (Table S5.2), indicating that the MOF pores are not accessible to $N_2$ gas in these MMMs under

the experimental conditions (see Appendix). It is possible that the pores of the MOF may be infiltrated partially by polyol chains of PUU as reported in other MOF-polymer systems,[11] but the steric bulk of the phenyl rings on the rigid PUU blocks should prevent full incorporation. Another hypothesis to explain the lack of porosity of these composites is that under the sub-ambient analysis conditions (77 K) of the gas sorption experiment, the polymer freezes, creating a gas-impermeable barriers on the MOF surface. In terms of PPE, lack of $N_2$ uptake precludes the materials for gas mask applications; however, it has potential as a barrier material for gloves or boots.

## 5.3 Strength and Flexibility of MOF/PUU Composites

To quantify the mechanical properties of the MOF polymer composites, three sets of MMMs subjected to tensile testing. The first set of UiO-66(Zr)/PUU MMMs varied loadings with 0, 20, 30, 40, and 50 wt% MOF (Figure 5.3). Next, UiO-66(Zr)-$NH_2$ with a similar particle size to UiO-66(Zr) (Figure S5.9) was also tested in a 50 wt% MMM to compare a different MOF in the same composite (Figure 5.4, Figures S5.2, S5.8-S5.9). Lastly, PVDF MMMs with 50 wt% UiO-66(Zr) and UiO-66(Zr)-$NH_2$ were prepared as comparator materials previously studied for PPE applications (Figure 5.4, Figures S5.2, and S5.10).[5, 6] Ultimate tensile strength of the PVDF composite was previously reported, but ductility was not.

The mechanical properties for the pure PUU film agreed well with literature values for high ductility that report elongation at break over 800%.[12] In fact, the films prepared in this study were so stretchable that they did not break inside the strain limits of the

Univert test stand and did not break <1500% (Table 5.1, Figure 5.3). In addition, films returned to their original size upon relaxation, as expected for an elastomer. The 50 wt% UiO-66(Zr)/PVDF and 50 wt% UiO-66(Zr)-$NH_2$/PVDF MMMs showed higher ultimate tensile strengths (8.2 and 10.0, respectively) but less than 6% elongation at break (Figure 5.4, Table S5.2). The strength of the PVDF composites is on the order of PPE polymers used in protective gloves like nitrile or butyl (22.7 and 9.1 MPa, respectively).[13, 14] However, PPE gloves require high ductility, as shown by nitrile and butyl having elongation at break over 550%.[13, 14]

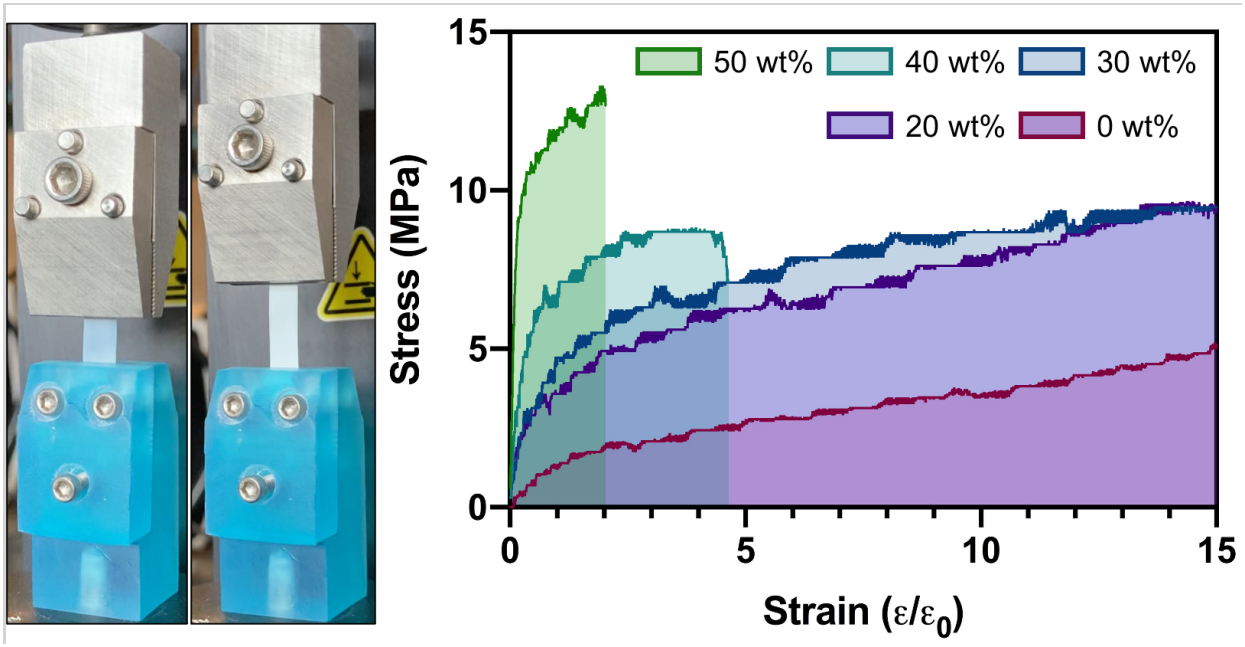


**Figure 5.3.** *Left:* Photograph of tensile testing for 50 wt% UiO-66/PUU MMM before test and just before failure. *Right:* Results of tensile testing for PUU film (0 wt%) and UiO-66/PUU MMMs (20-50 wt%).

Using the flexible PUU polymer yielded very ductile MOF composite materials. The 20 and 30 wt% UiO-66(Zr)/PUU MMMs show extremely high elongations and all tests

resulted in breaks above 1500% or no break at all within the limits of the test (Figure 5.3, Table S5.2). Higher weight loadings of UiO-66(Zr) in 40 and 50 wt% MMMs showed lower elongation at break, as expected, because of addition of filler to the polymer (Figure 5.3, Table 5.1).[15] However, the 50 wt% UiO-66(Zr)/PUU still showed an average elongation at break of 146% and toughness, or ability of material to absorb energy per unit volume quantified as the area under the stress-strain curve, of 16.7 J/cm$^3$ (Figures 5.3 and 5.4, Table 5.1). The yield strength of the 50 wt% MOF MMMs were all between 6.8 and 9.5 MPa, demonstrating that the PUU and PVDF composites could withstand similar amounts of force before deformation (Figure 5.4).

The addition of MOF to the PUU elastomer showed a rigidification that increased the strength of the composite as demonstrated by an increase toughness in all of the UiO-66(Zr)/PUU MMMs. There was a continuous increase in strength in composite over the PUU only film, with increased MOF. The 20 and 30 wt% MMMs both had high toughness (>140 J/cm$^3$) and may provide a balance mechanical properties and protection (Table S5.2). The tensile testing illustrates that UiO-66/PUU MMMs are strong, ductile materials.

**Table 5.1.** Mechanical properties from tensile testing and simulant hydrolysis rates from HTS for selected 50 wt% MMMs. (EAB = elongation at break, Str = Strength). *No definitive plastic yield point observed.

| Material | EAB (%) | Yield Str. (MPa) | Toughness (J/cm$^3$) |
|---|---|---|---|
| PUU Only | >1535 | N/A* | >47.8 |
| 50% UiO-66/PUU | 146 ± 47 | 9.5 ± 0.5 | 16.7 ± 5.3 |
| 50% UiO-66/PVDF | 6 ± 4 | 6.9 ± 1.2 | 0.4 ± 0.2 |
| 50% UiO-66-$NH_2$/PUU | 129 ± 11 | 6.8 ± 0.7 | 10.0 ± 1.7 |
| 50% UiO-66-$NH_2$/PVDF | 4 ± 1 | 8.4 ± 4.0 | 0.2 ± 0.1 |

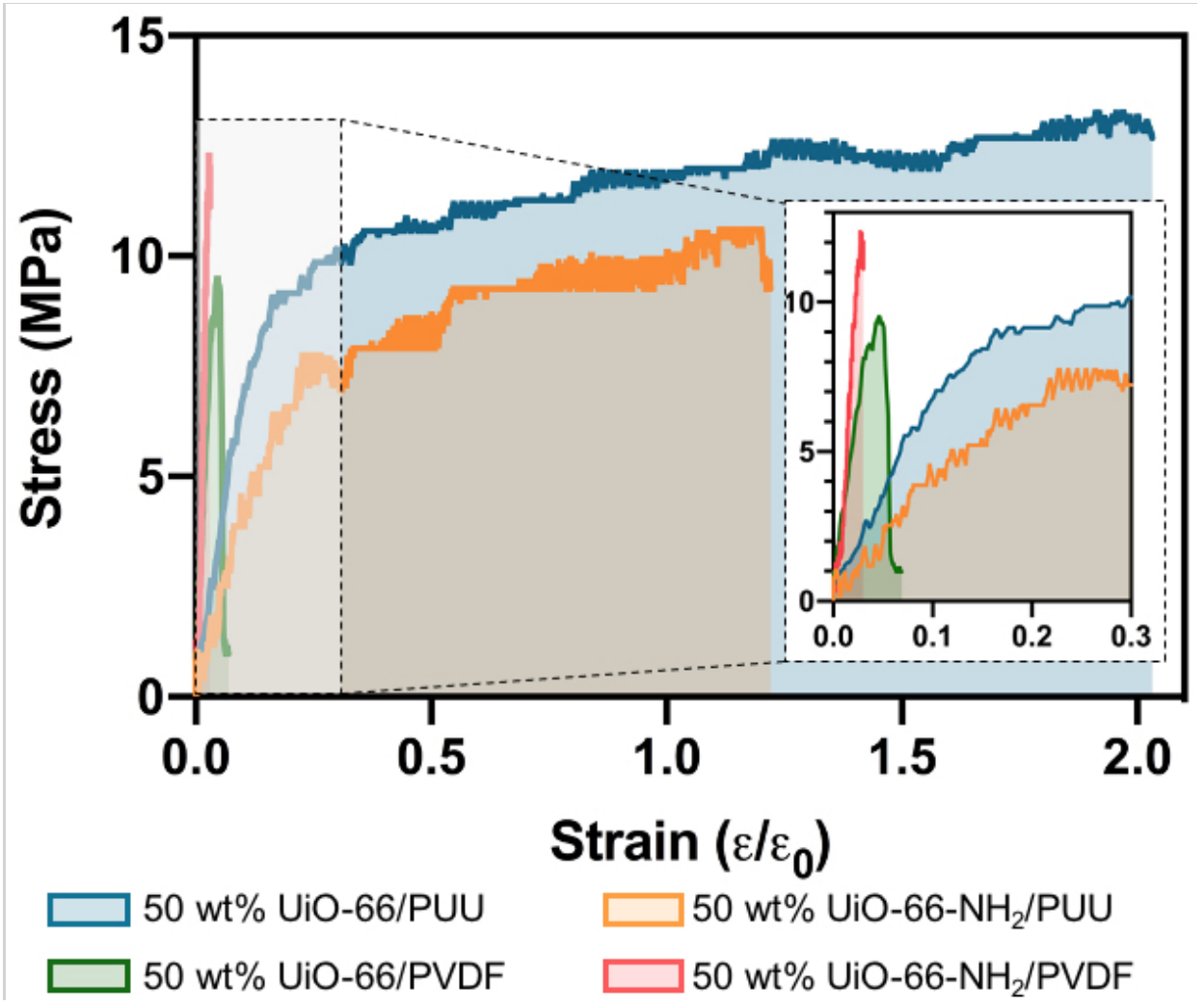


**Figure 5.4.** Results of tensile testing for 50 wt% MOF MMMs of PUU and PVDF with low strain region (0-0.3 $\varepsilon/\varepsilon_0$) expanded in inset.

## 5.4 MOF/PUU MMMs for CWA Simulant Degradation

With confirmation that MOF-PUU composites are strong and flexible, these materials were next tested for catalytic activity related to their desired protective function. To assess the activity of the MMMs for breakdown of organophosphorous nerve agents, DMNP was used as a simulant.[16] Using a previously developed method, samples were analyzed in triplicate and were monitored simultaneously in a 24-well plate format using a plate reader at pH = 8.0.[10, 17, 18]

A variety of MOF-PUU composites were tested for DMNP hydrolysis including composites with increasing MOF loading (20, 30, and 50 wt%) and differing MOF functionalization (UiO-66(Zr), UiO-66(Zr)-$NH_2$, UiO-66(Zr)-$NO_2$, UiO-66(Zr)-Naph). The MOF/PUU MMMs successfully degraded the simulant, indicating that the MOF is chemically accessible despite showing no $N_2$ gas sorption capacity or porosity (see above).[19] As expected, the increase in loading of MOF increases the hydrolysis rate up to 50 wt% PUU MMM (Table S5.4, Figure S5.12). The activities of PUU MMMs do not correlate with activities of as-synthesized MOF powders. For example, UiO-66(Zr) and UiO-66(Zr)-$NO_2$ show comparable activity as powders, but the UiO-66(Zr)/PUU MMM has a 6-fold faster rate over the UiO-66(Zr)-$NO_2$/PUU MMM. Also, the UiO-66(Zr)-$NH_2$ PUU MMM has the highest hydrolysis rate despite the as-synthesized MOF powder being much slower than either UiO-66(Zr) and UiO-66(Zr)-$NO_2$ powders. Deviations in properties for powder MOFs versus MOF-polymer composites has been observed gas sorption studies.[20, 21] Here, MOF ligand functionality is found to affect the catalytic rate

of a composite; although the origins of this effect are unclear at this time, it does provide a possible avenue for further study and optimization.

PUU-based MMMs of 50 wt% UiO-66(Zr) and UiO-66(Zr)-$NH_2$ were compared with analogous PVDF MMMs for DMNP hydrolysis. Interestingly, the UiO-66(Zr) and UiO-66(Zr)-$NH_2$ PVDF MMMs do correlate in activity to the reported hydrolysis rates of the pure MOF powders (Figure 5.5, Figure S5.12, Table S5.4).[17, 22] This shows that selection of both polymer and functionalized MOF effects the performance of the resulting composite. Indeed, MOF-based MMMs with PVDF have been shown to be more active than comparable UiO-66(Zr) MMMs prepared with polyethylene-co-vinylacetate (EVA) or polyethylene oxide (PEO) (see Chapter 3).[22] In the case of the 50 wt% UiO-66(Zr)-$NH_2$/PUU, the rate is almost equal to the PVDF MMM and previously reported crosslinked polythiourea-UiO-66-$NH_2$ coated fabric reported under similar assay conditions.[23] However, the mechanical properties of the self-standing PUU composite are far superior to the PVDF composites making it much more suited to practical uses in PPE.

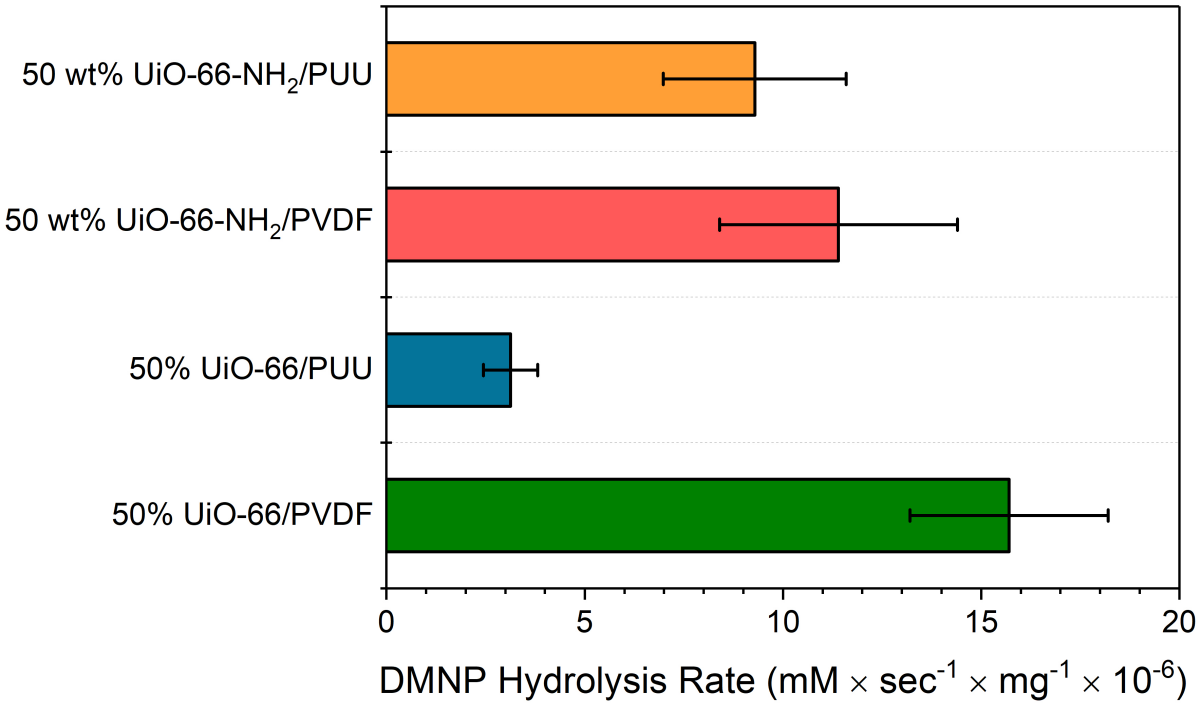


**Figure 5.5.** DMNP hydrolysis rates for MOF/PVDF MMMs compared to the corresponding MOF/PUU MMMs.

## 5.5 MOF/PUU Fibers

Spandex materials are typically used as woven materials from melt or wet spun fibers and incorporating MOFs into this process is important for their application in protective equipment. To test the viability of these composites in their anticipated form factor, 50 wt% UiO-66(Zr) and UiO-66(Zr)-$NH_2$/PUU fibers were drawn using a rudimentary wet spinning apparatus. Continuous fibers >3 m were made with phase inversion of the DMAC-based ink into a water bath and manually drawing the fiber. Despite being 50 wt% crystalline MOF (Figures S5.13-S5.15), the fiber can be manipulated and stretched. Figure 5.6 illustrates the practical handling of the fiber with a simple knot and weave that can be done without fracture. The preparation method also

results in a more porous microstructure of the composite due to the non-solvent contact in the drawing step (Figure 5.6, Figures S5.16 and S5.17). This proof-of-concept demonstrates that with optimization of fiber processing, MOF-based PUU fibers are viable.

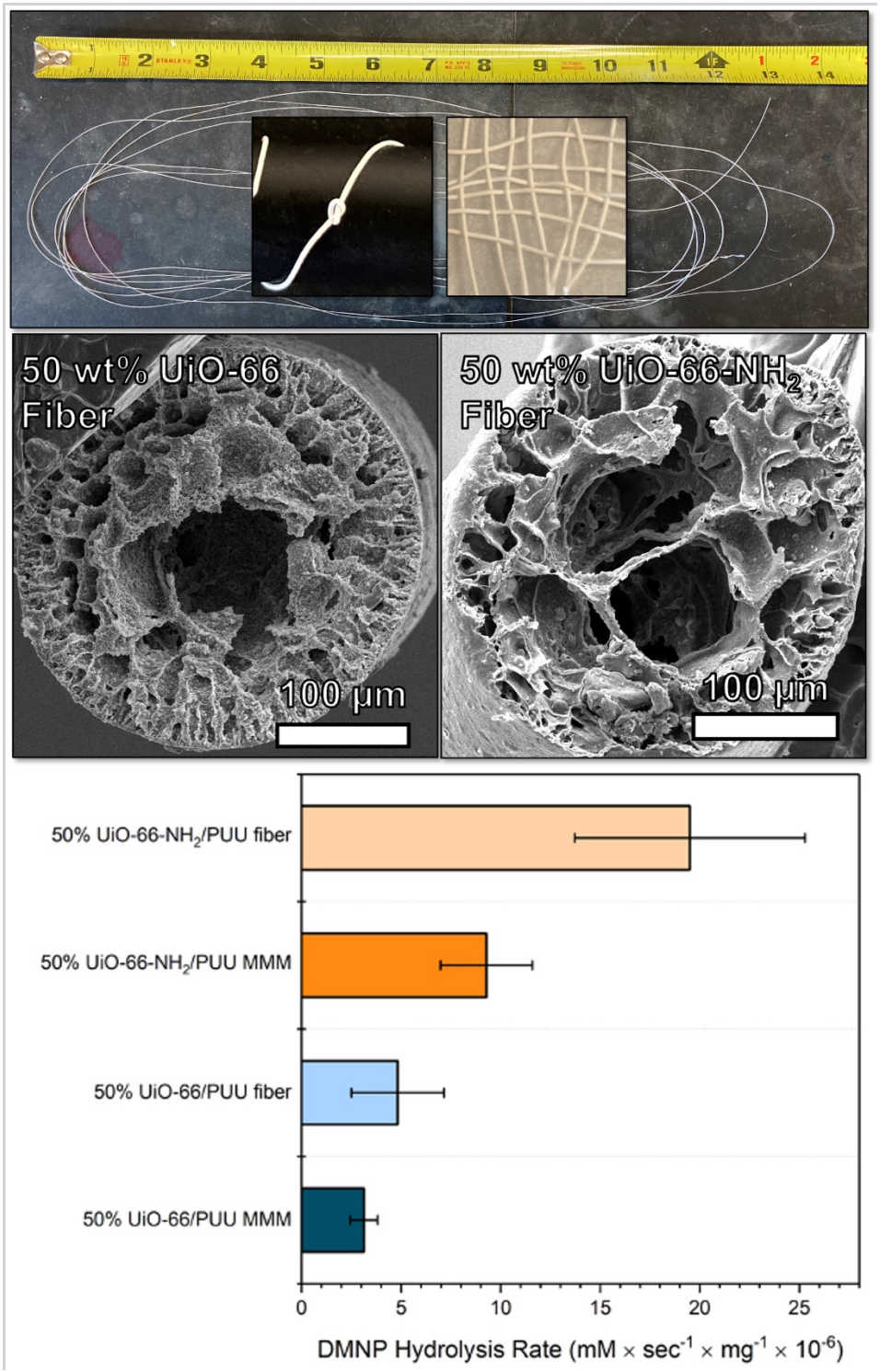


**Figure 5.6.** *Top:* Photographs of a single 3 m strand, knotted section, and woven threads of 50 wt% UiO-66/PUU Fiber and cross-section SEM images of 50 wt% MOF/PUU Fibers. *Bottom:* DMNP hydrolysis rates for MOF/PUU MMMs and fibers, normalized by mass of composite.

The fibrous, porous structure introduced into the composite affects the properties of the fiber composite compared to the equivalent MMM. Ductility of 50 wt% UiO-66/PUU fibers remains similar to MMM (elongation at break of 122% and 146%, respectively), but the strength is reduced by an order of magnitude (ultimate tensile strength of 1.02 and 9.53 MPa, respectively) (Table S5.2, Figure S5.18). The same trend holds true for 50 wt% UiO-66(Zr)-$NH_2$/PUU fibers and MMMs (Table S5.2, Figure S5.19). The porous morphology of the fibers likely led to the reduction in mechanical properties. Despite the lowering of strength, the 50 wt% UiO-66(Zr)/PUU fiber still had a higher toughness than 50 wt% UiO-66(Zr)/PVDF MMM (0.76 vs. 0.38 J/$cm^3$, respectively, Table S5.2).

The new fiber form factor was also tested for nerve agent simulant degradation using DMNP hydrolysis assay in the same way as for the MMMs. With the porous nature of the fiber, the transport of DMNP was improved as better activity was observed on a per MOF weight basis in both composites of both UiO-66(Zr) and UiO-66(Zr)-$NH_2$ (Figure 5.6, Figure S5.11). This effect was most pronounced in UiO-66(Zr)-$NH_2$ where rate almost doubles when in the fiber (Figure 5.6, Figure S5.12). This increase in hydrolysis rate indicates that the form factor of MOF-polymer composite is an important factor for successful application in PPE.

## 5.6 MOF/PUU MMMs Electrospun Nanofiber

While PUU/MOF composites were successfully processed into fiber form using wet spinning, the relatively large diameter may limit the utility for certain applications.

Therefore, the potential for processing nanofibers via electrospinning was explored. Nanofiber-based composites often are used in filtration applications for removal of aerosols, and the incorporation of MOFs can aid in filtration of toxic chemicals and pollutants.[9, 24]

Electrospinning of PUU-based composites was conducted to showcase the versatility of the materials using a variety of processing techniques. To a 10 wt% PUU electrospinning solution in DMF was added a suitable amount of MOF to achieve a 20 wt% MOF content in the final composite. SEM images for nanofibers electrospun from both UiO-66(Zr) and UiO-66(Zr)-$NH_2$ are shown in Figure 5.7. Fibers produced from electrospinning exhibited good dispersion of MOFs throughout the mat. Average fiber diameters for the materials were calculated to be ~350 ± 150 nm and ~425 ± 160 nm for the UiO-66(Zr)/PUU and UiO-66(Zr)-$NH_2$/PUU, respectively (see Figures S5.20 and S5.21), and the MOFs remained intact through the electrospinning process as evidenced by PXRD spectra (Figure S5.22). The ability of this composite to be electrospun into nanofibers adds to the versatility of MOF/PUU materials for PPE applications.

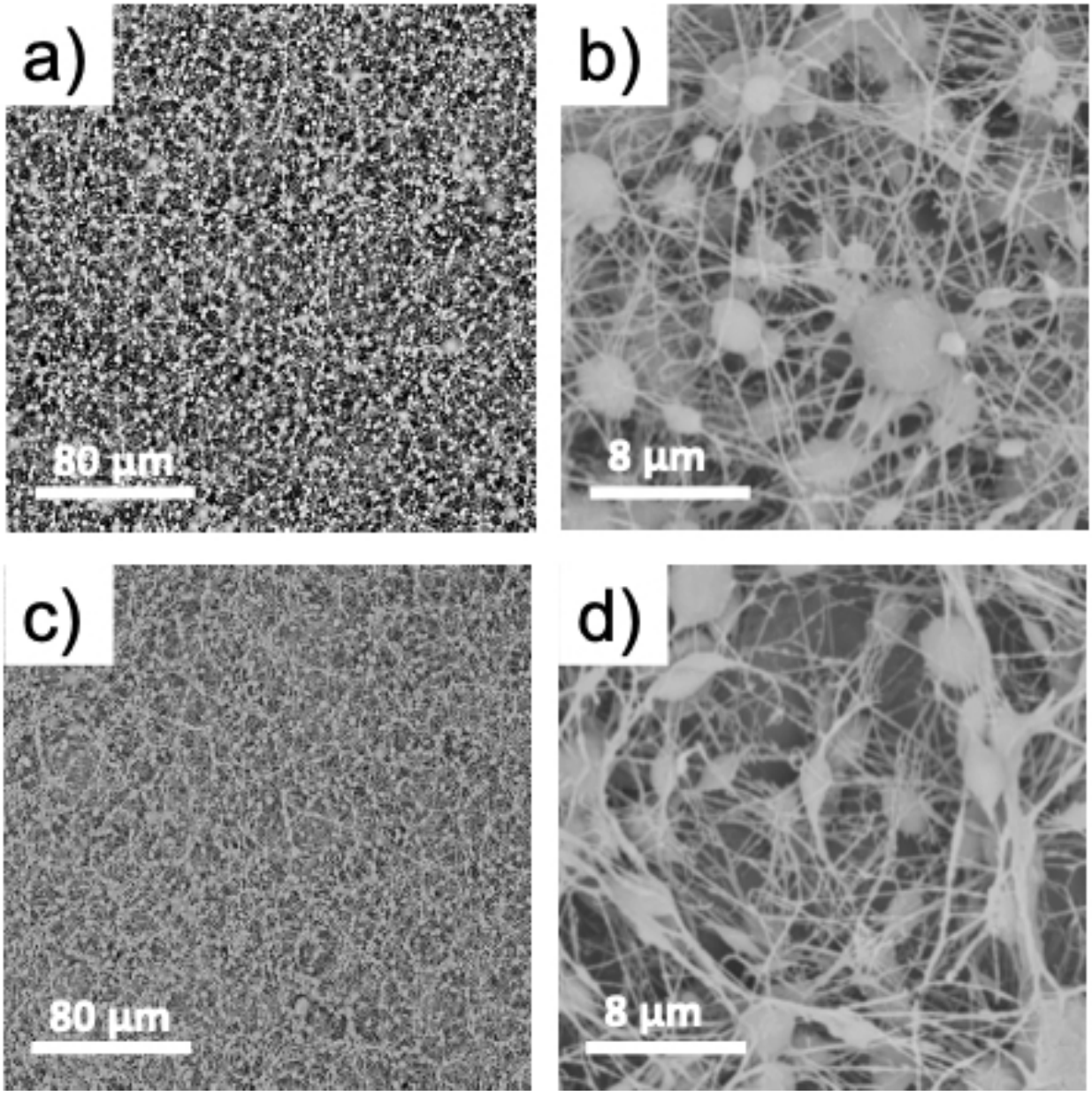


**Figure 5.7.** SEM images of 20 wt% UiO-66/PUU electrospun nanofiber composites magnified at: a) 1,000× and b) 10,000×. 20 wt% UiO-66-$NH_2$/PUU electrospun nanofiber composites magnified at: c) 1,000× and d) 10,000×.

## 5.7 Conclusions

Mechanically robust MOF-polymer composites for next generation PPE were achieved by focusing on a polymer with desired mechanical properties. Not only do the

MOF composites have improved tensile strength over the PUU-only polymer films, but they can be loaded to 50 wt% MOF and still retain suitable ductility. The highly loaded MOF/PUU composites were shown to have similar or improved nerve agent simulant hydrolysis when compared to the much more brittle PVDF polymer composites in MMM form factor. By processing the composite as fibers, the simulant hydrolysis was improved for MOF/PUU composites, especially for 50 wt% UiO-66-$NH_2$/PUU fiber that had the highest hydrolysis rate per gram. The proof-of-concept of electrospinning MOF/PUU further demonstrated that this composite has promise in a variety of applications.

The combination of modularity in both MOF and polymer allows for even more optimization to formulate superior PPE. By identifying a MOF-polymer combination that can be processed as MMMs, fibers, and electrospun mats, it greatly expands the possibilities of application into a range of PPE. This works represents the first exploration of exploration into MOF composites with durable mechanical properties at 50 wt% MOF and ability to break down chemical threats. In addition, the PUU system can be modified in the future to incorporate new polyols and diamines, resulting in new properties that can be used to tailor the final MOF-polymer composites.

## 5.8 Appendix: Supporting Information

**General Materials and Methods.** All solvents and starting materials were purchased from chemical suppliers and used without further purification (Sigma Aldrich, Arkema, Alfa Aesar, EMD, and TCI). Reaction solvents were stored in bottles with molecular sieves to remove residual water.

**Powder X-ray Diffraction (PXRD).** PXRD data was collected at room temperature on a Bruker D8 Advance diffractometer running at 40 kV, 40 mA for Cu Kα ($\lambda$ = 1.5418 Å), with primary slit of 1 mm, a scan speed of 0.5 sec/step, a step size of 0.01° in 2θ, and a 2θ range of 3-50° at room temperature.

**Gel Permeation Chromatography (GPC).** GPC was performed on a Malvern GPC with a D4000 single-pore column and a D6000M general-purpose mixed-bed weight divinylbenzene column connected in series with DMF as the mobile phase. Solutions were dissolved in DMF at ~1 mg/mL and filtered through a 0.4 μm PTFE membrane before being run at 0.7 mL/min using narrow polystyrene (PS) as calibration standards.

**Scanning Electron Microscopy (SEM).** MOFs, MMMs, and fibers were placed on conductive carbon tape on a sample holder and coated by using an Ir sputter-coater for 7 s. A FEI Quanta 250 scanning electron microscope was used for acquiring images using a 10 kV energy source under vacuum at a working distance of 10 mm. Fiber diameters of electrospun fiber mats were calculated using ThermoFisher Phenom FiberMetric software.

**$N_2$ Sorption Analysis.** Approximately 50 mg of sample were placed in a tare-weighed sample tube and degassed at 105 °C on a Micromeritics ASAP 2020 Adsorption

Analyzer until the outgas rate was <5 mmHg (12-48 h). Post-degas, the sample tube was weighed, and then $N_2$ sorption isotherm data was collected at 77 K on a Micromeritics ASAP 2020 Adsorption Analyzer using a volumetric technique. BET areas were then determined from analysis of the Rouquerol plots of the isotherm data, using 4-10 data points each.[25]

## Experimental

**Large-Scale Synthesis of UiO-66(Zr).** The synthesis of UiO-66 was adapted from a literature procedure.[11] Zirconium(IV) chloride (1.45 g, 6.2 mmol) and terephthalic acid (1.04 g, 6.2 mmol) were dissolved in 360 mL DMF under stirring. Glacial acetic acid (15 mL, 262 mmol) was added and the mixture was stirred for ~10 min to fully mix. The mixture was portioned evenly between 24 vials (20 mL, PTFE-lined caps). The vials were then placed in an oven preheated to 120 °C for 24 h. After cooling to ambient temperature, the particles were collected by centrifugation (fixed-angle rotor, 7000 rpm, 10 min), followed by washing with 3×200 mL DMF and 3×200 mL methanol. The particles were dried under vacuum at 60°C for 8 h, ground into a free-flowing powder with a mortar and pestle, and weighed. Yield: 1.58 g (92%).

**Large-Scale Synthesis of UiO-66(Zr)-$NH_2$.** The synthesis of UiO-66-$NH_2$ was adapted from a literature procedure.[11] Zirconium(IV) chloride (1.45 g, 6.2 mmol) and 2-aminoterephthalic acid (1.13 g, 6.2 mmol) were dissolved in 360 mL DMF under stirring. Glacial acetic acid (15 mL, 262 mmol) was added and the mixture was stirred for ~10 min to fully mix. The mixture was portioned evenly between 24 vials (20 mL, PTFE-lined

caps). The vials were then placed in an oven preheated to 120 °C for 24 h. After cooling to ambient temperature, the particles were collected by centrifugation (fixed-angle rotor, 7000 rpm, 10 min), followed by washing with 3×200 mL DMF, 1×200 mL methanol. The MOF was then resuspended in 200 mL methanol and 20 mL 1M HCl was added. The solution was then heated to reflux for 18 hours before being washed with 2×200 mL fresh methanol. The particles were dried under vacuum at 60°C for 8 h, ground into a free-flowing powder with a mortar and pestle, and weighed. Yield: 1.75 g (95%).

**Synthesis of Poly(urethane urea) Polymer.** Polytetrahydrofuran (polyTHF, $M_w$ = 2000 g/mol, 10.0 g, 5.00 mmol) was added as a solid to a 250 mL round bottom flask, dissolved in *N*,*N*-dimethylacetamide (DMAC, dried over molecular sieves) (10.0 g), and stirred under an Ar atmosphere at 80 °C for 10 min. To this 4,4'-methylene diphenyl diisocyanate (MDI, 2.55 mg, 10.0 mmol) was added in 5.0 mL of DMAC and stirred (>500 rpm) for an additional 10 min. To catalyze the reaction, 2.50 mL of a 0.1 wt% stannous octoate (5.35 µmol) solution in $CHCl_3$ was added and the reaction was stirred at 80 °C for 3 h. If necessary, DMAC (5-10 mL) was added to dilute the solution to allow for continuous stirring. After 3 h, the solution (termed the “prepolymer”) was diluted with 20 mL of DMAC and then ethylene diamine (334 µL, 5.00 mmol) in 10 mL of DMAC was added to the reaction mixture. Polymerization occurred upon addition and was complete in <20 min. Note, depending on the efficiency of stirring, more DMAC (10-50 mL) may be required to solubilize the final polymer. The final polymer was precipitated in 1 L of EtOH and washed with EtOH (2×800 mL) and dried at 60 °C for 12 h under vacuum.

**MOF/PUU MMM Fabrication**. UiO-66(Zr) and UiO-66(Zr)-$NH_2$ were synthesized according to literature procedures (see above).[11, 26] MOF (100–300 mg) was dispersed in an ethyl acetate solution (~8 mL) via sonication. Note, grinding MOF powders with a mortar and pestle and sonication for 30 min in the center of a Branson 2800 sonicator bath were important to make high quality MMMs. A 15 wt% PUU solution in DMAC was added to yield corresponding wt% MMMs (e.g., for a 50 wt% UiO-66 MMM 150 mg of UiO-66 was combined with 1.0 g of polymer solution). The MOF and polymer solutions were thoroughly mixed in a sonication bath for 1 h. The resulting 'ink' was then subjected to rotary evaporation to remove the ethyl acetate and concentrated to a honey-like viscosity. The MOF–polymer solution was then transferred to a substrate, either aluminum foil or glass, and then cast using a draw down method with a doctor blade set to a height of 950 μm at a speed of 25 mm/s. The cast films were then cured at 65 °C in a preheated oven under a thin-neck glass funnel for 12 h. After cooling, ~2 mL of iPrOH was dropped on the films to induce swelling and the films were delaminated with tweezers and allowed to dry.

**Tensile Testing.** Mechanical tensile testing was performed on a CellScale Univert mechanical testing apparatus with 100 N load cell. Tensile tests were carried out at an extension rate of 0.17 mm/s, an electronically configured pre-load of 0.2 N and a sampling rate of 15 Hz. Material test specimens were cut with a razor blade into rectangular test coupons 5 ± 2 mm in width, 20 ± 5 mm in length, and 100 ± 50 μm in thickness. Coupons were clamped vertically with an exposed distance between clamps ($\varepsilon_0$) of 4 ± 2 mm.

Cross sectional area was determined via caliper and micrometer measurements for films and cross-sectional SEM for fibers.

The force measurement on the CellScale Univert load cell was divided by the cross-sectional area of the fiber or film to obtain the engineering stress (σ) in MPa. The displacement measurement (ε) of the CellScale Univert was divided by the initial length between clamps ($\varepsilon_0$) to yield the dimensionless engineering strain ($\varepsilon/\varepsilon_0$). These values were computed for every time point using Excel during the data reduction.

Material properties were then determined using the graphs of computed engineering stress vs. strain. Ultimate Tensile Strength (UTS) was the final σ value before the point of failure of the material. EAB was the corresponding strain value ($\varepsilon/\varepsilon_0$) at this point. The point of yielding was qualitatively determined as the final point of yielding on the linear region of the stress-strain curves. The stress at this yield point was the Yield Strength. The slope of the linear region of the graph was computed using linear regression analysis in Excel and represented the Elastic Modulus.

Finally, the toughness ($U_T$) of the material was computed numerically by determining at each instantaneous point of measurement the value of stress times the increment of strain during that unit time and summing all of such values for the curve until failure. The relationship can be written as a summation:

$$U_T = \sum_{0}^{\varepsilon_f} \sigma * \Delta\varepsilon$$

Where $U_T$ is the toughness, Δε is the increment of strain applied between each increment of data, σ is the computed stress during that increment, and $\varepsilon_f$ is the failure point of the material.

**Screening of MMMs for DMNP Hydrolysis:** Membranes (~12×8 mm, prepared and measured in triplicate for each sample) were inserted into 3D printed plastic holders[3] and placed in individual wells of an Olympus Plastics clear, flat-bottom 24-well assay plate. In order to avoid beam blockage, a small rubber o-ring was used to keep the membrane in place along the wall of the well. Buffer solution (2 mL of 20 mM *N*-ethylmorpholine, pH = 8.0) was added to each well. A solution of dimethyl-4-nitrophenyl phosphate (DMNP, 20 µL of 25 mM in MeOH) was added and appearance of *p*-nitrophenoxide was monitored at $\lambda_{max}$ = 407 nm, every 12 s for 30 min. Slopes were calculated from the linear region of each plot (typically at 200-800 s) and normalized by the mass of membrane.

**MOF/PUU Fiber Spinning**. In analogy to MMM 'ink' above, 100–300 mg of MOF was dispersed in an ethyl acetate solution (~8 mL) via sonication. A 15 wt% PUU solution in DMAC was added to yield corresponding wt% fibers. The resulting 'ink' was then subjected to rotary evaporation to remove the ethyl acetate and concentrated to a honey-like viscosity. The MOF-polymer solution was then taken up in a 1 mL syringe fitted with a 0.9×100 mm, blunt tip needle and secured to a syringe pump. The end of the needle was bent slightly and immersed (~1 cm deep) in a 1 L water bath at room temperature. The syringe pump was set to 0.6 mL/h and the MOF-polymer solution was injected into the water bath and the resulting fiber was collected by wrapping around a large beaker. The fibers were dried at 65 °C in a preheated oven for 12 h.

**MOF/PUU Electrospinning**. MOF (120 mg) was dispersed in 5 mL of DMF in a 20 mL scintillation vial and sonicated for 5 min using a probe sonicator. Next, PUU (500

mg) was added to the vial, and the mixture was magnetically stirred for 72 h. The solution was loaded into a 6 mL plastic syringe and transferred to a programmable floor-stand MSK-NFES-4 electrospinning unit (MTI Corporation). An electric field of 15 kV was applied across a ~10 cm gap between a 20-gauge hypodermic needle and a stainless-steel cylinder with an aluminum foil covering. Spinning was conducted at a solution flow rate of 1 mL/h for 15 min.

## Supplemental Tables

**Table S5.1.** Number and weight average molecular weights ($M_n$ and $M_w$) and dispersity for starting polymer and resulting PUU polymer from GPC curves using polystyrene standards.

| Sample | $M_n$ (g/mol) | $M_w$ (g/mol) | Đ |
|---|---|---|---|
| polyTHF$_{2000}$ | 6,500 | 8,700 | 1.34 |
| PUU | 78,500 | 139,000 | 1.77 |

**Table S5.2.** Summary of tensile testing results for all films tested. EAB = Elongation at Break; UTS = Ultimate Tensile Strength; Str. = Strength. *No definitive plastic yield point observed. **EAB, Toughness and UTS estimated, could not pull to failure due to extension limits of instrumentation.

| **PUU Only**** | | | | | | |
|---|---|---|---|---|---|---|
| **Sample** | **Thickness ($\mu$m)** | **Yield Str. (MPa)** | **EAB (%)** | **Elastic Modulus (MPa)** | **Ultimate Str. (MPa)** | **Toughness (J/cm$^3$)** |
| 1** | 103 | N/A* | >1540% | 0.23 | >5.21 | >47.76 |
| 2** | 132 | N/A* | >1570% | 0.29 | >5.97 | >56.64 |
| 3** | 109 | N/A* | >1580% | 0.36 | >7.80 | >70.79 |
| *Average* | 115 | N/A* | >1540% | 0.29 | >5.21 | >47.76 |
| $\sigma$ | 15 | | - | 0 | - | - |
| **20 wt% UiO-66/PUU MMM**** | | | | | | |

| Sample | Thickness ($\mu$m) | Yield Str. (MPa) | EAB (%) | Elastic Modulus (MPa) | Ultimate Str. (MPa) | Toughness (J/cm$^3$) |
|---|---|---|---|---|---|---|
| 1** | 95 | 4.92* | >1960% | 1.71* | >10.98 | >148.72 |
| 2 | 90 | 4.19* | 2330% | 2.73* | 11.54 | 197.66 |
| 3** | 94 | 4.34* | >2120% | 3.06* | >11.05 | >168.65 |
| 4** | 96 | 4.22* | >1880% | 2.64* | >11.64 | >149.56 |
| *Average* | 94 | 4.42 | >1880% | 2.54 | >10.98 | >148.72 |
| $\sigma$ | 3 | 0.34 | - | 0.58 | - | - |
| **30 wt% UiO-66/PUU MMM**** | | | | | | |
| **Sample** | **Thickness ($\mu$m)** | **Yield Str. (MPa)** | **EAB (%)** | **Elastic Modulus (MPa)** | **Ultimate Str. (MPa)** | **Toughness (J/cm$^3$)** |
| 1** | 69 | 4.92 | >1600% | 2.85 | >9.96 | >118.41 |
| 2** | 66 | 5.83 | >1670% | 2.99 | >10.94 | >143.05 |
| 3 | 69 | 5.03 | 2170% | 2.08 | 8.42 | 142.12 |
| 4 | 79 | 5.33 | 2010% | 2.01 | 9.23 | 144.30 |
| *Average* | 71 | 5.28 | >1610% | 2.48 | >8.42 | >118.41 |
| $\sigma$ | 6 | 0.41 | - | 0.51 | - | - |
| **40 wt% UiO-66/PUU MMM** | | | | | | |
| **Sample** | **Thickness ($\mu$m)** | **Yield Str. (MPa)** | **EAB (%)** | **Elastic Modulus (MPa)** | **Ultimate Str. (MPa)** | **Toughness (J/cm$^3$)** |
| 1 | 79 | 6.03 | 465% | 9.65 | 8.79 | 35.10 |
| 2 | 76 | 6.21 | 506% | 9.66 | 9.77 | 40.98 |
| 3 | 78 | 5.90 | 417% | 9.58 | 9.23 | 31.76 |
| 4 | 71 | 6.13 | 527% | 9.80 | 9.51 | 41.92 |
| *Average* | 76 | 6.06 | 479% | 9.67 | 9.33 | 37.44 |
| $\sigma$ | 4 | 0.13 | 49% | 0.10 | 0.42 | 4.84 |
| **50 wt% UiO-66/PUU MMM** | | | | | | |
| **Sample** | **Thickness ($\mu$m)** | **Yield Str. (MPa)** | **EAB (%)** | **Elastic Modulus (MPa)** | **Ultimate Str. (MPa)** | **Toughness (J/cm$^3$)** |
| 1 | 71 | 8.97 | 200% | 53.1 | 12.95 | 22.78 |
| 2 | 56 | 9.73 | 119% | 73.7 | 13.40 | 13.35 |
| 3 | 84 | 9.88 | 120% | 74.1 | 13.55 | 14.00 |
| *Average* | 70 | 9.53 | 146% | 67.0 | 13.30 | 16.71 |
| $\sigma$ | 14 | 0.49 | 47% | 12.0 | 0.31 | 5.27 |

| **50 wt% UiO-66-$NH_2$/PUU MMM** | | | | | | |
|---|---|---|---|---|---|---|
| **Sample** | **Thickness ($\mu$m)** | **Yield Str (MPa)** | **EAB (%)** | **Elastic Modulus (MPa)** | **Ultimate Str. (MPa)** | **Toughness ($J/cm^3$)** |
| 1 | 57 | 7.57 | 122% | 31.3 | 10.60 | 10.02 |
| 2 | 57 | 6.55 | 141% | 35.1 | 9.83 | 11.62 |
| 3 | 57 | 6.23 | 122% | 25.0 | 8.60 | 8.25 |
| *Average* | 57 | 6.78 | 129% | 30.5 | 9.68 | 9.96 |
| $\sigma$ | 0 | 0.70 | 11% | 5.1 | 1.01 | 1.68 |
| **50 wt% UiO-66/PVDF MMM** | | | | | | |
| **Sample** | **Thickness ($\mu$m)** | **Yield Str. (MPa)** | **EAB (%)** | **Elastic Modulus (MPa)** | **Ultimate Str. (MPa)** | **Toughness ($J/cm^3$)** |
| 1 | 60 | 8.12 | 5.0% | 233.9 | 9.55 | 0.41 |
| 2 | 60 | 5.63 | 2.8% | 240.0 | 6.40 | 0.14 |
| 3 | 62 | 7.54 | 11.2% | 192.7 | 9.73 | 0.70 |
| 4 | 59 | 6.22 | 3.4% | 255.5 | 7.00 | 0.27 |
| *Average* | 60 | 6.88 | 5.6% | 230.5 | 8.17 | 0.38 |
| $\sigma$ | 1 | 1.15 | 3.8% | 26.8 | 1.72 | 0.24 |
| **50 wt% UiO-66-$NH_2$/PVDF** | | | | | | |
| **Sample** | **Thickness ($\mu$m)** | **Yield Str (MPa)** | **EAB (%)** | **Elastic Modulus (MPa)** | **Ultimate Str. (MPa)** | **Toughness ($J/cm^3$)** |
| 1 | 53 | 3.81 | 3% | 298.3 | 4.15 | 0.07 |
| 2 | 48 | 10.55 | 3% | 596.3 | 12.35 | 0.18 |
| 3 | 48 | 10.86 | 5% | 471.8 | 13.44 | 0.31 |
| *Average* | 50 | 8.41 | 4% | 455.5 | 9.98 | 0.19 |
| $\sigma$ | 3 | 3.98 | 1% | 149.7 | 5.08 | 0.12 |
| **50 wt% UiO-66/PUU Fiber** | | | | | | |
| **Sample** | **Thickness ($\mu$m)** | **Yield Str. (MPa)** | **EAB (%)** | **Elastic Modulus (MPa)** | **Ultimate Str. (MPa)** | **Toughness ($J/cm^3$)** |
| 1 | N/A | 1.04 | 122% | 5.69 | 1.57 | 0.88 |
| 2 | N/A | 1.02 | 137% | 7.58 | 1.59 | 1.09 |
| 3 | N/A | 1.02 | 107% | 3.50 | 1.02 | 0.30 |
| *Average* | - | 1.02 | 122% | 5.59 | 1.39 | 0.76 |
| $\sigma$ | | 0.01 | 15% | 2.04 | 0.32 | 0.41 |
| **50 wt% UiO-66-$NH_2$/PUU Fiber** | | | | | | |

| Sample | Thickness ($\mu$m) | Yield Str. (MPa) | EAB (%) | Elastic Modulus (MPa) | Ultimate Str. (MPa) | Toughness (J/cm$^3$) |
|---|---|---|---|---|---|---|
| 1 | N/A | 1.66* | 129% | 3.50 | 2.39 | 1.91 |
| 2 | N/A | 1.66* | 122% | 2.14 | 1.85 | 1.57 |
| 3 | N/A | 1.66* | 106% | 1.71 | 1.76 | 1.25 |
| *Average* | | 1.66* | 119% | 2.45 | 2.00 | 1.58 |
| $\sigma$ | | - | 12% | 0.93 | 0.34 | 0.33 |
| ***No definitive plastic yield point observed** | | | | | | |
| ****EAB, Toughness and UTS estimated, could not pull to failure due to extension limits of machine** | | | | | | |

**Table S5.3.** BET surface areas and standard deviations for MOF and composites determined from $N_2$ sorption.

| Material | BET Surface Area (m$^2$/g) | $\sigma$ |
|---|---|---|
| UiO-66 Powder | 1475 | 8 |
| 50 wt% UiO-66/PUU MMM | 4.4 | 0.1 |
| 50 wt% UiO-66/PUU fiber | 8.7 | 0.1 |

**Table S5.4.** DMNP Hydrolysis Rates for MOF-polymer composites, normalized by mass of composite.

| Material | Composite Hydrolysis Rate (mM sec-1 mg-1 × 10-6) | $\sigma$ |
|---|---|---|
| 20 wt% UiO-66/PUU MMM | 1.3 | 0.4 |
| 30 wt% UiO-66/PUU MMM | 2.6 | 0.4 |
| 50 wt% UiO-66/PUU MMM | 3.1 | 0.7 |
| 50 wt% UiO-66-NH2/PUU MMM | 9.3 | 2.3 |
| 50 wt% UiO-66-NO2/PUU MMM | 0.7 | 0.0 |
| 50 wt% UiO-66-Naph/PUU MMM | 1.5 | 0.3 |
| 50 wt% UiO-66/PVDF MMM | 15.7 | 2.5 |
| 50 wt% UiO-66-NH2/PVDF MMM | 11.4 | 3.0 |
| 50 wt% UiO-66/PUU Fiber | 4.8 | 2.3 |
| 50 wt% UiO-66-NH2/PUU Fiber | 19.5 | 5.8 |
| PUU Only | 0.5 | 0.5 |
| PVDF Only | 0.6 | 0.6 |

**Supplemental Figures**

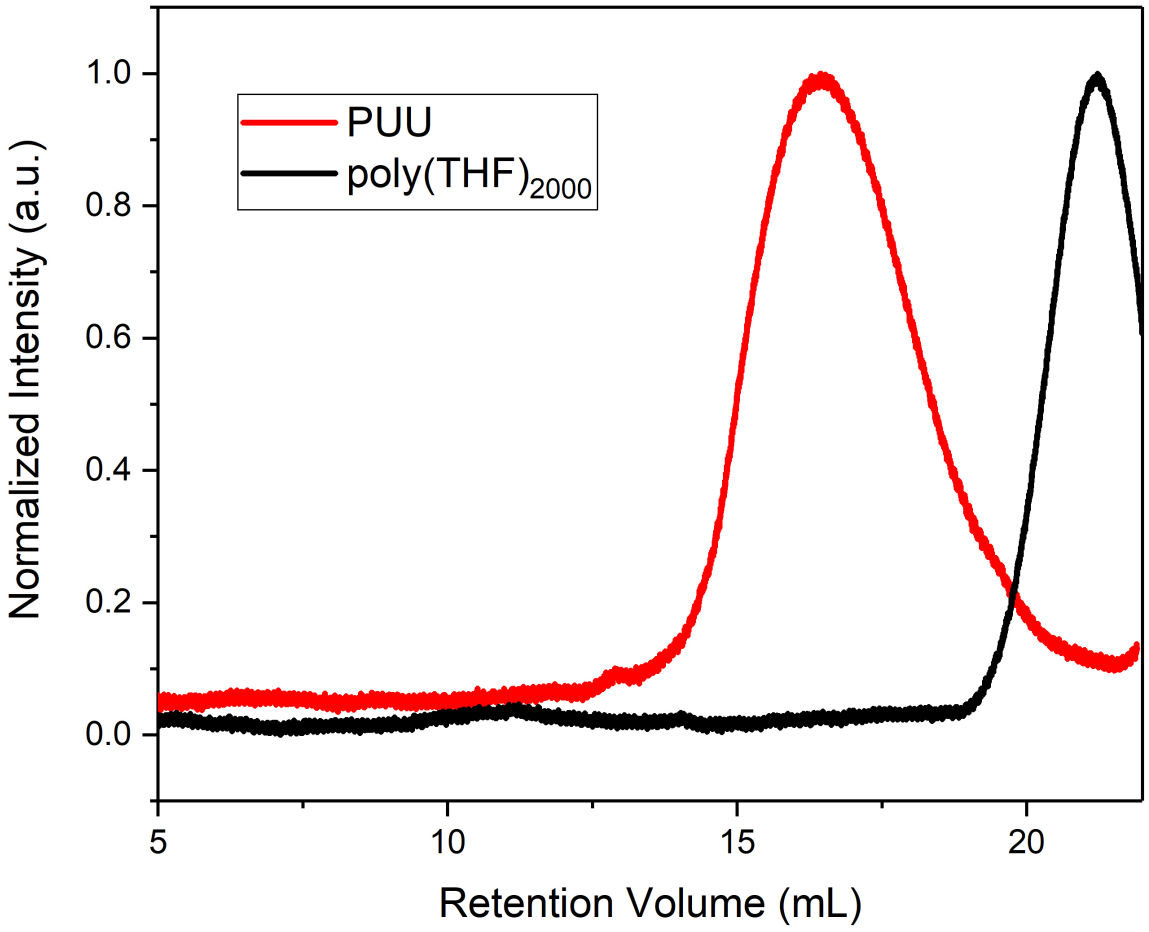


**Figure S5.1**. Gel permeation chromatography (GPC) trace of as-received polytetrahydrofuran ($M_w$ ~2000 g/mol, Sigma Aldrich, black trace) and synthesized polyurethane urea (red trace). Polystyrene (PS) standards were used to determine relative molecular weight of the polymer and dispersity.

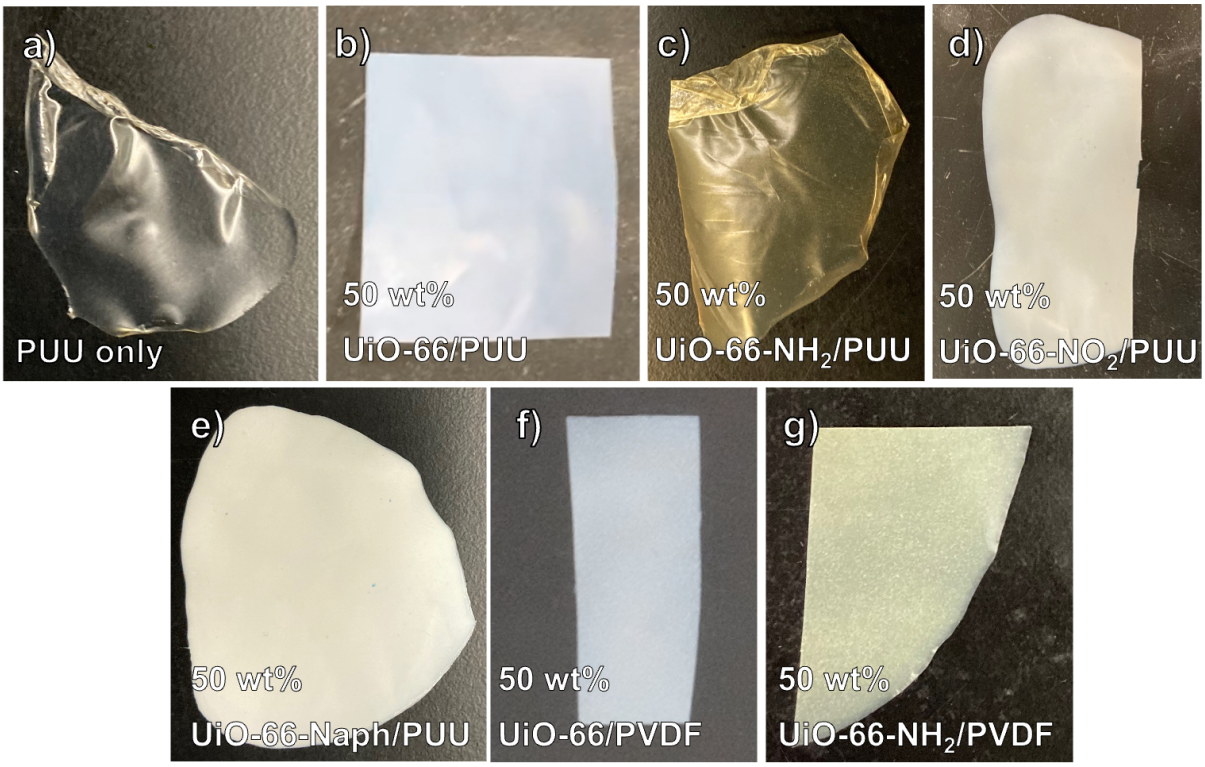


**Figure S5.2.** Representative images of cast, cured, and delaminated a) PUU only film, b) 50 wt% UiO-66(Zr)/PUU MMM, c) 50 wt% UiO-66(Zr)-$NH_2$/PUU MMM, d) 50 wt% UiO-66(Zr)-$NO_2$/PUU MMM, e) 50 wt% UiO-66(Zr)-Naph/PUU MMM, f) 50 wt% UiO-66(Zr)/PVDF MMM, and g) 50 wt% UiO-66(Zr)-$NH_2$/PVDF MMM.

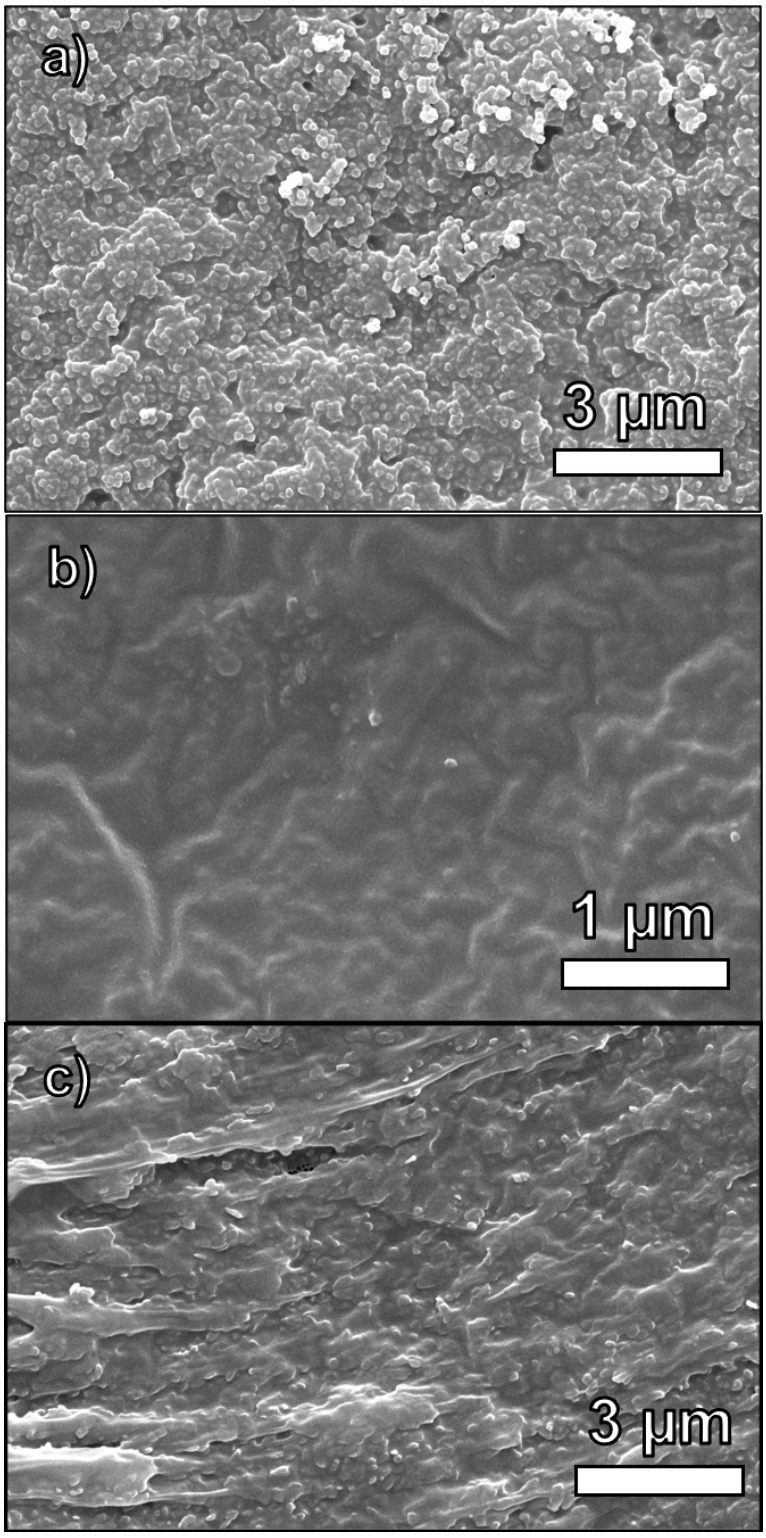


**Figure S5.3.** SEM images of: a) top, b) bottom, and c) cross-section of 50 wt% UiO-66(Zr)/PUU MMM.

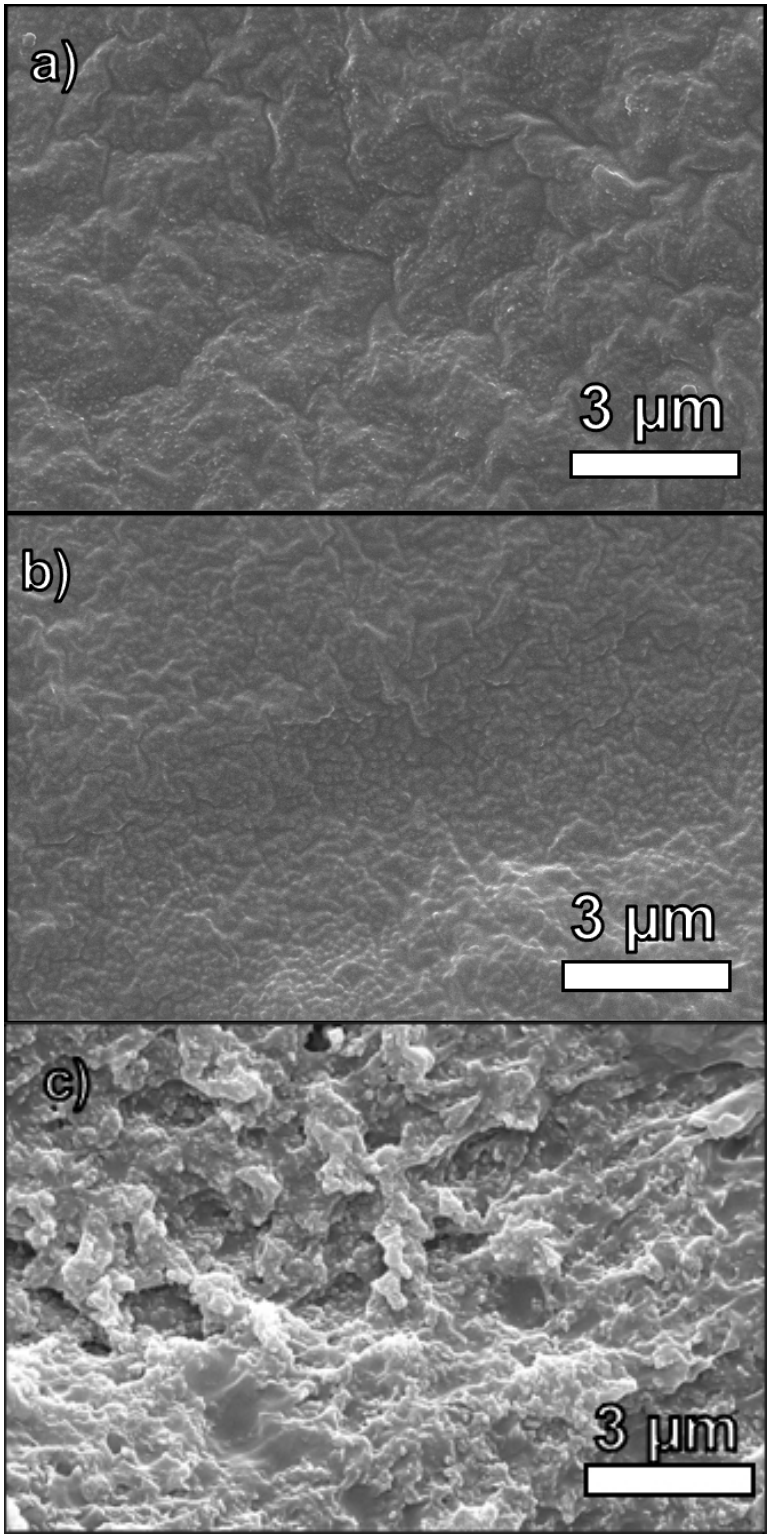


**Figure S5.4.** SEM images of: a) top, b) bottom, and c) cross-section of 40 wt% UiO-66(Zr)/PUU MMM.

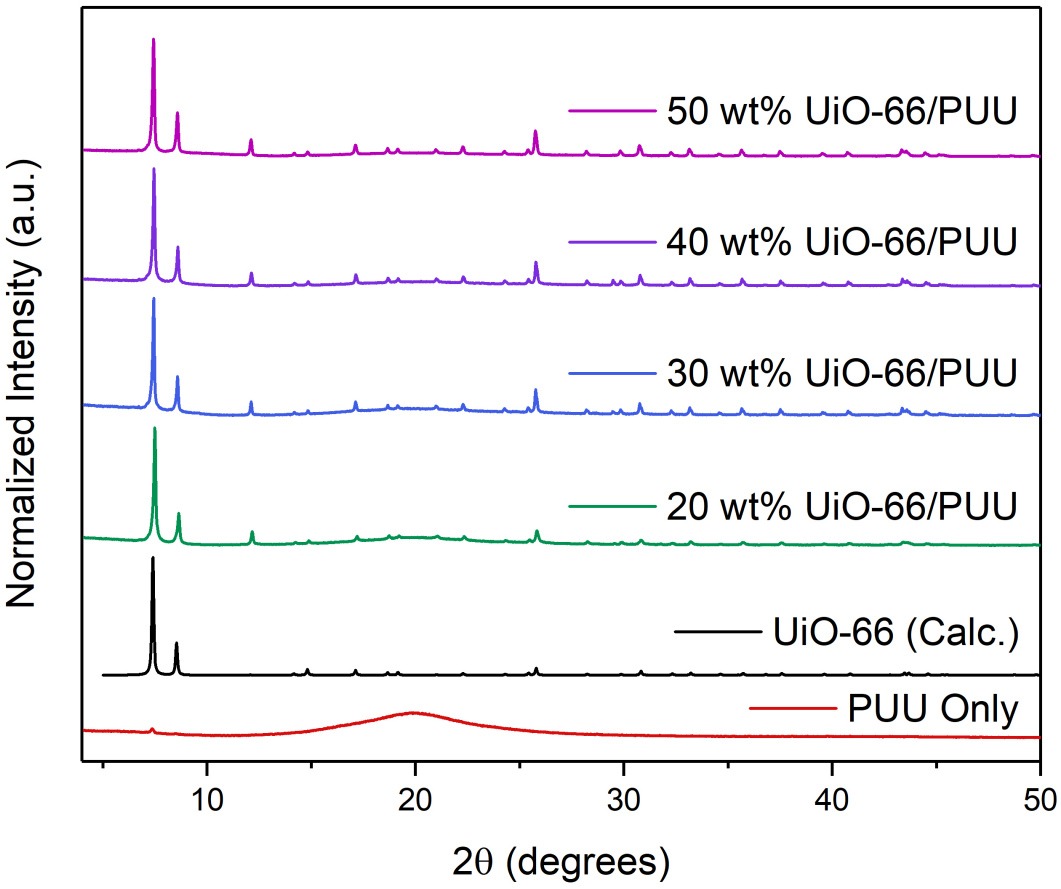


**Figure S5.5.** PXRD of PUU only film and UiO-66(Zr)/PUU MMMs.

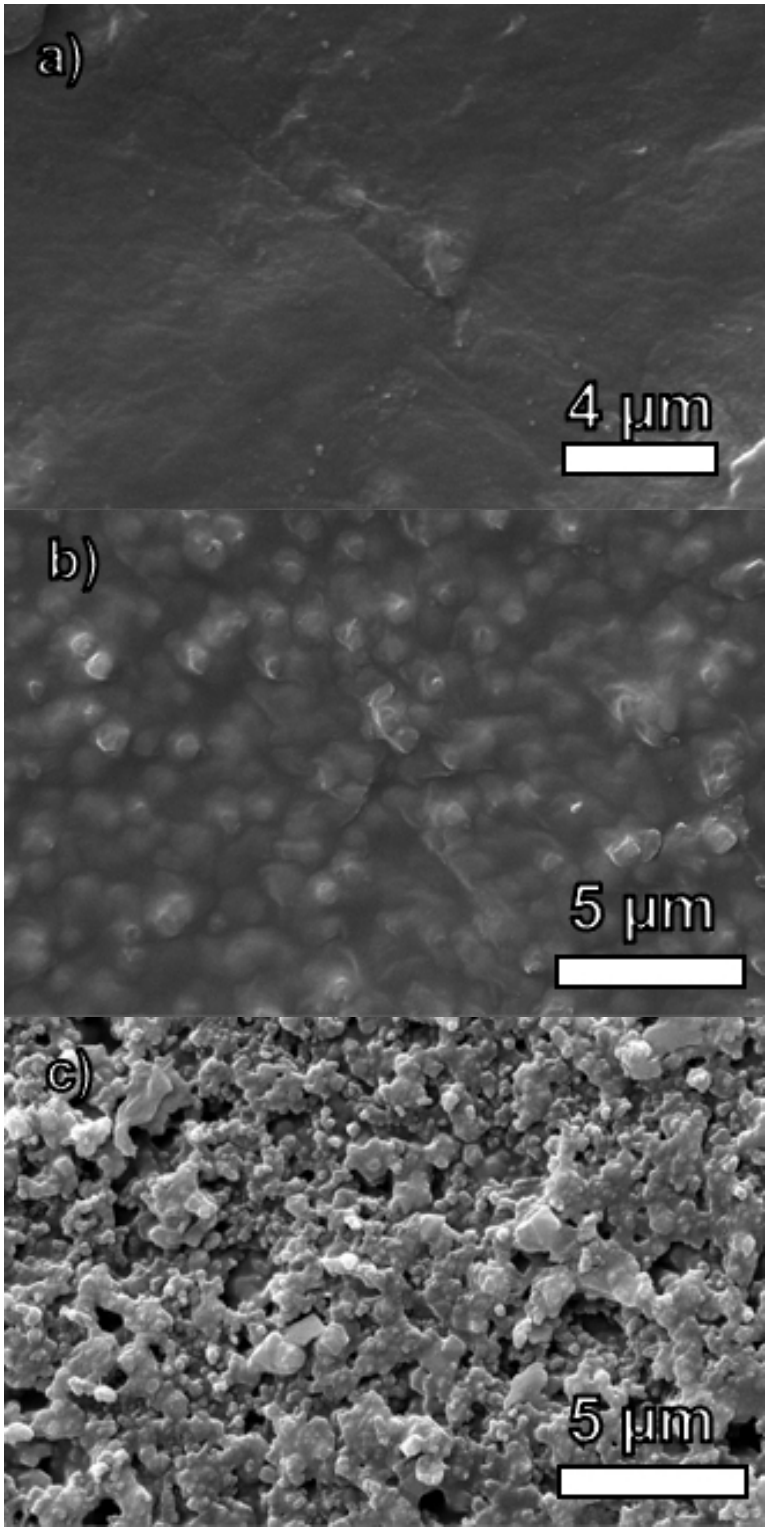


**Figure S5.6.** SEM images of top side of 50 wt% PUU MMMs with: a) UiO-66(Zr)-$NH_2$, b) UiO-66(Zr)-$NO_2$, c) UiO-66(Zr)-Naph.

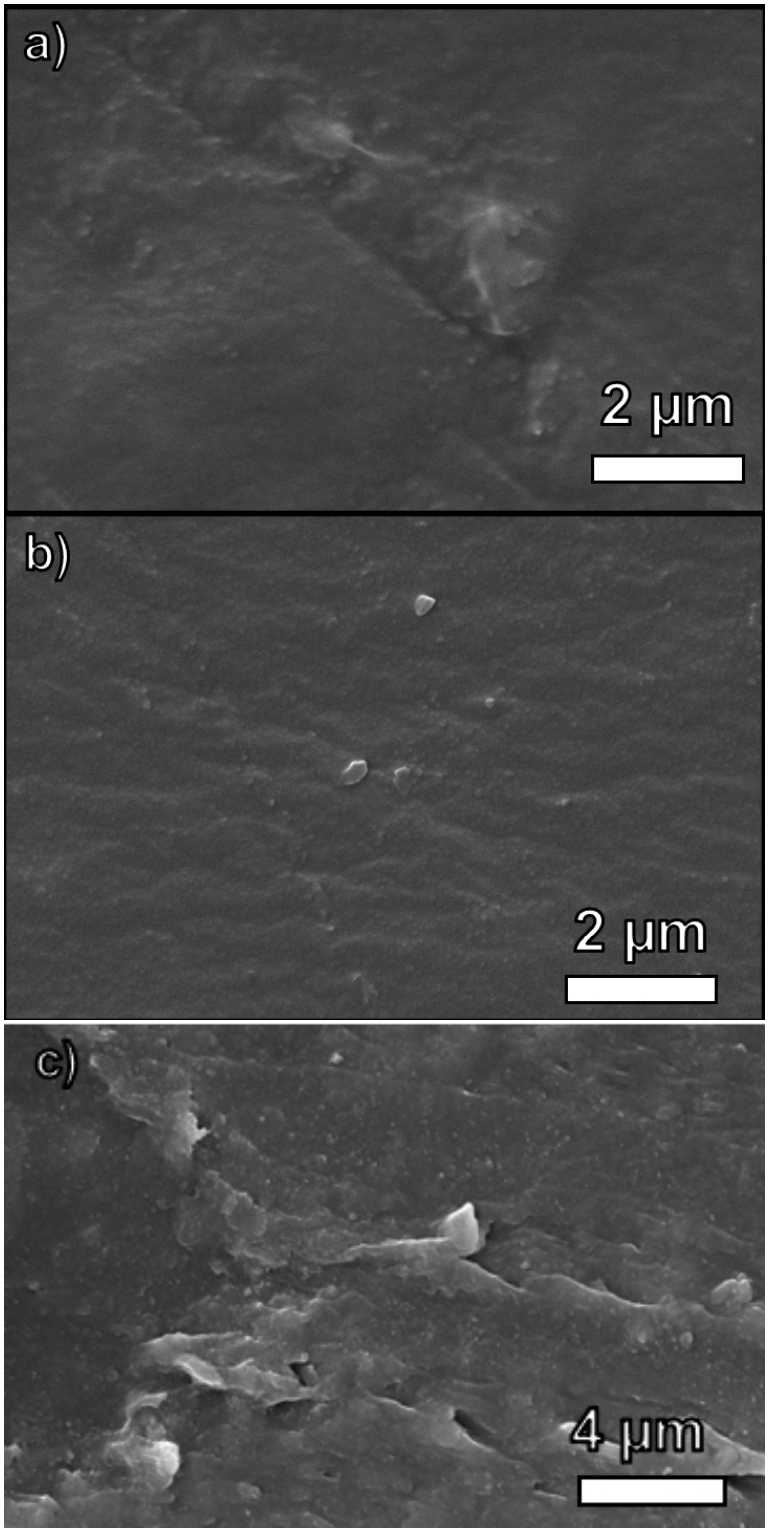


**Figure S5.7.** SEM images of: a) top, b) bottom, and c) cross-section of 50 wt% UiO-66(Zr)-$NH_2$/PUU MMM.

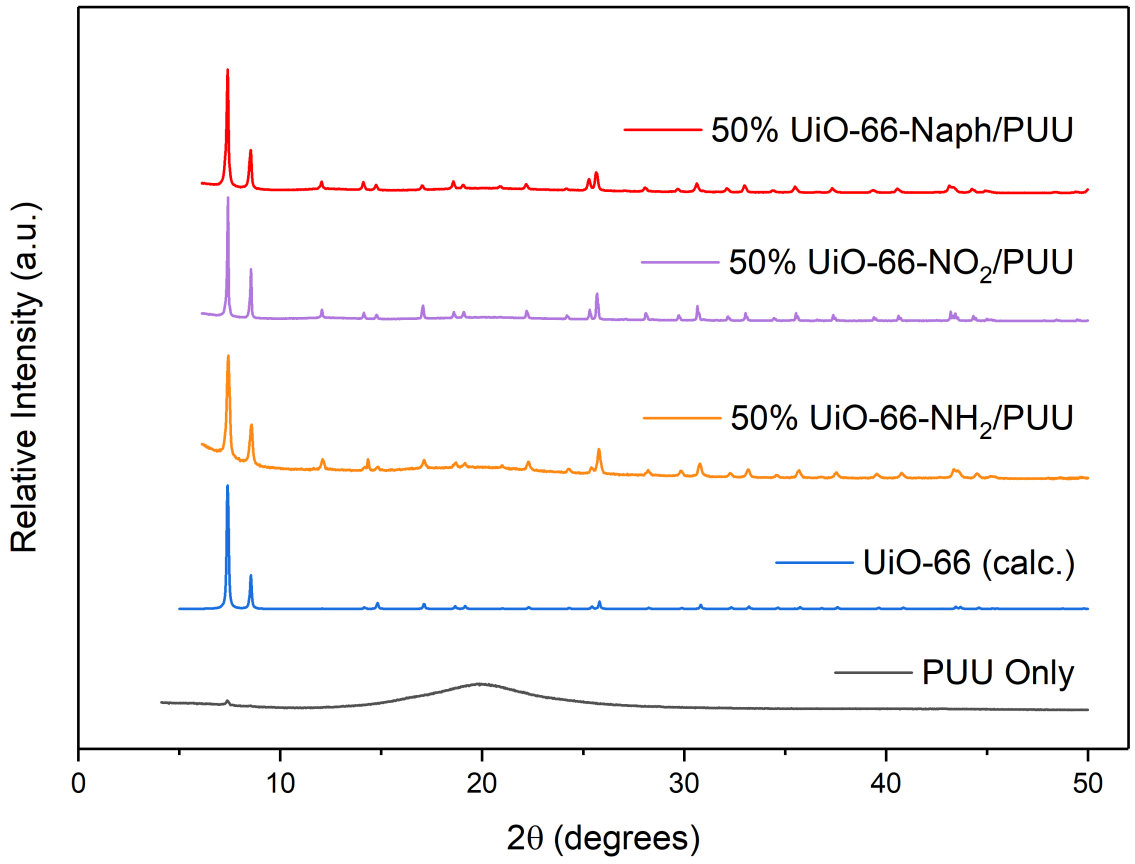


**Figure S5.8.** PXRD of PUU only and 50 wt% Modified UiO-66(Zr)/PUU MMMs.

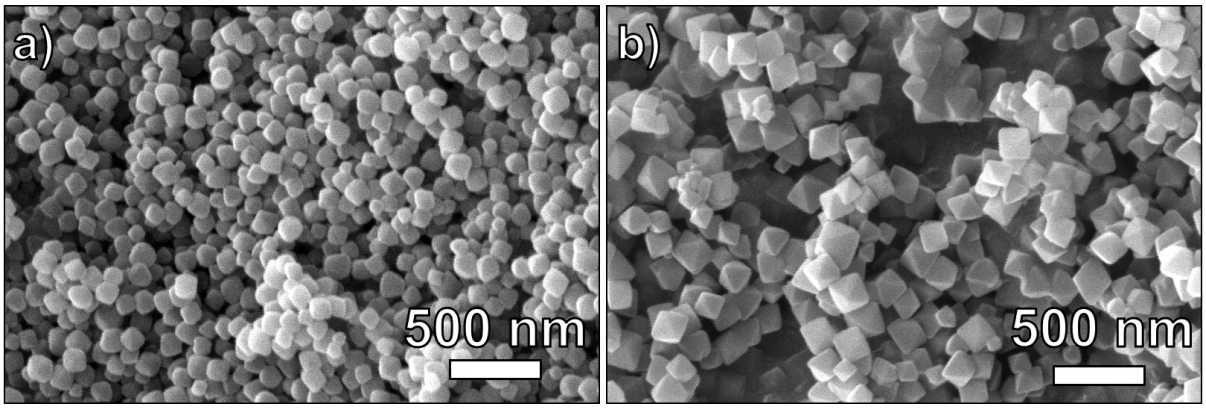


**Figure S5.9.** SEM images of UiO-66(Zr) and UiO-66(Zr)-$NH_2$ after mortar and pestle grinding.

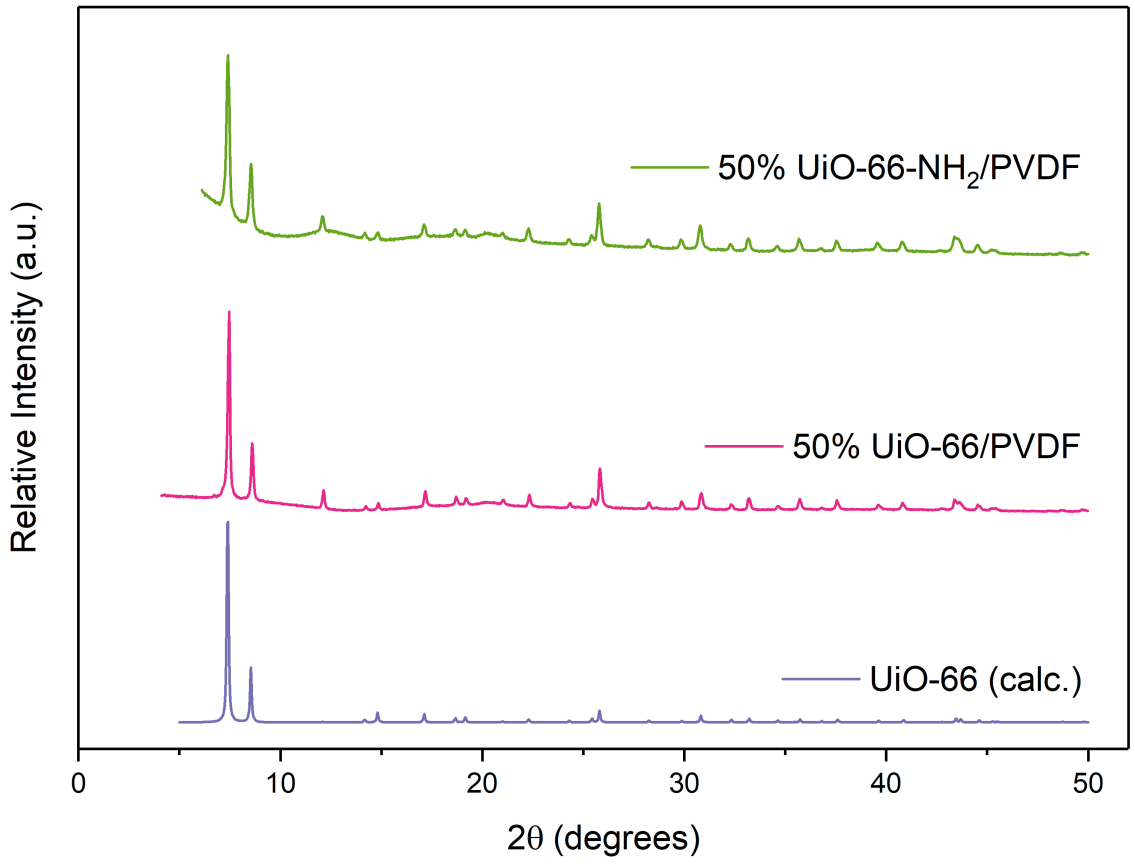


**Figure S5.10.** PXRD of 50 wt% UiO-66(Zr)/PVDF MMM and 50 wt% UiO-66(Zr)-$NH_2$/PVDF MMM.

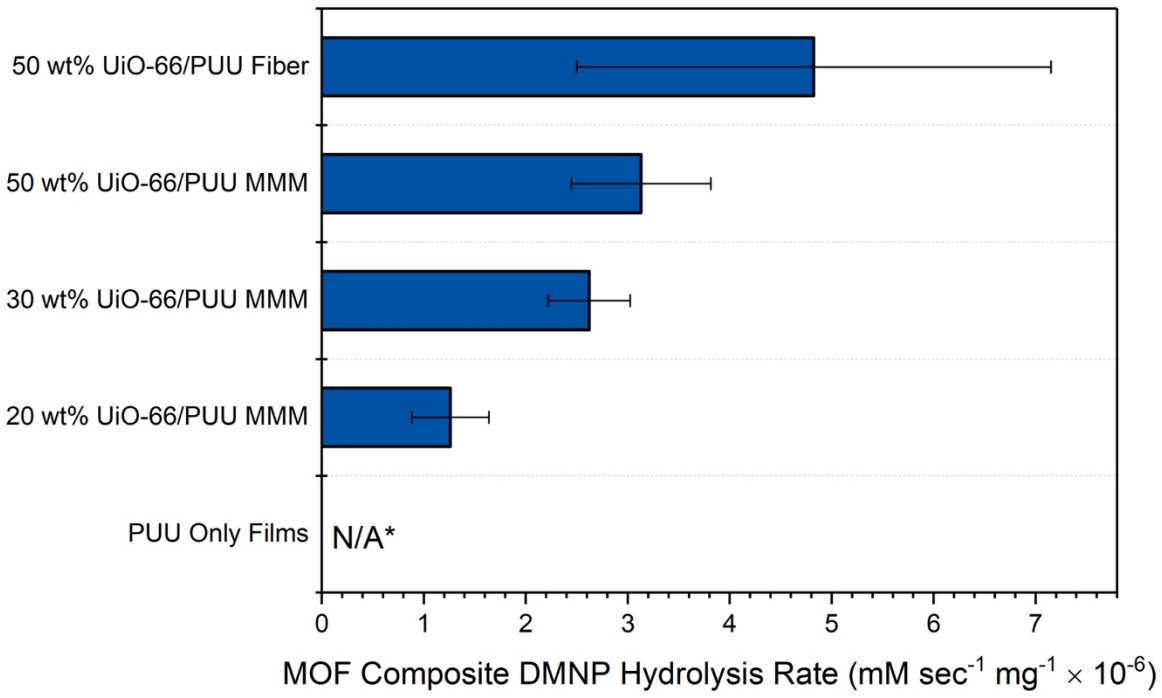


**Figure S5.11.** DMNP hydrolysis rate from HTS assay of UiO-66(Zr)/PUU composites of differing loading and fabrication method. *No appreciable hydrolysis so rate cannot be calculated.

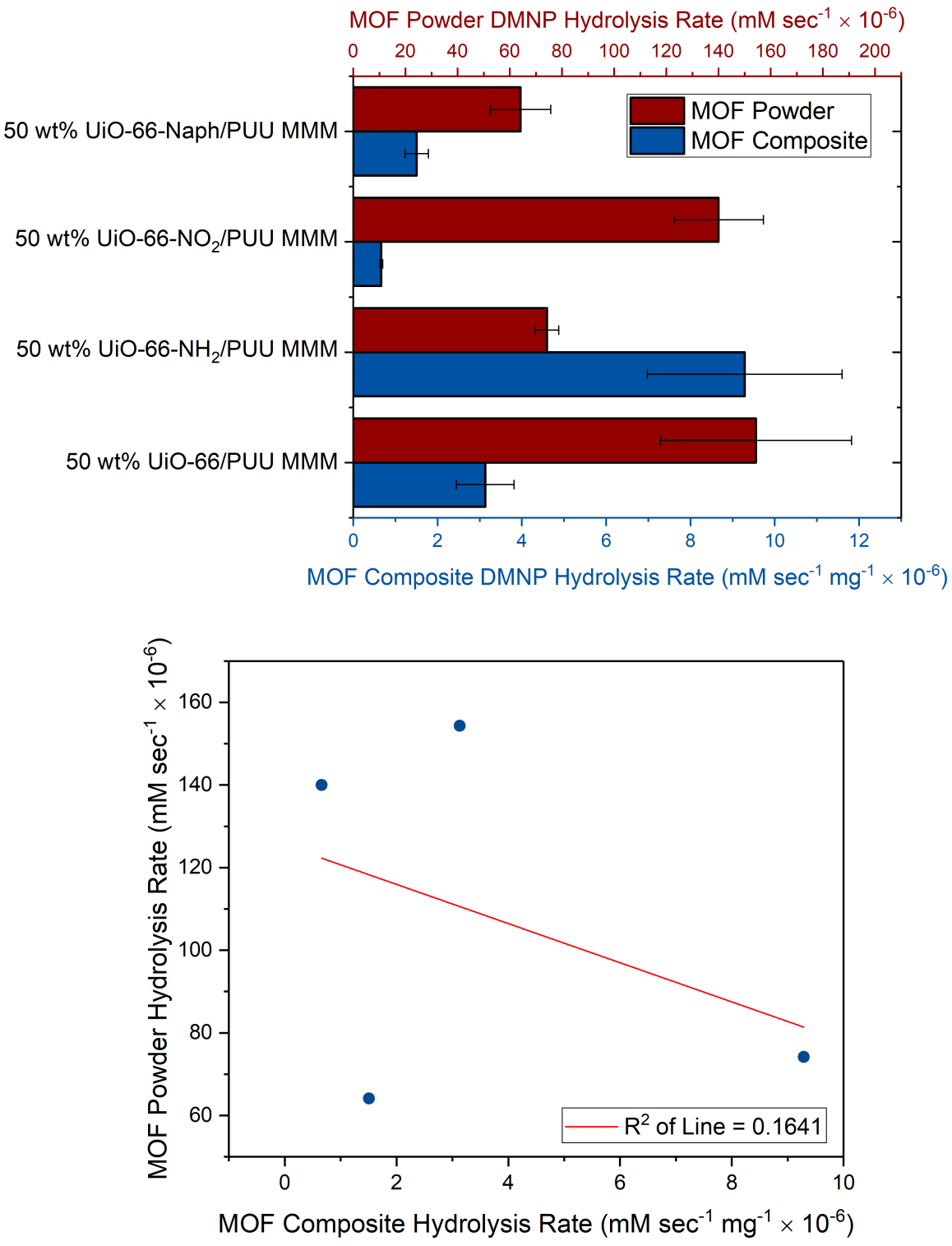


**Figure S5.12.** *Top:* DMNP hydrolysis rates for MOF powders (red) and MOF-polymer MMMs (blue, normalized to mass of composite). *Bottom*: Correlation plot of MOF powder and corresponding MOF/PUU MMM results.

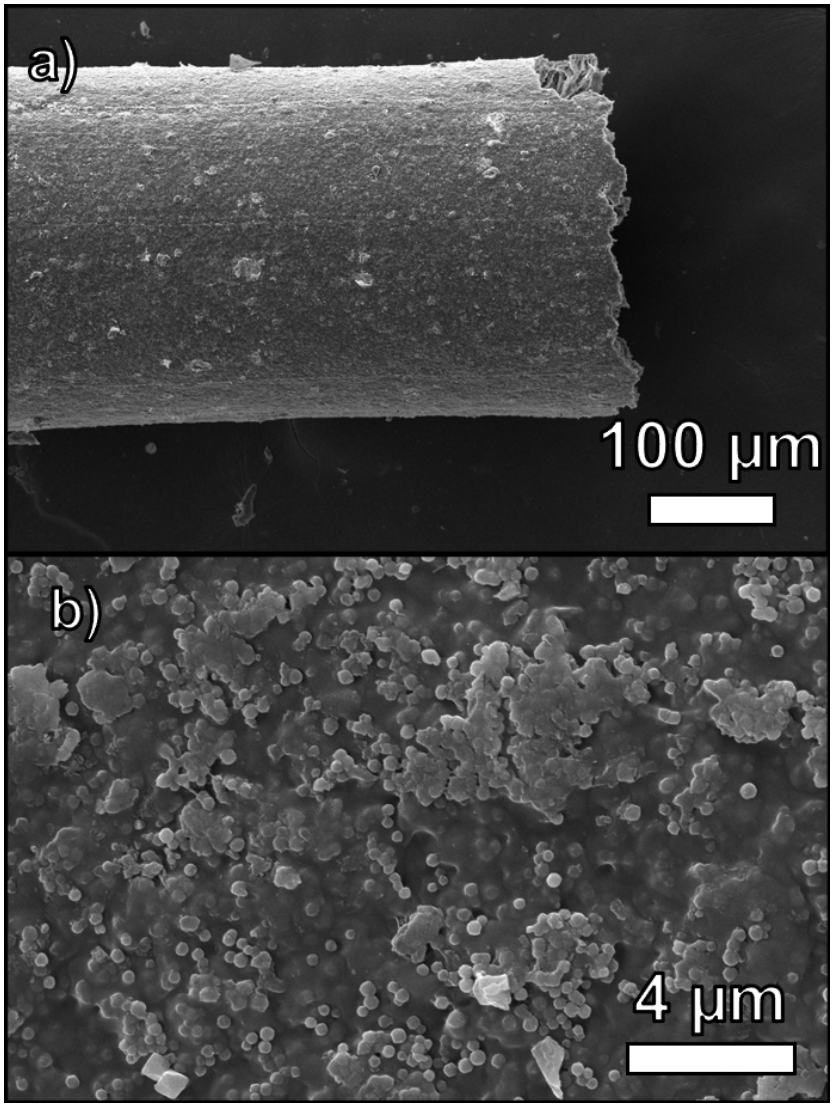


**Figure S5.13.** SEM images of exterior of 50 wt% UiO-66(Zr)/PUU fiber: a) full width end and b) surface structure.

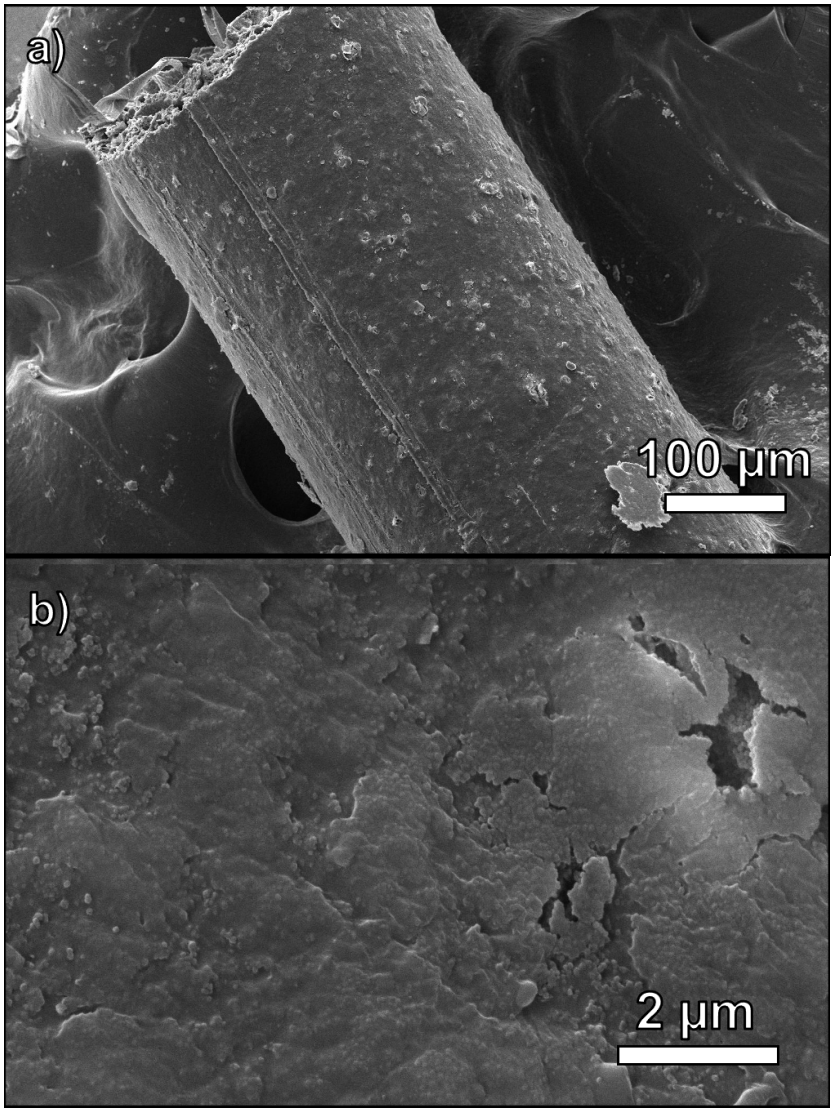


**Figure S5.14.** SEM images of exterior of 50 wt% UiO-66(Zr)-$NH_2$/PUU fiber: a) full width end and b) surface structure.

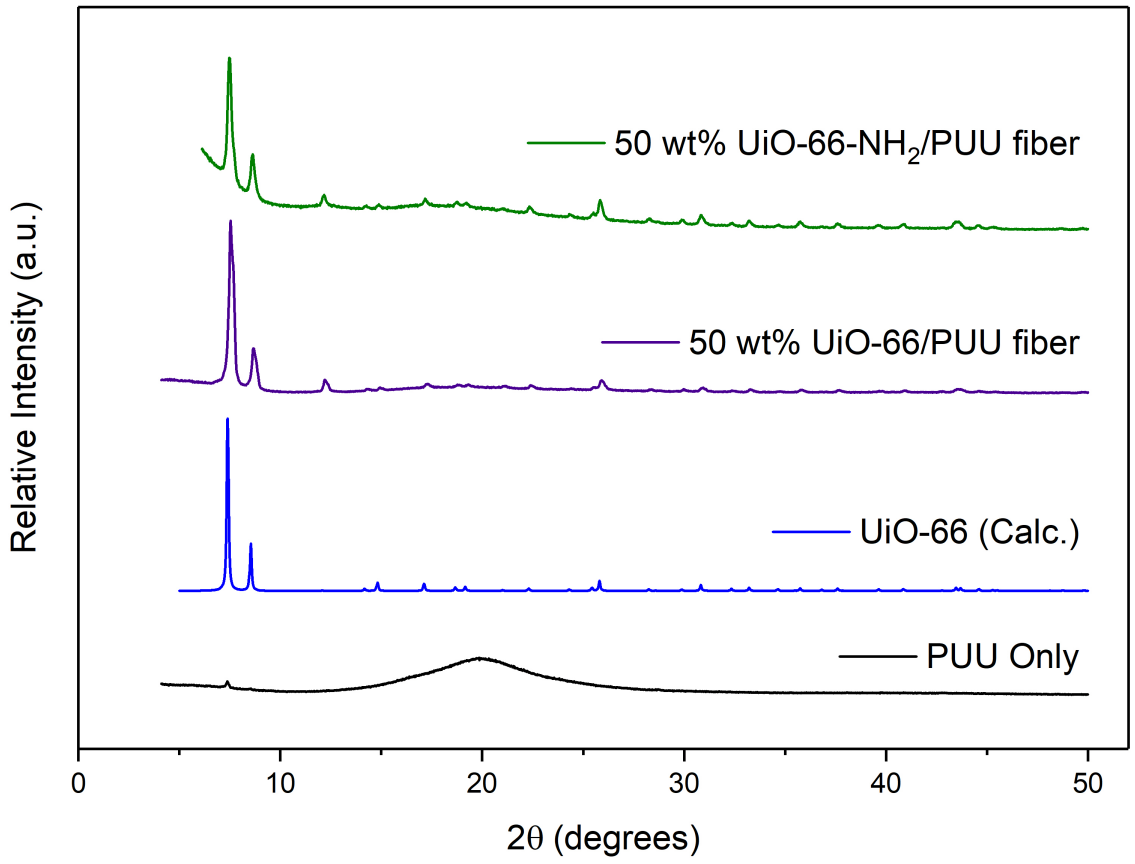


**Figure S5.15.** PXRD of PUU only, 50 wt% UiO-66(Zr)/PUU fiber, and 50 wt% UiO-66(Zr)-$NH_2$/PUU fiber.

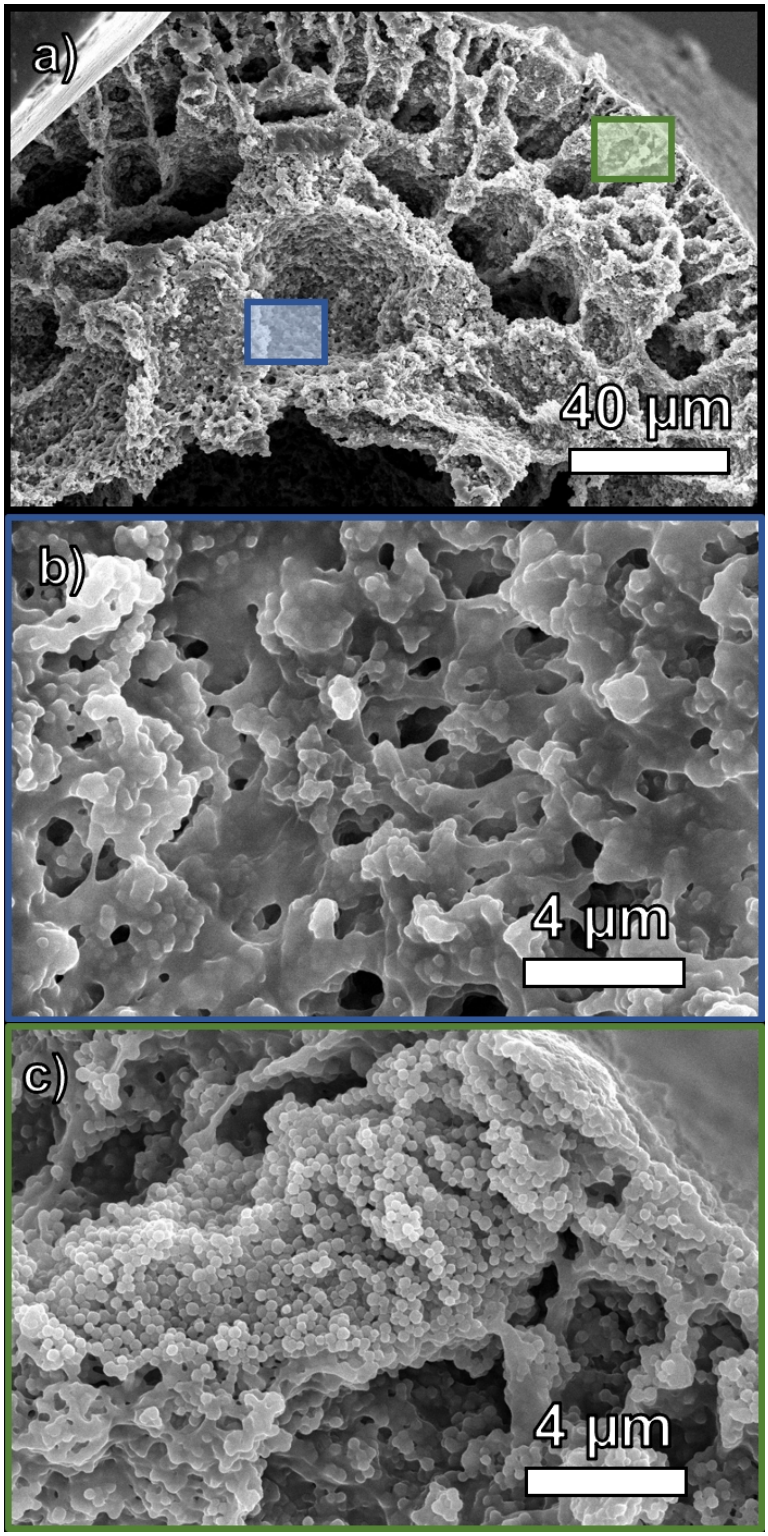


**Figure S5.16.** SEM images of interior of 50 wt% UiO-66(Zr)/PUU fiber: a) cross-section with highlighted segments, b) close up of blue highlighted area, and c) close up of green highlighted area.

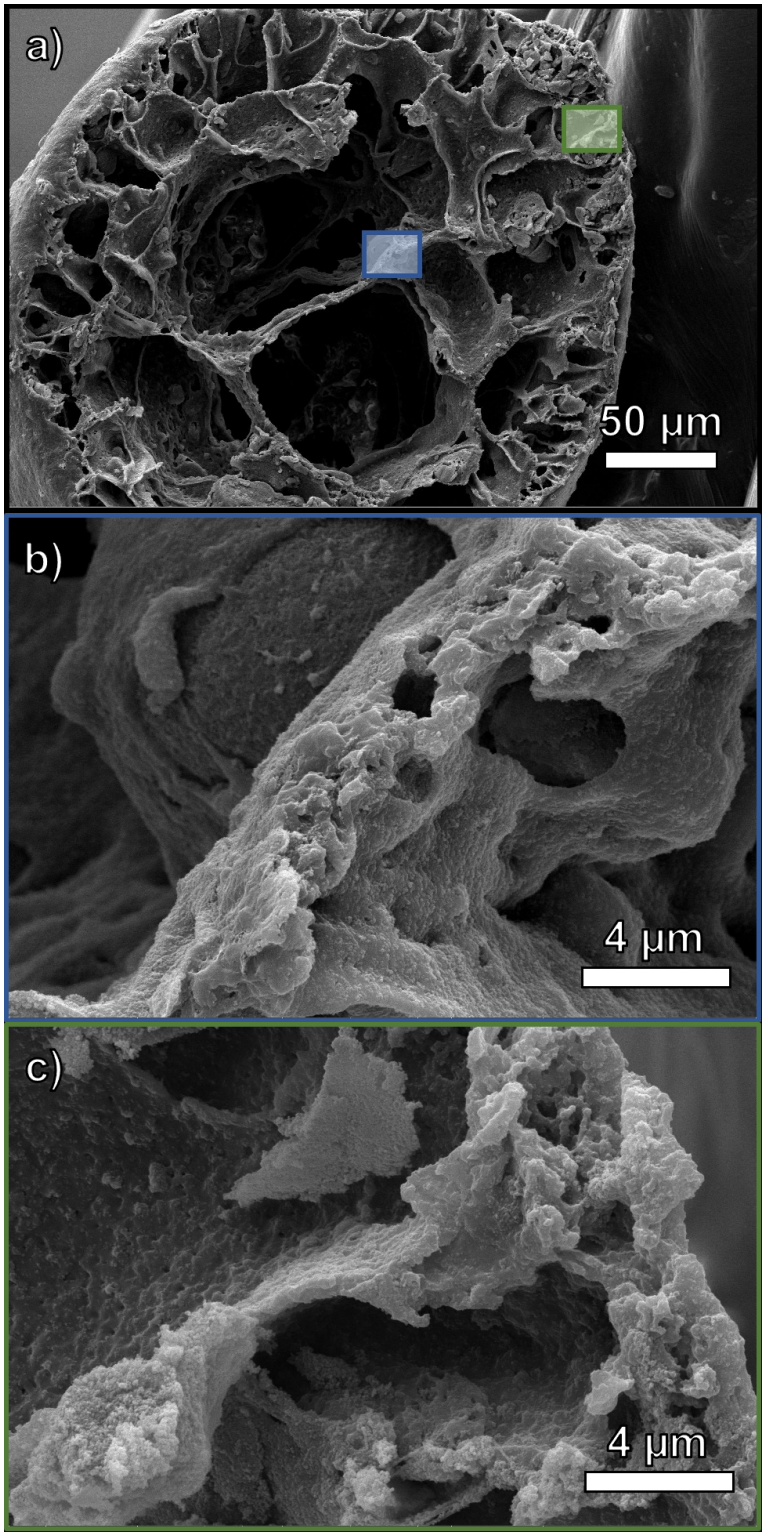


**Figure S5.17.** SEM images of interior of 50 wt% UiO-66(Zr)-$NH_2$/PUU fiber: a) cross-section with highlighted segments, b) close up of blue highlighted area, and c) close up of green highlighted area.

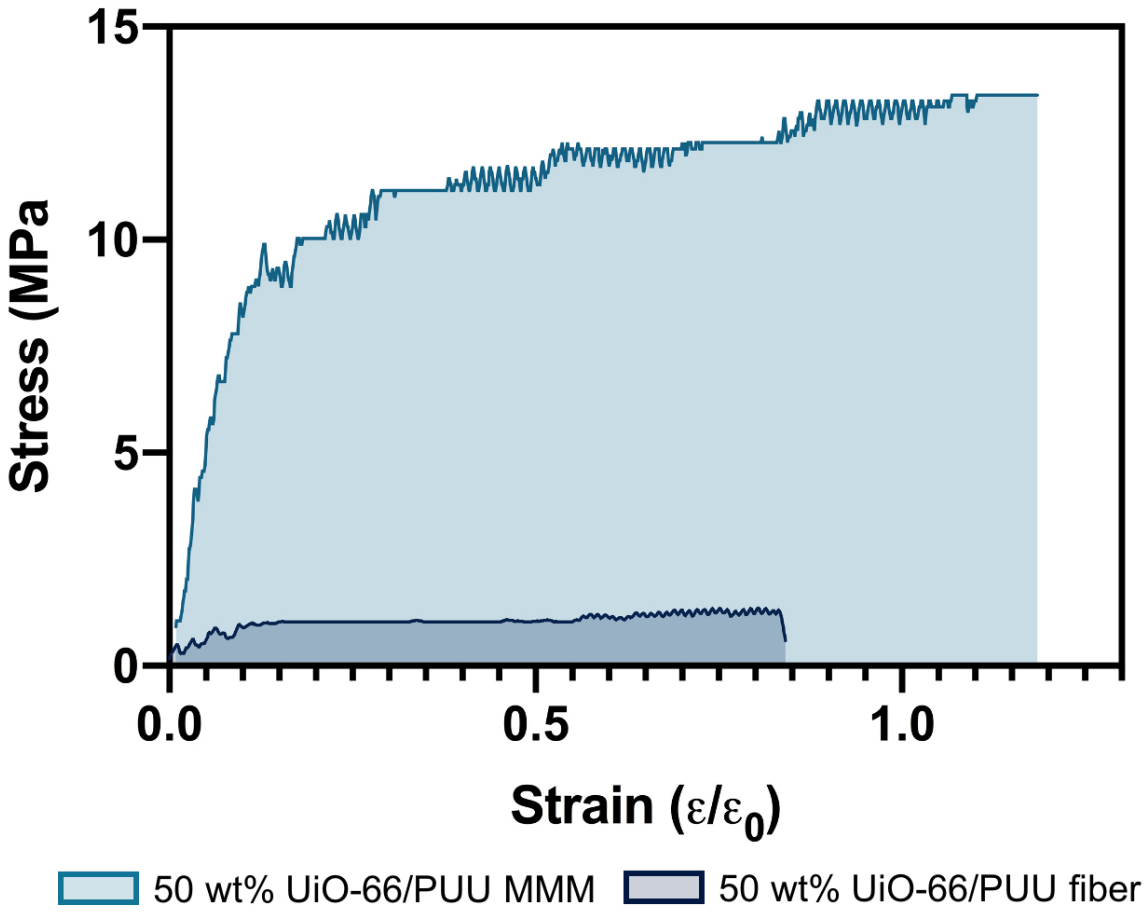


**Figure S5.18.** Tensile curves for representative samples of 50 wt% UiO-66(Zr)/PUU MMM and fiber.

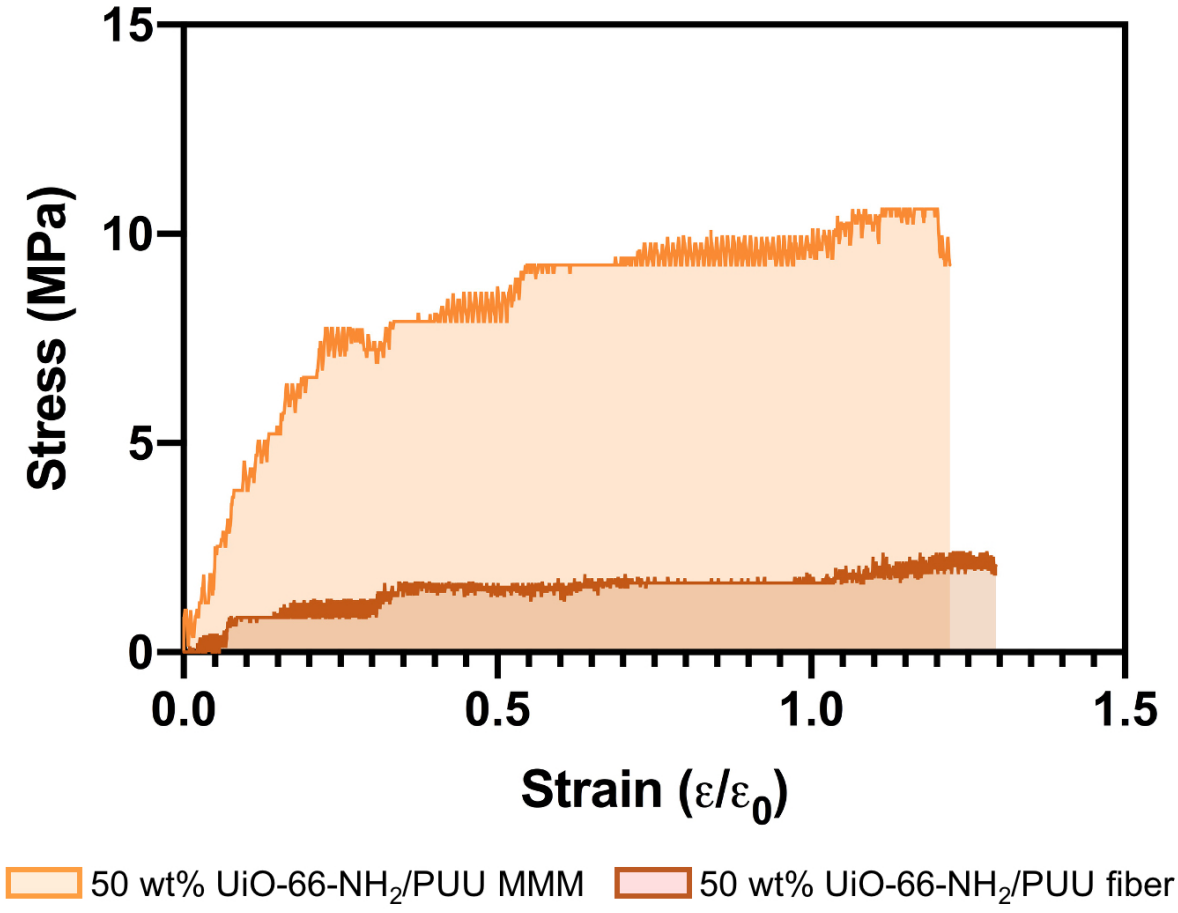


**Figure S5.19.** Tensile curves for representative samples of 50 wt% UiO-66(Zr)-$NH_2$/PUU MMM and fiber.

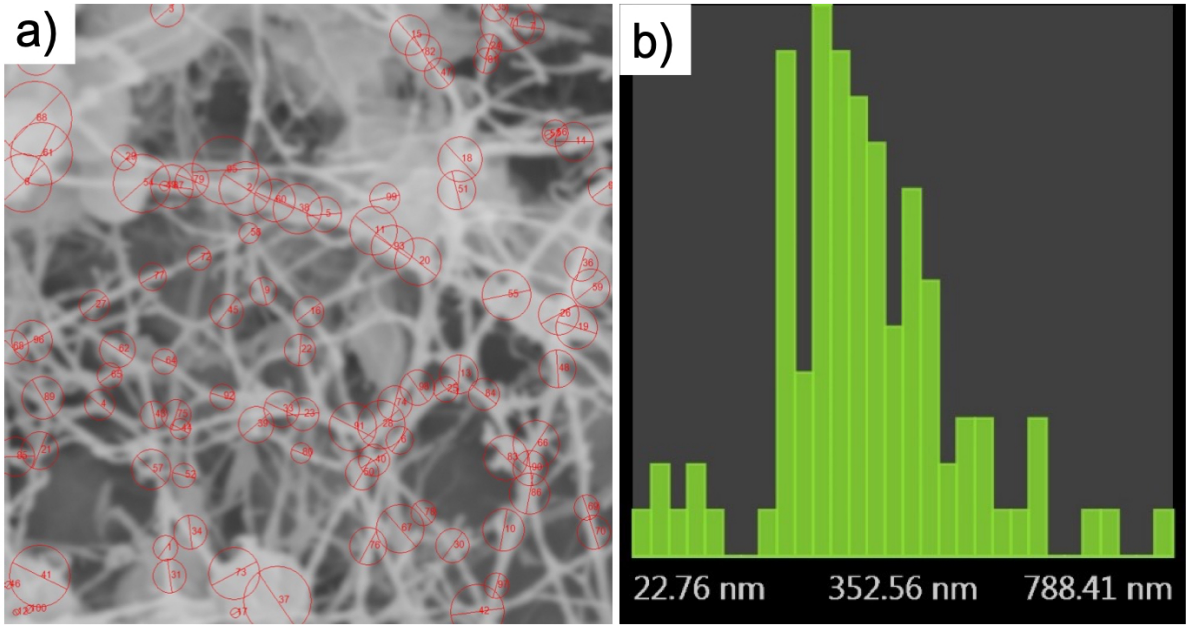


**Figure S5.20.** 20 wt% UiO-66(Zr)/PUU electrospun nanofiber diameter analysis.

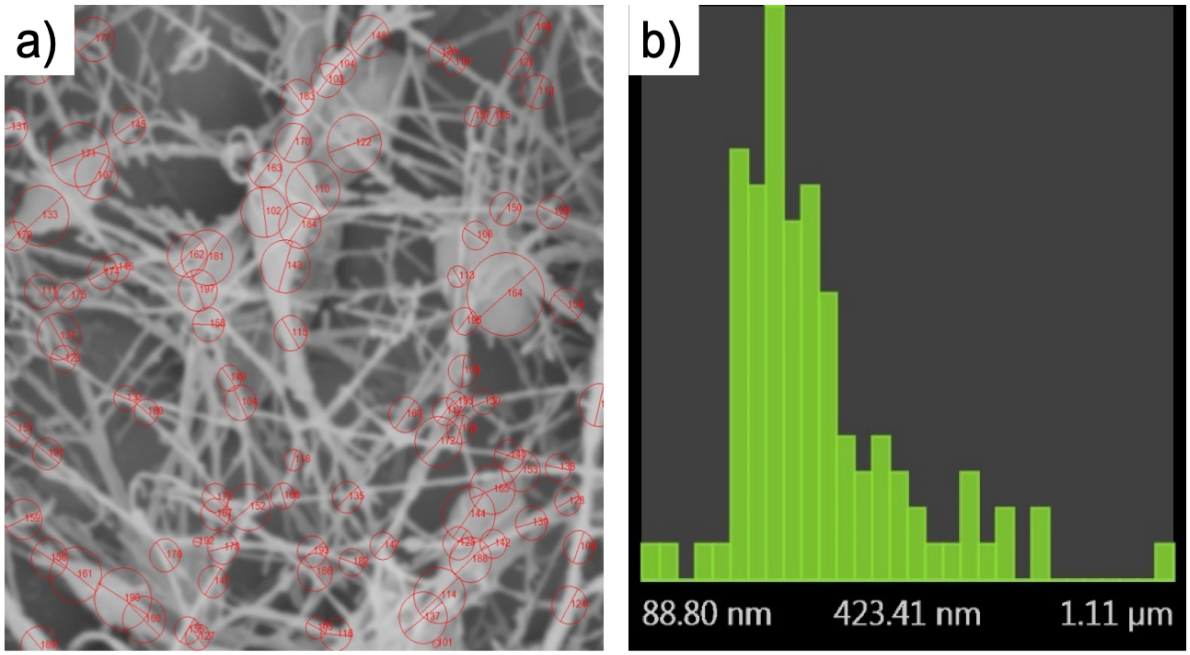


**Figure S5.21.** 20 wt% UiO-66(Zr)-$NH_2$/PUU electrospun nanofiber diameter analysis.

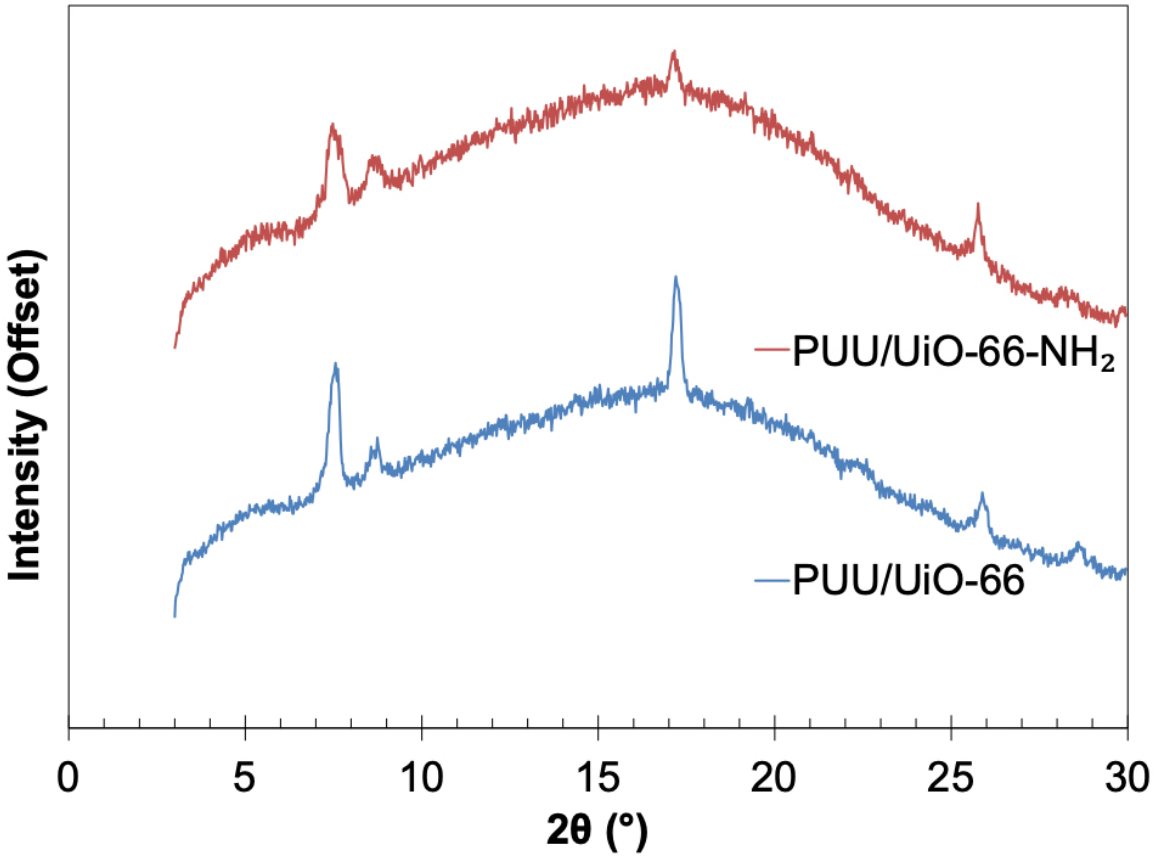


**Figure S5.22.** PXRD spectra for 20 wt% MOF/PUU electrospun nanofibers.

## 5.9 Acknowledgements

Chapter 5, in part, is a reprint of the following material "Joseph M. Palomba, David M. Wirth, Jin Yeong Kim, Evan M. Clarke, Gregory W. Peterson, Jonathan K. Pokorski, and Seth M. Cohen, Strong, Ductile MOF-Polyurethane Urea Composites" submitted for publication. The dissertation author was the primary author of this manuscripts and gratefully acknowledges the contributions of coauthors. The dissertation author also gratefully acknowledges the discussions and editing help of Dr. Brian R. Pimentel, Dr. Jessica C. Moreton, Dr. Sergio Ayala Jr., Dr. Kathleen E. Prosser, and Mark Kalaj.

## 5.10 References


1. Kalaj, M.; Bentz, K. C.; Ayala, S.; Palomba, J. M.; Barcus, K. S.; Katayama, Y.; Cohen, S. M., MOF-Polymer Hybrid Materials: From Simple Composites to Tailored Architectures. *Chem. Rev.* **2020,** *120*, 8267-8302.

2. Zhao, J.; Lee, D. T.; Yaga, R. W.; Hall, M. G.; Barton, H. F.; Woodward, I. R.; Oldham, C. J.; Walls, H. J.; Peterson, G. W.; Parsons, G. N., Ultra-Fast Degradation of Chemical Warfare Agents Using MOF–Nanofiber Kebabs. *Angew. Chem., Int. Ed.* **2016,** *55*, 13224-13228.

3. Barton, H. F.; Davis, A. K.; Parsons, G. N., The Effect of Surface Hydroxylation on MOF Formation on ALD Metal Oxides: MOF-525 on TiO2/Polypropylene for Catalytic Hydrolysis of Chemical Warfare Agent Simulants. *ACS Appl. Mater. Interfaces* **2020,** *12*, 14690-14701.

4. Peterson, G. W.; Lu, A. X.; Hall, M. G.; Browe, M. A.; Tovar, T.; Epps, T. H., MOFwich: Sandwiched Metal–Organic Framework-Containing Mixed Matrix Composites for Chemical Warfare Agent Removal. *ACS Appl. Mater. Interfaces* **2018,** *10*, 6820-6824.

5. Denny, M. S.; Kalaj, M.; Bentz, K. C.; Cohen, S. M., Multicomponent metal–organic framework membranes for advanced functional composites. *Chem. Sci.* **2018,** *9*, 8842-8849.

6. DeCoste, J. B.; Denny, J. M. S.; Peterson, G. W.; Mahle, J. J.; Cohen, S. M., Enhanced aging properties of HKUST-1 in hydrophobic mixed-matrix membranes for ammonia adsorption. *Chem. Sci.* **2016,** *7*, 2711-2716.

7. Liang, H.; Yao, A.; Jiao, X.; Li, C.; Chen, D., Fast and Sustained Degradation of Chemical Warfare Agent Simulants Using Flexible Self-Supported Metal–Organic Framework Filters. *ACS Appl. Mater. Interfaces* **2018,** *10*, 20396-20403.

8. Wang, S.; Pomerantz, N. L.; Dai, Z.; Xie, W.; Anderson, E. E.; Miller, T.; Khan, S. A.; Parsons, G. N., Polymer of intrinsic microporosity (PIM) based fibrous mat: combining particle filtration and rapid catalytic hydrolysis of chemical warfare agent simulants into a highly sorptive, breathable, and mechanically robust fiber matrix. *Mater. Today Adv.* **2020,** *8*, 100085.

9. Peterson, G. W.; Lu, A. X.; Epps, T. H., Tuning the Morphology and Activity of Electrospun Polystyrene/UiO-66-NH2 Metal–Organic Framework Composites to Enhance Chemical Warfare Agent Removal. *ACS Appl. Mater. Interfaces* **2017,** *9*, 32248-32254.

10. Kalaj, M.; Denny Jr, M. S.; Bentz, K. C.; Palomba, J. M.; Cohen, S. M., Nylon–MOF Composites through Postsynthetic Polymerization. *Angew. Chem., Int. Ed.* **2019,** *58*, 2336-2340.

11. Duan, P.; Moreton, J. C.; Tavares, S. R.; Semino, R.; Maurin, G.; Cohen, S. M.; Schmidt-Rohr, K., Polymer Infiltration into Metal–Organic Frameworks in Mixed-Matrix Membranes Detected in Situ by NMR. *J. Am. Chem. Soc.* **2019,** *141*, 7589-7595.

12. Sakurai, S.; Okamoto, Y.; Sakaue, H.; Nakamura, T.; Banda, L.; Nomura, S., Structure and properties of segmented poly(urethaneurea)s with relatively short hard-segment chains. *J. Polym. Sci. B* **2000,** *38*, 1716-1728.

13. Korinko, P.; Chapman, G. *Characterization Of Tensile Strength Of Glovebox Gloves*; United States, 2012; p 28.

14. Rego, A.; Roley, L., In-use barrier integrity of gloves: Latex and nitrile superior to vinyl. *Am. J. Infect. Control* **1999,** *27*, 405-410.

15. Wu, S., Phase structure and adhesion in polymer blends: A criterion for rubber toughening. *Polymer* **1985,** *26*, 1855-1863.

16. Katz, M. J.; Mondloch, J. E.; Totten, R. K.; Park, J. K.; Nguyen, S. T.; Farha, O. K.; Hupp, J. T., Simple and Compelling Biomimetic Metal–Organic Framework Catalyst for the Degradation of Nerve Agent Simulants. *Angew. Chem., Int. Ed.* **2014,** *126*, 507-511.

17. Kalaj, M.; Palomba, J. M.; Bentz, K. C.; Cohen, S. M., Multiple functional groups in UiO-66 improve chemical warfare agent simulant degradation. *Chem. Commun.* **2019,** *55*, 5367-5370.

18. Moreton, J. C.; Denny, M. S.; Cohen, S. M., High MOF loading in mixed-matrix membranes utilizing styrene/butadiene copolymers. *Chem. Commun.* **2016,** *52*, 14376-14379.

19. Moreton, J. C.; Palomba, J. M.; Cohen, S. M., Liquid-Phase Applications of Metal–Organic Framework Mixed-Matrix Membranes Prepared from Poly(ethylene-co-vinyl acetate). *ACS Appl. Polym. Materials* **2020,** *2*, 2063-2069.

20. Peterson, G. W.; Wang, H.; Au, K.; Epps III, T. H., Metal-Organic Framework-Polymer Composite Enhancement via Acyl Chloride Modification. *Polym. Inter.* **2020,** *n/a*.

21. Ma, L.; Svec, F.; Lv, Y.; Tan, T., Engineering of the Filler/Polymer Interface in Metal–Organic Framework-Based Mixed-Matrix Membranes to Enhance Gas Separation. *Chem. Asian J.* **2019,** *14*, 3502-3514.

22. Palomba, J. M.; Credille, C. V.; Kalaj, M.; DeCoste, J. B.; Peterson, G. W.; Tovar, T. M.; Cohen, S. M., High-throughput screening of solid-state catalysts for nerve agent degradation. *Chem. Commun.* **2018,** *54*, 5768-5771.

23. Kalaj, M.; Cohen, S. M., Spray-Coating of Catalytically Active MOF–Polythiourea through Postsynthetic Polymerization. *Angew. Chem., Int. Ed.* **2020,** *59*, 13984-13989.

24. Zhang, Y.; Yuan, S.; Feng, X.; Li, H.; Zhou, J.; Wang, B., Preparation of Nanofibrous Metal–Organic Framework Filters for Efficient Air Pollution Control. *J. Am. Chem. Soc.* **2016,** *138*, 5785-5788.

25. Rouquerol, J.; Llewellyn, P.; Rouquerol, F., Is the bet equation applicable to microporous adsorbents? In *Studies in Surface Science and Catalysis*, Llewellyn, P. L.; Rodriquez-Reinoso, F.; Rouqerol, J.; Seaton, N., Eds. Elsevier: 2007; Vol. 160, pp 49-56.

26. Denny Jr, M. S.; Cohen, S. M., In Situ Modification of Metal–Organic Frameworks in Mixed-Matrix Membranes. *Angew. Chem., Int. Ed.* **2015,** *54*, 9029-9032.